



Electron and phonon transport in disordered thermoelectric materials : dimensional confinement, resonant scattering and localization

Simon Thébaud

► To cite this version:

Simon Thébaud. Electron and phonon transport in disordered thermoelectric materials : dimensional confinement, resonant scattering and localization. Physics [physics]. Université de Lyon, 2019. English. NNT : 2019LYSE1168 . tel-02356350

HAL Id: tel-02356350

<https://theses.hal.science/tel-02356350v1>

Submitted on 8 Nov 2019

HAL is a multi-disciplinary open access archive for the deposit and dissemination of scientific research documents, whether they are published or not. The documents may come from teaching and research institutions in France or abroad, or from public or private research centers.

L'archive ouverte pluridisciplinaire **HAL**, est destinée au dépôt et à la diffusion de documents scientifiques de niveau recherche, publiés ou non, émanant des établissements d'enseignement et de recherche français ou étrangers, des laboratoires publics ou privés.



N° d'ordre NNT : xxx

THÈSE DE DOCTORAT DE L'UNIVERSITÉ DE LYON

opérée au sein de
l'Université Claude Bernard Lyon 1

École Doctorale ED52
Physique et Astrophysique de Lyon
Spécialité de doctorat : Physique

Soutenue publiquement le 25/09/2019, par :
Simon Thébaud

Electron and phonon transport in disordered thermoelectric materials: dimensional confinement, resonant scattering and localization

Devant le jury composé de :

Didier Mayou , Directeur de Recherche CNRS, Institut Néel	Rapporteur
Andrés Saúl , Directeur de Recherche CNRS, Université Aix-Marseille	Rapporteur
Abdul-Rahman Allouche , Professeur des Universités, Université Claude Bernard Lyon 1	Examinateur
Giorgia Fugallo , Chargée de Recherche CNRS, Université de Nantes	Examinatrice
Laurence Magaud , Directrice de Recherche CNRS, Institut Néel	Examinatrice
Jéléna Sjakste , Chargée de Recherche CNRS, École Polytechnique	Examinatrice
Georges Bouzerar , Directeur de Recherche CNRS, Université Claude Bernard Lyon 1	Directeur de thèse
Christophe Adessi , Maître de Conférences, Université Claude Bernard Lyon 1	Co-directeur de thèse

Acknowledgements

First of all, I would like to express my sincere gratitude toward my supervisors, whose guidance and leadership have been invaluable throughout my PhD work. Georges Bouzerar has always been extremely present to offer crucial insights and to share his vast knowledge of condensed matter. He has taught me a great deal about many aspects of academic research, going above and beyond his duty as a supervisor. His level of commitment and his true passion for physics should be honored, and his contribution to this work cannot be overstated. Christophe Adessi's expertise of *ab initio* simulations have been crucial for my PhD work and my training as a theoretician. I have greatly appreciated his presence, his support and his readiness to teach me. His door was always open, and I am very thankful for his patience and kindness.

I would like extend my appreciation to Didier Mayou and Andrés Saúl, who took the time to evaluate my manuscript, and to Abdul-Rahman Allouche, Giorgia Fugallo, Laurence Magaud and Jéléna Sjakste, who accepted to be part of my thesis committee. I feel honored that I had the opportunity to discuss my work with them.

I wish to thank Patrice Mélinon and the Materials for Energy team of the Institute of Light and Matter (ILM), for their support and discussions through my PhD years. I am also grateful to the Physics and Astrophysics (PHAST) doctoral school for their help. It is with their financial support that I could attend a three-week summer school in Trieste. I must acknowledge the administrative and maintenance staff of ILM, as well as the secretariat of the physics department at Claude Bernard Lyon 1 University, for taking care of many practical and administrative issues. Special thanks are due to the personnel managing the computer ressources of ILM and the Scientific Pole of Numerical Modelization (PSMN), which I used intensively in the course of my work.

I would be remiss if I failed to mention my friends who supported me during these last three years. I consider myself extremely lucky to have met at the lab such wonderful people as Lucile, who truly inspired me to be a better person, Mehdi, with whom I could endlessly discuss both physics and history, Cassandre with her inexhaustible positive energy, not to forget Bahareh, Ong, Akash, Nicolas, Romain, Fatemeh, Kevin, Samir... I wish them all success in their PhD and beyond. Even as they were far away, I could always count on the support of my dear friends from Ecole Normal Supérieure: Thibaud, Denis, Guillaume, Laura, Flora and Marion.

Last but not least, my gratitude goes to my family, with special thanks to my mother and sister. It was always a blast when they came to Lyon, and I am forever indebted to them for their help and for everything else.

Contents

1	Introduction: thermoelectricity	1
1.1	Thermoelectric power generation	4
1.1.1	The Seebeck effect	4
1.1.2	Device efficiency: the figure of merit	5
1.2	The search for efficient thermoelectric materials	9
1.2.1	Suppressing the thermal conductivity	12
1.2.2	Enhancing the power factor	15
1.3	Content of the thesis	19
2	Modelling thermoelectric transport from first-principles	21
2.1	Electron and phonon structure of solids	22
2.1.1	Density functional theory	23
2.1.2	From DFT to tight-binding: Wannier orbitals	30
2.1.3	Vibrations in solids: Dynamical matrix	33
2.2	Electron and phonon quantum transport	37
2.2.1	Semi-classical treatment of the diffusive regime	38
2.2.2	Ballistic regime: the Landauer formalism	47
3	Electronic transport in oxides	51
3.1	Unified modelling of the thermoelectric properties in SrTiO_3	51
3.1.1	The tight-binding Hamiltonian and transport calculations	52
3.1.2	The thermoelectric properties	55
3.2	Absence of confinement in $(\text{SrTiO}_3)/(\text{SrTi}_{0.8}\text{Nb}_{0.2}\text{O}_3)$ superlattices	59
3.2.1	Theoretical modelling of the thermoelectric properties	61
3.2.2	Ruling out the confinement scenario	62
3.3	Investigating the high-temperature thermoelectric properties of n-type rutile TiO_2	66
3.3.1	Modelling electron transport in rutile TiO_2	67
3.3.2	The thermoelectric properties from ambient to high temperatures	72
4	Dealing with disorder	77
4.1	Impurity states and resonances: Green's functions	78
4.1.1	Single-particle properties: the self-energy	78
4.1.2	The phonon Green's function	83

4.2	Quantum linear transport and localization: the Kubo formalism	85
4.2.1	Anderson localization	88
4.3	Practical calculations and numerical methods	90
4.3.1	Exact diagonalization	90
4.3.2	The Chebyshev Polynomial Green's Function method	91
5	Boosting the power factor: resonant states	95
5.1	Large enhancement of the thermoelectric power factor in disordered materials through resonant scattering	98
5.1.1	Disordered model Hamiltonian and methodology	98
5.1.2	Boosting the power factor	101
5.1.3	The influence of the model parameters	104
5.2	Ab initio investigation of the role of vanadium impurity states in SrTiO_3 for thermoelectricity	108
5.2.1	Computing the thermoelectric properties	109
5.2.2	vanadium doping	109
5.2.3	Co-doping	112
5.3	Resonant states and vanadium doping in SrTiO_3 , BaTiO_3 and CaTiO_3 : ef- fects of disorder and localization on the thermoelectric properties	115
5.3.1	Anderson localization from vanadium doping in SrTiO_3	115
5.3.2	Resonant states in SrTiO_3 , BaTiO_3 and CaTiO_3	121
6	Defects in two-dimensional materials	127
6.1	First principle investigation on thermoelectric properties of transition metal dichalcogenides: beyond rigid band model	128
6.1.1	Theoretical framework	129
6.1.2	Rigid band model	130
6.1.3	Realistic doping	133
6.1.4	Influence of the disorder	138
6.2	Drastic effects of vacancies on thermal transport in graphene	140
6.2.1	Exact disorder contribution to the phonon dispersion and lifetimes	141
6.2.2	Effects of vacancies on the thermal conductivity	147
6.2.3	Size effects and phonon mean free paths	151
	Conclusions and perspectives	157
A	The Callaway theory in graphene	163
B	The current density operator in tight-binding representation	165
C	The Kubo formalism of quantum transport	169
D	The Drude formalism and the sum rule	175
E	The convergence of the CPGF method	179

Chapter 1

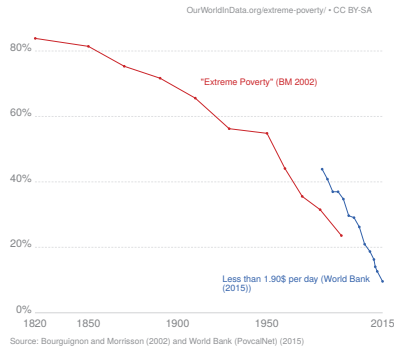
Introduction: thermoelectricity

The team that brings clean and abundant energy to the world will benefit humanity more than all of history's saints, heroes, prophets, martyrs, and laureates combined.

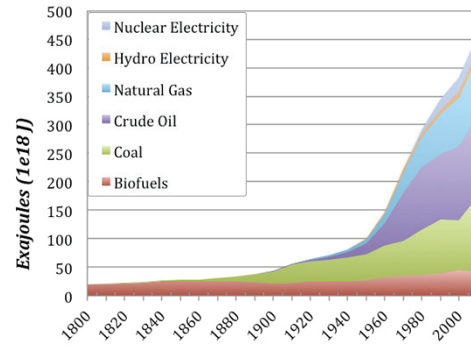
Steven Pinker, *Enlightenment Now: The Case for Reason, Science, Humanism, and Progress.*

Over the past decades, the world has grown increasingly aware that it is heading for disaster. Since the early XIXth century, when 90% of mankind was still living in extreme poverty and the industrial revolution was just starting to bear its fruits, humanity has been enjoying an ever greater degree of material wealth (see [1, 2, 3] and Fig 1.1a). Today, the proportion of people living in extreme deprivation is only 10% and the United Nations aim to eliminate extreme poverty by the middle of the XXIst century [4]. Thanks to machines and industries providing us with food, shelter, furniture, heating, transportation and entertainment, the average European lives like a king by our ancestors' standards [5]. However, this amazing, absolutely unprecedented progress has mostly been powered by the consumption of fossil fuel — coal, oil and natural gas, see [6] and Fig 1.1b — and this arrangement is now clearly unsustainable.

The issue with fossil fuels is twofold. First, as their names suggest, fossil fuels take millions of year to form, and we are burning them at a much faster rate. This was not an issue in the early days of the industrial revolution, because their amount seemed inexhaustible then, but if we keep going like this our proven reserves of oil and natural gas will be depleted by the end of the century [8]. Second, and this is even more alarming, fossil fuels emit greenhouse gas into the atmosphere when they burn, which is responsible for around two-thirds of anthropogenic greenhouse gas emissions, see [9] and Fig 1.2a. This is the primary cause of climate change, a process that comes with a host of extremely unpleasant consequences. Among them, the sea level is expected to rise due to the thermal expansion of water, leading to coastal flooding and threatening many large cities. At the same time, whole regions will suffer accelerated desertification and will be subjects to shortages of water and food. Extreme weather events, such as floods, droughts and storms,



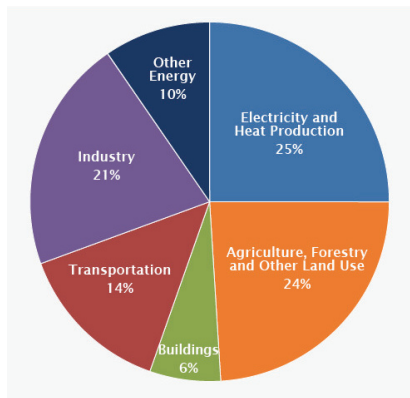
(a) From Ref. [3], share of the human population in extreme poverty from 1820 to 2015.



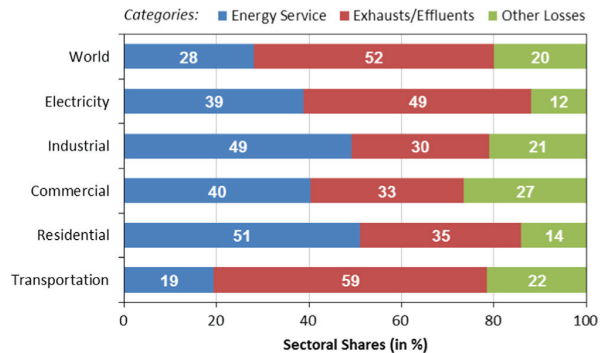
(b) From Ref. [7], Global energy consumption per year from 1800 to 2010.

Figure 1.1

will also be more frequent. Though estimates are flawed and unreliable [10], it seems clear that these changes will displace tens of millions of people by mid-century. The severity of these consequences will largely depend on the efficiency with which we will constrain our greenhouse gas emissions. If we are intent on preserving the basis of our modern way of life and on extending the fruits of progress to people still trapped in poverty, we must transition our energy sources from fossil fuels to carbon-free, sustainable alternatives. We also need to reduce our energy consumption, at least until our economy is sufficiently decarbonized to address the immediate danger of global warming.



(a) From Ref. [11], global greenhouse gas emissions by economic sector.



(b) From Ref. [12], the shares of energy that is useful (service) or lost (exhausts, others), by economic sector.

Figure 1.2

Scientists and engineers around the world have taken on the challenge. One obvious possibility is to exploit the abundant energy of the sun, and although the technology of

crystalline silicon photovoltaics is already quite mature, research is still ongoing to find cheaper and more efficient materials [13]. Solar and wind power have come to epitomize renewable energy solutions, but the power output of solar panels and wind turbines is as capricious as the weather. In order to manage these distributed and intermittent power sources and to accelerate the replacement of combustion-based vehicles by electric cars, researchers have been working on smart energy grids as well as cleaner, more efficient batteries and supercapacitors [14, 15]. Another avenue for low-emission electricity production is nuclear power, which is far safer than fossil fuels and emits very little greenhouse gas [16]. However, since expanding the use of current fission reactors face a number of economic and societal obstacles, research in next-generation nuclear power and fusion technology is crucial to the global energy transition [17]. It seems clear that the pathway towards a decarbonized economy will inevitably feature a mix of these innovative technologies [18] along with several others, such as carbon capture and storage techniques [19, 20], geothermal energy [21] and waste heat harvesting by thermoelectric devices.

Thermoelectric modules are essentially solid-state heat engines that create a voltage when placed in a thermal gradient, and can thus directly convert heat into electrical energy. This technology could have huge applications, because part of the energy transition is an effort to cut down waste and increase energy efficiency. Although much is being done to weatherize city buildings and individual houses, around two thirds of the energy used in the world is wasted in heat, see [12] and Fig 1.2b. The transportation and industrial sector, in particular, generate large amounts of high-temperature heat, a significant portion of which can theoretically be converted into electrical energy within the constraint of Carnot efficiency. There are considerable opportunities for improving the energy efficiency of many industrial manufacturing processes, such as steelmaking, if enough progress is made on thermoelectric devices [22]. In the transportation sector, prototypes of cars and trucks fitted with thermoelectric modules have been realized and tested, and it is estimated that the development of better, cheaper devices could cut fuel usage by around 10% [23, 24]. Aircraft engines and ship incinerators represent another potential source of energy. Research is also ongoing to improve photovoltaic generators by adding a thermoelectric device on it, or even to concentrate sunrays directly onto a thermoelectric module [25, 26, 27].

While much effort should be directed towards improving energy efficiency in the developed world, helping people currently trapped in extreme poverty to reach higher standards of living remains an ethical imperative. Around 15% of the world population still lacks access to electricity, and an even greater proportion has to use wood and organic waste for heating and cooking, which is inefficient and leads to indoor air pollution due to incomplete combustion [28]. In remote villages, connecting to the energy grid is simply not an option, so thermoelectric devices exploiting the heat from household stoves could significantly improve quality of life [23]. Such devices, which could fan air into the stove to make the combustion complete in addition to lighting up a LED or charging a mobile phone, would need to be cheap and widely available to make a difference.

Rising up to the global challenge of preserving and spreading the fruits of modernity will require a sustained research effort in many technological areas. It seems clear that thermoelectricity can be part of the solution if cheaper and more efficient heat harvesting devices are developed.

1.1 Thermoelectric power generation

1.1.1 The Seebeck effect

The physical effect behind thermoelectric power generation was discovered by T. J. Seebeck in 1821, and was thus named after him. An illustration of the Seebeck effect is shown in Fig 1.3. A material, say a semiconductor, is placed in a thermal gradient, with an extremity at the temperature T_c and the other at $T_h > T_c$. The charge carriers (electrons and holes) are more energetic at the hot end, so they move towards the cold end, generating a diffusive charge current density \vec{j}_T . This current creates a charge depletion at the hot end and an accumulation at the cold end, giving rise to a voltage ΔV across the material. A steady state is reached when the current density \vec{j}_V caused by this voltage compensates \vec{j}_T . The so-called Seebeck coefficient S (sometimes also noted α) can then be defined as the ratio of the voltage over the temperature difference:

$$S = -\frac{\Delta V}{T_h - T_c}. \quad (1.1)$$

The current generated by the thermal gradient, \vec{j}_T , can be derived from the balance equation $\vec{j}_T + \vec{j}_V = \vec{0}$. For a homogeneous material characterized by a conductivity σ , $\vec{j}_V = -\sigma \vec{\nabla} V$ with $\vec{\nabla} V = -S \vec{\nabla} T$, so we find

$$\vec{j}_T = -\sigma S \vec{\nabla} T. \quad (1.2)$$

This simple physical picture already gives valuable information. First, the voltage generated by the Seebeck effect is static. Second, the sign of S depends on the nature of the charge carrier. In Fig 1.3, the majority carriers are electrons (n-type) and $S < 0$, but if most carriers are holes (p-type), the surface charge and the sign of ΔV are reversed, giving $S > 0$. We will see later that this correspondance between the charge of the majority carrier and the sign of S , though verified in most cases, is not always true. Third, since minority carriers

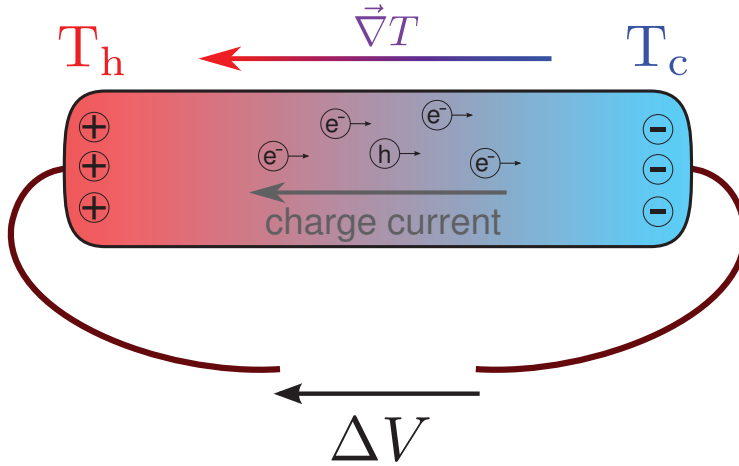


Figure 1.3: Illustration of the Seebeck effect.

transport charge in the direction opposite to majority carriers, their presence decreases the magnitude of the Seebeck coefficient. Indeed, bipolar conduction is one of the main limits on thermoelectric performance at high temperature. Finally, good metals tend to exhibit low Seebeck coefficients, because in these compounds a small voltage ΔV is sufficient to generate a large compensating current \vec{j}_V . For instance, S is around $\approx 1 \mu\text{V/K}$ in copper (a good metal), while it is $\approx -75 \mu\text{V/K}$ in bismuth (a semimetal) and $\approx 450 \mu\text{V/K}$ in intrinsic silicon (a semiconductor). Therefore, good thermoelectric materials are generally semimetals or semiconductors.

The reverse of the Seebeck effect also exists, and is called the Peltier effect. If a voltage is applied to a thermoelectric material, a heat current \vec{j}_Q is generated in addition to a charge current. Onsager showed that there is a symmetry between the two effects [29], so that

$$\vec{j}_Q = -\sigma ST \vec{\nabla} V. \quad (1.3)$$

The Peltier effect has been used for years in temperature control and refrigeration devices, and the development of more efficient thermoelectric modules would make them competitive as domestic refrigerators and heat pumps [24]. In particular, the replacement of R-134a in standard refrigerators by thermoelectric modules, in which the working gas is composed of electrons and holes, could yield significant environmental benefits. Though we will mostly have power generation in mind throughout this thesis, efforts to design better thermoelectric materials can also lead to applications in Peltier cooling.

1.1.2 Device efficiency: the figure of merit

The working principle of a thermoelectric generation module is shown in Fig 1.4. Like standard heat engines, it exploits the temperature difference between a heat source and

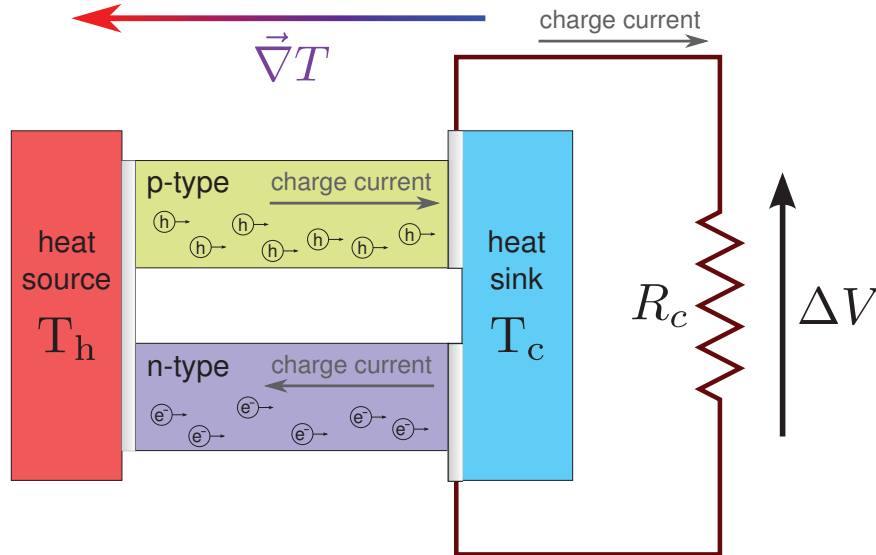


Figure 1.4: The concept of a thermoelectric generation module.

a heat sink. Two segments of thermoelectric material, called the legs of the module, are placed between the heat source and sink. They are connected to each other and to a charge resistance R_c by metallization layers. One segment is n-type and the other is p-type, so that the currents generated in the legs by the Seebeck effect reinforce each other. A portion of the heat flux ϕ pouring out of the heat source through the legs is therefore converted into an electrical current I , providing a power $R_c I^2$ to the charge. Neglecting the heat flux escaping in other ways and the energy sometimes needed to cool the heat sink, the efficiency of the device writes

$$\eta = \frac{R_c I^2}{\phi}. \quad (1.4)$$

It can be calculated by solving the full set of equations for the charge current density \vec{j} and the thermal current density \vec{j}_Q in the legs:

$$\vec{j} = -\sigma \vec{\nabla} V - \sigma S \vec{\nabla} T, \quad (1.5)$$

$$\vec{j}_Q = -\sigma S T \vec{\nabla} V - \kappa_0 \vec{\nabla} T, \quad (1.6)$$

where κ_0 is the thermal conductivity in the absence of electric field, i.e. in closed circuit. The last term in equation (1.5) comes from the Seebeck effect, equation (1.2), while the first term in the right hand side of equation (1.6) comes from the Peltier effect, equation (1.3). It is convenient to define a thermal conductivity κ in open circuit, when no electrical current is present, which differs from κ_0 due to the Seebeck effect. Replacing $\vec{\nabla} V$ from equation (1.5) in equation (1.6) yields:

$$\vec{j}_Q = S T \vec{j} - \kappa \vec{\nabla} T, \quad (1.7)$$

with

$$\kappa = \kappa_0 - \sigma S^2 T. \quad (1.8)$$

Assuming uniform conductivities and Seebeck coefficients in the thermoelectric legs, equations (1.5) and (1.7), together with the equations governing the charge conservation $\vec{\nabla} \cdot \vec{j} = 0$ and the energy conservation $\vec{\nabla} \cdot (\vec{j}_Q + V \vec{j}) = 0$, can be solved [30, 31]. This yields an expression for the heat flux and for the electrical current

$$\phi = (K_p + K_n)(T_h - T_c) + (S_p - S_n)T_h I - \frac{(R_p + R_n)I^2}{2}, \quad (1.9)$$

$$I = \frac{(S_p - S_n)(T_h - T_c)}{R_p + R_n + R_c}, \quad (1.10)$$

where K_p, S_p, R_p (resp. K_n, S_n, R_n) are the thermal conductance, Seebeck coefficient and electrical resistance of the p-type leg (resp. n-type leg). The combinations $K_p + K_n$ and $R_p + R_n$ appear because the legs are electrically in series and thermally in parallel. Also, recall that $S_p > 0$ and $S_n < 0$. The first term in the right-hand side of equation (1.9) is simply the usual heat diffusion that would flow from the heat source in the absence of current. The second is associated with the Peltier effect, and the third represents half the energy dissipated by joule heating in the legs (the other half is rejected to the heat sink).

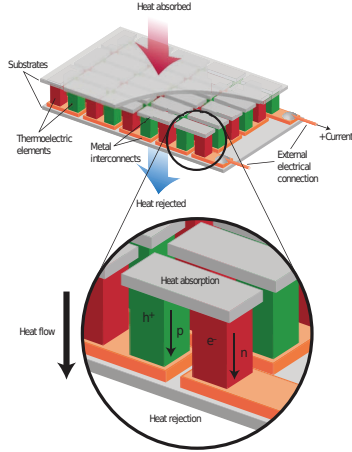
The thermoelectric module is electrically equivalent to a DC voltage generator of amplitude $(S_p - S_n)(T_h - T_c)$ in series with a resistance $R_p + R_n$, which gives equation (1.10). Replacing I and ϕ in equation (1.4) yields an expression for the device efficiency that depends on the charge resistance R_c , which should be dimensioned with respect to the module. Optimizing the efficiency with respect to the charge resistance gives R_c of the same order of magnitude as $R_n + R_p$, and an optimal efficiency

$$\eta = \frac{T_h - T_c}{T_h} \frac{\sqrt{1 + Z\bar{T}} - 1}{\sqrt{1 + Z\bar{T}} + \frac{T_c}{T_h}}, \quad (1.11)$$

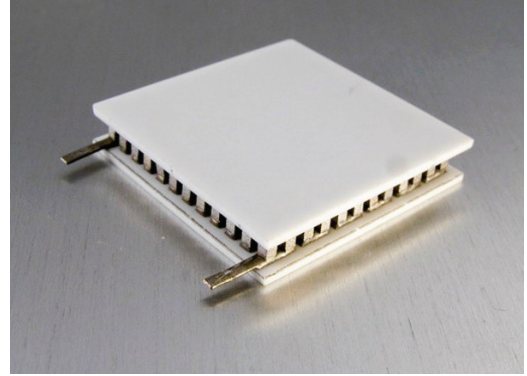
where $\bar{T} = \frac{T_h + T_c}{2}$ and $Z = \frac{(S_p - S_n)^2}{(R_p + R_n)(K_p + K_n)}$. If the sections of the legs are further optimized to minimize $(R_p + R_n)(K_p + K_n)$, $Z\bar{T}$ becomes [31, 32]

$$Z\bar{T} = \frac{(S_p - S_n)^2}{\left(\sqrt{\frac{\kappa_p}{\sigma_p}} + \sqrt{\frac{\kappa_n}{\sigma_n}}\right)^2 \bar{T}}, \quad (1.12)$$

where κ_p and σ_p (resp. κ_n and σ_n) are the thermal and electrical conductivities of the p-type leg (resp. n-type leg). $Z\bar{T}$ is called the figure of merit of the device, and depends only on intrinsic bulk properties of the thermoelectric materials composing the legs. It was calculated here assuming that the Seebeck coefficients and conductivities of these compounds are uniform, but in reality they depend on the temperature, which is non-uniform. Therefore, the relevant quantity is the temperature-average figure of merit, $\bar{Z\bar{T}}$. For given T_c and T_h , the optimal efficiency is an increasing function of $\bar{Z\bar{T}}$, and η tends to the Carnot efficiency if $\bar{Z\bar{T}} \rightarrow \infty$.



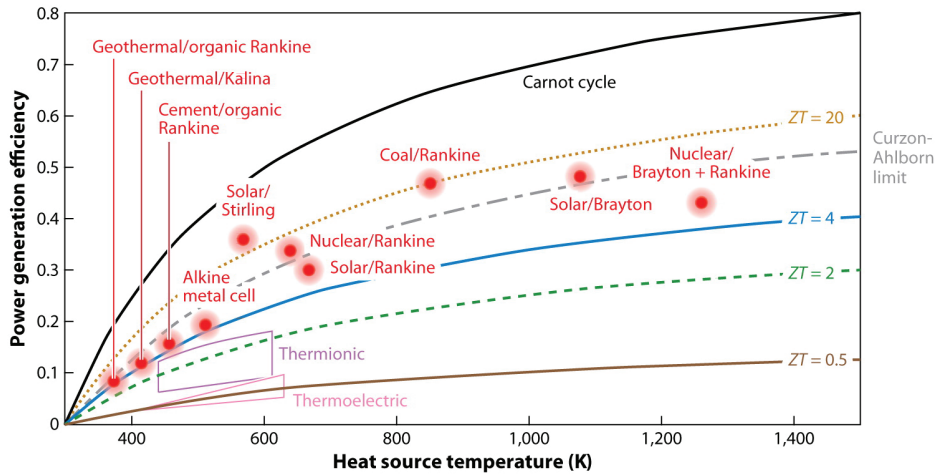
(a) From Ref. [33], illustration of a thermoelectric device, complete with plating and electrical connections.



(b) From Ref. [34], a commercially available thermoelectric module.

Figure 1.5

Actual thermoelectric devices are depicted in Fig 1.5. Many thermoelectric elements such as in Fig 1.4 are placed thermally in parallel and electrically in series using metal interconnects. Platings of ceramic materials such as aluminium oxide are used as substrate and encasing. In many applications, heat exchangers are needed to efficiently bring heat to the hot side of the device, and to evacuate heat from the cold side. In practice, most devices are segmented, meaning that their legs are made up of several thermoelectric materials, usually two or three, placed thermally in series [31, 24]. Each material is optimized to the temperature range corresponding to its position in the thermal gradient. This allows for better performances, but puts constraints on the thermoelectric compatibility between the different materials [35]. Moreover, thermal expansion imposes further mechanical constraints between the n-type and p-type legs [36]. It is therefore quite favorable for both types of legs to be composed of very similar materials. Thermoelectric modules have many advantages due to their mode of operation, which directly converts heat into electricity without any moving part or working fluid. This makes them exceptionally robust and reliable, as well as highly scalable from small domestic power generation to industrial and geothermal bottoming cycles. So far, however, their poor efficiency and high cost per watt have confined them to niche applications such as space exploration or remote areas, where their high reliability and small size are paramount.




 Shakouri A. 2011.
Annu. Rev. Mater. Res. 41:399–431

Figure 1.6: From Ref. [37], the power generation efficiency of mechanical engines and thermoelectric devices with several \overline{ZT} values, as a function of the heat source temperature for a heat sink at room temperature.

In Fig 1.6 is shown the efficiency as a function of T_h for $T_c = 300$ K and several values of \overline{ZT} [37]. Right now, commercial devices have $\overline{ZT} \lesssim 1$, which makes them much less efficient than mechanical heat engines, such as Stirling and Rankine [23, 38]. Unless a truly spectacular breakthrough happens, thermoelectric modules will not replace steam-

based cycles in large-scale power plants, but they are at an advantage when it comes to small-scale power generation [39]. Depending on the application area, the widespread use of thermoelectric devices would require cheaper modules and a figure of merit of at least 2 to 4 [24, 22, 39]. Furthermore, the cost per watt is another crucial factor to be considered, in addition to overall efficiency [40]. For comparison, the price of solar and wind power has gone down to around 1 \$/W while thermoelectric devices are at minimum in the 50 \$/W range for mid-temperature power generation (500-800 K) [37, 41, 42]. The price of the thermoelectric materials themselves, but also of the ceramic platings and the heat exchangers, are all important factors to determine the final cost per watt. On the one hand, some thermoelectric compounds are more expensive than others by up to two orders of magnitudes [41], which suggests focusing on researching cheap, earth-abundant materials like silicon. On the other hand, device design optimization can raise efficiency significantly if parasitic resistances are minimized [23], and can also bring down drastically the amount of thermoelectric materials used in each module if the legs can be made thin (so that they typically cover between 1% and 10% of the substrate) and short (typically a few millimeters long) [43]. For this optimized geometry, the overall device cost per watt is dominated by the price of the heat exchanger and the ceramic plating, so the ZT of the thermoelectric legs should be maximized regardless of the materials' cost. However, if reducing the dimensions of the legs is impossible due to other mechanical and electrical constraints, the thermoelectric materials' price per kilogram C can dominate the overall cost, and then $\frac{ZT}{\kappa C}$ should be maximized to optimize the device cost per watt [42].

From the point of view of the condensed matter physicist, the primary goal is therefore to find or design thermoelectric materials that maximize \overline{ZT} to reach at least 2 or higher. This would represent progress both in term of device efficiency and when it comes to device cost per watt. The secondary objective, which arises purely from economic and environmental considerations, is to find high- ZT materials that are cheap, earth-abundant, and non-toxic.

1.2 The search for efficient thermoelectric materials

For several decades now, the scientific community has been searching for better thermoelectric materials. Although the figure of merit \overline{ZT} is defined, strictly speaking, for a thermoelectric module and thus a pair of thermoelectric compounds, it is much easier to study, measure, or model the electrical and thermal properties of one material at a time. Consequently, in order to evaluate the thermoelectric performance of a given compound, it is useful to define the material figure of merit zT :

$$zT = \frac{\sigma S^2}{\kappa} T, \quad (1.13)$$

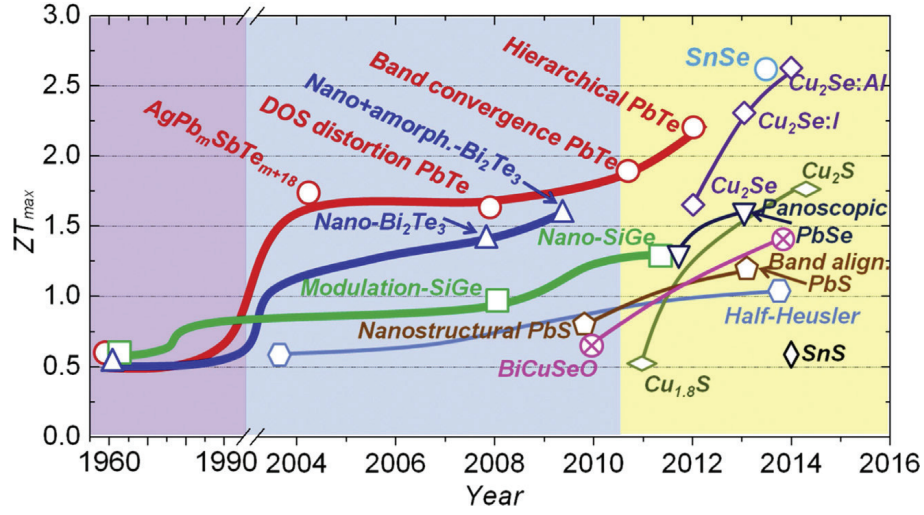
where σ is the electrical conductivity, S is the Seebeck coefficient and κ is the thermal conductivity of the material. The numerator, σS^2 , is called the power factor because it is directly linked to the power output that can be generated in a thermoelectric device. The objective is to find materials with zT reaching 2 or higher, on as wide a temperature

	σ (S cm ⁻¹)	S (μ V K ⁻¹)	σS^2 (μ W cm ⁻¹ K ⁻²)	κ (W m ⁻¹ K ⁻²)	zT
Copper	6×10^5	1.5	1.4	400	10^{-4}
Bismuth	8×10^3	-80	50	8	0.2
As-doped silicon	3×10^2	-400	50	120	0.01
Intrinsic silicon	4×10^{-6}	440	8×10^{-7}	150	10^{-10}

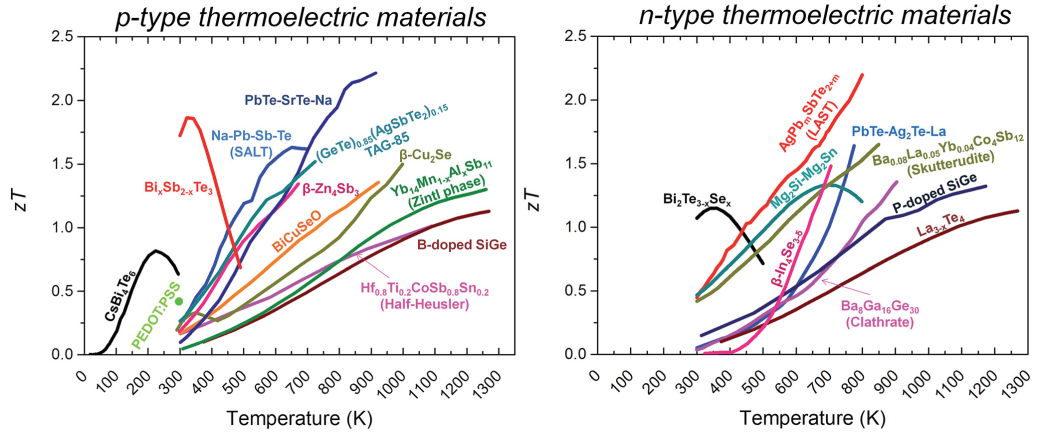
Table 1.1: Room-temperature thermoelectric properties of copper [44, 45], bismuth [46, 45], As-doped silicon [47], and intrinsic silicon [48, 45, 46].

range as possible. In order to grasp the orders of magnitudes involved, Table 1.1 summarizes the room-temperature thermoelectric properties of copper (a good metal), bismuth (a semimetal), As-doped silicon (a n-doped semiconductor), and intrinsic silicon (an intrinsic semiconductor). Metals like copper exhibit a very good electrical conductivity but a poor Seebeck coefficient, leading to mediocre power factors. Their thermoelectric performance is further ruined by their high thermal conductivity. Intrinsic semiconductors such as silicon are equally unimpressive, because their high Seebeck coefficient is rendered useless by their tiny electrical conductivity. Efficient thermoelectric materials are to be found in the middle ground between these extremes, i.e. semimetals and heavily doped semiconductors. Both bismuth and As-doped silicon, for instance, display a very good power factor around 50 μ W cm⁻¹ K⁻². Bismuth also has quite a low thermal conductivity of 8 W m⁻¹ K⁻², giving it a figure of merit of 0.2, which is almost good.

Since the advent of thermoelectric devices in the 1960's, the most widely used materials for room-temperature power generation (300-500 K) have been based on bismuth telluride, Bi₂Te₃, typically alloyed with antimony telluride Sb₂Te₃ (p-type) [51] or bismuth selenide Bi₂Se₃ (n-type) [52]. For mid-temperature power generation (500-800 K), lead telluride PbTe doped with various agents such as PbI₂ (n-type) or Ag₂Te (p-type) has been the most efficient compound [53]. At high temperatures (800-1300 K), the prominent materials have been Si-Ge alloys, either doped with boron (p-type) [54] or phosphorus (n-type) [55]. In 1993, renewed interest in thermoelectricity was sparked by Hicks and Dresselhaus when they theorized that confining electrons in two-dimensional or one-dimensional superlattices could greatly enhance the figure of merit [56, 57]. Since then, a huge amount of research has been devoted to thermoelectric compounds, and much progress has been made to improve the materials' performances through various strategies [58, 59, 60, 61, 62]. Fig 1.7a displays the evolution of zT over the years, and Fig 1.7b showcases the figure of merit as a function of temperature for several state-of-the-art p-type and n-type thermoelectric materials [49, 50]. Since 1993, the performances of Bi₂Te₃, PbTe and Si-Ge have increased significantly, and quite a few other compounds have joined them in the race for high zT values. We shall now review the main strategies that are followed to enhance the figure of merit.



(a) From Ref. [49], the evolution of thermoelectric materials through the years. The figures of merit are values at optimal temperature for each material.



(b) From Ref. [50], the figure of merit as a function of temperature for several state-of-the-art thermoelectric materials.

Figure 1.7

1.2.1 Suppressing the thermal conductivity

So far, most of the gains in thermoelectric efficiency (see Fig 1.7a) have been achieved by decreasing the thermal conductivity, i.e. the denominator in zT [63]. The thermal conductivity can be written $\kappa = \kappa_L + \kappa_e$, with a lattice contribution κ_L from the phonons and a charge carrier contribution κ_e from the electrons and holes. In doped semiconductors and semimetals, the lattice part of κ usually dominates, so this section will focus on the reduction of the phonon thermal conductivity. The typical shape of κ_L as a function of temperature is shown in Fig 1.8a. At $T = 0$ K, there is no phonon in the material, so κ_L vanishes. As the temperature is increased, more and more phonons populate the crystal vibration modes and are able to carry heat, giving rise to a finite thermal conductivity. In this low-temperature regime, κ_L is mostly limited by scattering on defects and grain boundaries. As T continues to rise, the resistive phonon-phonon scattering processes become dominant and the thermal conductivity reaches a maximum. It then decreases as more and more phonon-phonon scattering events take place. The precise shape of κ_L and the position of the maximum strongly depend on the particular forms of the scattering rates. The case of silicon and germanium is shown in Fig 1.8b as an illustration.

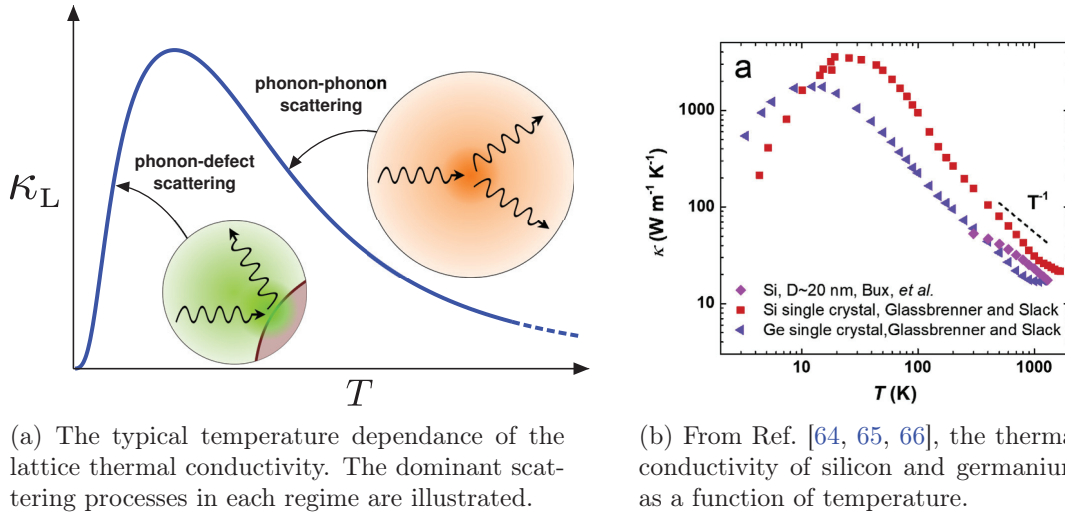
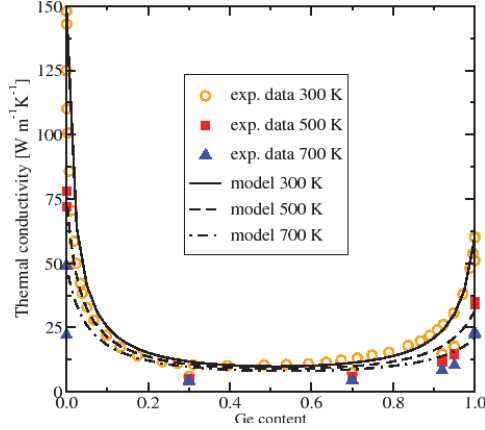


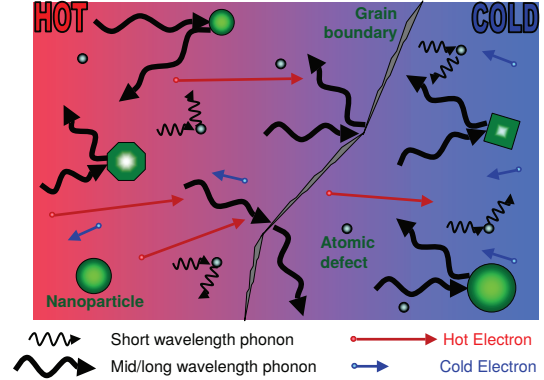
Figure 1.8

As a rule of thumbs, crystals featuring, heavy atoms, loose chemical bonds and complex structures tend to exhibit low lattice thermal conductivities [67, 68, 33], but researchers have been more proactive in the pursuit of high-efficiency thermoelectric materials. They have sought to suppress κ further by introducing defects, impurities and nanostructures in order to scatter away phonons as efficiently as possible. Such interventions, however, should be carried out in a way that preserves the electronic performances of the material. In this spirit, the ideal compound would be a "phonon glass, electron crystal" in which phonons have mean free paths as short as if they were in an amorphous material, while electrons propagate like in a perfect crystal [32]. With this restriction in mind, let us go over some

of the strategies used to suppress the thermal conductivity.



(a) From Ref. [69], the thermal conductivity of Si-Ge alloys as a function of the Ge content.



(b) From Ref. [70], a sketch of the phonon-impurity scattering in bulk nanostructured materials.

Figure 1.9

Point defects. One of the first methods employed to bring down κ , doping or alloying was used in bismuth telluride and silicon-germanium compounds to introduce mass disorder, scattering phonons and impeding heat transport [69]. Fig 1.9a shows the thermal conductivity of $\text{Si}_{1-x}\text{Ge}_x$ as a function of x . Clearly, huge gains of one order of magnitude in κ can be achieved in this way. Another type of point defect is the vacancy, which can be intentionally added to lower the thermal conductivity. For instance, Sn vacancies largely contribute to the κ reduction observed in SnTe upon alloying with AgSbTe₂ [71]. In this case, the vacancies also soften the phonon modes, decreasing the speed of sound in the material. A drawback of introducing point defects is that they tend to scatter long-wavelength phonons less efficiently than short-wavelength ones [67]. Another is that they may scatter electrons as well, which risks degrading the electronic properties.

Nanostructures. After 1993, experimentalists were spurred to design nanostructured superlattices of thermoelectric materials to enhance the figure of merit. Although Hicks and Dresselhaus' original idea was to boost the power factor through electron confinement, experimental performance gains in superlattices came mostly from a reduction in the thermal conductivity due to the nanostructures' interfaces [70, 67]. This fact, together with the cost and time needed to synthesize superlattice thin films, drove researchers to study bulk nanostructured compounds [72, 67, 70, 33, 63]. Such a material is sketched in Fig 1.9b: the idea is to randomly introduce nanoscale grain boundaries and large nano-inclusions so that phonons scatter off interfaces. The advantage of random nanostructures over superlattices is that they can be synthesized through bulk processes, without the need to precisely control the atomic planes like

in Molecular Beam Epitaxy. The advantage over alloys is that, since interfaces are extended defects, they may be able to scatter long-wavelength phonons more effectively than point defects. Additionally, by tuning the average distance between interfaces, it can be made shorter than the typical phonon mean free path but longer than the electron mean free path. If this is achieved, it can be hoped that the nanostructuring decreases the thermal conductivity without degrading the electronic properties. This strategy was used in Bi_2Te_3 alloys, for instance, yielding significant improvements in the figure of merit [51, 73, 52].

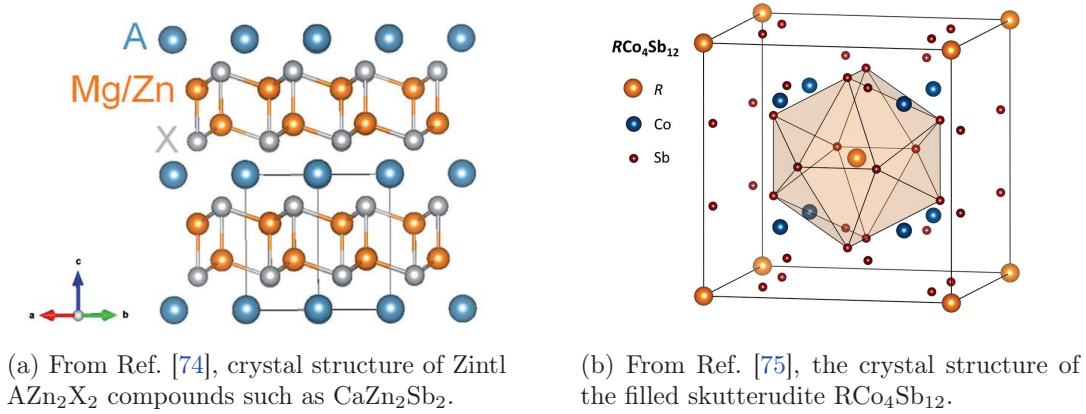


Figure 1.10

Zintl substructures. In the 2000's, Zintl phases emerged as a promising concept for thermoelectrics [76, 74]. The idea is to have spatially separated crystal substructures with different functionalities, e.g. one substructure conducts electrons or holes while the other scatter phonons. A typical Zintl compound is the semiconductor CaZn_2Sb_2 , whose crystal structure is shown in Fig 1.10a. The Zn and Sb atoms form covalently bound layers separated by Ca layers. The bonding between the Ca and Zn/Sb atoms is very ionic, with the Ca acting as cations and Zn/Sb as anions. Doping the Ca layer with less electropositive Yb introduce holes that propagate in the Zn/Sb layer. It is thus possible to introduce defects in the Ca layer, reducing the thermal conductivity without hindering electrical transport.

Rattler atoms. At the same time, excellent thermoelectric properties were found in crystals possessing cage-like structures in their unit cell, the two most well-known being clathrates and skutterudites [77]. Clathrates such as $\text{Ba}_8\text{Ga}_{16}\text{Si}_{30}$, for instance, can be viewed as a special case of Zintl compound in which the Ba cations are isolated in cages of Ga and Si atoms. The large distance between Ba and the Ga/Si atoms is typically associated with soft phonon modes, so the caged atom is called a rattler. Such materials tend to exhibit low thermal conductivities due to this mechanism. Skutterudites like CoSb_3 and FeSb_3 also have empty cage-like structures, which can

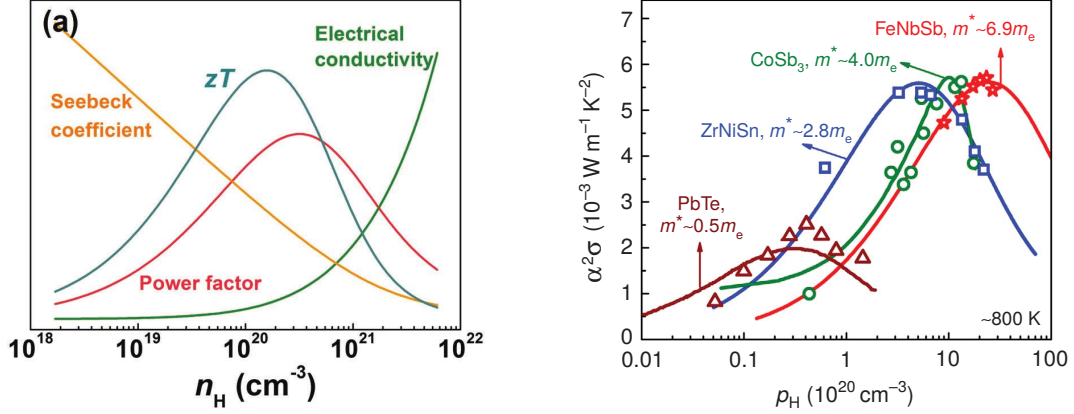
be partially filled with guest atoms to substantially lower the thermal conductivity (see Fig 1.10b) [50]. Introducing Sn atoms in the cages of FeSb₃, for instance, creates goldstone phonon modes, i.e. zero-energy degrees of freedom of the Sn guest, which could result in a very low κ below $1 \text{ W m}^{-1} \text{ K}^{-2}$ [78].

1.2.2 Enhancing the power factor

Another option to improve the figure of merit zT is to increase the power factor σS^2 , a quantity that is mostly governed by electronic properties. Contrary to the lattice thermal conductivity, the electrical conductivity and the Seebeck coefficients can be tuned by changing the charge carrier concentration, most often via doping. In Fig 1.11a is shown the hole concentration dependance of σ , S , σS^2 and zT for a typical p-type material, assuming that its electronic structure is not disrupted by doping. σ is more or less proportional to the carrier density, but S decreases as more holes are added in the compound. This interplay between the electrical conductivity and Seebeck coefficient gives rise to a maximum of the power factor, typically at intermediate or heavy doping. As an illustration, the experimental power factors of La-doped lead telluride [79], partially filled skutterudite CoSb₃ [80], and two doped Half-Heuslers, FeNbSb [81] and ZrNiSn [82], are shown in Fig 1.11b. The figure of merit zT has, broadly speaking, the same carrier concentration dependance as the power factor, with a maximum slightly shifted because of variations in the total thermal conductivity. The variations of the electrical conductivity with temperature vary wildly from one compound to another, depending on the statistics of the carriers (degenerate or non-degenerate) and on the scattering laws. The Seebeck coefficient tend to increase with temperature, before reaching a maximum at the onset of bipolar conduction, i.e. when the density of minority carriers (holes in n-type materials and vice versa) becomes comparable to concentration of majority carriers.

Naturally, researchers have been trying to reach the optimal power factor in Fig 1.11a by adjusting the carrier concentration through various means. Substitution doping or alloying are the most common procedures. For exemple, replacing a Pb atoms by Na atoms in lead telluride creates holes in the valence band, turning PbTe into a p-type material [84]. Controlling the amount of Na substitution allows for the tuning of the hole density. Another procedure is to introduce vacancies in the crystal structure. La deficient lanthanum telluride La_{3-x}Te₄, for instance, can be synthesized by mechanical alloying with a controlled amount of La vacancies [85]. In stoichiometric La₃Te₄, La atoms are electron donors, and the Fermi level lies in the conduction band [86]. Therefore, the presence of La vacancies leads to a decrease in the electron density of the material, which can be adjusted in this way to optimize the power factor.

The dopants and vacancies introduced to control the carrier concentration are also point defects which can disrupt both thermal and electrical transport, and distort the electronic structure of the material. Although degrading the thermal conductivity is always beneficial, the effects on the electronic properties often result in a deterioration of the power factor. Thus, for every thermoelectric material, scientists look for procedures that enable dopants to act as electron or hole reservoirs. Such tuning of the charge carrier density without any distortion of the electronic structure is called a rigid shift of the Fermi level, or a rigid band



(a) From Ref. [83], the typical carrier concentration dependence of σ , S , σS^2 and the figure of merit for a rigid shift of the Fermi level.

(b) From Ref. [81, 79, 80, 82], the power factor as a function of the measured charge carrier concentration for several thermoelectric materials.

Figure 1.11

shift. In some compounds, certain dopants naturally fulfill this condition, for instance Nb and La in strontium titanate (see section 3.1). In others, it is necessary to be more creative. Modulation doping (also called remote doping), for instance, consists in spatially separating the dopant species from the charge carriers [87]. In this spirit, nanograins of Si₇₀Ge₃₀ alloys were introduced as dopants in a Si₉₅Ge₅ host, yielding a significant improvement in the power factor compared to uniform Ge doping [88].

Nevertheless, even with perfect rigid band doping, the power factor is still limited by the optimal value in Fig 1.11a. Since the thermal conductivity has already been severely curtailed in most state-of-the-art thermoelectric materials, researchers now expect that further improvements of the thermoelectric performances will come from boosting the power factor beyond this rigid band optimum. In order to achieve this, it is necessary to distort the electronic structure in very specific ways that are beneficial to the power factor. These strategies usually exploit the fact that in degenerate semiconductors, the Seebeck coefficient can be approximated by the Mott formula [32, 89]:

$$S \approx -\frac{\pi^2 k_B^2 T}{3e} \frac{1}{\sigma(E)} \frac{\partial \sigma(E)}{\partial E}. \quad (1.14)$$

$\sigma(E)$ is the electrical conductivity at the Fermi energy E , and S is basically the logarithmic derivative of this quantity. Thus, while scaling factors in $\sigma(E)$ leave S unchanged, sharp variations of the conductivity with the Fermi level leads to high values of the Seebeck coefficient, as theorized by Mahan and Sofo in 1996 [90]. Let us now review a few of the strategies to boost the power factor.

Band convergence. This method is conceptually quite simple: since a scaling factor in the conductivity has no effect on the Seebeck coefficient, the power factor is di-

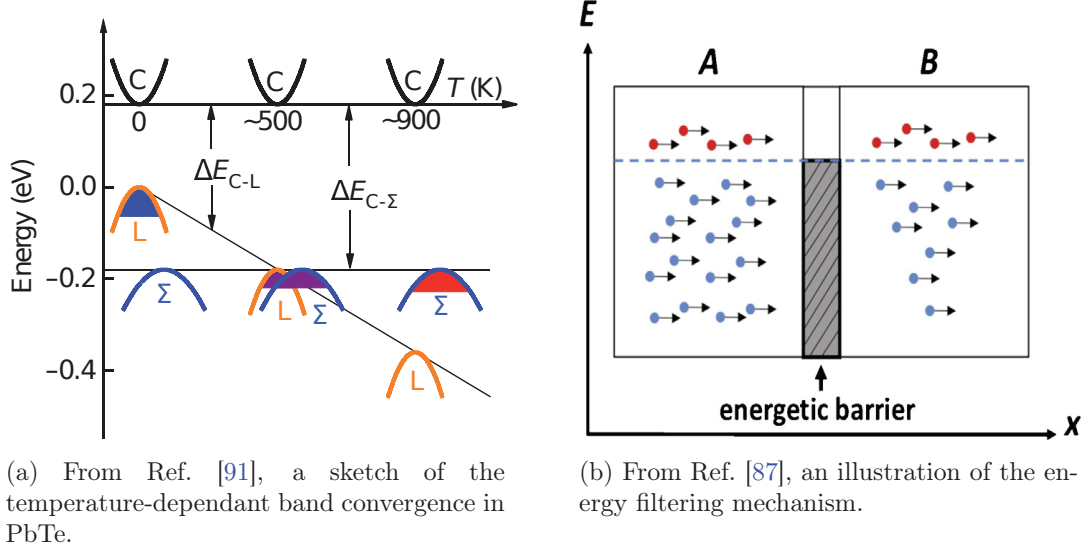


Figure 1.12

rectly proportional to the number of valleys occupied by the charge carriers. Accordingly, classic thermoelectric materials have several equivalent conduction valleys: 6 for Bi_2Te_3 , 4 for PbTe and 6 for SiGe [87]. The idea behind band convergence is to bring additional valleys to the same energy as the conduction band minimum or valence band maximum, thereby boosting the valley degeneracy [92]. This has been achieved in PbTe by Se doping and by exploiting the temperature dependance of the electronic structure (see Fig 1.12a), yielding a threefold boost of the power factor [91]. Substantial gains in the power factor were also realized by alloying Mg_2Si and Mg_2Sn , which have two low-lying conduction valleys with energies reversed from one compound to the other [93]. Note that this method is valid only if intervalley scattering negligible, otherwise the scattering may be enhanced and compensate the increase in the number of valleys.

Energy filtering. This approach aims at boosting the Seebeck coefficient by introducing energy barriers in the material. These barriers scatter preferentially the low-energy electrons, while the high-energy electrons can pass through (see Fig 1.12b). This mechanism should give rise to an strong energy dependance of $\sigma(E)$, leading to a boost of S at the cost of a decrease in σ [87, 67]. An experimental proof-of-principle was carried out using $\text{InGaAs}/\text{InGaAlAs}$ superlattices in which a boost of the Seebeck coefficient was observed [94]. For thermoelectric applications, it is hoped that the boost of the Seebeck coefficient overcompensates the drop in conductivity, thus enhancing the power factor. Such increases of the power factor due to energy filtering have been claimed in many compounds, for instance in BiSbTe_3 and CoSb_3 nanostructures, where the grain boundaries presumably act as energy barriers for the electrons [95, 96].

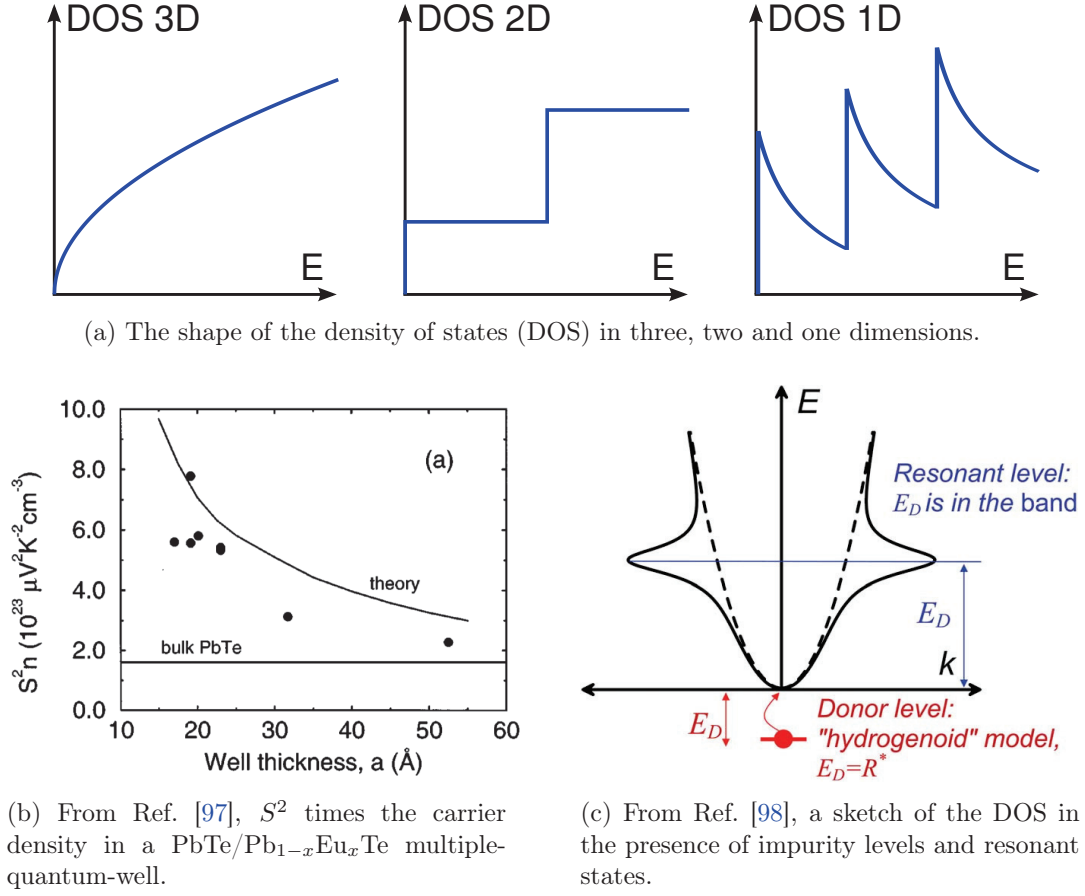


Figure 1.13

Dimensional confinement. Hicks and Dresselhaus' original idea in 1993 was that confining the charge carriers in two-dimensional or one-dimensional structures should drastically improve the power factor [56]. This can be understood by considering the density of state (DOS) of an electron gas in three, two and one dimensions, Fig 1.13a. Reducing the dimensionality of the system introduces sharp features and large values in the DOS, which could lead to strong energy variations of the conduction and thus to a boost of the Seebeck coefficient [99, 100]. The first experimental test of these ideas was carried out on PbTe/Pb_{1-x}Eu_xTe multiple-quantum-well structures, and it did yield a substantial boost of S^2n , with n the carrier density (see Fig 1.13b and [97]). Since then, several groups have investigated confinement effects in superlattices, including Bi₂Te₃/Sb₂Te₃ and SrTiO₃/SrTi_{0.8}Nb_{0.2}O₃ superlayers [101, 102], even though it is not always clear if the charge carriers are truly confined in two dimensions in such systems [70]. Either way, a boost of the power factor does not necessarily follows from a reduction of dimensionality, because the scattering rate

can also be affected by the change in the DOS. This may be part of the reason why the spectacular power factor gains predicted by Hicks and Dresselhaus have been so difficult to realize experimentally.

Resonant states. When a dopant is introduced in a material, it can create localized impurity levels in the band gap, acting as electron donors or acceptors if the energy separation E_D with the conduction (or valence) band is not too large compared to $k_B T$. It is also possible, however, for the impurity levels to be located inside the conduction band and to hybridize with the conduction states. In such a case, they are called resonant states and give rise to sharp peaks in the DOS of the host material (see Fig 1.13c and [98]). These steep variations of the DOS due to resonant impurities and the possibly strong energy dependence of the electron-impurity scattering rate may lead to a boost the power factor if the Fermi level can be positioned in the vicinity of the resonant peak. It has been claimed, for instance, that the enhancement of the Seebeck coefficient observed in Tl doped PbTe and Sn doped Bi₂Te₃ are due to resonant states introduced by the dopants [103, 104]. However, this remains somewhat controversial [105], and there is no clear consensus whether actual resonant boosts of the power factor have been observed experimentally, or over the precise enhancement mechanism.

This short review of the most prominent optimization strategies is obviously non-exhaustive, and there are many other families of materials that hold great promise for thermoelectric power generation, among them organic-inorganic hybrids, germanium-tellurium, transition metal dichalcogenides, superionic compounds... This wealth of possibilities is both a reason for optimism and a daunting challenge, as synthesizing a significant proportion of these compounds and measuring their properties would require a massive amount of time and money. Therefore, theoretical guidance is essential to guide the search for high-performance thermoelectric materials. As many of the techniques used to suppress the thermal conductivity and enhance the power factor involve introducing defects in the crystal structure, it appears crucial to develop theoretical methodologies that are capable of describing the effects of nanoscale disorder in thermoelectric materials.

1.3 Content of the thesis

In this work, we study the thermoelectric transport properties of several compounds using a combination of *ab initio* calculations and real-space methodologies. In chapter 2, we present the formalism of density functional theory, that gives access to the electronic and vibrational structure of specific materials with no adjustable parameters, and from which realistic tight-binding Hamiltonians and dynamical matrices can be extracted. We then cover the basics of electron and phonon diffusive transport in the framework of the Boltzmann transport equation, before providing a link to the Landauer formalism in order to include ballistic effects. These methodologies, which are valid in the absence of strong disorder effects, are applied in chapter 3 to model electron transport in oxides. The bulk

thermoelectric properties of n-type SrTiO_3 and rutile TiO_2 are investigated, allowing for a direct comparison between our theory and experimental data from the existing literature. The issue of quantum confinement in SrTiO_3 superlattices is then addressed, showing that the thermoelectric properties of these systems can be explained without assuming any confinement of the electrons. In chapter 4, we detail a real-space formalism capable of including strong disorder effects as well as our methodology to compute the electron and phonon transport properties of large disordered systems. Starting with the basic definitions of Green's functions, we introduce the concepts of self-energy and spectral function, explaining their relevance to the issue of transport and scattering. We then show how the fully quantum conductivity can be calculated from the Kubo formalism that includes Anderson localization. Numerical methods allowing for an exact treatment of disorder are presented. In chapter 5, these techniques are used to study the effects of resonant states on electronic transport in the context of thermoelectric power generation. A study on a minimal disordered Hamiltonian is carried out to extract the general properties of resonant impurities. We focus next on the specific case of vanadium doping in SrTiO_3 , first through a fully *ab initio* investigation and then by combining density functional theory calculations with real-space methods to fully include disorder and localization effects. Finally, chapter 6 is devoted to disordered two-dimensional materials. The influence of doping on electronic transport in single-layer transition-metal dichalcogenides is investigated through *ab initio* calculations. We then study phonon transport in graphene when randomly distributed monovacancies are present in the compound, using a realistic modelling of the vibrational properties obtained from density functional theory calculations. Our predictions for the thermal conductivity are compared with experimental data from the existing literature on suspended graphene.

Chapter 2

Modelling thermoelectric transport from first-principles

Freedom is the freedom to say that two plus two make four. If that is granted, all else follows.

George Orwell, 1984.

In this chapter will be covered the methodology used to model electron and phonon transport in thermoelectric materials when the deviations from crystalline order can be considered weak and perturbative. The presence of strong, non-perturbative disorder requires more sophisticated theoretical approaches such as Green's functions techniques, which will be presented in chapter 4.

In the context of thermoelectric power generation, the cause of transport is a temperature gradient between a heat source and a heat sink, which is not supposed to change very fast and exhibits strong thermal inertia in any case. Thus, a first restriction in our study of thermoelectricity is that we will be interested only in the static, zero-frequency values of the electrical conductivity, Seebeck coefficient and thermal conductivity, and we will consider only steady-state regimes.

A second and perhaps less obvious restriction is that we will make the approximation of near-equilibrium transport. Strong-field transport can be described by the Boltzmann transport equation [106, 107] and by fully quantum frameworks such as the Non-Equilibrium Green's Function (NEGF) formalism [108]. However, near-equilibrium thermoelectric transport in disordered materials is not only capable of estimating the performance of different materials through the figure of merit zT , but it also encompasses a wealth of subtle and interesting phenomena, such as those presented in section 1.2. Consequently, for our purposes there is no need to go far from equilibrium.

A first stepping-stone towards the study of near-equilibrium transport is the description of equilibrium itself. To evaluate the electrical conductivity and Seebeck coefficient of a given material, we have to compute its electronic band structure first. Likewise, in order to calculate its lattice thermal conductivity, we first need the phonon dispersion. The next section is devoted to the methodology by which we obtain such quantities.

2.1 Electron and phonon structure of solids

In principle, the Hamiltonian for the many-body wavefunction of the electrons and nuclei composing a crystalline solid is known. It can be written as

$$\begin{aligned} \hat{H} = & -\frac{\hbar^2}{2m_e} \sum_i \nabla_i^2 - \sum_{i,I} \frac{Z_I e^2}{4\pi\epsilon_0 |\vec{r}_i - \vec{R}_I|} + \frac{1}{2} \sum_{i \neq j} \frac{e^2}{4\pi\epsilon_0 |\vec{r}_i - \vec{r}_j|} \\ & - \sum_I \frac{\hbar^2}{2M_I} \nabla_I^2 + \frac{1}{2} \sum_{I \neq J} \frac{Z_I Z_J e^2}{4\pi\epsilon_0 |\vec{R}_I - \vec{R}_J|}, \end{aligned} \quad (2.1)$$

where i and j run over the electrons, I and J over the nuclei, Z_I and M_I are the charge and mass of the I nuclei respectively. The first term in equation (2.1) is the kinetic energy of the electrons, the second is the Coulomb electron-nuclei interaction, the third is the Coulomb repulsion between electrons, the fourth is the kinetic energy of the nuclei, and the last term is the Coulomb repulsion between the nuclei. Although it may appear relatively simple written in this form, solving this many-body Hamiltonian represents a formidable task even for very small systems.

A first approximation that is usually made to make the problem more tractable is the so-called Born-Oppenheimer approximation. Since the nuclei masses are much larger than the electron masses (typically by four orders of magnitude), the former can be expected to move much slower than the latter. Thus, the electrons can be assumed to follow adiabatically the movement of the nuclei. The full problem can then be tackled following a two-step procedure:

- First, consider the nuclei at rest and their positions as parameters for the electron Hamiltonian. Find the ground-state and the energy of the electrons as functions of these parameters.
- Second, study the movement of the nuclei in the energy surface obtained at step one.

The Born-Oppenheimer approximation breaks down when the coupling between electron and nuclei is essential in describing the phenomenon of interest. For instance, particularly strong electron-phonon coupling in certain polar materials may drastically alter the nature of the electronic states. The electrons in these compounds, dressed by the surrounding lattice deformation, are then called polarons [109, 110]. A less spectacular but far more ubiquitous consequence of electron-phonon interactions is the scattering of conduction electrons or valence holes, which represents the largest source of electrical resistance in most semiconductors and metals. Nevertheless, in condensed matter physics the Born-Oppenheimer approximation is always used as a starting point, even if the effects of electron-phonon coupling are to be reintroduced subsequently through perturbation theory or other techniques.

Even with the great simplifications brought by considering the nuclei as fixed and their position as mere parameters, directly solving the many-body electron Hamiltonian (2.1) is an impossible task for systems of even small size. The fundamental issue is that the many-body wavefunction for N electrons depends on $3N$ coordinates (ignoring the spin).

If we were to discretize the space using p points for every direction, the wavefunction would be represented by p^{3N} coefficients. If we had, say, $N = 10$ electrons and $p = 10$ discretization steps, that would be 10^{30} numbers or $\approx 10^{31}$ bytes of storage. This is far beyond the capabilities of modern computers, which can handle no more than 10^{12} bytes if they have a terabyte of RAM. Thus, a numerical method to solve the quantum problem of electrons in a crystal must necessarily avoid dealing with the many-body wavefunction, and must involve auxiliary quantities. In most first-principles simulations, this quantity is the electron density.

2.1.1 Density functional theory

Density Functional Theory (DFT) has sometimes been described as the standard model of condensed matter [111]. In its narrowest sense, DFT is an exact mathematical reformulation of the many-electron problem in terms of the electron density $n(\vec{r})$, bypassing the cumbersome many-body wavefunction. But in the last decades, it has come to designate a set of numerical first-principles techniques, procedures and tools that stem from this formalism of quantum chemistry and condensed matter. Today, the DFT methodology is widely used to provide the basis for studying the properties of most materials, including thermoelectric compounds. In this work, we use two software packages: the Spanish Initiative for Electronic Simulations with Thousands of Atoms (SIESTA) using mainly local orbitals [112], and the Quantum opEn-Source Package for Research in Electronic Structure, Simulation, and Optimization (Quantum ESPRESSO), based on plane-wave states [113]. We shall now briefly review the basics of DFT and its numerical implementation. Many important subtleties and precisions will be omitted, so the reader is referred to more complete textbooks on the topic, such as [114, 115].

Density Functional Theory in principle

The very basis of DFT lies in the famous Hohenberg-Kohn theorems, published in 1964 [116], which apply to any system of interacting electrons under the influence of an arbitrary external potential $V_{\text{ext}}(\vec{r})$. The first Hohenberg-Kohn theorem states that $V_{\text{ext}}(\vec{r})$ is uniquely determined (up to a constant) by the ground-state electron density $n_{GS}(\vec{r})$, i.e. no two different potentials can give the same density. It follows that all the properties of the system (including, for instance, the excitation energies, the response functions, etc...) are in principle determined by the ground-state density $n_{GS}(\vec{r})$, which can thus be viewed as the fundamental variable for the description of the system. The second Hohenberg-Kohn theorem states that there is a universal energy functional of the density $E[n]$, whose minimization with respect to $n(\vec{r})$ gives the ground-state energy E_{GS} and the ground-state density $n_{GS}(\vec{r})$. More precisely, the energy functional can be written [117, 118]

$$E[n] = F[n] + \int d^3\vec{r} V_{\text{ext}}(\vec{r})n(\vec{r}) + E_{\text{nuc}} \quad (2.2)$$

where $\int d^3\vec{r} V_{\text{ext}}(\vec{r})n(\vec{r})$ is the Coulomb potential energy of the electrons in the presence of the nuclei (second term in equation (2.1)), E_{nuc} is the interaction energy between the nuclei

(last term in equation (2.1)), the kinetic energy of the nuclei has been neglected following the Born-Oppenheimer approximation, and

$$F[n] = \min_{\Psi \rightarrow n(\vec{r})} \langle \Psi | \hat{T} + \hat{V}_{\text{int}} | \Psi \rangle \quad (2.3)$$

stands for the kinetic and interaction energies of the electrons (first and third term in equation (2.1)), minimized with respect to the many-body wavefunctions $|\Psi\rangle$ with an electron density $n(\vec{r})$. The functional $F[n]$ does not depend on the external potential $V_{\text{ext}}(\vec{r})$, hence the term "universal". The proofs of the Hohenberg-Kohn theorems are quite simple, and can be found in any textbook on DFT such as [114].

Elegant as it is, this formalism does not provide an operational procedure to find the ground-state density, other than minimization of the functional defined by equations (2.2) and (2.3), which again involve the full many-body wavefunction. The immense practical utility of DFT comes from the so-called Kohn-Sham ansatz [119], which assumes that the ground-state density of the real, interacting electron system is also the ground-state density of an auxiliary system of non-interacting particles obtained by minimizing the energy functional

$$E_{KS}[n] = T_0[n] + \frac{1}{2} \int d^3\vec{r} \int d^3\vec{r}' \frac{e^2 n(\vec{r}') n(\vec{r})}{4\pi\epsilon_0 |\vec{r} - \vec{r}'|} + \int d^3\vec{r} V_{\text{ext}}(\vec{r}) n(\vec{r}) + E_{xc}[n] + E_{\text{nuc}}. \quad (2.4)$$

Note that this assumption has never been proven in general, although it is considered reasonable and is widely accepted. The first three terms of equation (2.4) are the Hartree ansatz, where the electron-electron interaction appears as the mean-field classical Coulomb energy (the second term). The exchange energy and the effects of electronic correlation have been put together in a term called the exchange-correlation energy, E_{xc} . $T_0[n]$ is the kinetic energy minimized with respect to the non-interacting wavefunction of the auxiliary system with density $n(\vec{r})$. Imposing $E_{KS}[n] = E[n]$ yields

$$E_{xc}[n] = F[n] - T_0[n] - \frac{1}{2} \int d^3\vec{r} \int d^3\vec{r}' \frac{e^2 n(\vec{r}') n(\vec{r})}{4\pi\epsilon_0 |\vec{r} - \vec{r}'|}, \quad (2.5)$$

which can be viewed as a definition for the exchange-correlation functional $E_{xc}[n]$. From equation (2.5), it is manifest that $E_{xc}[n]$ is universal, in the sense that it does not depend on the external potential V_{ext} . Thus, it can in principle be determined once and for all, and if it is known exactly then the minimization of $E_{KS}[n]$ for the auxiliary non-interacting system should give the exact ground-state density and energy of the real interacting system. From there, all the properties of the real system can in principle be determined, as stated by the first Hohenberg-Kohn theorem.

Since the N particles in the auxiliary system are non-interacting, its many-body wavefunction must be a single Slater determinant of N single-particle wavefunctions $\psi_i(\vec{r})$. The minimization of the functional $E_{KS}[n]$ with respect to each $\psi_i(\vec{r})$ under the constraint that the wavefunction should be normalized yields a set of Schrödinger-like equations

$$\left(-\frac{\hbar^2}{2m_e} \nabla^2 + \int d^3\vec{r}' \frac{e^2 n(\vec{r}')}{4\pi\epsilon_0 |\vec{r} - \vec{r}'|} + \frac{\delta E_{xc}}{\delta n(\vec{r})} \right) \psi_\mu(\vec{r}) = \epsilon_\mu \psi_\mu(\vec{r}) \quad (2.6)$$

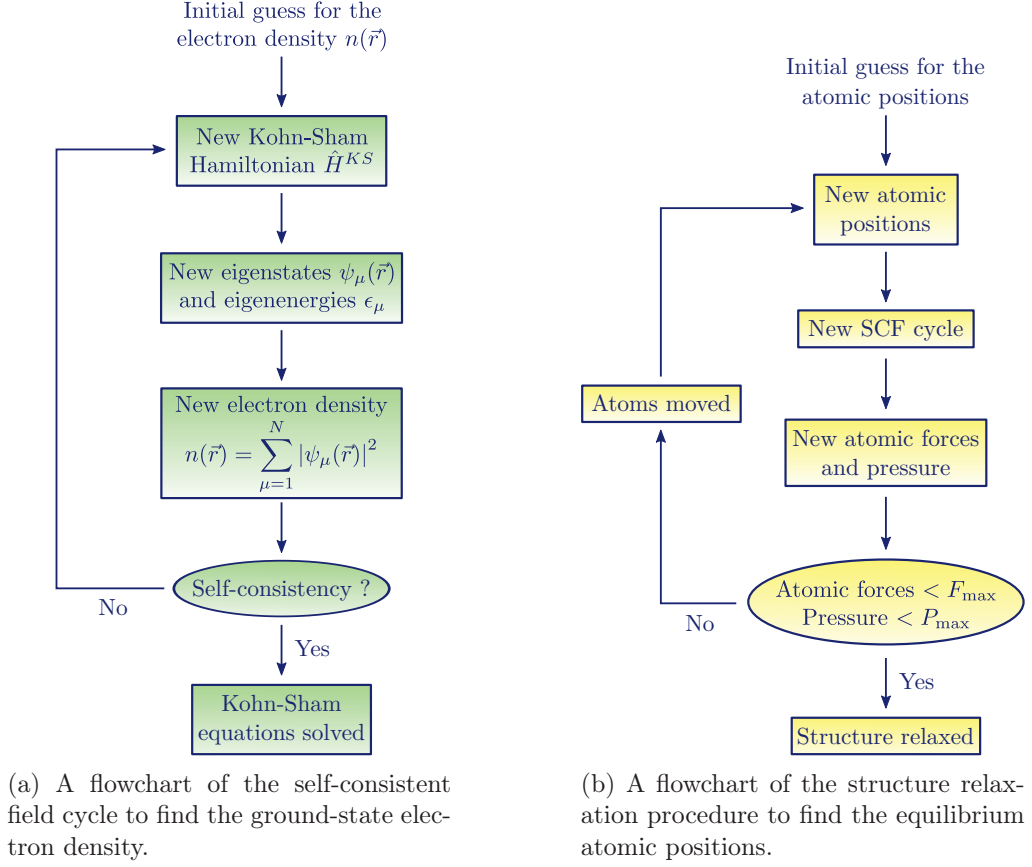


Figure 2.1

with ϵ_μ the Lagrange multipliers ensuring the normalization constraint. Equations (2.6) are called the Kohn-Sham equations, and solving them is the main computational workload of DFT packages such as SIESTA and Quantum ESPRESSO. When it is important to take spin polarization into account, there are two sets of Kohn-Sham equations, one for each spin. The operator on the left-hand side acting on $\psi_\mu(\vec{r})$ is called the Kohn-Sham Hamiltonian \hat{H}^{KS} , and depends explicitly on the density $n(\vec{r})$. This makes the Kohn-Sham equations self-consistent. The procedure to solve them, called a self-consistent field cycle (SCF cycle), is illustrated in Fig 2.1a. An initial guess is made for $n(\vec{r})$, which defines the initial Kohn-Sham Hamiltonian. This Hamiltonian is then diagonalized, giving a set of single particle eigenstates $\psi_\mu(\vec{r})$ and eigenenergies ϵ_μ . The N lowest eigenstates are filled (sometimes a non-integer filling factor is used, such as a Fermi-Dirac distribution) according to the *aufbau* principle, and the corresponding new density is calculated by

$$n(\vec{r}) = \sum_{\mu=1}^N |\psi_\mu(\vec{r})|^2. \quad (2.7)$$

This new density is used to define a new Kohn-Sham Hamiltonian, which is then solved in

turn, giving yet new eigenstates and a new density, and so on and so forth until convergence is reached. The criterion for self-consistency varies from one implementation to another. In SIESTA, for instance, the elements of the electron density matrix are compared between two successive steps, while in Quantum ESPRESSO it is the total energy of the system.

In principle, this procedure yields the exact ground-state density and energy for given positions of the nuclei. In a similar way, the crystal structure can be relaxed to predict the lattice constant, for instance, by minimizing the total energy with respect to the positions of the nuclei, see Fig 2.1b. A first SCF cycle is performed with an initial guess of the crystal geometry. Once it is done, the forces are computed using the Hellmann-Feynman theorem [120]:

$$\vec{F}_I = -\frac{\partial E_{KS}}{\partial \vec{R}_I} = -\left\langle \frac{\partial \hat{H}^{KS}}{\partial \vec{R}_I} \right\rangle = -\int d^3\vec{r} n(\vec{r}) \frac{\partial V_{\text{ext}}(\vec{r})}{\partial \vec{R}_I} - \frac{\partial E_{\text{nuc}}}{\partial \vec{R}_I}. \quad (2.8)$$

The pressure is calculated in a similar way. The nuclei are then moved a short distance (typically a tenth of an angström) in the direction of the force acting on them. A new SCF cycle is performed, yielding new forces. The nuclei are moved again, and so on until the forces and the pressure are judged sufficiently small. Typically, the optimization is stopped when the atomic forces are below $F_{\text{max}} = 10^{-2} \text{ eV/\AA}$ and the pressure below $P_{\text{max}} = 0.1 \text{ kbar}$. When the end goal is to compute phonon dispersions, the requirements have to be much more stringent, typically $F_{\text{max}} = 10^{-5} \text{ eV/\AA}$ and $P_{\text{max}} = 1 \text{ bar}$.

Density Functional Theory in practice

Although the DFT methodology described in the previous section should lead to an exact description of the interacting electron system, there are in practice several fundamental approximations that must be made beyond the numerical and convergence errors.

The first of these is related to the exchange-correlation functional (equation (2.5)). The entire method hinges on the availability of an expression for $E_{xc}[n]$ that is both practical and accurate enough. Since no formula for the exact functional has been discovered yet, a number of approximations have been made, most of them involving local functions of the density. The oldest is the Local Density Approximation (LDA), which can be written

$$E_{xc}^{\text{LDA}}[n] = \int d^3\vec{r} n(\vec{r}) \epsilon_{xc}^{\text{hom}}(n(\vec{r})) \quad (2.9)$$

with $\epsilon_{xc}^{\text{hom}}(n)$ the sum of the exchange energy density and the correlation energy density for the homogeneous electron gas of uniform density n . The exchange energy density is known analytically, while the (much smaller) correlation energy has been evaluated by Monte Carlo simulations. The LDA approximation is expected to work fairly well on systems exhibiting small spatial variations of the electron density, but it has yielded remarkably accurate results in a number of cases where it could have been expected to fail, such as atomic systems. Another, slightly more refined approximation is the Generalized Gradient Approximation (GGA). The basic idea is to make the local exchange-correlation energy dependant on the gradient of the density in addition to the density itself:

$$E_{xc}^{\text{GGA}}[n] = \int d^3\vec{r} n(\vec{r}) \epsilon_{xc}(n(\vec{r}), |\nabla n|). \quad (2.10)$$

Several flavours exist for the precise form of the expansion, the most common being the Becke (B88) [121], the Perdew and Wang (PW91) [122], and the Perdew, Burke and Ernzerhof (PBE) [123] functionals. The GGA exchange-correlation functionals yield robust improvements over the LDA, and they are the most widely used in condensed matter physics. For all their successes, however, the GGA and LDA functionals have serious limitations that should be kept in mind. They rely on an analogy with the uniform electron gas, which makes them unable to capture the physics of strongly correlated systems where a central role is played by the interplay of exchange-correlation with strong spatial variations of the electron density. The forms (2.9) and (2.10) are local while the analytical exchange energy from the Hartree-Fock approximation is known to be non-local. Most notoriously, the LDA and GGA functionals reliably and significantly underestimate the electronic band gap of insulators and semiconductors. To overcome these difficulties, several improvements can be made to the approximation for exchange and correlation. One possibility is to add on certain localized orbitals a Hubbard term of the form

$$E_U = U \hat{n}_{i,\uparrow} \hat{n}_{i,\downarrow}, \quad (2.11)$$

where $\hat{n}_{i,\uparrow}$ ($\hat{n}_{i,\downarrow}$) is the occupation operator for the spin up state (resp. spin down state) of the i orbital, to model the strong effects of exchange and correlation. In such "LDA+U" approaches, the Hubbard energy U can be fitted to experimental data or obtained from other first-principles calculations [124]. Another possible improvement to LDA and GGA is to introduce a measure of orbital-dependant Hartree-Fock exchange in the functional, thereby making it partly non-local. This is called a "hybrid functional". The drawbacks are, first, that the proportion of non-local exchange has to be chosen somewhat arbitrarily, and second, that the computational cost is much greater than with local functionals.

As second approximation layer consists in using so-called pseudopotentials to avoid dealing with atomic core electrons. In condensed matter, core electrons are usually tightly bound to their atoms and chemically inert, so they play no role in chemical bonding or electrical transport beyond a screening of the nuclei charge. Additionally, the orthogonality condition between core and valence atomic states of the same angular momentum give rise to sharp variations in the valence wavefunctions near the core, which would necessitate fine grids or large number of planewaves to describe. For these reasons, core electrons are usually not taken into account explicitly, instead they are replaced by effective atomic potentials called pseudopotentials. These are typically generated from *ab initio* calculations on isolated atoms, with several possible flavours corresponding to different requirements on the potentials. Typically, a reference atomic configuration is chosen (often it is the neutral atom), and the pseudopotentials are generated so that the valence eigenvalues and the valence wavefunctions beyond a certain cutoff radius are exactly reproduced. The so-called "norm-conserving" pseudopotentials, for instance, additionally impose that the charge density integrated from the nucleus to the cutoff radius be correct. Generally speaking, the softness of the pseudopotentials (eliminating strong spatial variations) should be balanced with their transferability (keeping their descriptive power in various chemical environments).

A third source of approximation comes from the choice of basis for the electron states. Most DFT software packages solve the Kohn-Sham equations (2.6) by decomposing the

eigenstates on a basis of functions ϕ_i :

$$\psi_\mu(\vec{r}) = \sum_i c_{i\mu} \phi_i(\vec{r}). \quad (2.12)$$

Thus, diagonalizing the Kohn-Sham equation amounts to solving the generalized eigenvalue problem

$$\sum_i (H_{ji}^{KS} - \epsilon_\mu S_{ji}) c_{i\mu} = 0 \quad (2.13)$$

in which $H_{ji}^{KS} = \langle \phi_j | \hat{H}^{KS} | \phi_i \rangle$ is the Kohn-Sham Hamiltonian matrix and $S_{ji} = \langle \phi_j | \phi_i \rangle$ is the overlap matrix. This is done using optimized algebra routine contained in specialized libraries such as Basic Linear Algebra Subprograms (BLAS) and Linear Algebra PACKage (LAPACK). In principles, this procedure is exact if a complete basis of the Hilbert space is used. However, that would require an infinite number of basis functions, and a limited number of them have to be selected for an approximate expansion of the eigenstates. The most well-known software packages, such as the Vienna Ab initio Simulation Package (VASP) [125] and Quantum ESPRESSO, use plane-waves for the basis $\phi_i(\vec{r})$. An energy cutoff is chosen to determine the size of the basis, excluding the plane waves corresponding to free electrons of energy greater than the cutoff. A typical value for the cutoff is 50 Ry. One advantage of this choice is the simplicity in systematically improving the quality of the basis expansion: just choose a higher cutoff. Another benefit is that all the quantities are expressed in the reciprocal space, in which the expressions for the matrix elements H_{ji}^{KS} have simple forms and the density and potentials can be efficiently computed by Fast Fourier Transform algorithms. The drawback is that convergence usually demands a large number of plane waves, and is particularly demanding for describing tightly bound states such as 3d orbitals. A second class of software packages, such as SIESTA, use localized atomic-like orbitals as basis. SIESTA, for instance, typically uses the solutions of the Kohn-Sham equations for isolated atoms in the presence of a confinement potential. The basis orbitals are taken from the eigenstates of this problem corresponding to the valence electrons, and more orbitals can be added by generating other radial ("multiple- ζ ") and angular ("polarization") shapes. The advantage of using such localized orbitals is that the basis size is typically small, leading to modest calculation times. The drawback is that there is no systematic way of improving the basis, although there are tools to optimize it (Simplex for SIESTA). In SIESTA, the matrix elements H_{ji}^{KS} corresponding to the kinetic energy are calculated in reciprocal space, while the potential terms that involve the electron density are calculated in real space using a discretized grid. Also worth mentioning is a third methodology, the so-called atomic sphere method that use localized functions near the nuclei but planewaves far from them. This is very accurate but more difficult to implement and very expensive in calculation time.

DFT calculations on solids exploit the periodicity of the crystal by using the Bloch theorem, which shows that the Hamiltonian is block-diagonal with blocks indexed by the crystal momentum \vec{k} taken in the first Brillouin zone. An eigenstate with momentum \vec{k} display a phase shift $e^{i\vec{k}\vec{R}}$ in a translation \vec{R} from one unit cell to another:

$$\psi_{n,\vec{k}}(\vec{r} + \vec{R}) = e^{i\vec{k}\vec{R}} \psi_{n,\vec{k}}(\vec{r}) \quad (2.14)$$

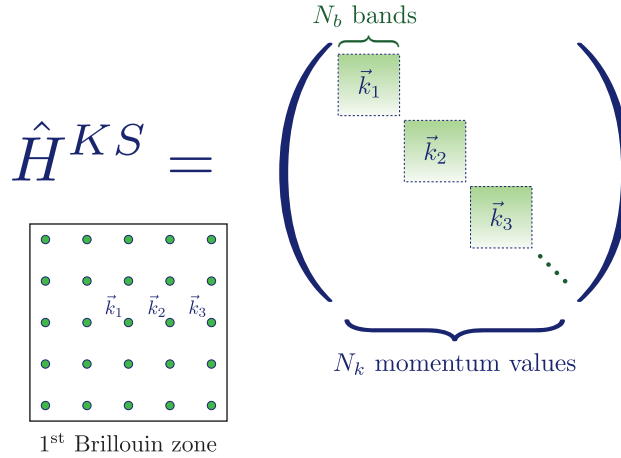


Figure 2.2: A sketch of the block-diagonal Kohn-Sham Hamiltonian.

where n is the band index distinguishing between different eigenstates of the same block \vec{k} . A finite, periodic system composed of N_c unit cells has N_c possible values of \vec{k} in the Brillouin zone. For an infinite system, the sum over \vec{k} becomes an integral. Here, an approximation has to be made again by sampling the Brillouin zone with a given number N_k of momentum values. Usually, a few hundred \vec{k} values are enough to perform the SCF cycle. The number of bands N_b is the number of reciprocal lattice vectors (for plane waves) or orbitals in the unit cell (for localized orbitals) included in the basis. The great advantage of using the Bloch theorem is that instead of having to diagonalize the $(N_k N_b) \times (N_k N_b)$ Kohn-Sham Hamiltonian, which scales as $\sim N_k^3 N_b^3$ in computation time, we just have to diagonalize $N_k N_b \times N_b$ blocks, which scales as $\sim N_k N_b^3$ (see Fig 2.2). This N_b^3 scaling highlights the computational time gained by using a small basis set.

The implementation of DFT methodology described in this section allows to find the ground-state electron density and the optimized structure of crystals with unit cells comprising up to several hundred atoms in a reasonable computation time (a few days or even hours). Once this has been achieved, there still remains the issue of finding the excitation spectrum to obtain the band structure, the density of states and other properties such as the electrical conductivity. Here, an approximation is made that has nothing to do with computational limitations. In principle, the first Hohenberg-Kohn theorem ensures that the excitation spectrum can be derived from the knowledge of the ground-state electron density. In practice, this requires further many-body calculations, or an extension of the Kohn-Sham approach that includes time-dependence in order to compute the dynamical response functions, a theory known as Time-Dependent Density Functional Theory (TDDFT). In materials science, a simpler method is usually followed: the single-particle excitation energies of the system are taken directly from the eigenvalues of the Kohn-Sham Hamiltonian (2.6) calculated with the correct electron density. When this is done, the Kohn-Sham system is no longer considered as a mere mathematical device, but as a mean-field representation of the real electron system. Standard mean-field approaches map a many-body problem onto a single-particle one by neglecting the correlations in the inter-

action terms of the Hamiltonian. For instance, in a mean-field theory of the Hubbard Hamiltonian, the Hubbard term (2.11) might be rewritten

$$E_U = U (n_{i,\uparrow} + (\hat{n}_{i,\uparrow} - n_{i,\uparrow})) (n_{i,\downarrow} + (\hat{n}_{i,\downarrow} - n_{i,\downarrow})) \approx U (n_{i,\uparrow} \hat{n}_{i,\downarrow} + n_{i,\downarrow} \hat{n}_{i,\uparrow} - n_{i,\uparrow} n_{i,\downarrow}), \quad (2.15)$$

where $n_{i,\uparrow}$ (resp. $n_{i,\downarrow}$) is the ground-state expectation value of the occupation operator $\hat{n}_{i,\uparrow}$ (resp. $\hat{n}_{i,\downarrow}$), and the product $(\hat{n}_{i,\uparrow} - n_{i,\uparrow})(\hat{n}_{i,\downarrow} - n_{i,\downarrow})$ has been neglected. The Hamiltonian, which now depends on the self-consistent parameters $n_{i,\uparrow}$ and $n_{i,\downarrow}$, can then be diagonalized. In such mean-field approaches, the correlations are lost and the electrons are taken to interact with the average field created by the other electrons. In DFT, the Kohn-Sham procedure does the same thing, except that the correlations effects are reintroduced approximately through the exchange-correlation term $E_{xc}[n]$, which is also self-consistent.

2.1.2 From DFT to tight-binding: Wannier orbitals

Even though the electronic band structure, density of states (DOS) and transport properties (electrical conductivity, Seebeck coefficient) can be computed directly from the Bloch eigenstates $|\psi_{n,\vec{k}}\rangle$ and eigenvalues $\epsilon_{n,\vec{k}}$ of the Kohn-Sham Hamiltonian, in certain cases it is more convenient to choose a different representation based on localized orbitals. This is especially necessary when one wishes to study defects and disorder from first principles, beyond the Boltzmann transport framework (see section 2.2.1). The formalism of Wannier functions, which dates back to the 1930's [126] but has been modernized in 1997 by Marzari and Vanderbilt [127] and subsequently implemented in efficient post-processing softwares [128], appears particularly suited to our needs. The idea behind Wannier functions is to perform linear combinations of Bloch eigenstates to construct an orthonormal basis of localized orbitals. To be more precise, consider a crystal composed of N_c unit cells (periodic boundary conditions are assumed) and suppose we are interested in a set of N_b isolated bands described by Bloch eigenstates $|\psi_{n,\vec{k}}\rangle$, with n ranging from 1 to N_b . Given a vector \vec{R} from the Bravais lattice of the crystal, it is straightforward to show that the linear combinations

$$|\vec{R}, i\rangle = \frac{1}{\sqrt{N_c}} \sum_{\vec{k}} e^{-i\vec{k}\cdot\vec{R}} \sum_{n=1}^{N_b} U_{ni}^{\vec{k}} |\psi_{n,\vec{k}}\rangle \quad (2.16)$$

define an orthonormal set of states if the $N_b \times N_b$ matrices $U^{\vec{k}}$ are unitary. Such states are called Wannier functions, and the $U^{\vec{k}}$ can be chosen such that the wavefunction $\langle \vec{r} | \vec{R}, i \rangle$ decreases exponentially as \vec{r} moves away from the unit cell \vec{R} , making $|\vec{R}, i\rangle$ localized on this unit cell. Marzari and Vanderbilt devised an algorithm to find the $U^{\vec{k}}$ that minimize the spread of the Wannier orbitals, resulting in so-called Maximally Localized Wannier Functions (MLWF). However, it is often sufficient to project the Bloch eigenstates over wisely chosen atomic orbitals [129]. Consider for instance the case of rutile TiO_2 , the most stable form of titanium oxide at high temperatures, which has 2 Ti atoms and 4 O atoms in its unit cell. The conduction band of this material is composed of 10 bands, primarily made up of the Ti 3d orbitals. One can project the conduction Bloch states onto the 3d

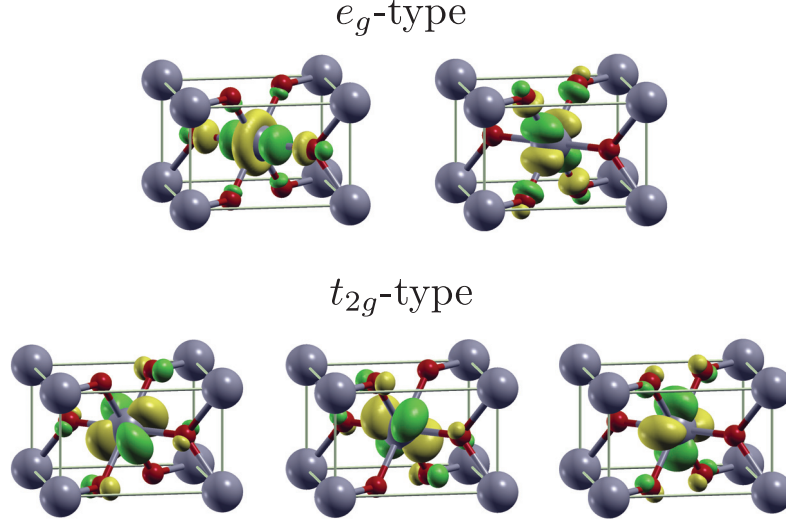


Figure 2.3: The Wannier orbitals associated with the conduction band of rutile TiO_2 .

atomic orbitals $|\chi_i\rangle$ of the Ti atoms in the $\vec{R} = \vec{0}$ unit cell:

$$|\tilde{\phi}_{i,\vec{k}}\rangle = \sum_{n=1}^{N_b=10} |\psi_{n,\vec{k}}\rangle \langle \psi_{n,\vec{k}} | \chi_i \rangle \quad (2.17)$$

where the Bloch-like states $|\tilde{\phi}_{i,\vec{k}}\rangle$ are not orthonormal. They can be orthonormalized using the overlap matrix $(S_{\vec{k}})_{ji} = \langle \tilde{\phi}_{j,\vec{k}} | \tilde{\phi}_{i,\vec{k}} \rangle$:

$$|\phi_{i,\vec{k}}\rangle = \sum_{j=1}^{N_b} |\tilde{\phi}_{j,\vec{k}}\rangle \left(S_{\vec{k}}^{-1/2} \right)_{ji} \quad (2.18)$$

and the Wannier orbitals are then calculated by

$$|\vec{R}, i\rangle = \frac{1}{\sqrt{N_c}} \sum_{\vec{k}} e^{-i\vec{k} \cdot \vec{R}} |\phi_{i,\vec{k}}\rangle. \quad (2.19)$$

This procedure is a particular case of the definition (2.16) with a physically motivated choice of the matrix $U^{\vec{k}}$, and it often yields Wannier orbitals as localized as the full MLWF algorithm would. The resulting orbitals from the central Ti atom of the unit cell in rutile TiO_2 (shown in Fig 2.3) can be classified as t_{2g} -like and e_g -like, and display a strong resemblance with the atomic 3d orbitals that make up the conduction band and were used for the projection.

Since the Wannier orbitals are localized on particular atoms of the crystal and more or less correspond to atomic orbitals, the Hamiltonian matrix elements $\langle \vec{R}', j | \hat{H} | \vec{R}, i \rangle = t_{ji}^{\vec{R}' \vec{R}}$ of the Kohn-Sham Hamiltonian can be interpreted as electron hopping terms between orbitals,

in the spirit of the Linear Combination of Atomic Orbitals (LCAO) and Tight-Binding (TB) methodologies. In the case of the diagonal terms, they can be interpreted as on-site potentials. Thus, the Wannier projection leads to a first-principles TB Hamiltonian, which can be cast in the formalism of second quantification:

$$\hat{H} = \sum_{j,i,\vec{R}',\vec{R}} t_{ji}^{\vec{R}',\vec{R}} c_{j,\vec{R}'}^\dagger c_{i,\vec{R}}$$

where $c_{i,\vec{R}}^\dagger$ is the electron creation operator on the Wannier orbital i of the unit cell \vec{R} . Since the Wannier basis is orthonormalized, the annihilation and creation operators satisfy the fermion anticommutation relation

$$\{c_{i,\vec{R}}, c_{j,\vec{R}'}^\dagger\} = \delta_{ij} \delta_{\vec{R}\vec{R}'} \quad \{c_{i,\vec{R}}, c_{j,\vec{R}'}\} = 0 \quad \{c_{i,\vec{R}}^\dagger, c_{j,\vec{R}'}^\dagger\} = 0. \quad (2.20)$$

In the case of a pristine crystal with periodic boundary conditions, the Bloch decomposition can be recovered by performing a Fourier transform of the operators:

$$c_{i,\vec{k}}^\dagger = \frac{1}{\sqrt{N_c}} \sum_{\vec{R}} e^{i\vec{k} \cdot (\vec{R} + \vec{r}_i)} c_{i,\vec{R}}^\dagger \quad c_{i,\vec{R}}^\dagger = \frac{1}{\sqrt{N_c}} \sum_{\vec{k}} e^{-i\vec{k} \cdot (\vec{R} + \vec{r}_i)} c_{i,\vec{k}}^\dagger \quad (2.21)$$

where \vec{r}_i is the position of the orbital i with respect to the unit cell position \vec{R} . Since the hopping terms between the unit cells \vec{R} and \vec{R}' depend only on the relative position $\Delta\vec{R} = \vec{R}' - \vec{R}$, i.e. $t_{ji}^{\vec{R}',\vec{R}} = t_{ji}^{\Delta\vec{R}}$, the Fourier transform of the Hamiltonian writes

$$\hat{H} = \sum_{\vec{k}} \sum_{i,j} \left(\sum_{\Delta\vec{R}} t_{ji}^{\Delta\vec{R}} e^{-i\vec{k} \cdot (\Delta\vec{R} + \vec{r}_j - \vec{r}_i)} \right) c_{j,\vec{k}}^\dagger c_{i,\vec{k}} = \hat{H} = \sum_{\vec{k}} \sum_{i,j} H_{ji}^{\vec{k}} c_{j,\vec{k}}^\dagger c_{i,\vec{k}}. \quad (2.22)$$

Diagonalizing the $N_c N_b \times N_b$ matrices $H_{ji}^{\vec{k}}$ yields the eigenvalues $\epsilon_{n,\vec{k}}$ and the Bloch eigenoperators $c_{n,\vec{k}}^\dagger$, where n is the band index. Thus, the band structure, density of states and other electronic properties can be efficiently calculated from the tight-binding Hamiltonian.

One could wonder if the machinery of Wannier functions is really necessary given that some DFT softwares already generate localized orbitals as a basis. Why not use directly the atomic-like orbitals provided by SIESTA, for instance? The first reason is that Wannier orbitals are orthonormal, which makes the diagonalization of the Hamiltonian much simpler and is essential for defining the creation and annihilation operators, the trace of observables, etc... The second reason is that, when studying transport properties, we are usually only interested in a few bands, either the conduction bands or the valence bands. The Wannier projections result in a minimal localized basis describing these bands. For instance, the conduction band of rutile TiO₂ is described by only 10 orbitals in the Wannier representation (see Fig 2.3). These orbitals look very much like the 3d orbitals of the Ti atoms, but notice that there is significant weight on the 2p orbitals of the neighbouring oxygens. If we had used the atomic orbital basis generated by SIESTA, we should have

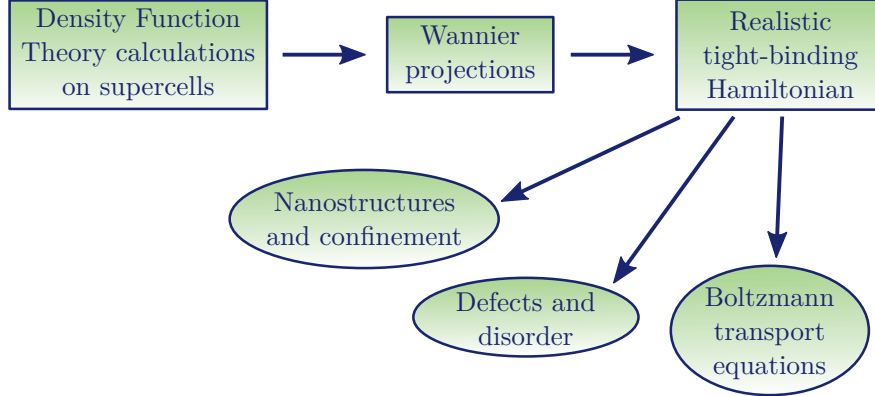


Figure 2.4: Our methodology to model electronic properties in thermoelectric materials.

included not only the 3d orbitals of the Ti atoms, but also the 2p orbitals of the oxygens, resulting in a much larger basis.

Thus, our methodology to study the electronic properties of a given material can be described in the following way, illustrated in Fig 2.4. First we perform DFT calculations using software packages, such as SIESTA or Quantum Espresso, to find the electronic structure of the pristine crystal. In particular, this yields the Bloch eigenstates and eigenvalues of the Kohn-Sham Hamiltonian. Second, we perform Wannier projections to extract a realistic tight-binding Hamiltonian expressed on a localized, orthonormal basis of Wannier orbitals. Once in possession of this tight-binding Hamiltonian, many possibilities offer themselves. We can compute the electronic transport properties (electrical conductivity and Seebeck coefficient) in the framework of the Boltzmann Transport Equation (see section 2.2.1). We can compute the electronic properties in real space in the presence of defects and disorder (see chapter 4), which can be modeled by studying the hopping terms obtained from DFT calculations on a supercell including a defect. We can investigate the effects of nanostructuring and dimensional confinement by reducing the size of the system, or carrying out additional *ab initio* calculations. We can even study electronic correlations by adding a Hubbard term, for instance. Occasionally, it is useful to solve a toy model for understanding the general properties of certain phenomena. In that case, it is possible to start with a simple tight-binding Hamiltonian, without any DFT calculations and Wannier projections which would involve specific materials. Such a model study of resonant states will be presented in section 5.1.

2.1.3 Vibrations in solids: Dynamical matrix

We are now interested in computing the phonon dispersion of the material of interest, i.e. the collective vibration modes whose quantization gives rise to phonons. The crystal structure relaxation described in Fig 2.1b yields the equilibrium geometry of the unit cell. In this configuration, the forces on the ions (the nuclei dressed by the pseudopotentials) vanish by definition. It is possible, however, to compute the energy and the forces for other

positions of the ions, keeping them fixed during the SCF cycle to compute the electronic ground-state. In the spirit of the Born-Oppenheimer approximation, this defines a potential energy surface $E_p(\{\vec{R}_i\})$, where \vec{R}_i is the position of the ion i . Writing $\vec{R}_i = \vec{R}_i^0 + \vec{u}_i$, with \vec{R}_i^0 the equilibrium position of the ion i , we can expand the E_p around the equilibrium configuration in powers of the displacements \vec{u}_i

$$E_p(\{\vec{R}_i\}) = E_p(\{\vec{R}_i^0\}) + \sum_{i,\alpha} \left. \frac{\partial E_p}{\partial u_i^\alpha} \right|_0 u_i^\alpha + \frac{1}{2} \sum_{i,j,\alpha,\beta} \left. \frac{\partial^2 E_p}{\partial u_i^\alpha \partial u_j^\beta} \right|_0 u_i^\alpha u_j^\beta + O(u^3), \quad (2.23)$$

where α and β are indices for the directions x , y and z . On the right-hand side of equation (2.23), the first term is a constant that can safely be ignored. The second term involve the quantities $\left. \frac{\partial E_p}{\partial u_i^\alpha} \right|_0$ which are the forces on the ions at the equilibrium configuration, therefore this term vanishes. The second derivatives $\left. \frac{\partial^2 E_p}{\partial u_i^\alpha \partial u_j^\beta} \right|_0$ are called the Interatomic Force Constants (IFC) and are usually noted $\phi_{ij}^{\alpha\beta}$. They can be interpreted classically as spring constants between the ions and they determine the phonon spectrum. Third-order and higher-order terms, which are neglected in this expansion known as the harmonic approximation, are responsible for the interactions between phonons. When they are taken into account, it is typically in the form of perturbative collision terms. When the ions are displaced, the force of the ion i writes, in the harmonic approximation:

$$F_i^\alpha = - \frac{\partial E_p}{\partial u_i^\alpha} = - \sum_{j,\beta} \phi_{ij}^{\alpha\beta} u_j^\beta. \quad (2.24)$$

This expression allows us to find the IFC through DFT calculations. They are performed on a supercell which contains several unit cells of the material. Each atom of the central unit cell is in turn displaced by a small distance (typically a few percents of angströms) in every direction. A SCF cycle is performed in this configuration and the forces on all the atoms of the supercell are recorded. They are divided by the magnitude of the displacement, yielding the IFC. This procedure is illustrated in Fig 2.5. The supercell should be large enough so that the IFC between atoms at the center and at the border of the supercell are negligible. Typically, supercells of $5 \times 5 \times 5$ unit cells are sufficient, sometimes $3 \times 3 \times 3$ unit cells are enough. Post-processing softwares such as Phonopy [130] can exploit the symmetries of the lattice to reduce the number of calculations. In addition, these programs usually enforce the symmetry constraint $\phi_{ij}^{\alpha\beta} = \phi_{ji}^{\beta\alpha}$ and the translation sum rule

$$\sum_{j,\beta} \phi_{ij}^{\alpha\beta} = 0, \quad (2.25)$$

which ensures that a rigid translation of the system does not create atomic forces, i.e. the acoustic branches have zero frequency at the Γ point. There is also a sum rule ensuring that no force is created by a rigid rotation of the system [131], but this constraint is rarely enforced.

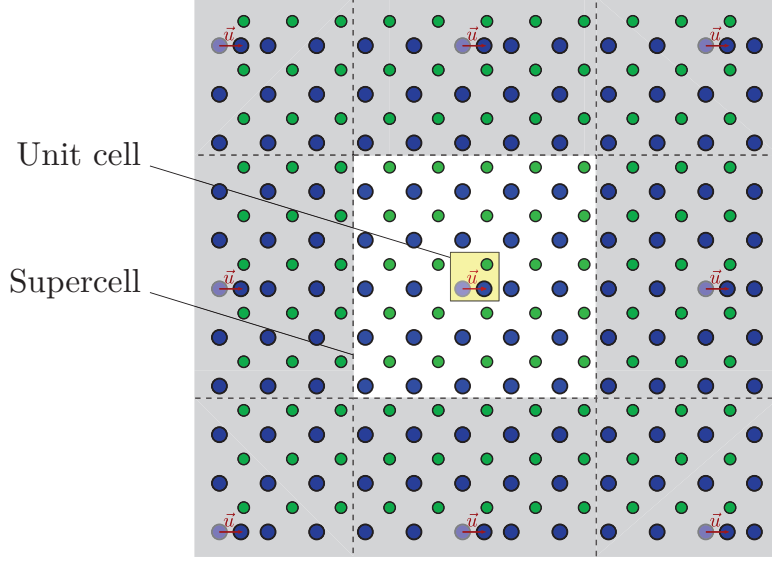


Figure 2.5: A sketch of the system used in IFC calculations. The yellow square is the unit cell, in which the blue atom is moved. The white square is a 5×5 supercell, in which the atomic forces are computed. The periodic images of the system are represented in the shaded regions.

Once the IFC have been obtained, the phonon spectrum can be computed. The Hamiltonian for the N_a ions in the crystal is the sum of their kinetic and potential energy:

$$\hat{H} = \sum_{i,\alpha} \frac{(\hat{p}_i^\alpha)^2}{2m_i} + \frac{1}{2} \sum_{i,j,\alpha,\beta} \phi_{ij}^{\alpha\beta} \hat{u}_i^\alpha \hat{u}_j^\beta \quad (2.26)$$

where m_i is the mass of the ion i and \hat{p}_i^α and \hat{u}_i^α are the impulsion and position operators of the ion i on the α direction. They are hermitian and satisfy the commutation relations

$$\left[\hat{u}_i^\alpha, \hat{p}_j^\beta \right] = i\hbar \delta_{\alpha\beta} \delta_{ij} \quad \left[\hat{u}_i^\alpha, \hat{u}_j^\beta \right] = 0 \quad \left[\hat{p}_i^\alpha, \hat{p}_j^\beta \right] = 0. \quad (2.27)$$

Defining the reduced impulsion and position operators $\hat{P}_i^\alpha = \hat{p}_i^\alpha / \sqrt{m_i}$ and $\hat{U}_i^\alpha = \sqrt{m_i} \hat{u}_i^\alpha$, which satisfy the same commutation relations, the Hamiltonian writes

$$\hat{H} = \frac{1}{2} \sum_{i,\alpha} \left(\hat{P}_i^\alpha \right)^2 + \frac{1}{2} \sum_{i,j,\alpha,\beta} \frac{\phi_{ij}^{\alpha\beta}}{\sqrt{m_i m_j}} \hat{U}_i^\alpha \hat{U}_j^\beta. \quad (2.28)$$

The $3N_a \times 3N_a$ matrix $D_{ij}^{\alpha\beta} = \phi_{ij}^{\alpha\beta} / \sqrt{m_i m_j}$ is called the Dynamical Matrix (DM), and is the key quantity to be diagonalized in order to compute the phonon dispersion. Since it is a real symmetric matrix, it can be diagonalized using a real ortogonal matrix A :

$$D_{ij}^{\alpha\beta} = \sum_{\mu} A_{i\mu}^\alpha \lambda_\mu A_{j\mu}^\beta \quad (2.29)$$

where μ is an index between 1 and $3N_a$ for the eigenvalues λ_μ . The λ_μ are real and positive since $u_i^\alpha = 0$ corresponds to an energy minimum, so they can be written $\lambda_\mu = \omega_\mu^2$. Defining the eigenoperators $\hat{P}_\mu = \sum_{i\alpha} A_{i\mu}^\alpha \hat{P}_i^\alpha$ and $\hat{U}_\mu = \sum_{i\alpha} A_{i\mu}^\alpha \hat{U}_i^\alpha$, which satisfy the same commutation relations as (2.27), the Hamiltonian writes

$$\hat{H} = \sum_{\mu} \left(\frac{1}{2} \hat{P}_\mu^2 + \frac{1}{2} \omega_\mu^2 \hat{U}_\mu^2 \right). \quad (2.30)$$

From this expression, it is clear that the vibrations of the crystal can be considered in the harmonic approximation as a set of decoupled harmonic oscillators, whose pulsation squared is found by diagonalizing the DM. Introducing the phonon creation operators

$$a_\mu^\dagger = \sqrt{\frac{\omega_\mu}{2\hbar}} \left(\hat{U}_\mu - \frac{i}{\omega_\mu} \hat{P}_\mu \right), \quad (2.31)$$

which satisfy the boson commutation relations

$$[a_\mu, a_\nu^\dagger] = \delta_{\mu\nu} \quad [a_\mu, a_\nu] = 0 \quad [a_\mu^\dagger, a_\nu^\dagger] = 0, \quad (2.32)$$

finally casts the Hamiltonian in the familiar form

$$\hat{H} = \sum_{\mu} \hbar \omega_\mu \left(a_\mu^\dagger a_\mu + \frac{1}{2} \right). \quad (2.33)$$

In the case of a pristine crystal, the Bloch decomposition can be recovered by noting the IFC between the atom i of unit cell at \vec{R} and the atom j of the unit cell at $\vec{R}' = \vec{R} + \Delta\vec{R}$ as $\phi_{\Delta\vec{R},ij}^{\alpha\beta}$, where i and j now run between 1 and the number n_a of atoms in the unit cell. By defining the Fourier transforms $\hat{P}_{i,\vec{k}}^\alpha$ and $\hat{U}_{i,\vec{k}}^\alpha$ of $\hat{P}_{i,\vec{R}}^\alpha$ and $\hat{U}_{i,\vec{R}}^\alpha$ in a way similar to equation (2.21), the atomic Hamiltonian writes

$$\hat{H} = \frac{1}{2} \sum_{\vec{k}} \left(\sum_{i\alpha} \hat{P}_{i,-\vec{k}}^\alpha \hat{P}_{i,\vec{k}}^\alpha + \sum_{ij\alpha\beta} D_{\vec{k},ij}^{\alpha\beta} \hat{U}_{i,-\vec{k}}^\alpha \hat{U}_{j,\vec{k}}^\beta \right) \quad (2.34)$$

with

$$D_{\vec{k},ij}^{\alpha\beta} = \sum_{\Delta\vec{R}} \frac{\phi_{\Delta\vec{R},ij}^{\alpha\beta}}{\sqrt{m_i m_j}} e^{i\vec{k} \cdot (\Delta\vec{R} + \vec{r}_j - \vec{r}_i)} \quad (2.35)$$

the \vec{k} -dependant dynamical matrix, which is now a set of $N_c \ 3n_a \times 3n_a$ matrices. Diagonalizing them yields the eigenvalues $\omega_{\vec{k}s}^2$ associated with the eigenoperators $\hat{P}_{\vec{k}s}$ and $\hat{U}_{\vec{k}s}$, where s is the branch index running from 1 to $3n_a$. Introducing the phonon creation operators

$$a_{\vec{k}s}^\dagger = \sqrt{\frac{\omega_{\vec{k}s}}{2\hbar}} \left(\hat{U}_{\vec{k}s}^\dagger - \frac{i}{\omega_{\vec{k}s}} \hat{P}_{\vec{k}s}^\dagger \right), \quad (2.36)$$

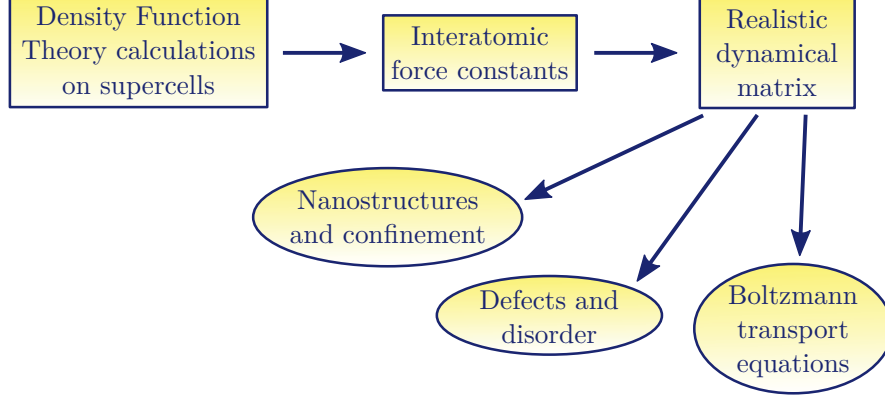


Figure 2.6: Our methodology to model phonon properties in thermoelectric materials.

which satisfy the commutation relations

$$\left[a_{\vec{k}s}, a_{\vec{k}'s'}^\dagger \right] = \delta_{ss'} \delta_{\vec{k}\vec{k}'} \quad \left[a_{\vec{k}s}, a_{\vec{k}'s'} \right] = 0 \quad \left[a_{\vec{k}s}^\dagger, a_{\vec{k}'s'}^\dagger \right] = 0, \quad (2.37)$$

again casts the Hamiltonian in the form

$$\hat{H} = \sum_{\vec{k}s} \hbar \omega_{\vec{k}s} \left(a_{\vec{k}s}^\dagger a_{\vec{k}s} + \frac{1}{2} \right). \quad (2.38)$$

To conclude this section, our approach to studying the vibrational properties from first principles is similar to our methodology for electrons, and is illustrated in Fig 2.6. The IFC are first obtained through *ab initio* calculations on the pristine material. The thermal conductivity can then be computed in the Boltzmann Transport Equation framework (see section 2.2.1), and the effects of disorder, nanostructuring or confinement can be investigated either through direct modelling or with the help of further *ab initio* calculations.

2.2 Electron and phonon quantum transport

The realistic TB Hamiltonian and the dynamical matrix obtained from *ab initio* calculations on a thermoelectric material give direct access, once diagonalized, to the band structure, dispersion relation and DOS of the compound. We now turn to the much more delicate task of computing the thermoelectric transport properties. What makes this endeavour so complicated is the fact that the electrical conductivity, Seebeck coefficient and thermal conductivity are very sensitive to the many-body interactions of electrons and phonons and to the material defects and impurities. There are three transport regimes that will be encountered in this thesis:

Diffusive transport. This regime is the most common in bulk thermoelectric materials. The electron and phonon mean free paths are small compared to the crystal size, but the particles can still be thought of as propagating between scattering events that

hinder transport. The Ohm and Fourier laws are valid, which makes the electrical and thermal conductivities well-defined quantities.

Ballistic transport. If the scattering processes become so weak or the sample so small that the mean free paths become substantially longer than the crystal length, the leads start to play an important role in the transport properties. The conductivities then depend on the dimensions of the material, so they become ill-defined.

Anderson localization. If the sample is very strongly disordered due to defects and impurities, the electron and phonons may become localized, in the sense that their wavefunction is spatially confined. Such localized states do not propagate and thus do not participate in conduction.

It is worth mentioning that there are other transport regimes due to many-body interactions, exhibited for instance by Mott insulators or superconducting phases. In this section, we will cover two formalisms, the Boltzmann Transport Equation and the Landauer formalism, that describe the diffusive and ballistic regimes. In chapter 4 will be presented the Kubo formalism, which can describe the effects of strong disorder, including Anderson localization.

2.2.1 Semi-classical treatment of the diffusive regime

The Boltzmann transport formalism (or, in the context of condensed matter, the Bloch-Boltzmann formalism) is by far the most widely used framework to predict the transport properties of thermoelectric materials. It is a semiclassical description of transport that considers electrons and phonons as wavepackets of Bloch states of the pristine material [89, 132]. The central quantity is the Boltzmann distribution function $g_n(\vec{r}, \vec{k}, t)$, whose physical meaning is that $g_n(\vec{r}, \vec{k}, t) \frac{d\vec{r}d\vec{k}}{(2\pi)^d}$ is the number of electrons or phonons of the band or branch n in the spatial region $d\vec{r}$ around \vec{r} and in the region $d\vec{k}$ around \vec{k} in the first Brillouin zone at time t (d is the dimension of the system, and a factor 2 should be added for electrons due to the spin degeneracy). In this picture, the electrons and phonons propagate like well-defined particles between collision events. These events do not change the propagative Bloch states but induce transitions from one state to another. Thus, the Boltzmann formalism breaks down when the character of the states is deeply affected by disorder or many-body interactions, i.e. when the band-structure is significantly distorted. This formalism cannot properly describe impurity states or resonant states formed by defects, for instance. As a semi-classical framework, it does not take into account the quantum interferences between propagative states, and thus it cannot include Anderson localization effects (see section 4.2.1). Although we will be interested only in the static limit, it is also worth mentioning that the dynamical conductivity predicted in this framework does not include interband transitions. Still, despite these important limitations, the power of the Boltzmann formalism should not be underestimated. It can be easily combined with *ab initio* calculations and it is able to incorporate a variety of scattering and relaxation processes in a relatively simple way. For instance, it has proven successful in describing the dynamics of hot electrons at the surface of metals in the context of laser pump-probe experiments

[133]. Another example is its ability to take into account the crucial distinction between Normal and Umklapp scattering for calculating the thermal conductivity of graphene [134] (see below and section 6.2). If the relaxation time approximation is made (see the next section), it gives very simple closed expressions for the electrical conductivity and Seebeck coefficient, which makes it well suited to provide a first evaluation of the thermoelectric performances.

A general form of the BTE can be written that is valid for both electrons and phonons. As we are interested in the static, steady-state regime, g_n does not depend explicitly on t . But if we follow with time a wavepacket in phase space, its position changes due to its velocity $\vec{v} = \dot{\vec{r}}$ and, in the case of electrons, its wavevector \vec{k} changes due to force fields $\vec{F} = \hbar \dot{\vec{k}}$ acting on it. Thus, in the absence of collisions, a wavepacket of position \vec{r} and wavevector \vec{k} at time t will end up with a position $\vec{r} + \vec{v}dt$ and a wavevector $\vec{k} + \vec{F}dt/\hbar$ at time $t + dt$. In this case, since the Liouville theorem states that phase space neither shrinks nor expands along a trajectory, the distribution function must also be conserved: $g_n(\vec{r} + \vec{v}dt, \vec{k} + \vec{F}dt/\hbar) = g_n(\vec{r}, \vec{k})$. In the presence of collisions, however, a certain number of particles are brought in the phase space region (\vec{r}, \vec{k}) by scattering events between t and $t + dt$, while a certain number are scattered away. The net result is a change in the number of particles around (\vec{r}, \vec{k}) that can be noted $(\frac{\partial g_n}{\partial t})_{\text{coll}} dt$. This leads to the steady-state Boltzmann transport equation:

$$\vec{v} \cdot \frac{\partial g_n}{\partial \vec{r}} + \frac{\vec{F}}{\hbar} \cdot \frac{\partial g_n}{\partial \vec{k}} = \left(\frac{\partial g_n}{\partial t} \right)_{\text{coll}}. \quad (2.39)$$

The force term and the collision term in this expression are different between electron and phonon transport, which we will now examine in turn.

The Boltzmann transport equation for electrons

In the presence of a static electric field $\vec{\mathcal{E}}$, the semiclassical movement of electron wavepackets can be described by the equations

$$\dot{\vec{r}} = \vec{v}_n = \frac{1}{\hbar} \frac{\partial \epsilon_n(\vec{k})}{\partial \vec{k}}, \quad (2.40)$$

$$\dot{\vec{k}} = \frac{\vec{F}}{\hbar} = -\frac{e\vec{\mathcal{E}}}{\hbar}, \quad (2.41)$$

where $\epsilon_n(\vec{k})$ is the energy of the Bloch eigenstate with a wavevector \vec{k} in the band n . In the Boltzmann formalism, a static electric field causes the distribution of electrons to drift in \vec{k} space. In the steady state regime, this is counteracted by the collisions which tend to bring the distribution back to an equilibrium value g_n^0 . This equilibrium value is given by the Fermi-Dirac distribution $f(E, T)$:

$$g_n^0(\vec{r}, \vec{k}) = f(\epsilon_n(\vec{k}), T(\vec{r})) = \frac{1}{e^{\frac{\epsilon_n(\vec{k}) - \mu}{k_B T(\vec{r})}} + 1}, \quad (2.42)$$

where μ is the chemical potential and T depends on \vec{r} in the presence of a temperature gradient. It is convenient to write the distribution function as a sum of its equilibrium and a perturbation: $g_n = g_n^0 + g_n^1$. The BTE then becomes

$$\vec{v}_n \cdot \frac{\partial T}{\partial \vec{r}} \left(\frac{\partial g_n^0}{\partial T} + \frac{\partial g_n^1}{\partial T} \right) - \frac{e\vec{\mathcal{E}}}{\hbar} \cdot \left(\frac{\partial g_n^0}{\partial \vec{k}} + \frac{\partial g_n^1}{\partial \vec{k}} \right) = \left(\frac{\partial g_n^1}{\partial t} \right)_{\text{coll}}, \quad (2.43)$$

where the driving forces (electric field and thermal gradient) have appeared explicitly in the left-hand side (spatial variations of the chemical potential can be included inside $\vec{\mathcal{E}}$, which is then the gradient of the electrochemical potential). Here, the hypothesis of near-equilibrium transport comes into play. We assume the driving forces to be small and retain only the first-order terms, so the derivatives of g_n^1 on the left-hand side can be discarded. The linearized BTE thus writes

$$\left(-\frac{\partial f}{\partial E} \right) \left[\frac{\epsilon_n(\vec{k}) - \mu}{T} \vec{v}_n \cdot \frac{\partial T}{\partial \vec{r}} + e\vec{v}_n \cdot \vec{\mathcal{E}} \right] = \left(\frac{\partial g_n^1}{\partial t} \right)_{\text{coll}}, \quad (2.44)$$

where only the collision term depends on the perturbation g_n^1 . In principle, the collision term should incorporate a detailed balance of the outgoing and ingoing scattered electrons. In practice, an approximation, called the relaxation time approximation (RTA), is very often made that simplifies considerably the calculation of the transport properties. It retains only the fact that the collisions tend to bring the distribution function back to its equilibrium value, and assigns a relaxation rate $\frac{1}{\tau_n(\vec{k})}$ to this process, such that the collision term is taken as

$$\left(\frac{\partial g_n^1}{\partial t} \right)_{\text{coll}} = -\frac{g_n^1(\vec{r}, \vec{k})}{\tau_n(\vec{k})}. \quad (2.45)$$

A closed form for the distribution function is then easily derived, and the transport properties can be found by calculating the charge and heat currents

$$\vec{j}(\vec{r}) = -2e \sum_n \int \frac{d\vec{k}}{(2\pi)^d} g_n^1(\vec{r}, \vec{k}) \vec{v}_n(\vec{k}), \quad (2.46)$$

$$\vec{j}_Q(\vec{r}) = 2 \sum_n \int \frac{d\vec{k}}{(2\pi)^d} (\epsilon_n(\vec{k}) - \mu) g_n^1(\vec{r}, \vec{k}) \vec{v}_n(\vec{k}), \quad (2.47)$$

where the factor 2 comes from the spin degeneracy, \vec{k} is integrated over the first Brillouin zone and g_n^1 appears instead of g_n because the currents vanish in equilibrium. A comparison with equations (1.5) and (1.6), yields the transport coefficients:

$$\sigma^i = 2e^2 \sum_n \int \frac{d\vec{k}}{(2\pi)^d} \left(-\frac{\partial f}{\partial E} \right) v_n^i(\vec{k}) v_n^i(\vec{k}) \tau_n(\vec{k}), \quad (2.48)$$

$$S^i = -\frac{2e}{\sigma^i T} \sum_n \int \frac{d\vec{k}}{(2\pi)^d} \left(-\frac{\partial f}{\partial E} \right) (\epsilon_n(\vec{k}) - \mu) v_n^i(\vec{k}) v_n^i(\vec{k}) \tau_n(\vec{k}), \quad (2.49)$$

$$\kappa_{e,0}^i = \frac{2}{T} \sum_n \int \frac{d\vec{k}}{(2\pi)^d} \left(-\frac{\partial f}{\partial E} \right) (\epsilon_n(\vec{k}) - \mu)^2 v_n^i(\vec{k}) v_n^i(\vec{k}) \tau_n(\vec{k}), \quad (2.50)$$

where the factors 2 all come from the spin degeneracy and $i = x, y, z$ are the directions of the crystal for which the conductivity is diagonal. It should be remembered that the open-circuit electronic thermal conductivity is given by $\kappa_e^i = \kappa_{e,0}^i - \sigma^i (S^i)^2 T$. It is apparent from equations (2.48) to (2.50) that the electronic transport properties can be derived from the knowledge of a single function of energy and temperature $\Sigma^i(E, T)$, called the transport distribution function (TDF) [135]:

$$\sigma^i = \int dE \left(-\frac{\partial f}{\partial E} \right) \Sigma^i(E, T), \quad (2.51)$$

$$S^i = -\frac{1}{eT\sigma^i} \int dE \left(-\frac{\partial f}{\partial E} \right) (E - \mu) \Sigma^i(E, T), \quad (2.52)$$

$$\kappa_{e,0}^i = \frac{1}{e^2 T} \int dE \left(-\frac{\partial f}{\partial E} \right) (E - \mu)^2 \Sigma^i(E, T). \quad (2.53)$$

In the framework of the Boltzmann formalism and within the RTA, the TDF is given by

$$\Sigma^i(E, T) = 2e^2 \sum_n \int \frac{d\vec{k}}{(2\pi)^d} v_n^i(\vec{k}) v_n^i(\vec{k}) \tau_n(\vec{k}) \delta(E - \epsilon_n(\vec{k})). \quad (2.54)$$

The existence of the TDF and the equations (2.51) to (2.53), however, are quite general. They are valid for independent electrons in the presence of static disorder, and it was proven by Jonson and Mahan that they approximately remain so even in the presence of electron-phonon interaction (there is a small correction to the Seebeck coefficient) [136, 137, 30]. The quantity $\left(-\frac{\partial f}{\partial E} \right)$ is basically a window function of width $\approx 4k_B T$ around the Fermi level μ . In degenerate systems, a Sommerfeld expansion gives

$$\sigma^i \approx \Sigma^i(\mu, T), \quad (2.55)$$

$$S^i \approx -\frac{\pi^2 k_B^2 T}{3e} \frac{1}{\Sigma^i} \frac{\partial \Sigma^i}{\partial E} \bigg|_{E=\mu}. \quad (2.56)$$

The Mott formula [138] is thus recovered and the Seebeck coefficient can be interpreted as the logarithmic derivative of the TDF at the Fermi level, while the electrical conductivity is the TDF evaluated at the Fermi level. If the scattering rate depends only on the energy ($\tau_n(\vec{k}) = \tau(\epsilon_n(\vec{k}), T)$), then the TDF can be recast as

$$\Sigma^i(E, T) = D^i(E) \tau(E, T), \quad (2.57)$$

where $D^i(E)$ is the so-called Drude weight, which can be calculated efficiently as the second derivative of the total ground-state energy with respect to a vector potential in the direction of transport (see appendix D). In the Boltzmann transport framework, the Drude weight is simply

$$D^i(E) = 2e^2 \sum_n \int \frac{d\vec{k}}{(2\pi)^d} v_n^i(\vec{k}) v_n^i(\vec{k}) \delta(E - \epsilon_n(\vec{k})). \quad (2.58)$$

Many studies of thermoelectric materials assume a constant relaxation time [139, 140, 105], which allows the calculation of the Seebeck coefficient without any assumption about

scattering and may provide a rough estimate of the thermoelectric performances. A proper treatment of the scattering processes, however, is often crucial for an accurate prediction of electronic transport over a wide range of temperature and carrier concentration. An exact solution of the BTE requires the full expression for the collision term:

$$\left(\frac{\partial g_n^1(\vec{k})}{\partial t}\right)_{\text{coll}} = - \sum_{n'} \int \frac{d\vec{k}'}{(2\pi)^d} [S_{\vec{k},\vec{k}'}^{n,n'} g_n(\vec{k})(1 - g_{n'}(\vec{k}')) - S_{\vec{k}',\vec{k}}^{n',n} g_{n'}(\vec{k}')(1 - g_n(\vec{k}))] \quad (2.59)$$

where $S_{\vec{k},\vec{k}'}^{n,n'}$ is the transition rate between states from band n with wavevector \vec{k} and states from band n' with wavevector \vec{k}' (spin-conserving scattering has been assumed). For electrons, though, it is usually sufficient to use the RTA with realistic expressions for the relaxation time. It may be chosen as the scattering rate of a single carrier with no other states occupied:

$$\frac{1}{\tau_n(\vec{k})} = \sum_{n'} \int \frac{d\vec{k}'}{(2\pi)^d} S_{\vec{k},\vec{k}'}^{n,n'}, \quad (2.60)$$

although this does not take into account the efficiency with which collisions scramble the momentum and energy of the carriers. In heavily doped semiconductors, three scattering mechanisms are present:

Electron-defect scattering. Ionized impurities, vacancies, grain boundaries and lattice imperfections can all scatter electrons, as illustrated in Fig. 2.7a and Fig. 2.7b. The simplest way to calculate the transition rate $S_{\vec{k},\vec{k}'}^{n,n'}$ is through second-order time-dependant perturbation theory, also called Fermi's golden rule:

$$S_{\vec{k},\vec{k}'}^{n,n'} = \frac{2\pi}{\hbar} |\langle \psi_{n',\vec{k}'} | \hat{H}_{\text{def}} | \psi_{n,\vec{k}} \rangle|^2 \delta(\epsilon_{n'}(\vec{k}') - \epsilon_n(\vec{k})), \quad (2.61)$$

where \hat{H}_{def} is the perturbation in the Hamiltonian due to the defects. The presence of the delta function indicates that this type of scattering is elastic: the energy and phase of the carriers are not changed by the scattering events. The validity of equation (2.61) is limited to cases in which the defects are dilute and their influence remain weak. We will present in chapter 4 a methodology to deal with strong disorder stemming from an arbitrary amount of defects.

Electron-phonon scattering. At room-temperature and above, electrons can emit or absorb a phonon as illustrated in Fig. 2.7c and Fig. 2.7d, which is often the dominant source of scattering. There are two major mechanisms for electron-phonon interaction. The first, called deformation potential scattering, is due to the fact that longitudinal phonons stretch and shrink the crystal unit cell, thus shifting the electronic bands. The second is present in polar materials such as GaAs and many oxides. Phonons in such materials represent an oscillating perturbation of the atomic dipoles, thus radiating electromagnetic waves that scatter electrons. This is a strong

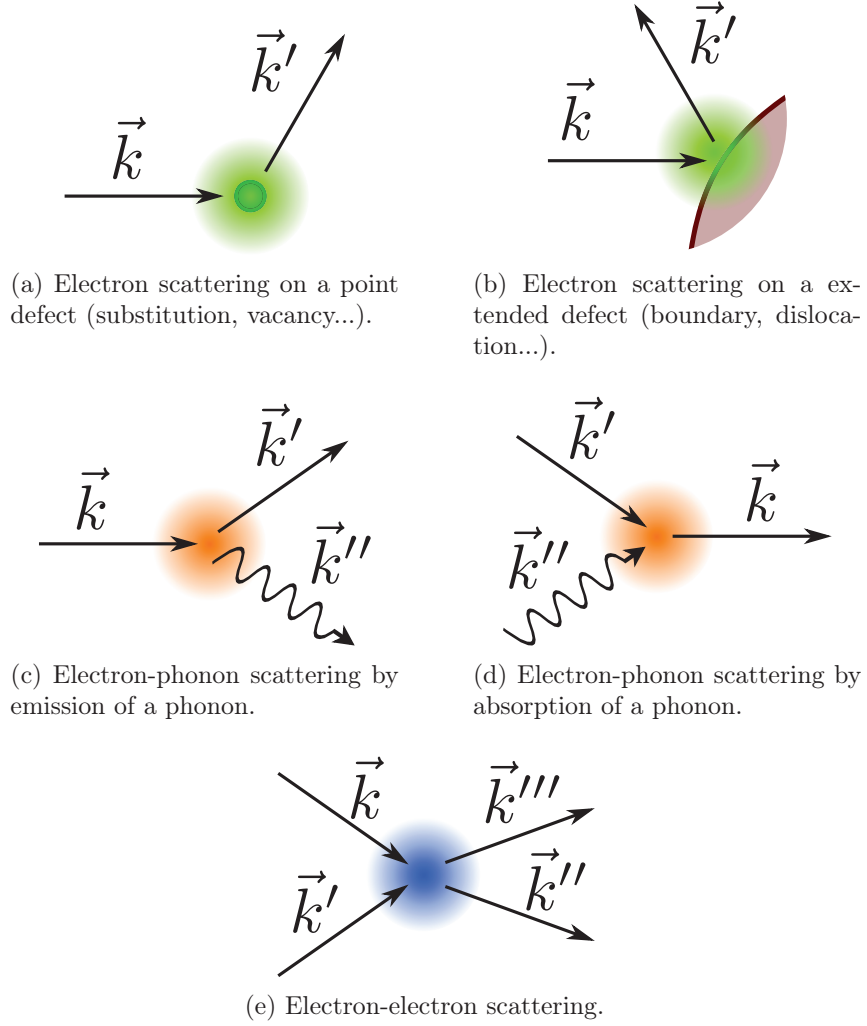


Figure 2.7: Illustrations of the electron scattering mechanisms.

effect for optical phonons (it is then called polar optical scattering), but much weaker for acoustic phonons (it is called piezoelectric scattering). A quantum treatment of electron-phonon scattering requires the formalism of many-body Green's functions, in which second-order perturbation theory (analogous to Fermi's golden rule) gives a scattering rate (2.60) of the general form [141, 142]

$$\frac{1}{\tau_n(\vec{k})} = \frac{2\pi}{\hbar} \sum_{\lambda, n'} \int \frac{d\vec{k}'}{(2\pi)^d} \left| M_{\vec{k}, \vec{k}'}^{\lambda, n, n'} \right|^2 \left[f_B(\omega_\lambda(\vec{q})) \delta(\epsilon_{n'}(\vec{k}') - \epsilon_n(\vec{k}) - \hbar\omega_\lambda(\vec{q})) \right. \\ \left. + (f_B(\omega_\lambda(-\vec{q})) + 1) \delta(\epsilon_{n'}(\vec{k}') - \epsilon_n(\vec{k}) + \hbar\omega_\lambda(-\vec{q})) \right] \quad (2.62)$$

where $\vec{q} = \vec{k}' - \vec{k}$, $\omega_{\vec{q}}$ is the frequency of the phonon in branch λ with wavevector \vec{q} and

f_B is the Bose-Einstein distribution (equation (2.67)). The first term in the bracket corresponds to phonon absorption and the last term to phonon emission. $M_{\vec{k},\vec{k}'}^{\lambda,n,n'}$ is a matrix element between states (n, \vec{k}) and (n', \vec{k}') from the electron-phonon interaction Hamiltonian. It can be calculated from first-principles [143, 144, 145], or it can be parametrized using simple models and then fitted to experimental results, as was done in section 3.3.

Electron-electron scattering. Finally, electrons may scatter off each other, as illustrated in Fig. 2.7e. Because the coulomb interaction is screened by the electron gas, this mechanism is usually negligible at room-temperature and above, though it might actually dominate in certain oxides (see section 3.1). An assumption for the screened potential has to be made in order to calculate the transition rates. In the case of a parabolic conduction band, a simple Thomas-Fermi screening gives [89, 146]

$$\frac{1}{\tau_n(\vec{k})} \propto \frac{(k_B T)^2}{\hbar \epsilon_n(\vec{k})} \quad (2.63)$$

where the origin of the energies is taken at the conduction band minimum.

When several sources of scattering have to be taken into account within the RTA, a common approximation is to sum the transitions probabilities from the different mechanisms, the so-called Matthiessen's rule:

$$\frac{1}{\tau_{\text{tot}}} = \frac{1}{\tau_{\text{def}}} + \frac{1}{\tau_{e\text{-ph}}} + \frac{1}{\tau_{e\text{-e}}}. \quad (2.64)$$

The Boltzmann transport equation for phonons

In the case of phonon transport, the same manipulations of the BTE can be performed to calculate the lattice thermal conductivity [147, 148, 149], although there are several important differences with electrons. There is no equivalent to the electric field, so the semi-classical equations of motion are:

$$\dot{\vec{r}} = \vec{v}_\lambda = \frac{\partial \omega_\lambda(\vec{k})}{\partial \vec{k}}, \quad (2.65)$$

$$\dot{\vec{k}} = \vec{0}, \quad (2.66)$$

where $\omega_\lambda(\vec{k})$ is the frequency of a Bloch eigenstate with a wavevector \vec{k} in the branch λ . The equilibrium distribution function is given by the Bose-Einstein distribution $f_B(\omega, T)$:

$$g_\lambda^0(\vec{r}, \vec{k}) = f_B(\omega_\lambda(\vec{k}), T(\vec{r})) = \frac{1}{e^{\frac{\hbar \omega_\lambda(\vec{k})}{k_B T(\vec{r})}} - 1}. \quad (2.67)$$

We can again linearize the BTE around the equilibrium distribution, which yields

$$\left(-\frac{\partial f}{\partial \hbar \omega}\right) \left[\frac{\hbar \omega_\lambda(\vec{k})}{T} \vec{v}_\lambda \cdot \frac{\partial T}{\partial \vec{r}} \right] = \left(\frac{\partial g_\lambda^1}{\partial t} \right)_{\text{coll}}. \quad (2.68)$$

The phonon heat current is

$$\vec{j}_Q(\vec{r}) = \sum_{\lambda} \int \frac{d\vec{k}}{(2\pi)^d} \hbar\omega_{\lambda}(\vec{k}) g_{\lambda}^1(\vec{r}, \vec{k}) \vec{v}_{\lambda}(\vec{k}), \quad (2.69)$$

The RTA is also called the single-mode approximation (SMA) in the context of phonon transport. It yields for the lattice thermal conductivity:

$$\kappa_{\text{ph}}^i = \int d(\hbar\omega) W_{\text{ph}}(\omega, T) \Sigma_{\text{ph}}^i(\omega, T) \quad (2.70)$$

where

$$W_{\text{ph}}(\omega, T) = \frac{3}{\pi^2} \left(\frac{\hbar\omega}{k_B T} \right)^2 \left(-\frac{\partial f_B}{\partial \hbar\omega} \right) \quad (2.71)$$

is a half-window of width $\approx 2k_B T$ centered on $\omega = 0$, analogous to the electronic quantity $\left(-\frac{\partial f}{\partial E} \right)$, and

$$\Sigma_{\text{ph}}^i(\omega, T) = \frac{\pi^2 k_B^2 T}{3} \sum_{\lambda} \int \frac{d\vec{k}}{(2\pi)^d} v_{\lambda}^i(\vec{k}) v_{\lambda}^i(\vec{k}) \tau_{\lambda}(\vec{k}) \delta(\hbar\omega - \hbar\omega_{\lambda}(\vec{k})) \quad (2.72)$$

is a transport distribution function for phonons. There are again three sources of scattering:

Phonon-defect scattering. All materials contain a certain amount of isotopes that represent a mass fluctuation and thus scatter phonons. Moreover, in thermoelectric materials, other type of defects such as vacancies, substitutions, grain boundaries and nanostructures are intentionally introduced for the express purpose of reducing the thermal conductivity by scattering phonons (see Fig. 2.8a and Fig. 2.8b). The simplest way to calculate the scattering rate for point defects is through the FGR (equation (2.61)). The matrix element of the perturbation is typically proportional to ω^2 , which gives the so-called Klemens formula for the scattering rate

$$\frac{1}{\tau_{\lambda}(\vec{k})} = g \omega^2 \rho(\omega_{\lambda}(\vec{k})), \quad (2.73)$$

where $\rho(\omega)$ is the phonon density of states and g is a factor that depends on the type and mass of the defects [150, 151]. Again, we will examine in chapter 4 more sophisticated treatments of defects and disorder.

Phonon-phonon scattering. Phonon-phonon interactions stem from the anharmonicity of the lattice potential energy (i.e. terms of order 3 and higher in equation (2.23)), and represent a very important source of scattering. The stronger contributions come from the third order terms of the form $a^{\dagger}a^{\dagger}a$ and $a^{\dagger}aa$, that are associated with three phonon processes represented in Fig. 2.8. In Fig. 2.8c, a phonon with wavevector \vec{k} decays into two phonons of wavevectors \vec{k}' and \vec{k}'' , while in Fig. 2.8d, two phonons of wavevectors \vec{k}' and \vec{k}'' coalesce into a phonon of wavevector \vec{k} . The conservation of crystal momentum implies $\vec{k} = \vec{k}' + \vec{k}'' + \vec{G}$, where \vec{G} is a vector of the reciprocal

lattice. Collisions with $\vec{G} = \vec{0}$, called Normal processes, cannot bring the phonon distribution back to equilibrium. Collisions with $\vec{G} \neq \vec{0}$, called Umklapp processes, must involve a phonon with a wavevector of magnitude $||\vec{G}||/2$ at least, so they are thermally activated.

Phonon-electron scattering. The same electron-phonon coupling seen in the previous section also act as phonon scatterers. They are often negligible though, as transport is dominated by defect and boundary scattering at low temperatures and by phonon-phonon scattering at high temperatures.

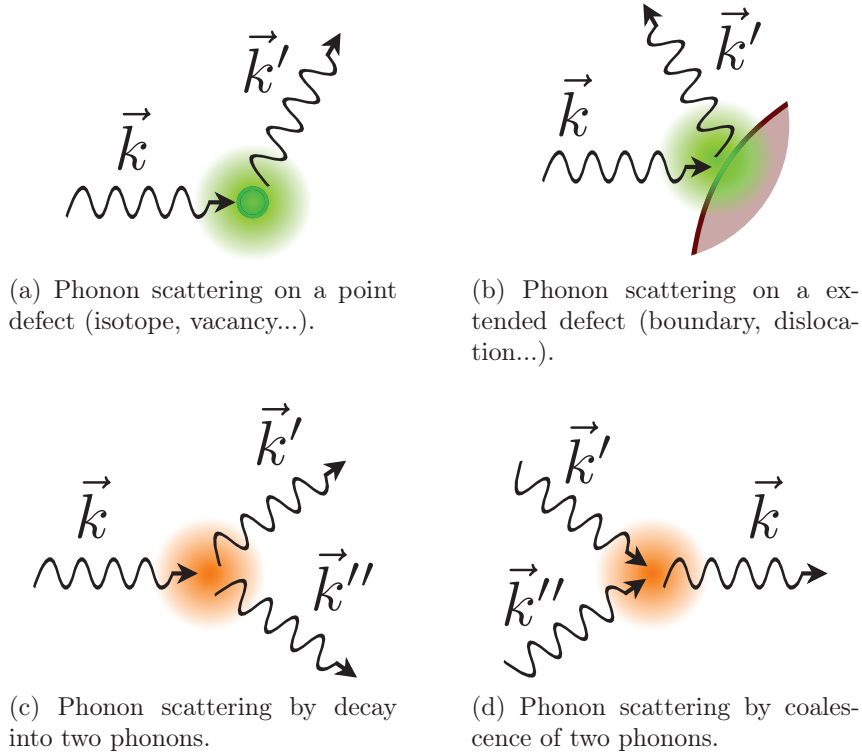


Figure 2.8: Illustrations of the phonon scattering mechanisms.

The fact that Normal phonon-phonon scattering processes cannot bring the phonon distribution back to equilibrium complicates the problem of solving the BTE. In the RTA, Matthiessen's rule lumps all the scattering processes together in a total relaxation time:

$$\left(\frac{\partial g_\lambda}{\partial t} \right)_{\text{coll}} = - \frac{g_\lambda(\vec{r}, \vec{k}) - g_\lambda^0(\vec{r}, \vec{k})}{\tau_\lambda^{\text{tot}}(\vec{k})}, \quad (2.74)$$

with

$$\frac{1}{\tau_\lambda^{\text{tot}}(\vec{k})} = \frac{1}{\tau_\lambda^{\text{N}}(\vec{k})} + \frac{1}{\tau_\lambda^{\text{U}}(\vec{k})} + \frac{1}{\tau_\lambda^{\text{def}}(\vec{k})} + \frac{1}{\tau_\lambda^{\text{ph-e}}(\vec{k})}. \quad (2.75)$$

But this places Normal processes on equal footing with the other sources of scattering, even though the former is not resistive. There are two methodologies to deal with this issue. A first option is to use a different approximation for the collision term, the so-called Callaway model [152, 153, 154]. In this approach, the Normal processes are considered to bring the phonon distribution back to a drifted Bose-Einstein distribution $g_{\lambda}^{\text{drift}}(\vec{r}, \vec{k})$ instead of the usual one centered around $\vec{k} = \vec{0}$. Thus, the Normal scattering rate is set apart in the collision term:

$$\left(\frac{\partial g_{\lambda}}{\partial t}\right)_{\text{coll}} = -\frac{g_{\lambda}(\vec{r}, \vec{k}) - g_{\lambda}^{\text{drift}}(\vec{r}, \vec{k})}{\tau_{\lambda}^{\text{N}}(\vec{k})} - \frac{g_{\lambda}(\vec{r}, \vec{k}) - g_{\lambda}^0(\vec{r}, \vec{k})}{\tau_{\lambda}^{\text{R}}(\vec{k})}, \quad (2.76)$$

where the resistive relaxation time $\frac{1}{\tau_{\lambda}^{\text{R}}(\vec{k})}$ includes all the other sources of scattering. This yields a closed expression for the thermal conductivity, with a correction to the RTA:

$$\kappa_{\text{Cal}}^i = \kappa_{\text{RTA}}^i + \frac{(A^i)^2}{B^i} \quad (2.77)$$

where

$$\begin{aligned} A^i &= \frac{1}{T} \sum_{\lambda} \int \frac{d\vec{k}}{(2\pi)^d} \left(-\frac{\partial f_B}{\partial \hbar\omega}\right) \hbar\omega_{\lambda}(\vec{k}) v_{\lambda}^i(\vec{k}) k^i \frac{\tau_{\lambda}^{\text{tot}}(\vec{k})}{\tau_{\lambda}^{\text{N}}(\vec{k})}, \\ B^i &= \frac{1}{T} \sum_{\lambda} \int \frac{d\vec{k}}{(2\pi)^d} \left(-\frac{\partial f_B}{\partial \hbar\omega}\right) k^i k^i \frac{\tau_{\lambda}^{\text{tot}}(\vec{k})}{\tau_{\lambda}^{\text{N}}(\vec{k}) \tau_{\lambda}^{\text{R}}(\vec{k})}. \end{aligned} \quad (2.78)$$

An alternative is to keep the full expression for the collision term (analogous to equation (2.59)), and solve the BTE numerically to obtain an exact solution. This method is the most accurate but also the most complex and demanding in computation time, although efficient iterative and variational schemes have been developed [148]. Comparisons of the three methods outlined above show that the RTA is generally reasonably accurate for three-dimensional systems at room-temperature and above [154, 147]. In two-dimensional systems, however, the Normal processes tend to remain dominant even around 300 K, in which case the RTA severely underestimate the thermal conductivity. In such cases, it becomes crucial to solve the exact BTE, or to use the Callaway model which is often quite successful in predicting the thermal conductivity (see [134] and section 6.2).

2.2.2 Ballistic regime: the Landauer formalism

The Boltzmann formalism describes electrons and phonons diffusing under an electric field or temperature gradient, subjected to scattering events with an average frequency $\frac{1}{\tau}$ with a mean free path $l = v\tau$ between collisions. In section 2.2.1, the size L of the sample was assumed to be large so that the boundaries were unimportant and $l \ll L$. In such a physical picture, the conductivity grows without bound if the sources of scattering become vanishingly small, as can be checked by taking $\tau \rightarrow \infty$ in equations (2.54) and (2.72). In reality, the system actually undergoes a crossover between the diffusive regime $l \ll L$ and the ballistic regime $l \gg L$. In this regime, what happens at the boundaries of the

system is crucial for the transport properties. In conductivity measurements, the sample is typically attached to macroscopic leads or contacts, which can be considered semi-infinite as illustrated in Fig. 2.9. The most natural theoretical framework to describe transport near and in the ballistic regime is called the Landauer formalism [155, 156, 157]. In the Landauer picture, the conductance is a measure of how Bloch waves are transmitted from one lead to another through the sample. It remains finite even in perfect conductors without any source of scattering. More precisely, if perfect contacts are assumed between sample and leads, the zero-temperature electrical conductance along the $i = x$ axis of a perfect conductor of size $L_x \times L_y \times L_z$ is given by:

$$G^x = \frac{2e^2}{h} M^x(E), \quad (2.79)$$

where the factor 2 comes from the spin degeneracy and E is the Fermi level. $M^x(E)$ is the number of modes at the energy E . It is calculated by plotting the Bloch energies $\epsilon_n(\vec{k})$ of the system as a function of $k_x > 0$ for all values of k_y, k_z and n , and counting the number of crossing points with the line of energy E (see Fig. 2.10). Each crossing point represents a conduction channel available to electrons, associated with a "quantum of conductance" $\frac{2e^2}{h}$. For the lattice thermal conductivity, the same formula holds but the "quantum of thermal conductance" is $\frac{\pi^2 k_B^2 T}{3h}$ for phonons [158, 159]. For large systems, the density of modes and thus the conductance are proportional to $L_y L_z$ but independant of the length L_x of the system in the transport direction. Thus, Ohm's law is broken in the ballistic regime: the conductivity depends on the system size and is not a well-defined property of the material.

At finite temperature and in the presence of disorder, reflections and defects, the electrical conductance can be recast as

$$G^x = \frac{2e^2}{h} \int dE \left(-\frac{\partial f}{\partial E} \right) M^x(E) T^x(E), \quad (2.80)$$

where $0 < T^x(E) < 1$ is the average transmission probability from one lead to another through a channel at energy E . For a perfect conductor, $T(E) = 1$ and equation (2.79) is recovered. This expression is conceptually simple but it hides the fact that the conduction channels are mixed by the presence of disorder and that the transmission varies

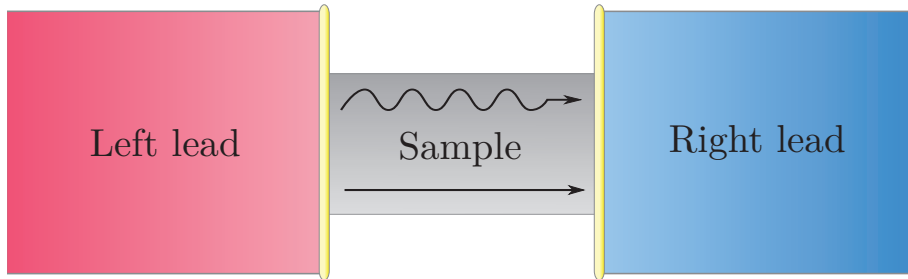


Figure 2.9: The typical geometry described by the Landauer formalism: electrons and phonons go from one semi-infinite lead to another through the sample.

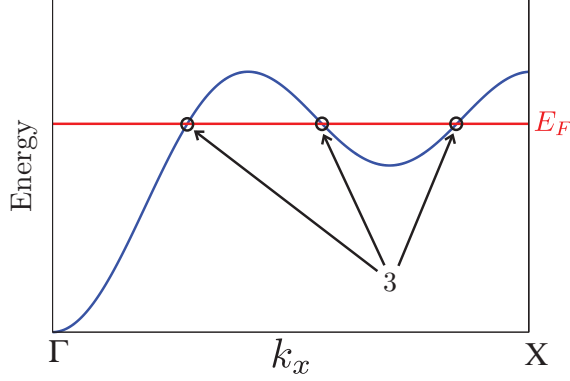


Figure 2.10: A sketch of the procedure for calculating the number of modes: the crossing of the energy bands for $k_x > 0$ with the Fermi level should be counted. The energies are shown for only one band and one value of (k_y, k_z) .

strongly from one channel to another [156]. It is difficult, moreover, to rigorously introduce inelastic sources of scattering like electron-phonon or phonon-phonon collisions. Indeed, this requires more sophisticated approaches such as the non-equilibrium Green's function (NEGF) formalism [155]. It is possible, however, to bridge the gap between the Boltzmann and Landauer formalisms in a somewhat phenomenological way [160, 158]. For electrons, the number of modes can be recast as

$$M^x(E) = L_y L_z \frac{h}{2} \sum_n \int \frac{d\vec{k}}{(2\pi)^d} |v_n^x(\vec{k})| \delta(E - \epsilon_n(\vec{k})). \quad (2.81)$$

Therefore, equation (2.80) gives the same TDF as the BTE with the RTA, equation (2.54), if the transmission is chosen to be $T^x(E) = \frac{l_x}{L_x}$ with the electron mean free path l_x defined as

$$l_x = 2 \frac{\langle v^x v^x \tau \rangle}{\langle |v^x| \rangle} = \frac{\sum_n \int d\vec{k} v_n^x(\vec{k}) v_n^x(\vec{k}) \tau_n(\vec{k}) \delta(E - \epsilon_n(\vec{k}))}{\sum_n \int d\vec{k} |v_n^x(\vec{k})| \delta(E - \epsilon_n(\vec{k}))}. \quad (2.82)$$

It is therefore possible to describe diffusive transport in the language of the Landauer formalism, in which the carrier scattering simply translates into a probability of non-transmission through the channels across the sample: excited carriers may "disappear" in the middle of the system. Conversely, one recovers the expression (2.79) for ballistic transport in a perfect conductor by using the solution (2.54) of the BTE with an energy-dependant scattering rate defined as

$$\frac{1}{\tau(E)} = \frac{2}{L_x} \frac{\langle v^x v^x \rangle}{\langle |v^x| \rangle}, \quad (2.83)$$

which is equivalent to setting the mean free path $l_x = L_x$. Thus, it is also possible to describe ballistic transport in the language of the BTE. The wavepackets are considered to propagate freely across the entire sample, and then a scattering event happens at the

interface with the lead: excited carriers "disappear" in the lead. This is consistent with the fact that the energy dissipation of ballistic conductors takes place mainly in the lead, not in the sample itself [155]. The same procedures can be carried out for the lattice thermal conductivity.

In the context of thermoelectricity, power generation devices involve thermoelectric materials a few millimeters long. The crystal length L_x is therefore very large compared to typical electron mean free paths of a few tens of nanometers [161] and typical phonon mean free paths of a few micrometers [162], so transport can be safely considered diffusive. The experimental study of transport in two-dimensional materials, however, tends to be carried out on small samples a few micrometers long, in which thermal transport may not be entirely diffusive. To compare the theoretical predictions with the measured thermal conductivities in these systems, it may thus be necessary to describe the crossover from the diffusive to ballistic regime. From the above discussion, this can be achieved in the Landauer formalism by choosing a transmission $T^x(E) = \frac{l_x}{L_x + l_x}$, or in the Boltzmann formalism by adding a "ballistic scattering" term $\frac{1}{\tau_n^{\text{bal}}(\vec{k})} = 2 \frac{|v_n^x(\vec{k})|}{L_x}$ or (2.83) in Matthiessen's rule. This phenomenological procedure can be justified in one dimension [155], but misrepresents the transmission distribution when several channels are present [156]. Still, it has the great merits of being simple and successful in providing a crossover between the correct limits of (semiclassical) diffusive and ballistic conductivities. We will see in chapter 4 how a more rigorous treatment of the leads could be achieved.

Chapter 3

Electronic transport in oxides

Quantity has a quality all its own.

A saying attributed to various historical figures.

Recently, transition metal oxides have prompted great interest as potential thermoelectric materials, especially for high-temperature power generation [163, 164, 165]. The classical materials for high-temperature thermoelectrics, SiGe compounds, exhibit a zT around 1 [54, 55]. The other high-performance materials, bismuth telluride and lead telluride based compounds, are mostly toxic and easily decompose at high temperatures. Oxides, on the other hand, tend to be very stable at high temperatures, composed of earth-abundant elements, unexpensive and environmentally benign. Although they are usually strongly polar, they can exhibit surprisingly high power factors at room-temperatures (see section 3.1). Transition metal oxides, and especially strontium titanate, have been the focus of numerous experimental studies aiming at suppressing the thermal conductivity by nanostructuring and boosting the power factor by quantum confinement of the electrons. It is therefore important to provide a theoretical understanding of the factors that determine the thermoelectric performances in these materials.

In this chapter, we will focus on electronic transport in two transition metal oxides, SrTiO₃ and TiO₂. Section 3.1, which has been published in [166], investigates the thermoelectric properties in n-doped SrTiO₃. Section 3.2, published in [167], deals with the issue of quantum confinement in SrTiO₃ superlattices. In section 3.3, we study electronic transport in bulk TiO₂ for high-temperature thermoelectricity [168].

3.1 Unified modelling of the thermoelectric properties in SrTiO₃

Among oxides, the perovskite material SrTiO₃ (STO) is particularly interesting because it has already a relatively large power factor of the order of $20 \mu\text{W}/\text{cm}\cdot\text{K}^2$ comparable to that of the best known thermoelectric (TE) materials such as Bi₂Te₃ [51]. However, because of its relatively high thermal conductivity of $\kappa \approx 11 \text{ W}/\text{m}\cdot\text{K}$ [169], the ZT of STO is only 0.1. It is thus clear that the nanostructuring of the material (reduction of the thermal

conductivity) combined with a judicious dopant could further boost the PF and thus lead to large values of ZT. In this work, we propose a detailed theoretical study of the TE transport in STO and compare our results with a wide panel of experimental published data for bulk and thin films. To complete the latter, we present our thermoelectric measurements on heavily La doped STO films epitaxially grown by MBE on STO (001) substrate [170].

3.1.1 The tight-binding Hamiltonian and transport calculations

First principles studies show that the lowest conduction bands (π^*) in STO have mainly the Ti d character [171, 172, 173, 174]. Therefore, instead of performing full ab initio calculations, our strategy consists in building up a minimum tight-binding (TB) Hamiltonian from the most relevant electronic bands. This allows more general discussions and facilitates the identification of the relevant underlying mechanisms just by tuning a single well-defined physical parameter. First, we define the minimal but realistic TB Hamiltonian for the t_{2g} orbitals and then we introduce the relevant scattering processes needed to address the TE properties beyond the constant relaxation time approximation.

The Hamiltonian reads, $\hat{H} = \hat{H}_0 + \hat{H}_{dis}$ where,

$$\hat{H}_0 = \sum_{\mathbf{ij}, \alpha\beta} t_{\mathbf{ij}}^{\alpha\beta} c_{\mathbf{j}\beta}^\dagger c_{\mathbf{i}\alpha}, \quad (3.1)$$

$$\hat{H}_{dis} = \sum_{\mathbf{i}, \alpha} \epsilon_{\mathbf{i}} c_{\mathbf{i}\alpha}^\dagger c_{\mathbf{i}\alpha}. \quad (3.2)$$

\hat{H}_0 is the TB part and \hat{H}_{dis} describes the effects of disorder (dopants substitution and intrinsic defects) where $c_{\mathbf{i}\alpha}$ is the annihilation operator for the α orbital at site \mathbf{i} . $|\alpha\rangle$, $|\beta\rangle$ denote $|xy\rangle$, $|yz\rangle$ or $|zx\rangle$, the 3 t_{2g} d-orbitals of Ti. The on-site scattering potentials $\epsilon_{\mathbf{i}}$ in \hat{H}_{dis} are chosen randomly within a box distribution of width W . The treatment of \hat{H}_{dis} is discussed in what follows. The integrals $t_{\mathbf{ij}}^{\alpha\beta}$ are restricted to nearest and next nearest neighbour only. We also assume no hopping between d-bands, e.g. $t_{\mathbf{ij}}^{\alpha\beta} = 0$ if $\alpha \neq \beta$. Resulting from the symmetry of the orbital, we have for the d_{xy} -band the following set of intra-orbital hoppings: for \mathbf{i} and \mathbf{j} nearest neighbors in the xy plane, $t_{ij} = t_1$; for \mathbf{i} and \mathbf{j} next-nearest neighbors in the xy plane, $t_{ij} = t_3$; and for \mathbf{i} and \mathbf{j} nearest neighbors along the z axis, $t_{ij} = t_2$. The parameters are $t_1=0.277$ eV, $t_2=0.031$ eV and $t_3=0.076$ eV as estimated in Ref. [175]. The other two bands (d_{yz} and d_{zx}) are obtained by applying a circular permutation $(x,y,z) \rightarrow (y,z,x) \rightarrow (z,x,y)$. The TB Hamiltonian becomes, $\hat{H}_0 = \sum_{\mathbf{k}, \alpha} \epsilon_{\alpha}^0(\mathbf{k}) c_{\mathbf{k}\alpha}^\dagger c_{\mathbf{k}\alpha}$ where $\epsilon_{xy}^0(\mathbf{k}) = -2t_1 (\cos(k_x a) + \cos(k_y a)) - 2t_2 \cos(k_z a) - 4t_3 \cos(k_x a) \cos(k_y a)$, where the lattice parameter $a = 3.9 \text{ \AA}$ in STO.

The conductivity and the Seebeck coefficient are calculated using equations (2.51) and (2.52) where the transport distribution function (TDF) can be written $\Sigma(E, T) = D(E)\tau(E, T)$ (equation (2.57)). $D(E)$ is the Drude weight calculated at $T=0$ K. By analogy with the classical Drude formalism, one can write $D(E) = \frac{ne^2}{m_t}$ where n is the carrier density and m_t the transport effective mass. $\tau(E, T)$ is the energy and temperature dependent electron lifetime.

$D(E)$ is the order parameter for the metal-insulator phase transition, and can be directly extracted from the following sum rule [176, 177, 178, 179, 180] (see appendix D),

$$D(E) = -\frac{2}{\pi} \int_0^{+\infty} \sigma_{reg}(\omega, E) d\omega - \frac{\sigma_0}{N\hbar} \langle \hat{K}_x \rangle(E), \quad (3.3)$$

where σ_{reg} is the regular (incoherent) part of the optical conductivity corresponding to intraband transitions, $\sigma_0 = \frac{e^2}{\hbar a} = 6258 \text{ } \Omega^{-1} \cdot \text{cm}^{-1}$, N is the number of sites and $\hat{K}_x = -\frac{\partial^2 \hat{H}}{\partial \kappa_x^2}$ ($\kappa_x = k_x a$).

In this study, we restrict ourselves to weak disorder regime, a justified approximation for samples exhibiting a good metallic behaviour. This regime corresponds to $k_F l_e \gg 1$, where k_F is the Fermi wave vector and l_e the mean free path. As will be seen, this is indeed the case for most samples considered here. In the weak disorder regime, $D(E)$ is reduced to the second term in equation (3.3), since the transfer of weight from the Drude peak to finite frequencies is small, hence $D(E) \approx -\frac{\sigma_0}{N\hbar} \langle \hat{K}_x \rangle(E)$. Note also that $D(E)$ is dominated by d_{xy} and d_{xz} bands that contribute equally, whilst d_{yz} band has a negligible contribution (the hopping in the x -direction is very small for this band).

We now briefly discuss the nature of the scattering rate. It has two contributions: $\frac{1}{\tau(E, T)} = \frac{1}{\tau_{dis}(E)} + \frac{1}{\tau_{th}(T, E)}$. $\tau_{dis}(E)$ denotes the effect of disorder resulting from the cationic substitutions and presence of other defects (intrinsic, dislocations, grain boundaries) whilst $\tau_{th}(T, E)$ is the temperature dependent part. Its origin is electron-phonon processes (e-ph) and electron-electron (e-e) scattering. In oxides such as STO, several studies showing a T^2 dependent resistivity suggest that the e-e mechanism dominates over the e-ph contribution up to relatively large temperatures [181, 182, 183, 184]. Thus, we consider this term only. Using the Fermi golden rule we get $\frac{\hbar}{\tau_{dis}(E)} = 2\pi \langle \epsilon_i^2 \rangle \rho(E) = \frac{\pi W^2}{6} \rho(E)$ where $\rho(E)$ is the density of states. The thermal contribution has the form, $\frac{\hbar}{\tau_{th}(E)} = C \frac{(k_B T)^2}{E - E_b}$ where C is a dimensionless constant and E_b the energy at the bottom of the conduction band. There is no simple and direct way to estimate C , it depends on the Thomas-Fermi screening length scale, carrier concentration and topology of the Fermi surface. Below, we explain the procedure that allows to set free parameters (C, W).

It is interesting to mention, regarding the nature of the charge carriers, that it has been argued that transport properties in electron doped STO could be understood within the polaronic framework [185, 186, 187, 188, 189]. Nevertheless, as discussed in ref.[182], the T^2 dependent resistivity in electron doped STO could result from an effective polaron-polaron scattering mechanism. Concerning the heavier polaron mass, which amounts in our picture to a renormalization of the hopping integrals, this can be directly absorbed in the (C, W) parameters. Therefore, whether the charge carriers in n-doped STO are described in terms of electrons or polarons (electrons dressed by the interactions with the phonons) does not affect our modelization.

Let us now discuss our results. Fig. 3.1(top) shows the dispersion obtained from both (i) *ab initio* calculations (QuantumEspresso [113] (QE) and SIESTA [112]) and (ii) TB model described previously. Both SIESTA and QE calculations are performed using the PBE functional [123] and a Monkhorst-pack of $10 \times 10 \times 10$ k-points. For QE calculations, Vanderbilt Ultra-soft pseudopotentials [190] are used with a plane wave cut-off of 100 Ry.

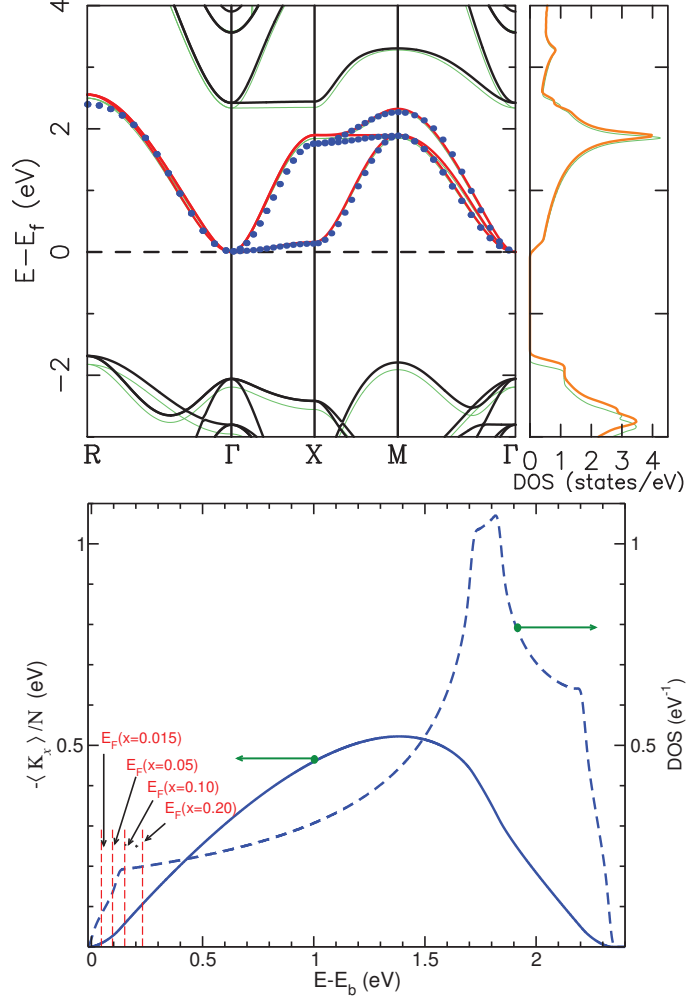


Figure 3.1: From [166]. (Top) Density of states and dispersion for SrTiO₃ obtained with SIESTA (continuous red and black lines), QuantumEspresso (continuous green line) and within the minimal TB model for the 3 t_{2g} bands (blue dots). (Bottom) Tight binding model calculations of (i) the normalized density of states (blue dashed line, right axis) and (ii) the reduced Drude weight $-\langle K_x \rangle / N$ (blue continuous line, left axis) as a function of E . The dashed vertical lines indicate the position of the Fermi level for a carrier charge per unit cell ranging from $n.a^3=0.015$ to 0.20.

For SIESTA calculations we use Troullier-Martin norm-conserving pseudopotentials [191], a mesh cut-off of 400 Ry and a $d\zeta p$ basis optimized with the simplex tool. As can be clearly seen, SIESTA and QE lead to very similar results.

We find an excellent agreement between *ab initio* and TB approach, that fully supports the 3 t_{2g} bands Hamiltonian modelization. In Fig. 3.1(bottom) we have also plotted both the calculated DOS and the reduced Drude weight $-\langle K_x \rangle / N$ as a function of E . It can

be seen that beyond an electron concentration $n.a^3=0.10$, $D(E)$ increases almost linearly. The corresponding Fermi energy coincides with that of the kink in the DOS or edge of the heavy electron bands as plotted in Fig. 3.1(top). Below a carrier density $n.a^3=0.10$, we find $D(E) \propto (E - E_b)^{\frac{5}{3}}$, in contrast with the free electron model for which the power is $3/2$.

3.1.2 The thermoelectric properties

In what follows, and because La, Nb are single electron donors and act as a reservoir we will systematically assume for the comparison that the carrier density in measured samples is $n_{exp} \approx x/a^3$. The sign \approx means that the system may contain intrinsic compensating defects such as oxygen vacancies that may affect the electron density. In Fig. 3.2 the resistivity is plotted as a function of temperature. We set the free parameters C and W in such a way that we reproduce the resistivity measurements for 10% La doped sample of Ref.[192] corresponding to a carrier density of $n = 1.7 \cdot 10^{21} \text{ cm}^{-3}$. More precisely W is set to reproduce $R(T=0 \text{ K})$ and C adjusted to give $R(T=300 \text{ K})$ measured experimentally. The motivation for this choice is the good metallic behaviour found for this concentration of dopant. This leads respectively to $W = 0.17 \text{ eV}$ and $C = 24.5$. These parameters are now set for the whole study. This value of W is consistent with the assumption of weak disorder regime, indeed $W \ll W_b$ where the bandwidth of the conduction band W_b is of the order of

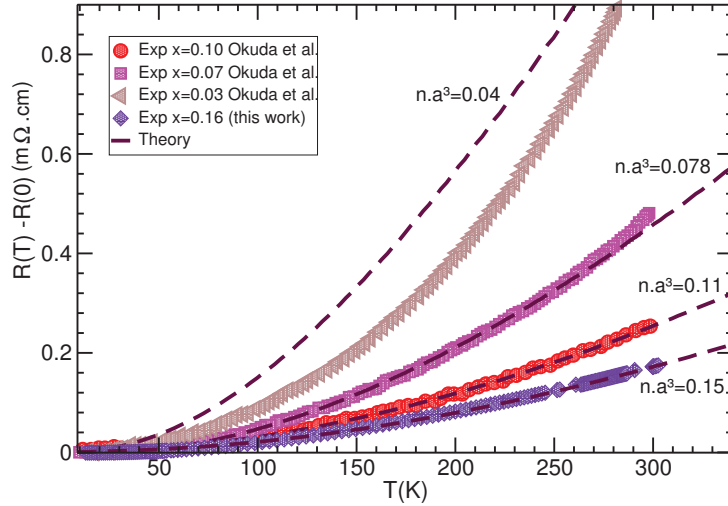


Figure 3.2: From [166]. Resistivity as a function of temperature: theory (dashed lines) vs experiments for $\text{La}_x\text{Sr}_{1-x}\text{TiO}_3$ (symbols). The data points on bulk and thin films are taken from Ref. [192] and our measurements. In the theoretical calculations, the concentration of carriers (n) is directly indicated in the figure.

2 eV. We now discuss the results of our calculations. First, for sufficiently large doping ($n.a^3 \geq 0.06-0.07$) we observe a very good quantitative agreement between theory and experiment for the whole range of temperature. Below (between $n.a^3 = 0.03-0.05$) some deviations at low temperature between theory and experiment are visible. Theory leads to slightly larger values of the resistivity, the reasons for this could be manifold. First, the simplicity of the model: the low energy band structure (below the kink in the DOS) should be improved. Secondly, the electron-electron scattering rate used here does not include the true nature of the d-orbitals. In other words, the non spherical nature of the Fermi surface resulting from the strong hopping anisotropy is not taken into account. Finally, the presence of native defects, such as oxygen vacancies, not included here, should also have an effect. Oxides are known to contain oxygen vacancies, with a typical concentration of 1 or 2% per unit cell. Because of their donor character, the effects on the carrier concentration are expected to be more visible at low electron doping. A full quantitative analysis of these effects goes beyond the scope of this study, and requires much more involved numerical calculations. Below $n.a^3 = 0.015$, it is experimentally observed that the resistivity increases strongly [192]. A possible explanation could be that at low density the Fermi level gets closer to the mobility edge (separating extended from localized states). Localization effects, not included in the present study, should lead to a strong suppression of the Drude weight (significant transfer of weight to the regular part of the conductivity) and thus to an increase of the resistivity. If we further decrease the carrier density, we expect a metal to insulator transition below a critical concentration as seen in Ref.[192].

In Fig. 3.3 we have plotted the measured Seebeck coefficient (S) as a function of temperature in both La and Nb doped samples, together with the theoretical calculations. For large concentration (beyond $n.a^3=0.05$), we observe an overall good quantitative agreement between theory and experiments. At lower concentration, the agreement is very good above 100 K, and below this temperature the experimental data slightly deviates from the calculations. This larger measured $|S|$ could be a consequence of the Fermi level proximity to localized states region. This feature is expected to become more pronounced as the carrier density is further reduced, leading eventually to a minimum in $|S|$ at low temperature. This is for instance observed in 1.5% La doped samples in ref.[192] and [194]. A well defined minimum is clearly seen in both papers when the electron density is small enough. Such a minimum is often attributed to phonon-drag. However, the relevance of this mechanism is still highly debated. Thus, it would be of great interest to clarify for low doped STO, whether the minimum is a signature of Anderson localization or due to phonon drag.

We propose now to compare the calculated carrier dependent electrical conductivity and Seebeck coefficient at $T = 300$ K to available experimental data. The results are depicted in Fig. 3.4. The agreement found between theory and experiments is very good for carrier densities spreading over four decades (extremely low to heavily doped). The agreement is almost insensitive to the electron donor (La, Nb & B) and to the nature of the sample (bulk or thin films). The conductivity varies over four decades and is impressively well reproduced by the theory. This is especially surprising considering the simplicity of our realistic TB model. The Seebeck coefficient varies from $-60 \mu V \cdot K^{-1}$ at about $n.a^3=0.20$ to $-900 \mu V \cdot K^{-1}$ for $n.a^3=10^{-5}$. The quantitative agreement is again very good for the overall range of carrier concentrations and weakly depends on the dopant and nature of the sample.

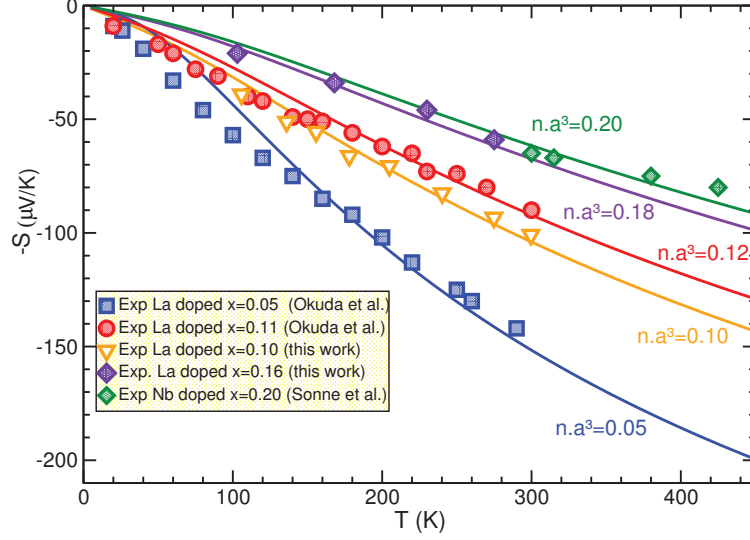


Figure 3.3: From [166]. Seebeck coefficient S as a function of temperature: theory vs experiment. The squares and circles are data extracted from ref.[192] and the green diamonds from ref. [193]. Both triangles and purple diamonds have been obtained in the present study. The continuous lines are the calculated values. The electron concentration n is indicated in the figure.

A deviation can be seen below $n.a^3=0.001$, the measured S are more dispersed but slightly higher than those calculated by about 10-15%. This small deviation could be attributed to localization effects. It is important to remember that as the temperature is reduced the effect of localization should become more pronounced. In the inset, we have plotted the calculated power factor (PF) as a function of $n.a^3$ for three different temperatures. First, we observe a maximum located at $n.a^3 \approx 0.1$ (for $T=300$ K) that progressively shifts towards lower concentrations as the temperature is decreased. The PF increases significantly with the temperature. This results from a stronger increase of S^2 that overcompensates the reduction of the conductivity. At $T=300$ K, we obtain a relatively high value for the power factor $PF=43 \mu W/cm \cdot K^2$ that is in good agreement with recent measurements in La doped thin films [196]. A secondary peak in PF is observed for the lowest temperature, this is attributed to the kink in the DOS (see Fig. 3.1). This figure illustrates nicely the universal character of the present theoretical approach for the TE properties in STO. It is important to stress that, at $T=300$ K and over the whole range of carrier densities, our calculations reveal that the scattering rate is controlled by C only. Thus, the conductivity is inversely proportional to C and the Seebeck coefficient is independent on both parameters. Thus, the crucial ingredients are (i) the realistic band structure and (ii) the T^2/E dependence of the e-e scattering rate.

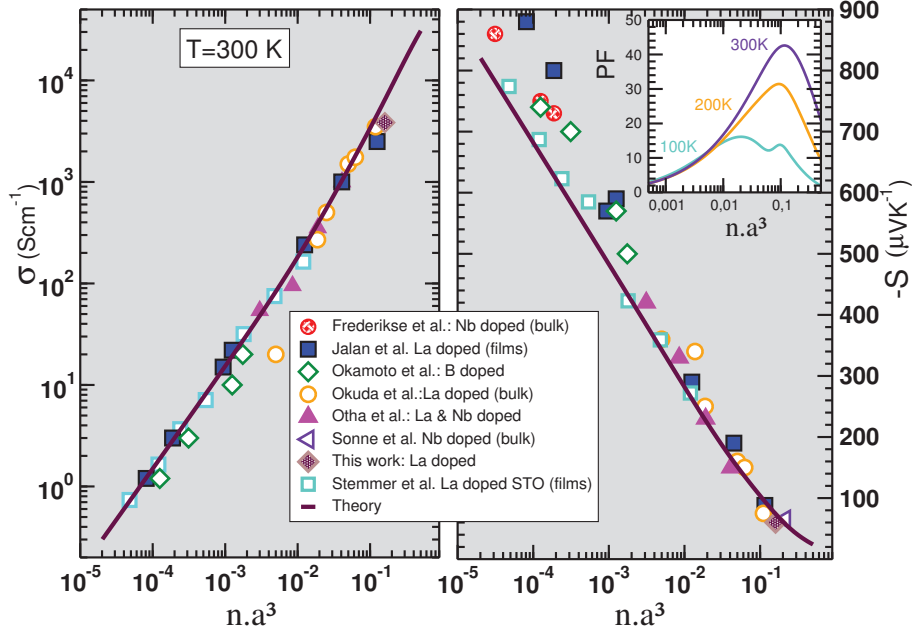


Figure 3.4: From [166]. Conductivity and Seebeck as a function of the carrier concentration (n) at $T = 300$ K. From very dilute up to $n.a^3=0.20$: Theory vs experiment. The inset shows the calculated power factor PF (in $\mu Wcm^{-1}K^{-2}$) for 3 different temperatures. Experimental data (symbols) have been extracted from ref. [192, 193, 195, 196, 197, 198, 199, 194] and from our measurements. The nature of the dopant and material (bulk or film) is indicated in the figure.

In the last section we discuss the T dependence of the resistivity (in metallic samples only). Due to the e-e scattering mechanism, the resistivity can be accurately fitted by $R(T) = R(0) + AT^2$. Indeed, it has been shown recently by Lin et al. [201] that the T^2 law persists down to very low concentration of dopants. Similar experimental results have been reported as well in Ref.[202]. In Fig. 3.5 we plot the variation of A with the electron density, but our concern here is the comparison between theory and experiment. Thus, it is sufficient to restrict ourselves to data ranging from intermediate to heavy doping. In Fig. 3.5, we find that the agreement is very good above $n.a^3=0.03$. Beyond $n.a^3=0.08$ doping, the variation of A with respect to n is very weak (almost flat). Below $n.a^3=0.03$ -0.04, A varies very strongly as n is reduced, and a deviation from the measured values is observed. Note however, that the data become very dispersed as seen for instance in the 2% ($n.a^3=0.02$) doped compounds. It should also be mentioned that the measured carrier concentrations are not precisely known which could also contribute to the observed deviation. In addition, at low carrier densities, the details and nature of the disorder may play a role. From this figure we can conclude that the overall agreement is rather good.

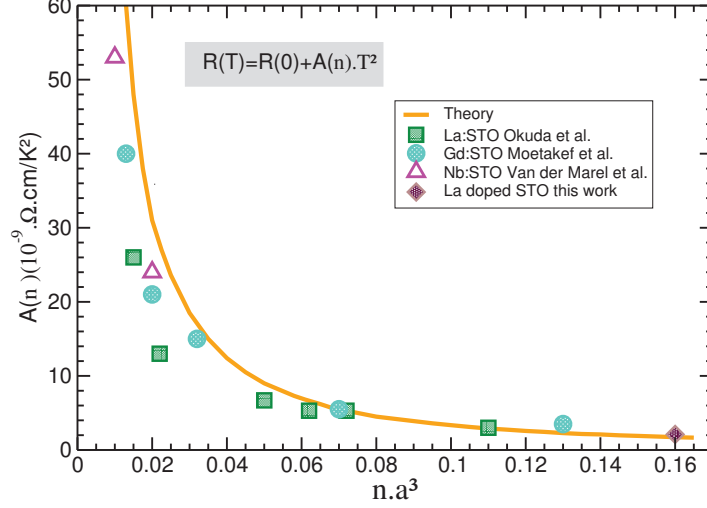


Figure 3.5: From [166]. Resistivity coefficient A as a function of the electron density n : Theory and experiment. Experimental data have been extracted from ref. [192, 200, 182] for La, Nb, and Gd doped STO and our measurements on La doped STO films .

To conclude, in this study that combines theory and experiments we have addressed the thermoelectric properties in electron doped SrTiO_3 . Our theory based on a realistic 3 bands tight binding model that includes relevant scattering processes (weak disorder and e-e scattering mechanism) captures qualitatively and quantitatively well the electronic transport properties in these compounds. The agreement found between theory and experiments covers a wide range of concentrations, from very low to heavily doped. The results are weakly sensitive to the dopant La, Nb, B and even Gd and to the nature of the material, thin films or bulk. The calculations show that STO can already exhibit a relatively high power factor of $43 \mu\text{W} \cdot / \text{cm} \cdot \text{K}^2$ at room temperature for about 10% doping. This is in good agreement with recent experimental data. This study provides an efficient procedure to explore new pathways to improve the thermoelectric properties in oxides and other families of compounds. It should also facilitate the search for new dopants and allow for including effects such as nanostructuration and localization.

3.2 Absence of confinement in $(\text{SrTiO}_3)/(\text{SrTi}_{0.8}\text{Nb}_{0.2}\text{O}_3)$ superlattices

Recent studies in nanostructured thermoelectric materials have opened interesting pathways towards materials exhibiting large ZT [57, 90, 203, 204, 205]. The main ideas behind nanostructuring are twofold. First, it leads to quantum confinement of the carriers, induc-

ing sharp peaks in the density of states, therefore giving rise to a simultaneous increase of both the S and σ . Second, the nanostructuring suppresses κ by increasing the phonon scattering. This strategy has for instance been applied to thin films superlattices such as $\text{Bi}_2\text{Te}_3/\text{Sb}_2\text{Te}_3$ [206, 101], quantum dot superlattices $\text{PbSeTe}/\text{PbTe}$ [207] and bulk alloys BiSbTe [51]. However, achieving quantum confinement in superlattices is not a simple and straightforward task [70]. As an example, it has been claimed in Ref. [208] that the strong enhancement (with respect to the bulk compound) of both S and ZT in $\text{PbSeTe}/\text{PbTe}$ quantum dot superlattices originated from the quantum confinement. It has been shown later [209], that the carrier densities were actually incorrect leading to a wrong interpretation of the measured Seebeck coefficients. Therefore it has been concluded that this $\text{PbSeTe}/\text{PbTe}$ superlattice did not exhibit any confinement. Thus, experimental measurements that do not constitute a direct probe of the confinement effects should be analysed carefully.

Recently, it has been argued that resulting from the two dimensional carrier confinement in $(\text{SrTiO}_3)_x/(\text{SrTi}_{0.8}\text{Nb}_{0.2}\text{O}_3)_y$ superlattices (x and y are respectively the number of undoped and Nb doped layers), giant Seebeck coefficients have been measured [210, 102]. In particular, in the extreme limit of a single Nb doped layer ($y = 1$ and x varies), the measured S as a function of x could saturate at values almost 6 times larger than that of the bulk material. In addition, it has been concluded that the critical barrier thickness for quantum confinement was about 6.25 nm (16 unit cells of STO). However, it is important to notice that the large increase of the Seebeck coefficient does not provide a direct signature of the 2D quantum confinement. In this work, we demonstrate that the data could be explained assuming the absence (or weakness) of quantum confinement in these superlattices.

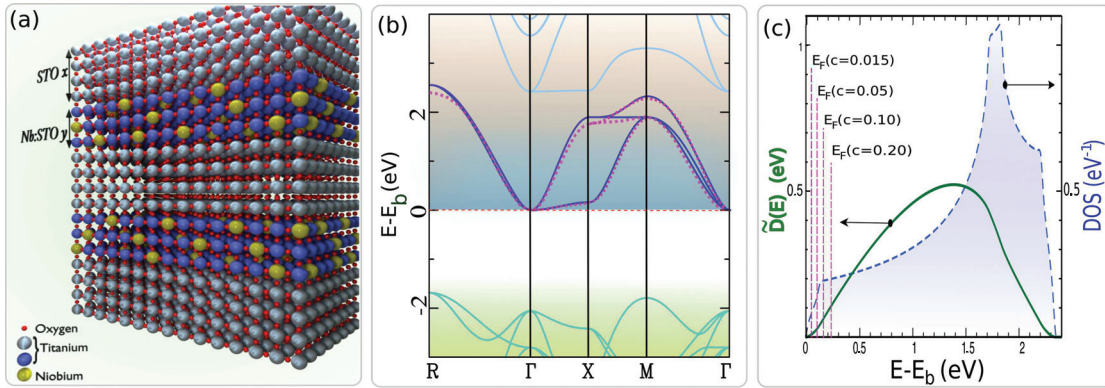


Figure 3.6: From Ref. [167]. (a) Schematic view of $(\text{STO})_x(\text{STO:Nb})_y$ (b) Bulk band structure from *ab initio* (continuous lines) and minimal tight binding (TB) model (pink dashed lines). Green lines correspond to the valence band blue lines to the conduction bands. (c) TB calculations of the density of states and reduced Drude weight $\tilde{D}(E) = \frac{\hbar}{\sigma_0} D(E)$, E_b is the energy of the bottom of the conduction band. Vertical dashed lines indicate the position of the Fermi level for various carrier concentrations.

3.2.1 Theoretical modelling of the thermoelectric properties

In the previous section, we have shown that the thermoelectric properties of electron doped STO (conductivity and Seebeck coefficient) could be well understood and reproduced within the framework of a realistic Tight Binding (TB) Hamiltonian (3 t_{2g} bands) that includes electron-electron scattering mechanism and disorder treated in the Born approximation. The hopping integrals of the TB Hamiltonian were directly extracted from ab initio based studies. The Hamiltonian reads, $\hat{H}_0 = \sum_{\mathbf{k},\alpha} \epsilon_{\alpha}^0(\mathbf{k}) c_{\mathbf{k}\alpha}^{\dagger} c_{\mathbf{k}\alpha}$ where α denotes the orbital index. The d_{xy} band dispersion is $\epsilon_{xy}^0(\mathbf{k}) = -2t_1 (\cos(k_x a) + \cos(k_y a)) - 2t_2 \cos(k_z a) - 4t_3 \cos(k_x a) \cos(k_y a)$, where a is the lattice parameter. The two other bands (d_{yz} and d_{zx}) are obtained straightforwardly by a circular permutation of (x, y, z) . The hopping parameters obtained from Wannier projections are $t_1=0.277$ eV, $t_2=0.031$ eV and $t_3=0.076$ eV. The electrical conductivity σ and the Seebeck coefficients S are calculated as in section 3.1, using the same values of the fitting parameters C and W , and will be directly compared to the existing and available experimental data. In Fig. 3.6 is plotted, (a) a schematic view of the super-lattice structure, (b) the bulk band structure from ab initio (SIESTA) [112] and from the minimal TB model and (c) the TB calculations for the bulk density of states and reduced Drude weight. The position of the Fermi level for various carrier concentrations per unit cell is also shown.

We now consider the scenario in which there is no 2D quantum confinement in the superlattices $(\text{STO})_x(\text{STO:Nb})_y$. In order to calculate S we assume a uniform carrier density per unit cell in the overall superlattice. Some indication that would support the absence of confinement scenario are the experimental observations that suggest that Nb acts essentially as an electron reservoir in STO. This is supported by several DFT studies that show that the band structure, the density of states and appear to be weakly affected by the substitution of Ti by Nb [211, 212, 213]. The Nb concentration per unit cell in the doped regions in the measured samples is $c_D = 0.20$ (Ref. [102]). Since we assume no 2D quantum confinement, the additional electrons introduced by the Nb atoms in the doped regions disperse in the entire compound, leading to a uniform carrier density per unit cell $c = \frac{y}{x+y} c_D$, which corresponds to the measured electron density denoted $n_{e_{obs}}$ in table 1 of Ref. [102]. Note that our conclusions would not be changed significantly if the carrier concentration was not strictly uniform, but slightly modulated in the z-direction. The important point is the absence of true quantum confinement, i.e. the electronic wavefunctions should not decrease exponentially in the undoped regions. It is important to stress that from now on, our theory is completely free of fitting parameters. We would like to emphasize that for the temperature range considered here (300 K to 900 K), the Seebeck coefficient is almost independent from both C and W . Thus, the only relevant physical ingredients are (i) the details and accuracy of the band structure and (ii) the form of $\tau_{th}(T, E)$. If the electrons are really confined in the growth direction in these superlattices, we should expect a strong disagreement between our calculations and the experimental measurements, that would completely invalidate our procedure.

3.2.2 Ruling out the confinement scenario

In Fig. 3.7(a) the Seebeck coefficient at $T=300$ K in the super-lattice $(\text{STO})_x(\text{STO:Nb})_y$ is shown as a function of x for $y = 1, 2$ and 4 . We clearly observe an overall good agreement between the measured values and the calculated ones. In Fig. 3.7(b) the data are now plotted as a function of $c = \frac{y}{x+y}c_D$, we find that the experimental data are well reproduced by the theoretical curve that assumes a uniform distribution of the carriers in the superlattice. The experimental data points exhibit some dispersion that may reflect the quality of the samples, the presence of native defects such as oxygen vacancies, dislocations, interface defects/deformations, sample history and also the fact that the Nb concentration may fluctuate from sample to sample.

In Fig. 3.8 we now focus on the effect of the thickness of the Nb doped region assuming a

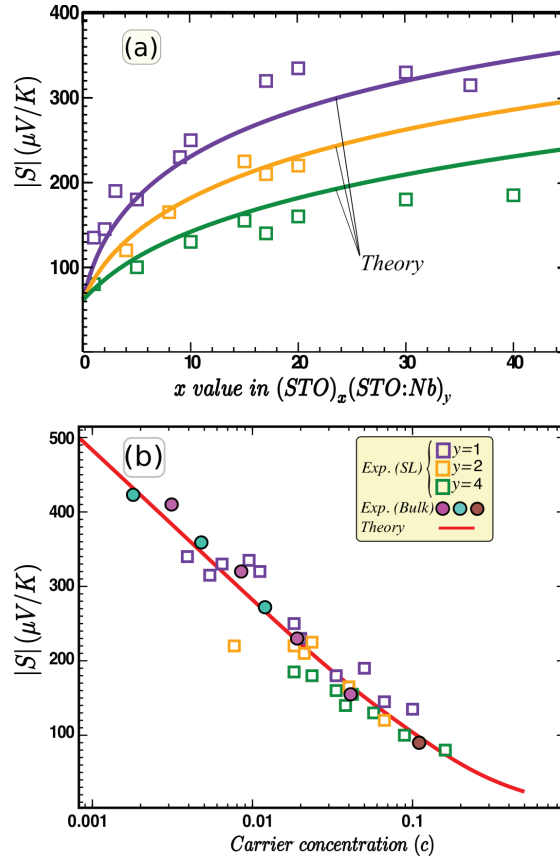


Figure 3.7: From Ref. [167]. (a) Seebeck coefficient at $T=300$ K in $(\text{STO})_x(\text{STO:Nb})_y$ $y=1, 2$ and 4 and x varies from 0 to 50. Open squares are experimental data from Ref. [102], the continuous lines are the TB calculations. (b) S as a function of $c = \frac{y}{x+y}c_D$, where $c_D = 0.20$ (Nb concentration in the doped regions). The experimental data are extracted from Refs. [194, 198, 199, 196]. The continuous line are the TB calculations.

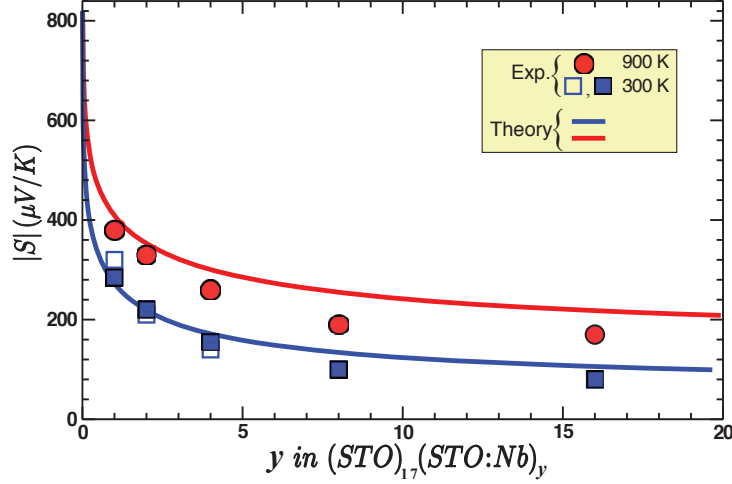


Figure 3.8: From Ref. [167]. Seebeck coefficient at $T = 300$ K and 900 K in $(\text{STO})_{x=17}(\text{STO:Nb})_y$ as a function of y . Symbols are experimental data from Ref. [102, 214] and continuous lines are the TB calculations.

fixed value for the undoped one. We have now plotted the Seebeck coefficient as a function of y for two different temperatures, namely $T=300$ K and 900 K, the number of undoped layers is set to $x = 17$. As we increase y the amplitude of the Seebeck coefficient decreases as a consequence of the increase of the overall carrier density. We again find a good agreement between the theory of a uniformly distributed electron gas and the experimental data, this agreement is even excellent at room temperature. In addition, we expect a saturation of the Seebeck coefficient for large y at $S_{\text{Bulk}}(c_D)$, which appears to be the case already for $y = 20$.

In the next figure, Fig. 3.9, we now focus on the particular case of a δ -doped compound, $y = 1$ for which a large increase of the Seebeck has been reported in Ref. [102, 214]. We plot the enhancement factor $|\frac{S}{S_{\text{Bulk}}}|$ as a function of x and for two different temperatures ($T=300$ K and 900 K) where S_{Bulk} refers to the 20% doped bulk material that corresponds to $x = 0$. As mentioned above, the density of carriers can not be precisely tuned experimentally, as a result of various mechanisms. Indeed, as seen from Hall measurements in Ref. [102], the density of electrons per doped layer can fluctuate by as much as 30% from sample to sample. Therefore, we include the effects of these variations by adding typically 1% additional carriers per unit cell. To be more specific, we perform the calculations for $c = \frac{y}{x+y}c_D + \delta c$ with δc up to 1% per unit cell. Note that performing realistic calculations including defects such as oxygen vacancies or dislocations would be extremely complicated and demanding (requires extremely large supercells) and would go beyond the scope of the present manuscript. Let us now discuss the results. First notice that the experimental data, for a given value of x , are sample sensitive especially for large x (see full squares and empty squares), the enhancement factor can vary by about 20%. More generally, there is some dispersion in the experimental data, especially strong around $x = 10$. However, the agreement between theory and experiments is rather good, and even better at large

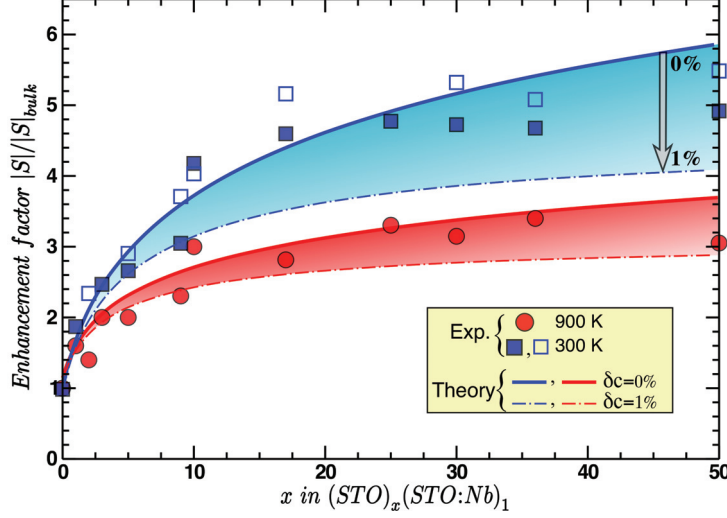


Figure 3.9: From Ref. [167]. Enhancement factor $|\frac{S}{S_{Bulk}}|$ of the Seebeck coefficient in $(\text{STO})_x(\text{STO:Nb})_1$ as a function of x for both $T = 300$ K and 900 K. The filled region indicate the effects of an additional concentration of carriers δc up to 1%. The experimental data (symbols) are extracted from Refs [102, 214].

temperature. As expected, the effect of additional carriers becomes more pronounced as we increase x . Thus, if δc is constant, it would result in the saturation of the enhancement factor at large x but it should be noticed, that no critical or characteristic length-scale can be extracted.

We now study the effect of temperature (it varies from $T = 300$ K to 900 K) on the Seebeck coefficient S in the super-lattice $(\text{STO})_x(\text{STO:Nb})_1$, where x ranges from 0 (20% doped bulk material) to 36. The results are depicted in Fig. 3.10. First, regarding the bulk data ($x = 0$) we observe that the theory agrees very well with the data from Ref. [193]. The measured bulk data of Ref. [214] are slightly smaller and appear to fluctuate with the temperature. Note that, for these data, the calculations would fit better assuming a slightly larger Nb concentration of the order of 23% instead of 20%. On the other hand, our calculated Seebeck coefficient agrees perfectly well with the experimental data for both $x = 1$ and $x = 3$, for the overall range of temperature. For $x = 9$ the calculated Seebeck coefficients are slightly larger (by 10-15%). However, assuming a small additional amount of electrons ($\delta c = 1\%$ only), the agreement between theory and experiment now becomes excellent. Note also, that adding a small concentration of electrons for both $x = 1$ and $x = 3$ would only weakly affect the results (the average concentration would only weakly change). Regarding larger values of x ($x = 25, 30$ and 36) we first notice that the experimental data strongly fluctuates with the temperature, the average carrier concentrations in these superlattices are relatively low: 0.8%, 0.7% and 0.5% respectively. For $\delta c = 0$ the agreement is good but the theoretical Seebeck coefficients are still slightly larger. However, by adding just 0.25% of carriers, the agreement between theory and experiment becomes excellent.

At this stage, we have shown that the experimental data can be well explained quali-

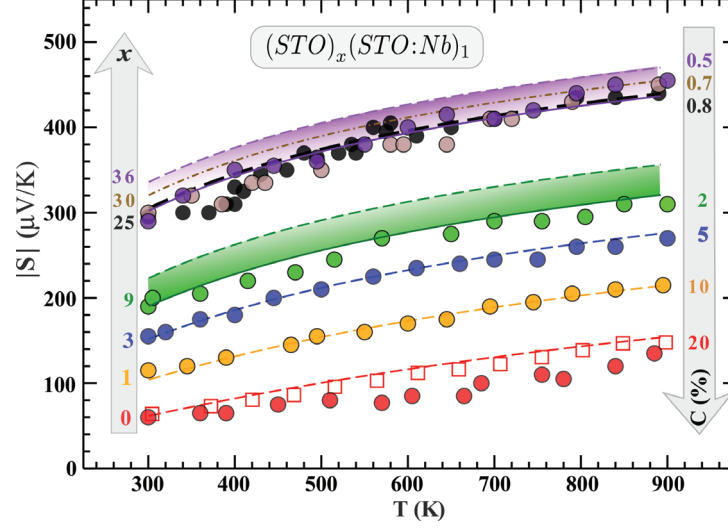


Figure 3.10: From Ref. [167]. Seebeck coefficient as a function of temperature in $(\text{STO})_x(\text{STO:Nb})_1$, x varies from 0 (20% doped bulk material) to 36. Filled and open symbols are experimental data from Ref. [214] and Ref. [193] respectively. Dashed and continuous lines are the TB calculations. The shaded regions correspond to the effect of δc up to 1% for $x = 9$ and δc up to 0.25% for $x = 36$. The effective concentration $c = \frac{y}{x+y} c_D$ is also plotted in the figure.

tatively and quantitatively assuming the absence of carrier confinement. To complete our demonstration, we now propose to analyse the effects of a full confinement of the electrons in the doped regions. This is achieved by assuming infinite potential barriers at the interfaces between doped and undoped regions. The calculated Seebeck coefficients (with and without confinement) and the experimental data are depicted in Fig. 3.11. Let us first compare the two theoretical scenarii. Starting from large values of the doped region thickness y (bulk limit) clear opposite trends in the calculated Seebeck coefficients are visible as y is reduced towards δ -doping. In the delocalized electron scenario, the Seebeck coefficient increases (in absolute value) as y is reduced. In contrast, in the fully confined electron picture, $|S|$ is almost flat down to $y = 5$ and then is strongly reduced to values much smaller than that of the bulk compound. As can clearly be seen, the apparent enhancement of the measured Seebeck coefficient is only consistent with the absence of confinement scenario. In particular, for $y = 1$, the measured Seebeck coefficient was around $300 \mu\text{V}/\text{K}$ at 300 K and $400 \mu\text{V}/\text{K}$ at 900 K, while perfect confinement predicts only $25 \mu\text{V}/\text{K}$ at 300 K and $80 \mu\text{V}/\text{K}$ at 900 K. The suppression of the Seebeck coefficient for $y \leq 5$ in the confined scenario results from the fact that the two out of plane orbitals (d_{xz} and d_{yz}) are sent to higher energy. Mechanically, the carrier concentration in the lowest orbital increases, resulting in an upward shift of the Fermi energy and thus a reduction of the Seebeck coefficient.

To conclude, we have demonstrated that the recently reported giant increase of the Seebeck coefficients in $(\text{SrTiO}_3)_x/(\text{SrTi}_{0.8}\text{Nb}_{0.2}\text{O}_3)_y$ superlattices is fully consistent only with

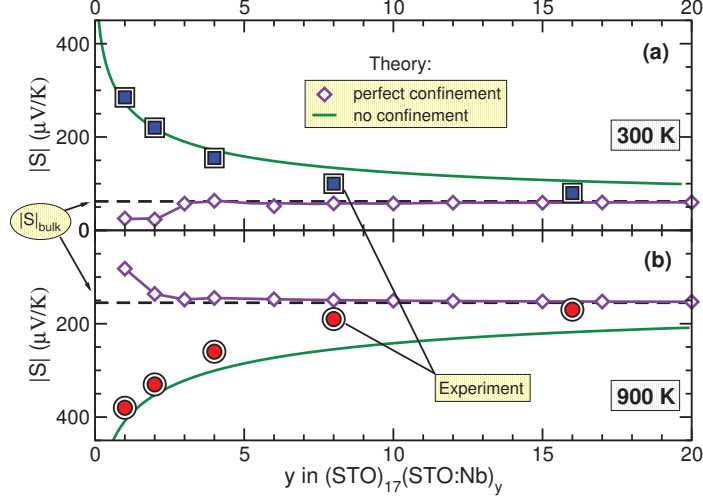


Figure 3.11: From Ref. [167]. Seebeck coefficient at (a) $T = 300$ K and (b) 900 K in $(\text{STO})_{x=17}(\text{STO:Nb})_y$ as a function of y . Filled symbols (squares and circles) are experimental data from Ref. [214]. The calculated Seebeck coefficients correspond to the green continuous lines (no confinement) and diamonds (perfect confinement of the carriers in the doped regions).

the absence of 2D quantum confinement of the carriers in the doped regions. Indeed, in the electron confinement picture the opposite trend is found, namely the suppression of the Seebeck coefficient. Our conclusion is further supported by the observation that the power factor (σS^2) measured in these superlattices is close to that of the bulk electron doped STO [215]. It would be of great interest to confirm whether our scenario is correct by direct measurements such as transverse resistivity, Angle Resolved Photoemission Spectroscopy, or by a direct probe of the depth profile of the carrier concentration. Oxide based thermoelectric superlattices are promising materials for high ZT devices but achieving a true 2D quantum confinement requires (i) a suitable choice of dopant that has a drastic effect on the host band structure in the vicinity of the Fermi level or (ii) a more appropriate choice for the undoped compound.

3.3 Investigating the high-temperature thermoelectric properties of n-type rutile TiO_2

As we have seen in the previous sections, despite an excellent room-temperature power factor around $40 \mu\text{W cm}^{-1} \text{K}^{-2}$, optimization of bulk SrTiO_3 by doping and nanostructuring has been unable so far to yield figures of merit exceeding 0.5 [163]. Therefore, it is worth studying the thermoelectric properties of other transition metal oxides that might equal of

even surpass the performances of strontium titanate. Another well-known oxide compound is TiO_2 , which comes in three naturally occurring phases: rutile, anatase and brookite. Of these, rutile is particularly stable at high temperatures with a melting point around 2100 K, while anatase and brookite undergo a phase transition to rutile near 1000 K. Additionally, the carrier concentration of rutile can be tuned by doping with several elements such as boron, niobium or cobalt, or by using reduction processes to introduce oxygen vacancies acting as electron donors. [216, 217, 218, 219] Therefore, this compound would represent a very promising prospect for waste heat recovery applications if its thermoelectric properties could be optimized.[140]

In this section, we investigate the electron transport properties of n-type rutile TiO_2 by combining first-principle calculations with a modelling of electron-phonon interactions and donor defects. This method allows us to directly compare our results with reported measurements of scattering rates, mobility, electrical conductivity, Seebeck coefficient and power factor. TiO_2 being a very polar material, it is known that strong interactions between electrons and optical phonons in rutile give rise to the formation of intrinsic small polarons at low temperature, i.e. the electrons are self-trapped by the surrounding deformation of the lattice. [110] This behaviour has been observed both experimentally [220] and in Density Functional Theory (DFT) calculations using hybrid functionals [221] or DFT+U methodology. [222] On the other hand, the small polarons have been found to be highly unstable at room-temperature and above. Several DFT calculations also find these states to be only slightly favoured energetically compared to delocalized conduction states, with an energy barrier hindering the localization of extended electrons. [223, 224] Furthermore, the mobility predicted by the small polaron hopping mechanism is orders of magnitudes lower than the experimental estimates in reduced samples. [225] The measured mobility above 100 K also decreases when the temperature is elevated, [226] suggesting conduction band transport rather than small polaron hopping. Therefore, it is considered likely that the transport properties at room-temperature and above are dominated by delocalized electrons (large polarons) in the conduction band. For these reasons, we will investigate the thermoelectric properties of rutile TiO_2 assuming that the electrons are delocalized in the conduction band. Although the standard Generalized Gradient Approximation functional of Perdew, Burke, and Ernzerhof [123] (PBE) is unable to describe small polaron states, it predicts the same band structure for the conduction band as the Heyd, Scuseria, and Ernzerhof [227, 228] hybrid functional, that has been used to investigate small polarons. [229] Therefore, we will compute the conduction band structure with the PBE functional, and we will introduce parameters to model the electron scattering and mass renormalization that are expected to result from strong electron-phonon coupling. These parameters will be set by direct comparison with carrier lifetime and transport measurements.

3.3.1 Modelling electron transport in rutile TiO_2

We perform *ab initio* calculations with the DFT package SIESTA [112] on the rutile structure of TiO_2 (see Fig 3.12). The GGA-PBE functional and Troullier-Martins norm-conserving pseudopotentials [191] are used. We perform an optimization of the double- ζ -polarized basis with the Simplex tool of the SIESTA package. The unit cell is relaxed to

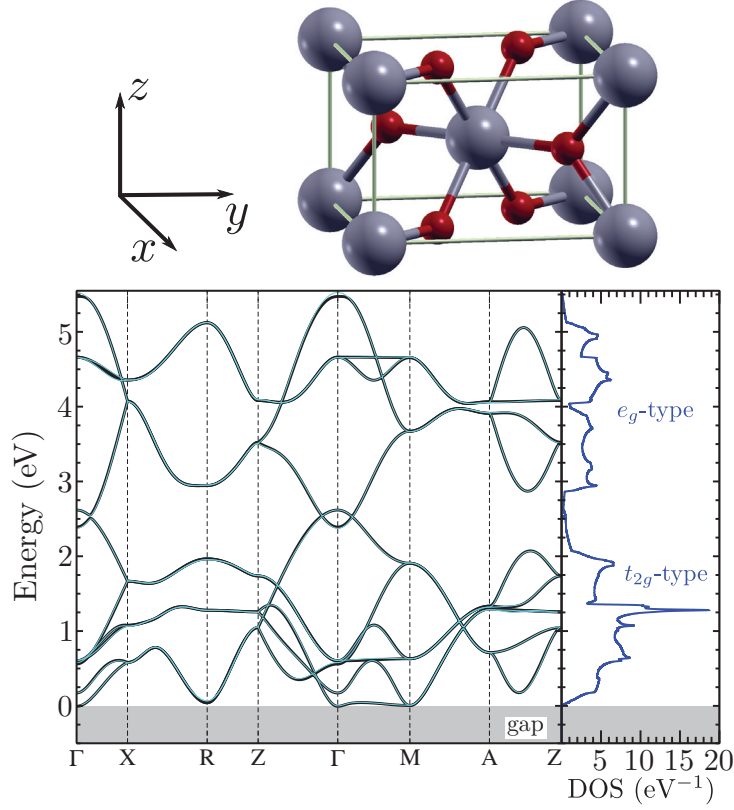


Figure 3.12: From Ref. [168]. Top: the conventional cell of rutile TiO_2 , where the grey and red spheres represent the Ti and O atoms respectively. Bottom: The band structure and density of states of the conduction band, from full DFT calculations (black lines) and from Wannier projections (cyan lines and DOS).

forces less than 0.01 eV/\AA and to a pressure less than 0.15 kbar . The self-consistent field cycles have been performed with a Monkhorst-Pack of $4 \times 4 \times 4$ k-points and a mesh cutoff of 400 Ry . We have checked that the band-structure predicted by the plane-wave based DFT package Quantum ESPRESSO [113] is consistent with the results from SIESTA. The electron dispersion and the density of states (DOS) of the conduction band are shown in Fig 3.12. The black lines corresponds to the SIESTA results, and the cyan lines and the DOS are calculated from Wannier projections of the Bloch states onto the 3d orbitals of the Ti atoms, using the Wannier90 software. [128] The 10 Wannier orbitals (shown in Fig. 2.3) can be classified as low-energy t_{2g} -type and high-energy e_g -type following the crystal field classification. The partial density of states (PDOS) of the t_{2g} and e_g orbitals are shown in Fig. 3.13. Although the lower half of the conduction band is overwhelmingly composed of the t_{2g} orbitals, there is still some weight from the e_g ones at the bottom of the band, thus it is necessary to take the ten of them into account in order to properly describe the band-structure in the energy region of interest. In the Wannier basis, the Hamiltonian matrix

elements with an amplitude lower than 1 meV have been cut, which still yields an excellent agreement with the full SIESTA band structure. Since the experimental bandgap of rutile TiO_2 is rather large (more than 3 eV), a description of the valence band is unnecessary for the transport properties (we have checked that bipolar conduction is negligible in all our results). The conduction band effective mass in the z direction is $m_b^z = 0.63 m_e$, while the effective masses in the x and y directions are $m_b^x = m_b^y = 1.3 m_e$. There is some anisotropy, but much less than in SrTiO_3 in which the ratio of the effective masses is as high as 10.

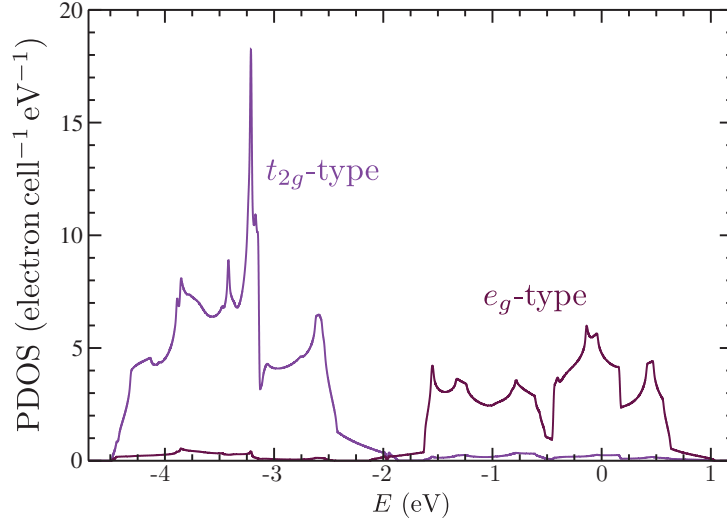


Figure 3.13: From Ref. [168]. The partial density of state (PDOS) associated with the t_{2g} and e_g orbitals of the conduction band.

We calculate the electron transport properties of n-type rutile TiO_2 within the framework of the Boltzmann transport equation [89, 132] (BTE), using the relaxation time approximation (RTA), equations 2.51, 2.52 and 2.54. The Fermi level μ_F is determined by integrating the DOS to find the correct electron concentration. The TDF is calculated efficiently using the Drude formalism (see equation (2.57) and appendix D).

The description of the thermoelectric properties requires an accurate modelling of the electron lifetime. It is especially important to get the correct temperature dependance since we are interested in high-temperature power generation. The scattering rate \hbar/τ has been measured in Ref. [230] from 11 K to 300 K. It increases with temperature, exhibiting rather high values around 80 meV at room temperature (see Fig 3.14, left panel). The temperature dependance between 100 K and 300 K is inconsistent with the typical $\frac{3}{2}$ power-law of the acoustic deformation potential mechanism, indeed a fit gives an exponent between 2.5 and 3. On the other hand, the large interaction between electrons and optical phonons can be expected to dominate scattering in such a polar compound, provided that the optical modes are sufficiently populated. [145] First-principle calculations [231] and inelastic neutron scattering measurements [232] of the phonon spectrum in rutile TiO_2 indicate the presence of optical modes from 15 meV to 100 meV. Thus, longitudinal optical (LO) modes should be populated at 300 K and above, leading to a significant polar-optical scattering rate.

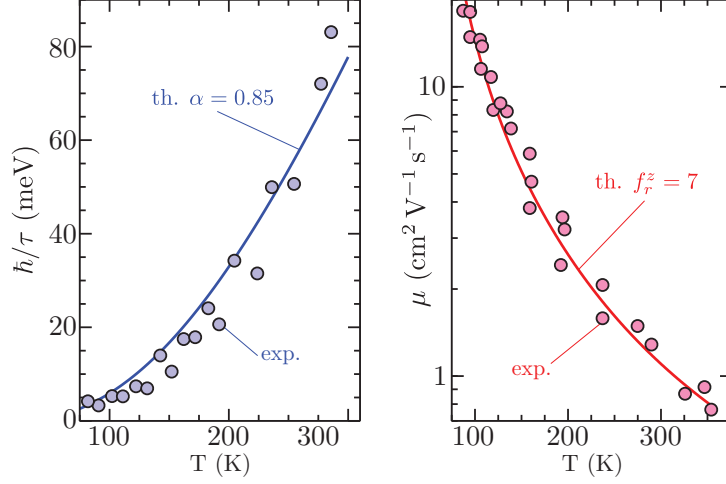


Figure 3.14: From Ref. [168]. Left: the experimental (circles, Ref. [230]) and theoretical scattering rate \hbar/τ in meV. The theoretical values correspond to the bottom of the conduction band at the Γ point. Right: The experimental (circles, Ref. [226]) and theoretical mobility μ in the z direction, in $\text{cm}^2 \text{V}^{-1} \text{s}^{-1}$.

Assuming a parabolic dispersion for the conduction band electrons and a flat one for the LO branches, second order perturbation theory gives [141, 142]

$$\begin{aligned} \frac{\hbar}{\tau_{\mathbf{k},\lambda}} = \frac{2\alpha}{\sqrt{\epsilon_{\mathbf{k},\lambda}}} \sum_{\nu} (\hbar\omega_{\nu})^{\frac{3}{2}} & \left[N_{\nu} \text{Argsh} \left(\sqrt{\frac{\epsilon_{\mathbf{k},\lambda}}{\hbar\omega_{\nu}}} \right) \right. \\ & \left. + \Theta(\epsilon_{\mathbf{k},\lambda} - \hbar\omega_{\nu}) (N_{\nu} + 1) \text{Argsh} \left(\sqrt{\frac{\epsilon_{\mathbf{k},\lambda}}{\hbar\omega_{\nu}} - 1} \right) \right], \end{aligned} \quad (3.4)$$

where Θ is the Heaviside function, α is the Fröhlich coupling constant, ν is a branch index running over the LO branches, ω_{ν} is the Γ -point frequency of the branch ν and $N_{\nu} = 1/(e^{\beta\hbar\omega_{\nu}} - 1)$ is the Bose-Einstein occupation factor. The first term inside the bracket corresponds to the absorption of an optical phonon, while the second term is associated with the emission of an optical phonon and thus requires the electron energy to be higher than the optical mode frequency. For simplicity, we have included all optical modes in the sum and divided the resulting scattering rate by 3. The optical mode frequencies, extracted from Ref. [231], are listed in Table 3.1. We have also assumed α to be the same for all modes, thus our scattering law depends only on this single parameter. To set the value of α , we compare the calculated scattering rate at the bottom of the conduction band with the experimental values between 100 K and 300 K. As shown in Fig. 3.14 (left panel), the choice $\alpha = 0.85$ leads to a good agreement between theory and experiment, thus validating our assumption of dominant polar-optical electron scattering. This value corresponds to a weak Fröhlich interaction with each phonon mode, which is consistent with the use of second order perturbation theory. The scattering rate as a function of energy is shown in Fig. 3.15 for several temperatures. The discontinuities in the derivative are caused by the absorption processes that activate when the energy reaches the phonon mode frequency.

branch	$\hbar\omega$ (meV)
1	14.4
2	16.2
3	22.2
4	24.7
5	46.8
6	50.4
7	52.2
8	53.0
9	56.1
10	59.6
11	60.5
12	62.7
13	78.9
14	102.2
15	104.7

Table 3.1: The optical mode frequencies used in the calculation of the electron scattering rate.

The next step is to reproduce the experimental mobilities that have been measured in Ref. [226] for the z direction. However, if we calculate the TDF from the *ab initio* band-structure shown in Fig. 3.12, the predicted mobility is an order of magnitude higher than the measurements, indicating a large transport mass renormalization of the delocalized carriers due to electron-phonon interactions. This could seem surprising given the relatively low coupling constant $\alpha = 0.85$, but the conduction electrons in rutile TiO_2 interact with five different LO branches: in such cases, the effective coupling constant α_{eff} for a one-branch interaction is given by $\alpha_{\text{eff}} = \sum_{\nu} \alpha_{\nu}$. [233, 234] This gives $\alpha_{\text{eff}} = 4.25$ which corresponds to the intermediate to strong coupling regime, consistent with the existence of small polarons and a large mass renormalization of the delocalized conduction electrons. A natural question then arises whether the perturbative expression (3.4) should be valid, given the strong overall electron-phonon interaction. It must be kept in mind that the delocalized electrons in TiO_2 are very close to a metal-insulator transition, since small polarons are estimated to be slightly favoured energetically. In such cases, the single-particle properties, such as the band mass and the scattering rate obtained from the spectral function, are not critical quantities. However, the transport mass calculated from the conductivity can be much more sensitive and may be considerably enhanced due to vertex corrections [141]. This scenario is our best hypothesis to resolve the apparent contradiction between a large mass renormalization and the delocalized behaviour exhibited by electrons in rutile TiO_2 .

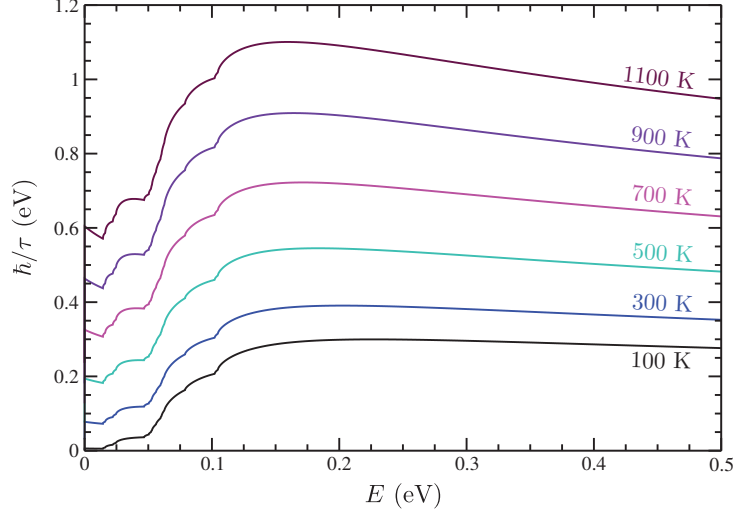


Figure 3.15: From Ref. [168]. The electron scattering rate as a function of energy for several temperatures.

To take this effect into account in the simplest way, we introduce the renormalization parameters f_z and $f_x = f_y$ for transport in the z and xy directions, respectively. Only the TDF is renormalized: $\Sigma_i(E, T) \rightarrow \Sigma_i(E, T)/f_i$, and the electron mobilities are calculated to be compared with experiment. As shown in Fig. 3.14 (right panel), the large value $f_z = 7$ leads to an excellent agreement between theory and experiment. In the xy direction, the measurements are reproduced by an even larger renormalization factor $f_x = f_y = 23.5$. These values are comparable to the effective masses found in Ref. [226] by fitting the transport measurements.

3.3.2 The thermoelectric properties from ambient to high temperatures

The transport properties can then be calculated as functions of the electron density n , and compared with experimental measurements. We show in Fig. 3.16 (left panel) the room-temperature electrical conductivity in the z direction (red), in the xy directions (green) and in polycrystalline materials (orange) for which an orientational average was taken. Experimental data from Ref. [226, 235, 236, 217] are also plotted. The agreement between theory and experiment is very good over a wide range of carrier concentration (five orders of magnitude). In the right panel of Fig. 3.16 is shown the predicted Seebeck coefficient as a function of the conductivity, together with experimental data from Ref. [235, 236, 217, 218, 219]. Although the theory may somewhat underestimate the Seebeck coefficient in some samples, overall it agrees well with experiments. This success of the theory at 300 K confirms that the electronic transport properties in rutile TiO_2 are consistent with a band conduction mechanism based on delocalized carriers, as opposed to small polaron hopping. Moreover, it should be noted that renormalizing the DOS by the parameters f_z and f_x in addition to the TDF would have lead to a large discrepancy between the predicted and measured

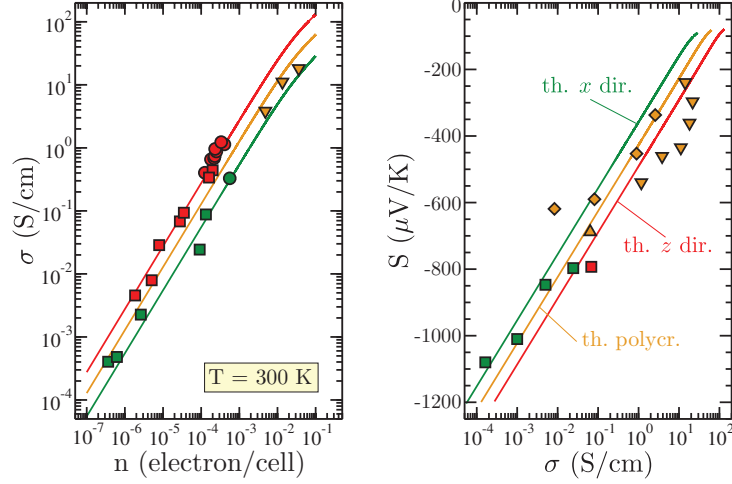


Figure 3.16: From Ref. [168]. Left: the predicted room-temperature electrical conductivity in the z direction (red line), the xy directions (green line) and in polycrystalline samples (orange line), as a function of the carrier density n . Right: the predicted Seebeck coefficient as a function of the conductivity for the same directions. The experimental data are taken from Ref. [226] (circles), Ref. [235, 236] (squares), Ref. [217] (downward triangles), Ref. [218] (upward triangles) and Ref. [219] (diamonds).

Seebeck coefficients. This supports our hypothesis that the large mass enhancement results from vertex corrections and is absent from the one-particle properties.

As high-temperature generation is the main application prospect for TiO_2 as a thermoelectric material, it is crucial to accurately predict the transport properties between 300 K and 2000 K. In Ref. [219], the electrical conductivity and Seebeck coefficients of reduced rutile samples, subjected to spark plasma sintering (SPS) at different temperatures, have been measured up to 523 K. The conductivity displays a very weak temperature dependence, even though the scattering rate (3.4) increases substantially with elevated temperature. This suggests an activation mechanism for the number of electrons in the conduction band, as confirmed by the Hall measurements in Ref. [226] that clearly show an increase of the carrier density with temperature. On the theoretical side, several first-principle calculations of oxygen vacancies in rutile TiO_2 find energetically favored electronic bound states localized on neighboring Ti atoms. [224, 222, 221, 237, 238, 239] There is no consensus on the binding energy, although most experimental and theoretical estimates fall between 50 meV and 200 meV. The situation is similar for Ti interstitials, another important intrinsic defect, [240, 241] and for extrinsic dopants such as Nb and F substitutions. [224]

To capture the effects of this activation mechanism in a simple and general way, we model the presence of oxygen vacancies by adding localized defects levels inside the gap at an energy ϵ in the DOS. Thus, TiO_{2-x} is modeled by adding a term $4x\delta(E - \epsilon)$ in the pristine DOS, while the TDF is unchanged (the impurity states have zero conductivity). The total carrier density is set at $4x$ electron/cell (each oxygen vacancy is assumed to bring 2 electrons), leading to an activation mechanism with more and more carriers populating the

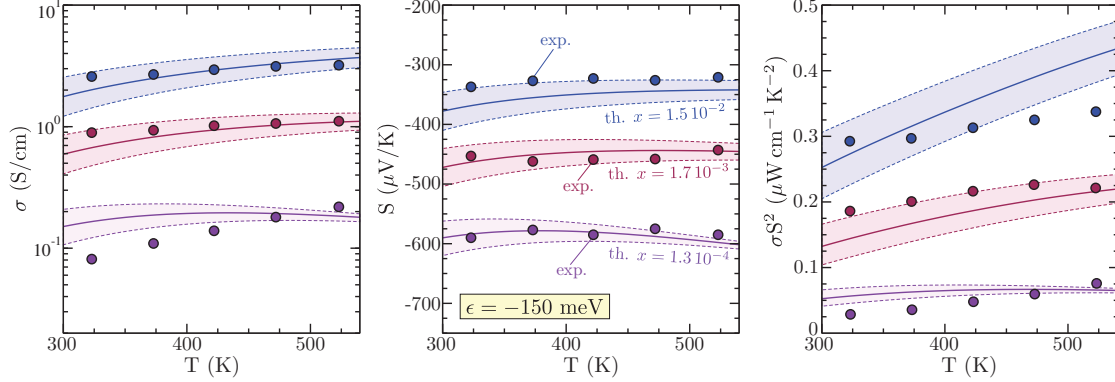


Figure 3.17: From Ref. [168]. The predicted electrical conductivity (left), Seebeck coefficient (center), and power factor (right) of polycrystalline TiO_{2-x} as a function of temperature for $x = 1.3 \times 10^{-4}$ (purple), $x = 1.7 \times 10^{-3}$ (red) and $x = 1.3 \times 10^{-2}$ (blue). The shaded regions correspond to a binding energy $\epsilon = -150 \pm 20$ meV. The circles are experimental data from Ref. [219] for three samples subjected to SPS at 1173 K (purple), 1173 K (red) and 1173 K (blue).

conduction band from the defect states as temperature is increased. We adjust the parameters ϵ and x to reproduce the experimental conductivities from the samples in Ref. [219] subjected to SPS at 1173 K, 1173 K and 1173 K. Fig. 3.17 show the polycrystalline electrical conductivity, Seebeck coefficient and power factor for $\epsilon = -150$ meV and three vacancy concentrations $x = 1.3 \times 10^{-4}$, $x = 1.7 \times 10^{-3}$ and $x = 1.3 \times 10^{-2}$. These values lead to a rather good agreement with experimental data, and in particular they reproduce the weak temperature dependence of the conductivities, Seebeck coefficient and power factor, thus validating our approach. The important disparities in the predicted vacancy concentration between samples (two order of magnitudes) reflect the measured resistivities that exhibit similarly large variations.

The thermoelectric power factor σS^2 of rutile TiO_2 can now be calculated between 300 K and 2000 K. Fig. 3.18 shows the predicted polycrystalline PF as a function of the conduction electron density for several temperatures (top) and as a function of temperature for several oxygen vacancy concentrations (bottom). The optimum carrier concentration is quite large around 0.2 electron/cell, corresponding to a maximum value of $\approx 1.15 \mu\text{W cm}^{-1} \text{K}^{-2}$ (see the inset). Unsurprisingly, a large number of oxygen vacancies (more than 10%) are necessary to provide these carriers, but the activated conduction makes the power factor very stable with temperature between 500 K and 1800 K. Still, $1 \mu\text{W cm}^{-1} \text{K}^{-2}$ is a rather low value compared to other oxides such as SrTiO_3 , which has an optimum power factor 40 times larger at room temperature. This poorer performance of titanium oxide is likely caused by two important features of TiO_2 . First, and as noted previously, its band structure exhibits only modest anisotropy due to its crystal structure. In SrTiO_3 , by contrast, the t_{2g} orbitals that make up the conduction bands are oriented along the crystal axis, thus leading to a very two-dimensional character of electron transport. This is not the case in

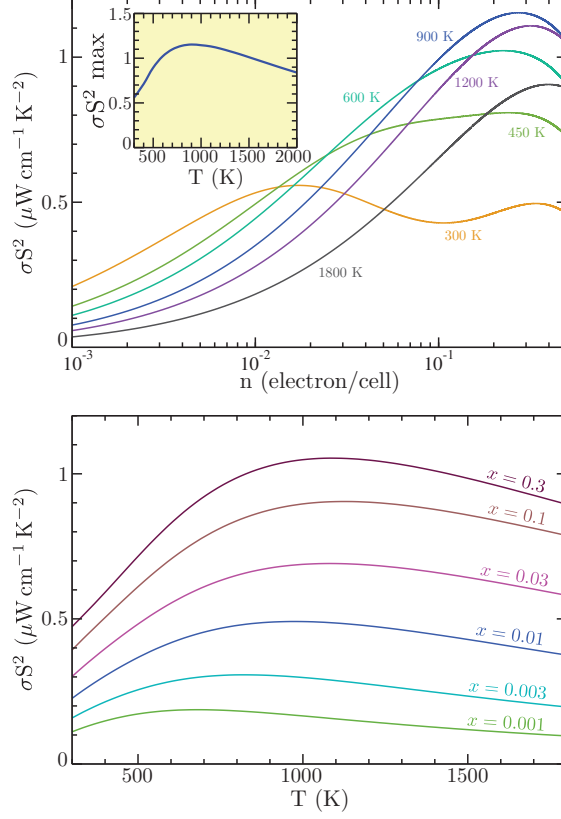


Figure 3.18: From Ref. [168]. Top: the polycrystalline power factor σS^2 as a function of the electron density for several temperatures. Inset: the maximum PF as a function of temperature. Bottom: the PF as a function of temperature for several oxygen vacancy concentrations.

TiO₂. Second, the electron-phonon interactions lead to a strong mass enhancement and to a lower mobility in TiO₂ than in SrTiO₃, which is detrimental to the power factor.

The maximum value of the figure of merit zT_{max} in rutile can be roughly estimated assuming an amorphous value $\kappa \approx 1 \text{ W m}^{-1} \text{ K}^{-1}$ for the thermal conductivity, as was done in Ref. [140]. This leads to $zT_{\text{max}} \approx 0.15$ around 1800 K. This value is six times lower than the estimate of Ref. [140], which aimed at comparing the different TiO₂ phases and thus did not include the temperature dependance of the scattering rate. Even accounting for the occasional underestimation of the predicted Seebeck coefficient, we do not expect the figure of merit to exceed 0.6, which is insufficient for widespread applications in power generation. Therefore, if rutile TiO₂ is to be useful as a thermoelectric material, significant changes in its electronic structure must be engineered in order to boost the power factor beyond what can be reached by simply increasing the carrier concentration.

In conclusion, we have investigated thermoelectric transport in n-type rutile TiO₂ through a combination of *ab initio* calculations for the band-structure and model descrip-

tions for the electron-phonon interaction and oxygen vacancies. The parameters for the polar-optical coupling scattering rate, mass renormalization and defect binding energy were set by a comparison between the predicted transport properties and the available experimental measurements. A very good agreement between theory and experiment is obtained over a wide range of carrier concentrations, supporting a band conduction picture of electronic transport at room-temperature and above. We predict a maximum power factor of $1.15 \mu\text{W cm}^{-1} \text{K}^{-2}$ reached at 900 K for a large carrier density of 0.2 electron/cell, which requires more than 10% oxygen vacancies in reduced samples. Such a low value of the power factor leads to an estimate of around 0.15 for the maximum figure of merit if the thermal conductivity is reduced to its amorphous limit. Therefore, the power factor must be boosted significantly before rutile TiO_2 can be widely used as a thermoelectric material in power generation modules. This might possibly be achieved using quantum confinement and energy filtering effects, for instance.

Chapter 4

Dealing with disorder

Uniformity of opinion seems to require either a reliable and thorough method to knowledge, or the brazenly unacceptable: complete and utter totalitarianism.

James. A. Lindsay,
Everybody Is Wrong About God.

In the previous chapter, we assumed that the systems under study were sufficiently clean to neglect disorder or treat it as a small perturbation, using Fermi's Golden Rule. But, as we have seen in chapter 1, many strategies to enhance the figure of merit require introducing strong disorder in the material. To reduce the thermal conductivity, for instance, nanostructures and defects are often engineered in order to scatter off phonons, and a full calculation of the scattering rate (beyond second-order perturbation theory) is necessary to evaluate the success of the procedure (see section 6.2). Resonant defects, used to optimize the power factor, are meant to distort the band structure and bring about significant changes in the character of the electronic states, introducing impurity states, resonant states, and sometimes even leading to Anderson localization effects (see section 5.3). In such cases, the impurities and their effects must be treated explicitly. For electronic systems, the single-particle Hamiltonian should then be written $\hat{H} = \hat{H}_0 + \hat{H}_d$, with H_0 the clean Hamiltonian and \hat{H}_d standing for the defects and impurities. Similarly for phonons, the dynamical matrix can be written $D = D_0 + D_d$. It is often natural and simple to describe the perturbations \hat{H}_d and D_d in real space as modifications of certain hopping terms, on-site potential or interatomic force constants in the neighborhood of the defect position. This makes real-space methodologies, based on tight-binding Hamiltonians or dynamical matrices, particularly suited to deal with such disorder. In this chapter, we will describe in particular the formalism of Green's functions, a very powerful framework to describe quantum dynamics and transport. Green's functions are often introduced and presented in the context of many-body physics, where they constitute the building blocks of Feynman diagrams [141]. It is possible, however, to describe Green's functions entirely in the single-particle framework [242]. This is especially useful when the crucial challenge

is disorder and not many-body interactions, as is the case here. Therefore, and although some definitions and results that are valid in many-body will be presented, we will mostly adopt single-particle notations throughout this chapter.

4.1 Impurity states and resonances: Green's functions

Let us consider the case of a disordered electronic Hamiltonian $\hat{H} = \sum_{\mu} \epsilon_{\mu} c_{\mu}^{\dagger} c_{\mu}$, with ϵ_{μ} the single-particle eigenstates and c_{μ}^{\dagger} the creation eigenoperators, both *a priori* unknown. The retarded, zero-temperature, many-body Green's function for the eigenstate μ is defined as

$$G_{\mu}(t) = -\frac{i}{\hbar} \Theta(t) \langle 0 | \{c_{\mu}(t), c_{\mu}^{\dagger}\} | 0 \rangle = -\frac{i}{\hbar} \Theta(t) e^{-i\epsilon_{\mu}t/\hbar}, \quad (4.1)$$

where $|0\rangle$ is the vacuum state (no electron in the system) and $c_{\mu}(t)$ is the annihilation operator at time t in the Heisenberg representation. Physically, the state μ is created (or destroyed) at time 0, left to propagate for a while and then destroyed (or created) at time t . Thus, the Green's function contains informations about the quantum dynamics from time 0 to time t . Since we have chosen to propagate an eigenstate, this dynamics is not very interesting: it is just a phase $e^{-i\epsilon_{\mu}t/\hbar}$. The Heaviside factor ensures that no state propagates backward in time, hence the adjective "retarded" for the Green's function. Introducing the evolution operator $\hat{U}(t) = e^{-i\hat{H}t/\hbar}$, the Green's function is written in single-particle notations

$$G_{\mu}(t) = -\frac{i}{\hbar} \Theta(t) \langle \mu | \hat{U}(t) | \mu \rangle. \quad (4.2)$$

Thus, it is possible to define the Green's function operator $\hat{G}(t)$ and its energy-dependant Fourier transform $\hat{G}(E) = \int dt \hat{G}(t) e^{iEt/\hbar}$:

$$\hat{G}(t) = -\frac{i}{\hbar} \Theta(t) \hat{U}(t) = -\frac{i}{\hbar} \Theta(t) \sum_{\mu} e^{-i\epsilon_{\mu}t/\hbar} |\mu\rangle \langle \mu|, \quad (4.3)$$

$$\hat{G}(E) = \frac{1}{E - \hat{H} + i\eta} = \sum_{\mu} \frac{|\mu\rangle \langle \mu|}{E - \epsilon_{\mu} + i\eta}, \quad (4.4)$$

where η is an infinitely small positive imaginary part. The Green's function (4.4) contains as much information on the system as the Hamiltonian \hat{H} . It may seem like we haven't done anything very useful by defining $\hat{G}(E)$, but as we will see in section 4.3, it is more efficient to compute the exact transport properties of strongly disordered systems through the Green's function than by simply diagonalizing the Hamiltonian. Moreover, we will now show that valuable single-particle informations, such as the density of states and relaxation times, can be easily extracted from this formalism.

4.1.1 Single-particle properties: the self-energy

To simplify the discussion, let us consider a clean Hamiltonian \hat{H}_0 on a simple cubic lattice with just one wannier orbital $|\vec{R}\rangle$ per site \vec{R} . It can be written in diagonal form in the basis

of Bloch states $|\vec{k}\rangle$: $\hat{H}_0 = \sum_i |\vec{k}\rangle \epsilon_{\vec{k}} \langle \vec{k}|$. The Green's function of this clean system can be defined:

$$\hat{P}(E) = \frac{1}{E - \hat{H}_0 + i\eta} = \sum_{\vec{k}} \frac{|\vec{k}\rangle \langle \vec{k}|}{E - \epsilon_{\vec{k}} + i\eta}. \quad (4.5)$$

Suppose now that a concentration x of defects is introduced in the crystal, and that each defect traps or repulses electrons with an on-site potential ξ . This perturbation can be modeled by a disorder Hamiltonian $\hat{H}_d = \sum_{\vec{R}} |\vec{R}\rangle \xi_{\vec{R}} \langle \vec{R}|$, where $\xi_{\vec{R}}$ is either equal to ξ if the site is occupied by a defect (probability x), or to 0 if the site is unoccupied (probability $1 - x$). The full Hamiltonian, $\hat{H} = \hat{H}_0 + \hat{H}_d$ is no longer diagonal in the Bloch state basis. The Green's function, however, simply writes

$$\begin{aligned} \hat{G}(E) &= \frac{1}{E - \hat{H}_0 - \hat{H}_d + i\eta} = \hat{P}(E) \left(1 - \hat{H}_d \hat{P}(E)\right)^{-1} \\ &= \hat{P}(E) + \hat{P}(E) \hat{H}_d \hat{P}(E) + \hat{P}(E) \hat{H}_d \hat{P}(E) \hat{H}_d \hat{P}(E) + \dots \end{aligned} \quad (4.6)$$

The so-called T-matrix $\hat{T}(E)$ can be defined by $\hat{G}(E) = \hat{P}(E) + \hat{P}(E) \hat{T}(E) \hat{P}(E)$, yielding

$$\hat{T}(E) = \hat{H}_d + \hat{H}_d \hat{P}(E) \hat{H}_d + \hat{H}_d \hat{P}(E) \hat{H}_d \hat{P}(E) \hat{H}_d + \dots \quad (4.7)$$

Calculations of the T-matrix for a single defect are computationally feasible and yield important informations about the electron-defect scattering rate in the dilute limit [242, 243]. However, when the amount of disorder is large, it becomes necessary to take into account the scattering of electrons on multiple impurities.

If the phase coherence length of electrons is much smaller than the system size, the electronic properties will be averaged incoherently over many parts of the system [244]. Thus, the physical quantities should be averaged over all disorder configurations. For single-particles properties such as the density of states, it is sufficient to calculate the disorder-averaged Green's function $\langle \hat{G} \rangle(E)$ (things are different for the conductivity, see section 4.2). The perturbation expansion (4.6) then becomes

$$\begin{aligned} \langle \hat{G} \rangle(E) &= \hat{P}(E) + \sum_{\vec{R}} \hat{P}(E) |\vec{R}\rangle \langle \xi_{\vec{R}} \rangle \langle \vec{R}| \hat{P}(E) \\ &\quad + \sum_{\vec{R}, \vec{R}'} \hat{P}(E) |\vec{R}\rangle \langle \xi_{\vec{R}} \langle \vec{R}| \hat{P}(E) |\vec{R}' \rangle \xi_{\vec{R}'} \rangle \langle \vec{R}'| \hat{P}(E) + \dots \end{aligned} \quad (4.8)$$

The term $\sum_{\vec{R}} |\vec{R}\rangle \langle \xi_{\vec{R}} \rangle \langle \vec{R}|$ is just the scalar $\langle \xi_{\vec{R}} \rangle = x\xi$. The third term is more complicated. The case $\vec{R} = \vec{R}'$ involves the quantities $\langle \xi_{\vec{R}}^2 \rangle = x\xi^2$ and $\langle \vec{R}| \hat{P}(E) |\vec{R}\rangle = P_0(E)$, which is independent of \vec{R} since the clean system is homogeneous. The case $\vec{R} \neq \vec{R}'$ involves the quantity $\langle \xi_{\vec{R}} \xi_{\vec{R}'} \rangle = \langle \xi_{\vec{R}} \rangle \langle \xi_{\vec{R}'} \rangle = x^2 \xi^2$ (where it was assumed that different sites are uncorrelated) and a restricted sum $\sum_{\vec{R}} \sum_{\vec{R}' \neq \vec{R}}$. If we ignore for now the restriction on the sum (termed a multiple-occupancy correction), then the expansion (4.8) becomes

$$\langle \hat{G} \rangle(E) = \hat{P}(E) + \hat{P}(E) x \xi \hat{P}(E) + \hat{P}(E) x \xi^2 P_0(E) \hat{P}(E) + \hat{P}(E) x \xi \hat{P}(E) x \xi \hat{P}(E) + \dots \quad (4.9)$$

It is convenient to visualize this expansion using Feynman diagrams, as shown in Fig. 4.1. The solid lines represent the unperturbed Green's function $\hat{P}(E)$ describing free electron propagation, while the dashed lines represent successive scattering on impurities.

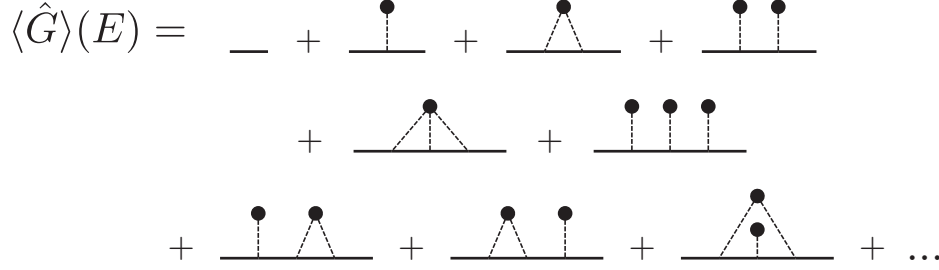


Figure 4.1: A diagrammatic representation of the perturbation expansion (4.9).

The series can be resummed by noticing that certain diagrams are just combinations of simpler diagrams linked by $\hat{P}(E)$. Those diagrams that cannot be separated into two diagrams by cutting just one solid line are called irreducible. Summing all those irreducible diagrams with their external legs removed, as shown in Fig. 4.2, gives a very important operator called the self-energy $\hat{\pi}^d(E)$. The link between the Green's function and the self-energy is called Dyson's equation:

$$\begin{aligned} \langle \hat{G} \rangle(E) &= \hat{P}(E) + \hat{P}(E)\hat{\pi}^d(E)\hat{P}(E) + \hat{P}(E)\hat{\pi}^d(E)\hat{P}(E)\hat{\pi}^d(E)\hat{P}(E) + \dots \\ &= \hat{P}(E) + \hat{P}(E)\hat{\pi}^d(E)\langle \hat{G} \rangle(E). \end{aligned} \quad (4.10)$$

Note that, contrary to the T-matrix, the Dyson equation implies an infinite number of impurities, and thus an infinite system. Since the disorder average restores the translation invariance, $\langle \hat{G} \rangle(E)$ and thus also $\hat{\pi}^d(E)$ are diagonal in the Bloch states basis. The Dyson equation implies

$$\langle \hat{G} \rangle(E) = \frac{1}{E - \hat{H}_0 - \hat{\pi}^d(E) + i\eta} = \sum_{\vec{k}} \frac{|\vec{k}\rangle \langle \vec{k}|}{E - \epsilon_{\vec{k}} - \pi_{\vec{k}}^d(E) + i\eta}. \quad (4.11)$$

The meaning of the self-energy can be further illuminated by defining another important



Figure 4.2: A diagrammatic representation of the self-energy.

quantity, the spectral function $A(\vec{k}, E)$:

$$\begin{aligned}
A(\vec{k}, E) &= -\frac{1}{\pi} \text{Im} \left(\langle \vec{k} | \langle \hat{G} \rangle(E) | \vec{k} \rangle \right) = \sum_{\mu} |\langle \vec{k} | \mu \rangle|^2 \delta(E - \epsilon_{\mu}) \\
&= \begin{cases} \frac{1}{\pi} \frac{|\text{Im}(\pi_{\vec{k}}^d(E))|}{\left(E - \epsilon_{\vec{k}} - \text{Re}(\pi_{\vec{k}}^d(E))\right)^2 + \text{Im}(\pi_{\vec{k}}^d(E))^2} & \text{if } \text{Im}(\pi_{\vec{k}}^d(E)) \neq 0 \\ \delta(E - \epsilon_{\vec{k}} - \text{Re}(\pi_{\vec{k}}^d(E))) & \text{if } \text{Im}(\pi_{\vec{k}}^d(E)) = 0 \end{cases} \quad (4.12)
\end{aligned}$$

$A(\vec{k}, E)$ represents the energy distribution of the Bloch state $|\vec{k}\rangle$, and accordingly it obeys the sum rule $\int dE A(\vec{k}, E) = 1$. It can be measured by angle-resolved photoemission spectroscopy (ARPES) experiments. In the clean case, it is simply a Dirac delta centered on $\epsilon_{\vec{k}}$, describing the fact that $|\vec{k}\rangle$ is an eigenstate with energy $\epsilon_{\vec{k}}$. In the presence of disorder, the real part of the self-energy shifts the Dirac delta from $\epsilon_{\vec{k}}$ to another value $\tilde{\epsilon}_{\vec{k}}$, while the imaginary part broadens it into a approximately lorentzian shape, with a width at half-maximum $\gamma_d = 2|\text{Im}(\pi_{\vec{k}}^d(\tilde{\epsilon}_{\vec{k}}))|$, (see Fig. 4.3). This is associated to a time evolution $e^{-i\tilde{\epsilon}_{\vec{k}}t/\hbar} e^{-\gamma t/2\hbar}$ for the amplitude of the $|\vec{k}\rangle$ state, and to a decay $e^{-\gamma t/\hbar}$ for its norm. Thus, in a Boltzmann picture, the presence of disorder can be associated to a lifetime $\tau_{\vec{k}}$ for the plane-wave excitations, with

$$\frac{\hbar}{\tau_{\vec{k}}} = 2|\text{Im}(\pi_{\vec{k}}^d(\tilde{\epsilon}_{\vec{k}}))|. \quad (4.13)$$

Summing the spectral function over the N Bloch eigenstates $|\vec{k}\rangle$ gives the disorder-averaged density of states (DOS) $\rho(E)$

$$\rho(E) = -\frac{1}{N\pi} \text{Im}(\text{Tr}(\hat{G})(E)) = \frac{1}{N} \sum_{\vec{k}} A(\vec{k}, E). \quad (4.14)$$

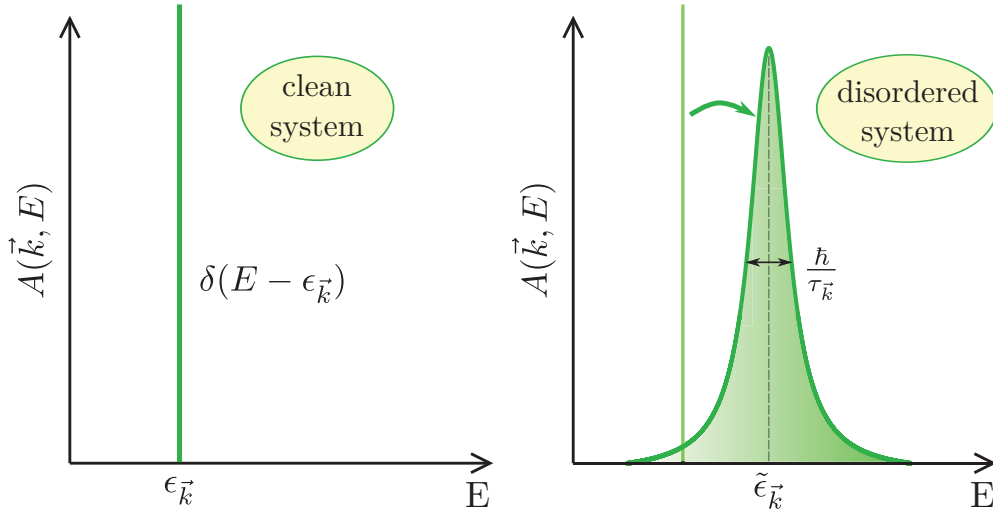


Figure 4.3: A sketch of the spectral function in clean (left) and disordered systems (right).

Thus, the averaged Green's function and the self-energy contain extremely useful information about the single-particle properties of the system. Certain transport properties, however, are not captured by these quantities and require averaging over a product of two Green's functions, as will be explained in section 4.2.

It is instructive to examine the physical meaning of the diagrams appearing in the expansion of Fig. 4.2. In each diagram, the number of dots corresponds to the power of the defect concentration and the number of dashed lines to the power of the on-site potential ξ . Therefore, when both x and ξ are small, it is necessary to include only the first diagrams. The very first one simply gives $x\xi$ for the self-energy. It just shifts the entire spectrum by this quantity, without giving any scattering. This approximation, called the virtual crystal approximation (VCA), is equivalent to taking the average of the Hamiltonian \hat{H} before calculating the properties of the system. To obtain a scattering rate, it is necessary to go to second order and include the second diagram, which gives a self energy $x\xi^2 P_0(E)$. Taking the imaginary part gives a scattering rate $\frac{\hbar}{\tau_k} = 2\pi x\xi^2 \rho_0(\epsilon_k)$, with ρ_0 the DOS of the clean system. This is nothing but Fermi's golden rule, recovered through the Green's function formalism. If the defect concentration x is small but not the on-site potential ξ , an infinity of diagrams must be included. Those associated with the lowest-order in x are the single-impurity diagrams, such as the first three in Fig. 4.2. Summing up all the single-impurity diagrams is called the "bare single-site approximation" [245] (the word "bare" means that the multiple-occupancy corrections are not included. It yields for the self-energy and scattering rate:

$$\pi_k^d(E) = \frac{x\xi}{1 - \xi P_0(E)}, \quad (4.15)$$

$$\frac{\hbar}{\tau_k} = \frac{2\pi x\xi^2 \rho_0(\epsilon_k)}{|1 - \xi P_0(\epsilon_k)|^2}. \quad (4.16)$$

These expressions contain important features of strong disorder. There are three cases, depending on the relative amplitude of ξ to the half-bandwidth W of the clean DOS (see Ref. [242] for more details):

- If $|\xi|$ is small with respect to W , then the numerator in equations (4.15) and (4.16) can be ignored and Fermi's golden rule is valid.
- As $|\xi|$ becomes comparable to W , there is an energy inside the band for which the real part of $1 - \xi P_0(E)$ vanishes. This may lead to a peak in the scattering rate, called resonant scattering. It is typically associated with a resonant bump in the DOS at this energy.
- There is a crossover at a certain value $\xi_c \approx W$. If $|\xi| > \xi_c$, there is an energy outside the band for which $1 - \xi P_0(E)$ vanishes and the self-energy becomes infinite. From the case $\text{Im}(\pi_k^d(E)) = 0$ of equation (4.12), an impurity band forms below (if $\xi < 0$) or above (if $\xi > 0$) the main band. It is made up of states localized around the defects. In the limit $|\xi|/W \rightarrow \infty$, the spectral function outside the clean band tends to $A(\vec{k}, E) \approx x\delta(E - \xi)$.

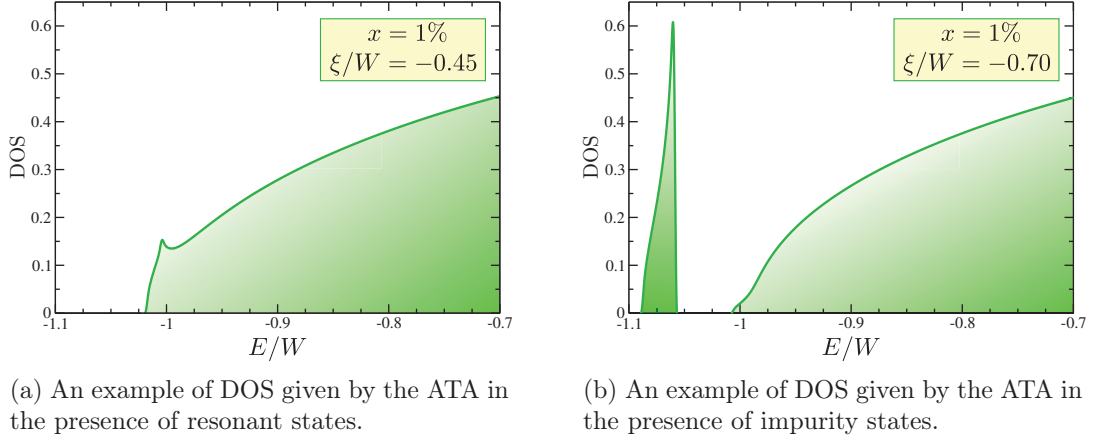


Figure 4.4

The typical shape of the DOS in the presence of resonant and impurity states is shown in Fig. 4.4. Including the multiple-occupancy corrections in the single-site approximation simply adds a factor $1 - x$ to $P_0(E)$ at the denominator of equations (4.15) and (4.16). This is called the average T-matrix approximation (ATA). The nested diagrams, such as the last one in Fig. 4.2, can be included in the self-energy by replacing the clean Green's functions \hat{P} (straight lines) in Fig. 4.2 by the full Green's function $\langle \hat{G} \rangle$. This procedure, known as the coherent potential approximation (CPA), yields a self-consistent equation that can be solved numerically [246]. Note that all these procedures lead to a scalar, i.e. \vec{k} -independent self-energy.

Although we have defined the self-energy for a particular type of defects, it is a very general concept and can be used to describe different forms of disorder. The case of a lorentzian disorder, for instance, has a particularly simple solution: if the potential on each lattice site is given by a lorentzian distribution with a broadening Γ , then the self-energy is just $-i\Gamma$ [247]. This type of disorder does not give rise to resonant or impurity states, but only to a uniform broadening of the clean eigenstates. An inelastic self-energy can also be defined for many-body interactions, such as electron-phonon or electron-electron scattering [141]. Therefore, a simple way to include these interactions in the problem of disordered conductors is to add an inelastic self-energy $\Sigma^{\text{in}} = -i\gamma_{\text{in}}/2$, where γ_{in} is the electron-phonon or electron-electron scattering rate.

4.1.2 The phonon Green's function

The problem of harmonic vibrations in a disordered crystal can also be tackled with the formalism of Green's functions. The dynamical matrix can be decomposed between a clean part D_0 and a disorder part D_d . We could define, by direct analogy with the electron case, the phonon's Green function as $-\frac{i}{\hbar}\Theta(t)\langle 0| [a_\mu(t), a_\mu^\dagger] |0\rangle$, where a_μ^\dagger is the phonon creation eigenoperator defined in equation (2.31), and $|0\rangle$ is now the phonon ground state

(no excitations of the vibration modes). However, this would lead to a time evolution $e^{-\omega_\mu t}$ involving the eigenfrequency and thus the square root of the dynamical matrix. It is possible to proceed in this way [248], but the square root leads to numerical issues in real-space representation. It is more convenient [249, 245] to define the phonon Green's function using the reduced position operators \hat{U}_μ introduced in section 2.1.3

$$G_\mu(t) = -\frac{i}{\hbar} \Theta(t) \langle 0 | [\hat{U}_\mu(t), \hat{U}_\mu] | 0 \rangle = -\frac{\Theta(t)}{\omega_\mu} \sin(\omega_\mu t), \quad (4.17)$$

and its Fourier transform $G_\mu(\omega) = \int dt G_\mu(t) e^{i\omega t}$:

$$G_\mu(\omega) = \frac{1}{2\omega_\mu} \left(\frac{1}{\omega - \omega_\mu + i\eta} - \frac{1}{\omega + \omega_\mu + i\eta} \right) = \frac{1}{\omega^2 - \omega_\mu^2 + 2i\omega\eta}, \quad (4.18)$$

where η is again an infinitely small positive imaginary part. By analogy with the electron case, we can consider the dynamical matrix and the phonon Green's function as operators on a Hilbert space of dimension $3N$ (with N the number of atoms in the system):

$$\hat{G}(\omega) = \sum_\mu \frac{|\mu\rangle \langle \mu|}{\omega^2 - \omega_\mu^2 + 2i\omega\eta} = \frac{1}{\omega^2 - \hat{D} + 2i\omega\eta} \quad (4.19)$$

where \hat{D} is the dynamical matrix and $|\mu\rangle$ is an eigenvector of \hat{D} . Technically, $|\mu\rangle$ should be considered not as an eigenstate of the Hamiltonian (2.30), but simply as the coefficients $A_{i\mu}^\alpha$ describing the vibration eigenmodes. The expression (4.19) is in complete formal analogy with the electron Green's function (4.4). This allows electrons and phonons to be treated on equal footing, with the same analytical and numerical techniques. It is possible, therefore, to introduce a self-energy $\hat{\pi}^d(\omega)$ and a spectral function $A_s(\vec{k}, \omega)$ for phonons (here s denotes the branch index). To give these quantities the same interpretations and usefulness as their electronic counterparts, the disorder-averaged Green's function should be expressed as

$$\langle \hat{G} \rangle(\omega) = \frac{1}{\omega^2 - \hat{D}_0 - 2\omega\hat{\pi}^d(\omega) + 2i\omega\eta} = \sum_{\vec{k}, s} \frac{|\vec{k}, s\rangle \langle \vec{k}, s|}{\omega^2 - \omega_{\vec{k}s}^2 - 2\omega\pi_{\vec{k}s}^d(\omega) + 2i\omega\eta}, \quad (4.20)$$

and the spectral function should be defined as

$$A_s(\vec{k}, \omega) = -\frac{2\omega}{\pi} \text{Im} \left(\langle \vec{k}, s | \langle \hat{G} \rangle(\omega) | \vec{k}, s \rangle \right) = \sum_\mu \left| \langle \vec{k}, s | \mu \rangle \right|^2 \left(\delta(\omega - \omega_\mu) + \delta(\omega + \omega_\mu) \right). \quad (4.21)$$

The spectral function is symmetric in ω , so broadening the Dirac delta should be done carefully at low frequencies. It obeys the sum rule $\int_{-\infty}^{\infty} d\omega A_s(\vec{k}, \omega) = 2$. The phonon DOS $\rho(\omega)$ can then be defined as

$$\rho(\omega) = -\frac{2\omega}{3N\pi} \text{Im}(\text{Tr} \langle \hat{G} \rangle(\omega)) = \frac{1}{3N} \sum_{\vec{k}s} A_s(\vec{k}, \omega). \quad (4.22)$$

Table 4.1 summarizes the correspondance between the electron and phonon Green's functions.

electrons Green's function	phonon Green's function
Hamiltonian \hat{H}	dynamical matrix \hat{D}
energy E	pulsation squared ω^2
self energy $\hat{\pi}^d(E)$	2ω times self-energy $2\omega\hat{\pi}^d(\omega)$
Bloch eigenstate $ \vec{k}, n\rangle$	Bloch eigenvector $ \vec{k}, n\rangle$
spectral function $A(\vec{k}, E) = -\frac{1}{\pi}\text{Im}(\langle \vec{k} \langle \hat{G} \rangle(E) \vec{k} \rangle)$	spectral function $-\frac{2\omega}{\pi}\text{Im}(\langle \vec{k}, s \langle \hat{G} \rangle(\omega) \vec{k}, s \rangle)$
DOS $\rho(E) = -\frac{1}{N\pi}\text{Im}(\text{Tr}\langle \hat{G} \rangle(E))$	DOS $\rho(\omega) = -\frac{2\omega}{3N\pi}\text{Im}(\text{Tr}\langle \hat{G} \rangle(\omega))$

Table 4.1: The important quantities related to the electron and phonon Green's function.

4.2 Quantum linear transport and localization: the Kubo formalism

We will now present a fully quantum formalism of electronic transport in disordered systems, known as the Kubo formalism [250, 157, 141, 244]. Our goal is to calculate the transport distribution function (TDF) without making any semi-classical assumption as was done in the Boltzmann transport approach (section 2.2.1). This will be achieved by calculating the electrical conductivity while neglecting all many-body interactions. The effects of electron-electron and electron-phonon scattering can be reintroduced later by adding an inelastic self-energy in the Green's function. This allows us to focus on the disorder effects within the single-particle framework. Fig. 4.5 illustrate the situation to be described: a large, disordered sample is contacted by two (or more) leads and subjected to an electric field \vec{E} . For our purpose, the leads can be modelled by perfectly clean, semi-infinite conductors.

It is useful at this point to provide a more careful definition of the electrical conductivity. In quantum physics, the current density at position \vec{r} is an operator $\hat{j}(\vec{r})$, whose expression is discussed in appendix B. The electrical conductivity is a tensor $\sigma^{ij}(\omega, \vec{r}, \vec{r}')$ that relates the Fourier component of the expectation value of the current density to that of the electrical field:

$$j^i(\omega, \vec{r}) = \text{Tr}(\hat{\rho}(t)\hat{j}^i(\omega, \vec{r})) = \sum_j \int d\vec{r}' \sigma^{ij}(\omega, \vec{r}, \vec{r}') E^j(\omega, \vec{r}'), \quad (4.23)$$

where i and j are direction indices and $\hat{\rho}(t)$ is the density matrix. The Kubo formalism provides an expression for the conductivity tensor derived from quantum linear response theory. At time $t = -\infty$, the system is assumed to be unperturbed in equilibrium. The density matrix at that time, $\hat{\rho}_0$, is just the grand-canonical density matrix. Then, a small electric field is adiabatically switched on, creating a current. It can be chosen to derive from a vector potential

$$A^i(t, \vec{r}) = \int \frac{d\omega}{2\pi} \frac{E^i(\omega, \vec{r})}{i(\omega + i\eta)} e^{-i(\omega + i\eta)t}, \quad (4.24)$$

where a small positive imaginary part η has been introduced to force the adiabatic turn-on. Since we are interested only in the steady-state regime, the limit $\eta \rightarrow 0$ should be taken

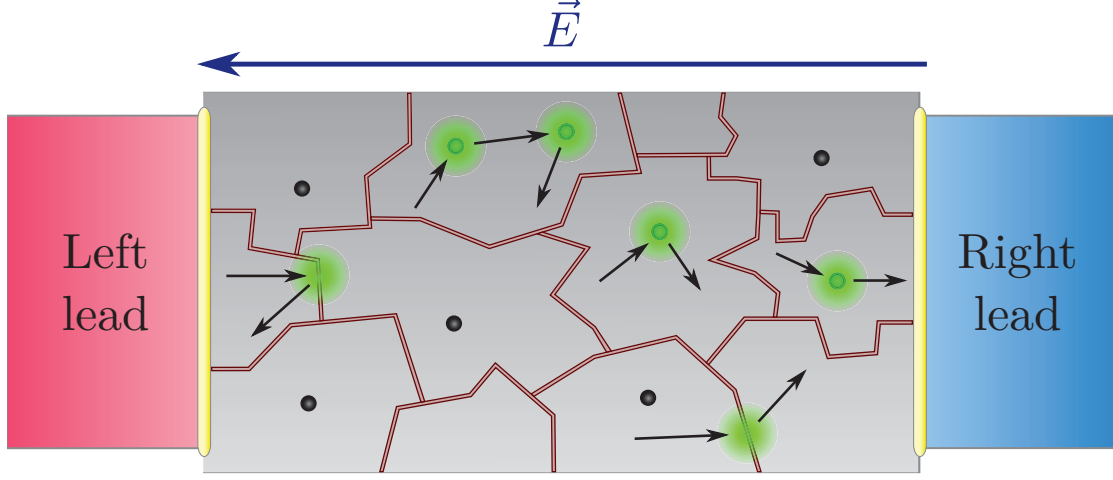


Figure 4.5: An illustration of the system in which electron transport takes place.

in the final result. Time-dependant quantum perturbation theory gives a linear-response expression for the conductivity tensor in terms of the continuous eigenstates $|\alpha\rangle$ of the entire system including the leads (see appendix C and Ref. [250]) :

$$\sigma^{ij}(\omega, \vec{r}, \vec{r}') = i \int d\alpha \int d\beta \frac{f(\epsilon_\alpha) - f(\epsilon_\beta)}{\epsilon_\beta - \epsilon_\alpha} \frac{\langle \alpha | \hat{j}^i(\vec{r}) | \beta \rangle \langle \beta | \hat{j}^j(\vec{r}') | \alpha \rangle}{\omega + \frac{\epsilon_\alpha - \epsilon_\beta}{\hbar} + i\eta}, \quad (4.25)$$

where η is an infinitely small imaginary part, ϵ_α is the energy associated to $|\alpha\rangle$, $f(E)$ is the Fermi-Dirac distribution and it must be specified that when $\epsilon_\alpha = \epsilon_\beta$, the fraction $\frac{f(\epsilon_\alpha) - f(\epsilon_\beta)}{\epsilon_\beta - \epsilon_\alpha}$ should be replaced with $-\frac{\partial f}{\partial E}(\epsilon_\alpha)$. In the absence of magnetic fields, this expression can be recast in terms of the Green's function $\hat{\mathcal{G}}$ of the entire system, leads included:

$$\sigma^{ij}(\omega, \vec{r}, \vec{r}') = \frac{\hbar}{\pi} \int dE \frac{f(E) - f(E + \hbar\omega)}{\hbar\omega} \text{Tr} \left(\hat{j}^i(\vec{r}) \text{Im} \hat{\mathcal{G}}(E + \hbar\omega) \hat{j}^j(\vec{r}') \text{Im} \hat{\mathcal{G}}(E) \right). \quad (4.26)$$

Of course, this formula cannot be implemented in practical calculations since the Green's function involves the Hamiltonian of the leads, which is an infinite matrix in tight-binding representation. However, as demonstrated in Ref. [156], the left and right leads can be "integrated out" by introducing non-hermitian self-energies operators $\hat{\pi}^L$ and $\hat{\pi}^R$ into the Green's function of the sample alone, without the lead i.e. with open boundary conditions. The trace in equation (4.26) can then be taken on the sample sites only, and the Green's function $\hat{\mathcal{G}}$ can be replaced with

$$\hat{G}_{LR}(E) = \frac{1}{E - \hat{H} - \hat{\pi}^L(E) - \hat{\pi}^R(E) + i\eta}, \quad (4.27)$$

where η is again infinitely small. If the Green's function (4.27), with the correct self-energies for the leads, is plugged into the Kubo formula (4.26), then the results are equivalent to

those predicted by the Landauer formalism or by the non-equilibrium Green's function (NEGF) method in the linear regime [156, 251]. It is a rigorous procedure to study electronic transport in the ballistic or ballistic-to-diffusive regime. In the context of thermoelectric power generation, however, the samples are typically a few millimeters long. For these system sizes, the regime for electron transport is squarely diffusive, and the leads should not enter the modelling and influence the simulation results. In other words, we will only be interested in the thermodynamic limit. For this reason, we will neglect the self-energy operators and only use the usual Green's function (4.4). An immediate issue arises from this choice: in finite systems, this gives either a vanishing or an infinite conductivity due to the delta functions contained in the imaginary part of the Green's function (4.4). It simply reflects the fact that no dissipation mechanism is present in the system. One was provided by the leads through the self-energies $\hat{\pi}^L$ and $\hat{\pi}^R$, but now we have removed them. A solution is to reintroduce the electron or phonon bath as an energy sink through electron-electron or electron-phonon scattering. This can be achieved by adding an inelastic self-energy $\Sigma^{\text{in}} = -i\gamma_{\text{in}}/2$ into the Green's function, defining a dephasing lifetime $\tau_{\text{in}} = \hbar/\gamma_{\text{in}}$ after which the electrons lose their coherence and memory of past collision events. If the disorder is strong enough such that the transport along a sample of length L is diffusive, a relevant energy scale is the Thouless energy $E_T = \hbar D_e/L^2$, with D_e the electronic diffusivity [252]. The thermodynamic limit is reached if $\gamma_{\text{in}} \gg E_T$ or, equivalently, if $L \gg \sqrt{D_e \tau_{\text{in}}}$ i.e. the sample is much longer than the typical distance covered by an electron before phase relaxation. In the case of weak disorder and ballistic transport, the Thouless energy should be replaced by the inverse time-of-flight $\hbar v_F/L$, with v_F the Fermi velocity, and the criterion for the thermodynamic limit simply becomes $L \gg v_F \tau_{\text{in}}$. Note that this last condition implies that the conductance of the system is much lower than the ballistic Landauer conductance (2.79). To summarize: if the sample length in the transport direction is smaller than the phase relaxation length, then the leads and the boundary conditions have a physical influence on the conductivity. If it is larger, then the leads can be ignored and the system is insensitive to the boundary conditions, open or periodic. We will generally choose periodic boundary conditions as they make size effects easier to eliminate. As for the width of the sample in the transverse direction, it should be large enough to make the separation of the discrete energy levels much smaller than the broadening γ_{in} .

Our formula for the TDF can finally be written. We are not interested in the spatial distribution of the current inside the sample, so we average the current density over the whole sample, in the presence of a uniform electric field. The current density integrated over the sample is simply the velocity operator times the electron charge (see appendix B):

$$\int d\vec{r} \hat{j}^i(\vec{r}) = -e \hat{v}^i = -\frac{e}{i\hbar} [\hat{r}^i, \hat{H}], \quad (4.28)$$

with \hat{r}^i the position operator along direction i . In the static ($\omega \rightarrow 0$) limit of the Kubo formula, the factor $\frac{f(E) - f(E + \hbar\omega)}{\hbar\omega}$ becomes $-\frac{\partial f}{\partial E}$. Thus, the TDF is given by

$$\Sigma^i(E) = \frac{\hbar e^2}{\pi \Omega} \langle \text{Tr}(\text{Im} \hat{G}(E) \hat{v}^i \text{Im} \hat{G}(E) \hat{v}^i) \rangle, \quad (4.29)$$

where Ω is the sample size and the brackets denote disorder averaging. Since the sample is

chosen much longer than the phase relaxation length, the average over disorder configurations is typically redundant and only a few or even one configuration is sufficient.

4.2.1 Anderson localization

If the averaged Green's function (4.11) has been calculated, using for instance ATA or CPA methods, it can be plugged into the Kubo formula (4.29) to obtain an estimation of the TDF. In the case of weak, perturbative disorder, this procedure recovers the result predicted by the Boltzmann transport equation under the relaxation time approximation (RTA), equation (2.54) [141]. However, this method makes an important approximation because it replaces the disorder averaged product of two Green's functions by a product of two disorder averaged Green's functions, and in doing so neglects the off-diagonal terms of $\hat{G}(E)$ in the \vec{k} basis. A diagrammatic expansion of the Kubo formula is shown in Fig. 4.6, featuring so-called bubble diagrams in which the Green's functions loop due to the trace. The thick shaded lines represent the full, disordered Green's function, the solid lines represent as before the unperturbed Green's function $\hat{P}(E)$, and the brown squares represent the \hat{v}^i operators. Taking the product of the disorder averaged Green's functions take the first three diagrams into account, but not the last two, which are called vertex diagrams or vertex corrections. These diagrams feature impurity scattering connecting the Green's functions on the opposite sides of the bubble. Because they incorporate the \vec{k} -space off-diagonal elements of the Green's function into the conductivity, they keep track of the efficiency with which the defect scattering events scramble the momentum of the carriers [141]. They also contain the effects resulting from coherent interference between the two Green's functions. In particular, diagrams such as the last one in Fig. 4.6, in which crossed scattering lines feature prominently, include the phenomenon of Anderson localization.

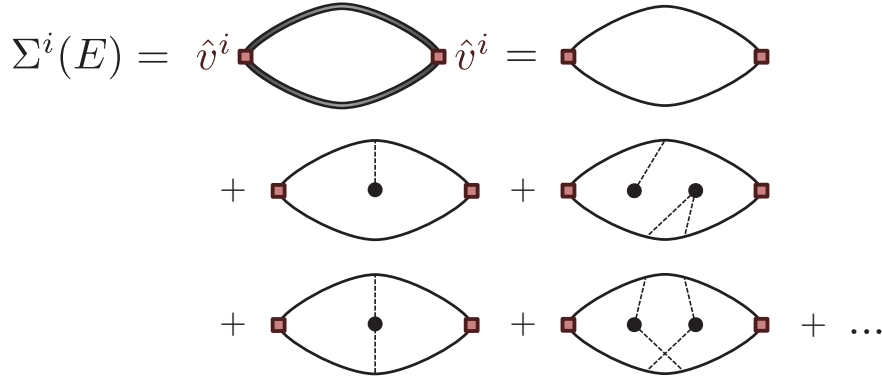


Figure 4.6: A diagrammatic representation of the Kubo formula. The thick shaded lines represent the full disordered Green's functions.

Anderson localization denotes the spatial localization of eigenstates in a strongly disordered system, in the sense that the wavefunction is not extended but decays with distance as $e^{-||\vec{r}||/\xi_l}$, where ξ_l is the so-called localization length [253, 254, 242]. It is considered here in the context of electrons in solids, but it is a general phenomenon of waves propagation in

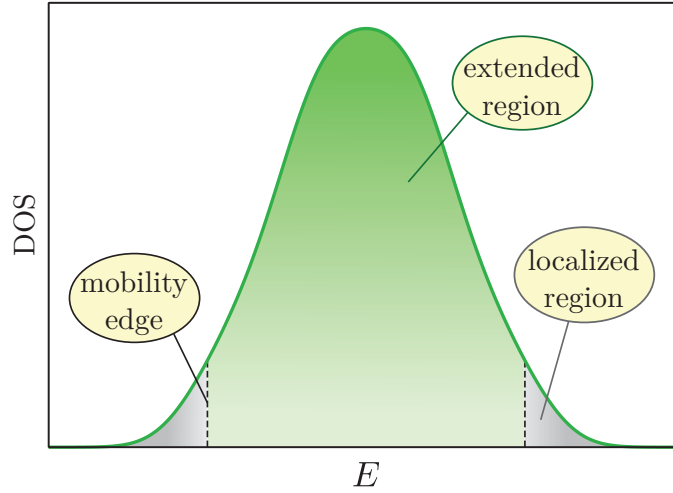


Figure 4.7: A sketch of a disordered density of states. The localized region in grey is associated with vanishing conductivities at zero temperature. It is separated from the extended region in green by mobility edges (black dashed lines).

strongly disordered media. The localization of electronic wavefunctions results from the fact that constructive interferences from collision events involving two or more impurities survive the disorder averaging only when the initial and final momenta are opposite (backscattering processes). A rule of thumb for evaluating the importance of localization corrections to the conductivity is the Ioffe-Regel criterion, that compares the Fermi wavevector k_F to the disorder mean free path l_e . If $k_F l_e \gg 1$, the mean free path is much greater than the wavelength and quantum interferences effects may be neglected. If not, localization effects are likely to come into play. This criterion is consistent with perturbative calculations (weak localization corrections) in three-dimensions, but breaks down in one and two dimensions [254, 242]. The DOS of a typical disordered system is shown in Fig. 4.7. At the edges of the bands, the states are localized in keeping with the Ioffe-Regel criterion. Then, at higher Fermi energies, the wavelength becomes smaller than the mean free path and the states loose their localized character. The localized part of the spectrum is characterized by a vanishing conductivity at zero temperature, as the localized eigenstates cannot transport electrons. The limit between the two regions called the mobility edge E_c . If the Fermi level crosses the mobility edge, a disorder-induced metal-insulator phase-transition occurs. Like other phase transitions, the Anderson transition exhibits universal characters: the existence of mobility edges and the critical exponents do not depend on the particular type of disorder. If the disorder strength is increased, the mobility edges move towards the center of band. Eventually, they merge as a critical disorder strength is reached, and the entire spectrum becomes localized. It is worth noting that in one and two-dimensional systems, this is always the case. There is no mobility edge and the entire spectrum is localized, no matter how weak the disorder.

Since Anderson localization arises from quantum interferences between two or more impurities, the presence of dephasing inelastic processes, such as electron-electron or electron-phonon scattering, tend to destroy localization effects. Thus, the introduction of an imaginary self-energy $\Sigma^{\text{in}} = -i\gamma_{\text{in}}/2$ leads to finite conductivities in the localized regions of the spectrum, even at zero temperature. This is in violation of Matthiessen's rule (equation (2.64)), which predicts that the conductivity is always decreased by the addition of scattering processes.

4.3 Practical calculations and numerical methods

Despite the elegance of the formalism presented in the previous sections, it is difficult to carry out analytical calculations on realistic models for electrons and phonons in the presence of disorder. Therefore, numerical simulations must be employed in order to formulate quantitative predictions. In this section are presented the practical methodologies that we use to compute the properties of disordered systems (we will focus on electrons for the sake of simplicity, but the case of phonon is analogous, see section 4.1.2). They constitute an exact treatment of disorder, in the sense that every diagram is included in the expansion of the Kubo formula, Fig. 4.6. They are real-space approaches, meaning that the Hamiltonian is always manipulated in the basis of Wannier orbitals as opposed to the Bloch basis. This tight-binding representation is particularly suited to the study of disorder, since defects and impurities can be readily modeled by their local influence on the on-site potentials and hopping terms of neighboring orbitals.

4.3.1 Exact diagonalization

Perhaps the simplest and most natural approach in dealing with disordered systems is exact diagonalization (ED). In principle, it is possible to store the full Hamiltonian matrix for a given disorder configuration into an array and then to diagonalize it using dedicated linear algebra libraries such as BLAS and LAPACK. This would give access to the eigenstates and eigenvalues, and from these to all the properties of the system. The quantities of interest, say the conductivity, could be computed from each configuration and then averaged. In practice, however, the size of the systems that can be studied by this approach is severely limited. For a cubic system composed of L^3 unit cells, the diagonalization of the Hamiltonian scales as L^9 . Thus, the maximum length attainable through ED is typically $L \approx 30$ unit cells. For samples of this size, the transport regime is generally not diffusive and the absence of leads in the simulation is likely to produce unphysical size effects.

It is still possible, however, to extract meaningful physical information from the diagonalization of small systems. The scaling of the eigenstate wavefunctions with increasing system size, for instance, yields clear indications about the presence or absence of Anderson localization. Let us consider for simplicity a d -dimensional lattice with one orbital per unit cell and a normalized eigenstate $|\mu\rangle = \sum_{\vec{R}} c_{\vec{R}}^{\mu} |\vec{R}\rangle$. For extended states such as Bloch states, the coefficients $c_{\vec{R}}^{\mu}$ in the Wannier basis scale as $1/L^{\frac{d}{2}}$. For localized states, on the other hand, they can be considered independent of the system size if L is greater than the

localization length ξ_l . It can be roughly considered that $c_{\vec{R}}^\mu = 1/\xi_l^{\frac{d}{2}}$ in a box of size ξ_l^d and vanishes outside the box. A useful quantity to define is the inverse participation ratio (IPR) [255, 256]. The IPR for the eigenstate $|\mu\rangle$ is defined as

$$\text{IPR}_\mu = \sum_{\vec{R}} \left| c_{\vec{R}}^\mu \right|^4. \quad (4.30)$$

For extended states, we expect $\text{IPR}_\mu \propto 1/L^d$ and for localized states $\text{IPR}_\mu \approx 1/\xi_l^d$ if $L \gg \xi_l$. Thus, a finite size study of the IPR should provide a robust indication on the extended or localized character of the eigenstates at a given Fermi energy.

Another quantity of interest that can be evaluated through ED is the diffusivity, as was done in Ref. [156]. For a degenerate conductor, the electronic diffusion coefficient along direction i D_e^i can be defined by the Einstein relation $\Sigma^i = e^2 \rho D_e^i$, where ρ is the DOS per unit volume at the Fermi level. Expressing the Kubo formula (4.29) in terms of the eigenstates $|\mu\rangle$ yields

$$\Sigma^i = e^2 \left\langle \frac{1}{\Omega} \sum_{\mu} \delta(E - \epsilon_\mu) D_\mu^i \right\rangle, \quad (4.31)$$

with

$$D_\mu^i = \pi \hbar \sum_{\nu} \left| \langle \mu | \hat{v}^i | \nu \rangle \right|^2 \delta(\epsilon_\mu - \epsilon_\nu). \quad (4.32)$$

The quantity D_μ^i can be interpreted as the diffusivity for the eigenstate $|\mu\rangle$ in direction i . As indicated by the presence of delta peaks, this expression was obtained assuming no inelastic self-energy in the Green's function, i.e. without any electron-electron or electron-phonon scattering. To estimate the value of D_μ^i at the thermodynamic limit, we broaden the delta peaks into lorentzians of half-width η , with η typically a multiple of the average level separation. This is just a trick to simulate infinite systems without inelastic scattering, and no physical meaning can be attached to η . Therefore, the values obtained for the diffusivities through ED represent an upper limit to the actual diffusivity, which can be decreased by inelastic processes in extended regions of the spectrum.

4.3.2 The Chebyshev Polynomial Green's Function method

A powerful method to compute quantities dependant on disordered Green's functions consists in using Chebyshev polynomials. This methodology has been pioneered by J. Wheeler, M. Prais and C. Blumstein [257] and has been developped in the context of electronic transport and magnetic interactions by D. Mayou and S. Roche [258, 259, 260]. Excellent reviews have been published in Ref. [261] and Ref. [262], the latter of which presents a recent formulation, known as the Chebyshev Polynomial Green's Function method (CPGF), that we will use in this work. The central idea is to expand the Green's function $\hat{G}(E)$ on the orthogonal basis of Chebyshev polynomials of the first kind $T_n(x) = \cos(n \arccos(x))$. Since they are defined only for $x \in [-1, 1]$, this requires rescaling the energies $E \rightarrow \tilde{E}$ and the Hamiltonian $\hat{H} \rightarrow \tilde{\hat{H}}$ so that the spectrum falls between -1 and 1 . The Green's function

can then be expressed as a semi-analytic series:

$$\hat{G}(\tilde{E}) = \sum_{n=0}^{\infty} g_n(\tilde{z}) T_n(\tilde{H}), \quad (4.33)$$

where $\tilde{z} = \tilde{E} + i\tilde{\eta}$ and

$$g_n(\tilde{z}) = -i(2 - \delta_{n,0}) \frac{(\tilde{z} - i\sqrt{1 - \tilde{z}^2})^n}{\sqrt{1 - \tilde{z}^2}}. \quad (4.34)$$

It is instructive to visualize the imaginary part of a typical g_n function (only the imaginary part of the Green's function is used to calculate the DOS, spectral function and TDF). In Fig. 4.8 is plotted the imaginary part of g_{100} as a function of \tilde{E} . $\text{Im}(g_n)$ has n nodes so, roughly speaking, it oscillates at a frequency $n/4$. Thus, the Chebyshev polynomial basis can be considered analogous to the Fourier basis for quantities defined on finite segments, and it is very often used in numerical expansions due to its superior convergence properties [263]. The imaginary part $\tilde{\eta}$ mainly influences the overall amplitude of $\text{Im}(g_n)$, which is approximately $e^{-n\tilde{\eta}}$. Therefore, the presence of a finite $\tilde{\eta}$ renders negligible all terms of the series beyond, say, $5/\tilde{\eta}$. Since it can be interpreted as an inelastic self-energy, two strategies can be adopted towards setting the value of η . If one wishes to study the effects of disorder only (as is typically the case when computing the DOS or the spectral function), η should be taken smaller and smaller until the quantity of interest no longer depends on it, at which point the disorder dominates. If, on the other hand, one wishes to include inelastic scattering effects in the calculation (of particular interest for the TDF), η should be set equal to $\gamma_{\text{in}}/2$.

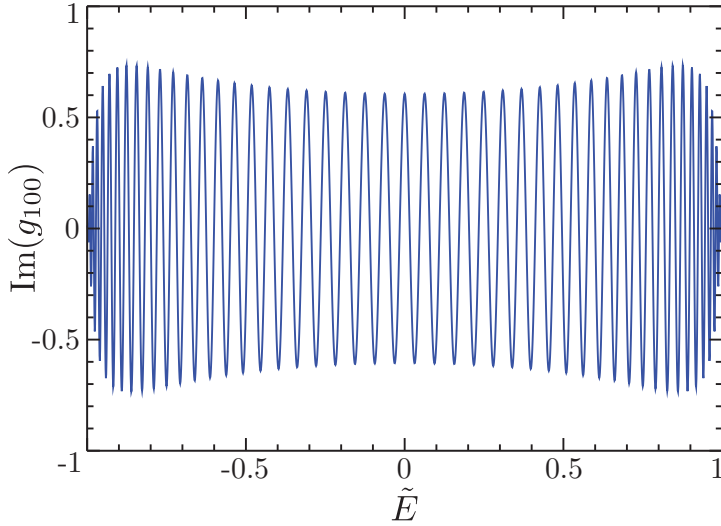


Figure 4.8: The imaginary part of g_{100} as a function of \tilde{E} .

Inserting the series (4.33) into the Kubo formula (4.29) for the TDF yields

$$\Sigma^i(\tilde{E}) = \frac{\hbar e^2}{\pi \Omega} \sum_{n,n'} \mu_{n,n'}^i \text{Im} g_n(\tilde{z}) \text{Im} g_{n'}(\tilde{z}), \quad (4.35)$$

with

$$\mu_{n,n'}^i = \langle \text{Tr}(T_n(\tilde{H}) \tilde{v}^i T_{n'}(\tilde{H}) \tilde{v}^i) \rangle. \quad (4.36)$$

The quantities $\mu_{n,n'}$ are called the moments and their calculation represents the main workload of CPGF implementations. The power of this method comes from its use of a recursion relation between the Chebyshev polynomials. They satisfy the relation

$$T_{n+1}(\tilde{H}) = 2\tilde{H}T_n(\tilde{H}) - T_{n-1}(\tilde{H}), \quad (4.37)$$

with $T_0(\tilde{H}) = 1$ and $T_1(\tilde{H}) = \tilde{H}$. Thus, the moments can be efficiently computed by iterative multiplications of the Hamiltonian matrix operator. They can then be stored and the TDF can be calculated on an arbitrarily fine energy grid due to the simple analytical expressions for the g_n . This is especially useful in the context of thermoelectricity, as the TDF must basically be differentiated to compute the Seebeck coefficient.

The calculation of the trace in equation (4.36) is performed using a stochastic method. For each disorder configuration, we define N_r random vectors $|r\rangle = \sqrt{2} \sum_{\vec{R}} \cos(\phi_{\vec{R}}) |\vec{R}\rangle$, with $\phi_{\vec{R}}$ random phases, and the moments are approximated by

$$\mu_{n,n'}^i = \frac{1}{N_r} \sum_r \langle r | T_n(\tilde{H}) \tilde{v}^i T_{n'}(\tilde{H}) \tilde{v}^i | r \rangle. \quad (4.38)$$

If enough random vectors are used, the cross-terms do not survive the averaging of the random phases and one is left with the trace. It should be noted that the moments $\mu_{n,n'}^i$ are in principle symmetric in n and n' . However, the stochastic procedure introduces an error that breaks the symmetry in practical calculations. Because of error cancellations in the Chebyshev polynomial expansion, the convergence of equation (4.38) with the number of random vectors is much improved if all the moments are calculated (as opposed to just half of them). This is particularly true for low values of the TDF, which is highly relevant when localization phenomena are involved. The convergence properties of the CPGF method are further detailed in appendix E.

The calculation of the DOS is much simpler than the TDF, as it involves moments featuring only one Chebyshev polynomial, $\langle \text{Tr}(T_n(\tilde{H})) \rangle$. Similarly, the spectral function $A(\vec{k}, E)$ requires calculating moments of the form $\langle \langle \vec{k} | T_n(\tilde{H}) | \vec{k} \rangle \rangle$. The CPGF method gives access to other quantities of interest, such as the local DOS (LDOS) and the typical DOS. For a particular disorder configuration c , the local DOS at site \vec{R} is defined as

$$\rho_{\vec{R}}^c(E) = -\frac{1}{\pi} \langle \vec{R} | \hat{G}^c(E) | \vec{R} \rangle \quad (4.39)$$

and can be interpreted as the energy distribution at site \vec{R} for this configuration. The DOS is simply the arithmetic average of $\rho_{\vec{R}}^c(E)$ over the lattice sites and disorder configurations.

The typical DOS ρ_t is defined as

$$\rho_t(E) = \exp \left(\frac{1}{N_c N} \sum_c \sum_{\vec{R}} \ln(\rho_{\vec{R}}^c(E)) \right) = \left(\prod_c \prod_{\vec{R}} \rho_{\vec{R}}^c(E) \right)^{\frac{1}{N_c N}}, \quad (4.40)$$

where N_c is the number of disorder configurations. It is a geometric average instead of an arithmetic average, which makes it a critical quantity with respect to Anderson localization. In principle, it vanishes in the localized regions of the spectrum, contrary to the DOS. This is because the geometric average is much more sensitive to small values than the arithmetic one. Thus, if one of the local terms $\rho_{\vec{R}}^c(E)$ is exactly zero, the entire average also vanishes. In practice, the limited number of sites and disorder configurations, as well as the necessary presence of an imaginary part η , lead to finite values of the typical DOS. Nevertheless, the localized regions are likely to be indicated by much smaller values of the typical DOS with respect to the DOS.

In contrast to exact diagonalization, the CPGF algorithms scale linearly with the system size. As for the number of moments N_m , they scale linearly when calculating the DOS and spectral function, and they scale as N_m^2 when calculating the TDF. These favorable scalings allows the simulation of large systems consisting of tens of millions of sites, with lengths that can reach the micrometer scale. This methodology is thus extremely powerful for the study of large disordered systems, and will be used extensively in the following chapters.

Chapter 5

Boosting the power factor: resonant states

*I never thought I'd see a resonance cascade...
Let alone create one.*

Dr. Kleiner, *Half-Life*.

A promising method to boost the power factor (PF) consists in using resonant states [98, 90, 205], as mentioned in section 1.2.2. The concept is illustrated in Fig. 5.1. Dopants introduce impurity or defect states inside the conduction band that hybridize with the extended states. This way, a sharp peak in the density of states (DOS) of the host compound is created, which alters the electronic transport properties when the Fermi level lies in its vicinity. In the context of thermoelectric transport, the presence of a resonant peak is thought to be favorable for the PF, for reasons that will be detailed shortly. An enhancement of the thermoelectric properties through resonant impurity states has been claimed in various compounds, such as Tl-doped PbTe [103], Sn-doped Bi₂Te₃ [104], In-doped SnTe [264], Al-doped PbSe [265], or Sn-doped β -As₂Te₃ [266]. It has also been suggested [90] that the very high power factor of YbAl₃ [267, 268] could be explained by the presence of a sharp f-level peak in its DOS [269]. The case of Tl-doped PbTe is controversial since first-principles calculations reproduced the experimental values for the Seebeck coefficient with a simple rigid-band shift of the pristine material [105]. Subsequently, numerical studies using the Coherent Potential Approximation (CPA) coupled with first-principles calculations [270] have been conducted to investigate the effects of random Tl doping in PbTe [271, 272, 273]. However, transport properties were calculated in the absence of electron-phonon scattering, and the treatment of disorder by CPA methods is known to ignore the vertex corrections and thus localization effects [242]. More importantly, no clear improvement in the PF over a rigid-band shift of the Fermi level was shown for Tl-doped PbTe. As it stands, there is still no consensus in the literature whether actual resonant enhancement of the thermoelectric properties have been observed experimentally. Indeed, despite such intense activity around resonant states in thermoelectricity, there are still a few widespread misconceptions about how resonant levels affect thermoelectric transport.

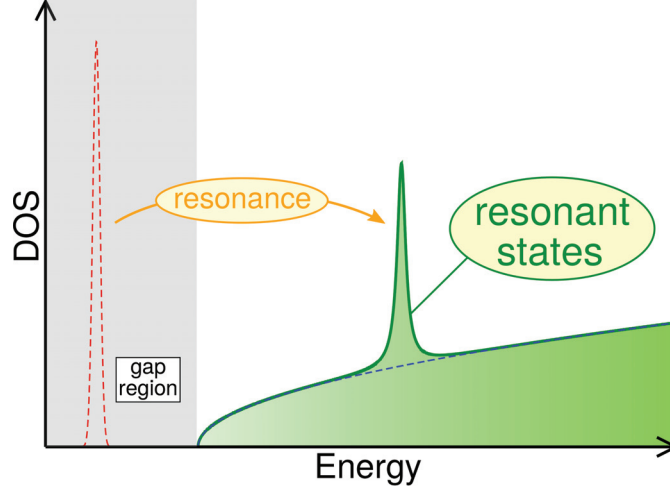


Figure 5.1: From Ref. [274]. Sketch of the density of states as a function of energy corresponding to a conduction band in the presence of resonant states.

Let us now describe the mechanisms that are commonly found in the literature to explain how resonant states can enhance the PF. The electronic transport properties of any compound depend solely on the transport distribution function (TDF) $\Sigma(E, T)$, see equations 2.51 and 2.52 (note that we omit from now the direction index for the transport properties). The Mott formula, equations 2.55 and 2.56, imply that maximizing the power factor σS^2 requires finding a material in which the TDF has a high amplitude (high conductivity) as well as sharp variations (high Seebeck coefficient).

Mahan and Sofo [90] found that the shape of the TDF most conducive to good thermoelectric properties is the delta function. Writing the Einstein formula:

$$\Sigma(E, T) = e^2 \rho(E) v_x^2(E) \tau(E, T), \quad (5.1)$$

in which $\rho(E)$ is the DOS, $v_x(E)$ is the band velocity along the transport direction x , and $\tau(E, T)$ is the relaxation time, they suggested that a sharp peak in the DOS would translate to a sharp peak in the TDF (Fig. 5.2a), provided that the velocity v_x and scattering rate are not suppressed significantly around resonance. In this case, they also calculated that the presence of a background DOS could destroy the resonant effect, which would encourage looking for resonant states very near the host valence or conduction band edge. Notice how the sign of the slope of the TDF changes around the resonant state in this physical picture. Consequently, one should expect the sign of the Seebeck coefficient to change as the Fermi level crosses the resonant band. This interpretation has been invoked to explain the results of ab-initio calculations for ZnSe containing O impurities [275].

Another slightly different mechanism is used to explain the effects of resonant states throughout the literature [98, 92, 103, 265]. Since the TDF is basically the conductivity at low temperature, one can write

$$\Sigma(E, T) \approx e n(E) \mu_x(E, T), \quad (5.2)$$

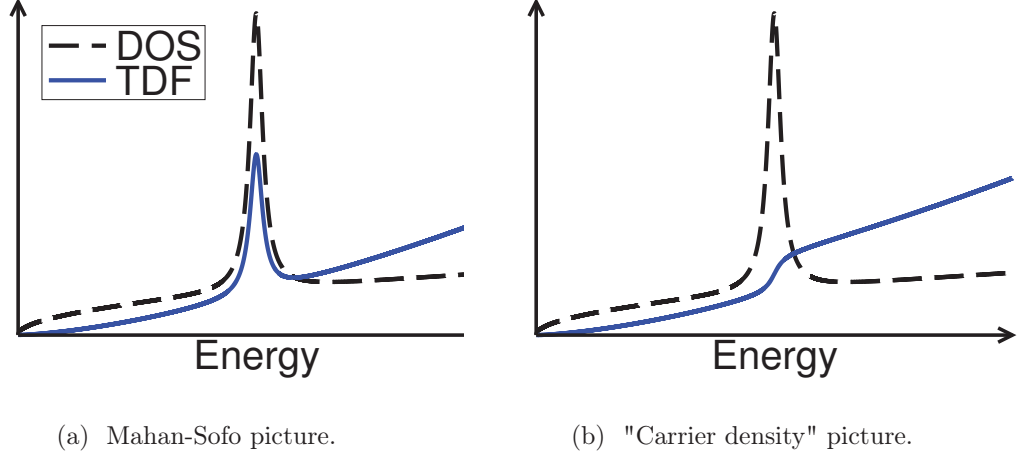


Figure 5.2: From Ref. [276]. Schematic representation of the density of state (black dashed line) and transport distribution function (blue line) in the presence of a resonant peak.

in which $n(E)$ is the total carrier density and $\mu_x(E, T)$ is the carrier mobility along the transport direction. The Mott formula then yields

$$S \approx -\frac{\pi^2 k_B^2 T}{3e} \left(\frac{1}{n} \frac{\partial n}{\partial E} + \frac{1}{\mu_x} \frac{\partial \mu_x}{\partial E} \right). \quad (5.3)$$

The first term, $\frac{1}{n} \frac{\partial n}{\partial E} = \frac{\rho(E)}{n(E)}$, depends very little on temperature and is associated with band structure effects, it is straightforward to see that a local increase in the DOS would cause a local boost in the Seebeck coefficient. The second term, $\frac{1}{\mu_x} \frac{\partial \mu_x}{\partial E}$, is associated in the literature with scattering. If the resonant states bring about a drastic change in the carrier scattering, the Seebeck coefficient might be boosted through this term. The effects of resonant scattering are thought to vanish at high temperature, as the scattering becomes dominated by phonons. Assuming no resonant scattering, then, the carrier mobility is thought not to change violently around the resonance, and the TDF is approximatively proportional to the carrier density n (Fig. 5.3). Note that in this picture, the slope of the TDF remains positive, so the sign of the Seebeck coefficient is not expected to change. Moreover, the Fermi level should be located right at the resonance for maximum effect.

Both mechanisms in Fig. 5.2 require the resonant states to participate in conduction, meaning that either the band velocity v_x or the mobility μ_x must not be drastically suppressed by the resonance. This seems incompatible with the requirement that the resonant peak in the DOS be sharp since a flat band implies low velocities and low mobilities. From the point of view of the Bloch states, a resonant peak is typically associated with a high scattering rate (resonant scattering, see section 4.1.1). If we consider instead the eigenstates of the disordered system, the hybridization between the extended and impurity states gives a more localized character to the eigenstates near the resonant peak, leading to low velocities. As noted by Heremans et al. [98], if the two types of states are not hybridized

with one another, the transport properties are entirely dominated by the extended states (which have the highest conductivity) and the defect states are useless. Therefore, some hybridization is needed to boost the power factor. Thus, a single very flat band, for instance a doping impurity band in the gap of the host material, leads to bad thermoelectric properties despite having a very delta-like DOS [205, 277]. Confinement techniques work around this problem because they introduce flat dispersions only in the confinement directions. For the same reason, highly anisotropic orbitals like d orbitals are naturally conducive to good thermoelectric properties, and it is possible to boost the power factor by making them come into play [278]. Even then, they must have both a strong weight in the DOS and a sufficient dispersion in the transport direction to enhance the thermoelectric properties [211].

In this chapter, we will investigate the effects of resonant states on thermoelectric transport. In section 5.1, published in Ref. [274], this is done on very general grounds using a disordered tight-binding model. In section 5.2, we focus on the specific case of vanadium doping in SrTiO_3 using first-principle calculations [279]. In section 5.3, we combine the two methodologies to address the influence of disorder and localization in V-doped SrTiO_3 , and more generally to study resonant states in similar oxide perovskites [280].

5.1 Large enhancement of the thermoelectric power factor in disordered materials through resonant scattering

The discussion above raises a few questions about the general properties of resonant states. What exactly happens to the TDF in the presence of resonant impurities? What is the right hybridization between the extended and defect states? Where should the resonant level be, with respect to the edge of the host band? Where should the Fermi level be, with respect to the resonant level? What kind of boost can we expect for the power factor? In this section, our goal is to answer these questions and to clarify the general conditions required for a boost of the PF using resonant substitution impurities, independantly of the material-specific band-structure or scattering law. In particular, we will investigate the influence of the impurity concentration x , the effects of inelastic scattering, and finally we will examine the case of anisotropic orbitals, all with a full treatment of the disorder and resonant scattering.

5.1.1 Disordered model Hamiltonian and methodology

To that end, we consider a single-orbital tight-binding Hamiltonian featuring hopping terms t between nearest neighbors on a cubic lattice. Here the charge carriers are electrons (n-type), but because of electron-hole symmetry, our results are valid for p-type materials as well. The resonant impurities are modelled by an on-site potential ϵ on the defect sites and an hybridization V between the host and impurity sites. The position of the defects are

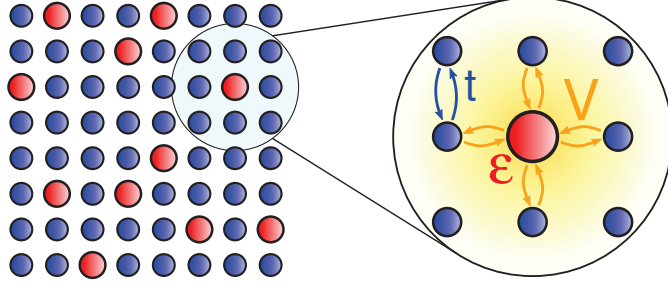


Figure 5.3: From Ref. [274]. A sketch of the disordered lattice and tight-binding Hamiltonian.

chosen randomly. Hence, the Hamiltonian, as illustrated in Fig. 5.3, reads:

$$\begin{aligned} \hat{H} = & -t \sum_{\langle \mathbf{i}, \mathbf{j} \rangle, \sigma} \left(c_{\mathbf{i}, \sigma}^\dagger c_{\mathbf{j}, \sigma} + c_{\mathbf{j}, \sigma}^\dagger c_{\mathbf{i}, \sigma} \right) \\ & + \epsilon \sum_{\mathbf{m}, \sigma} c_{\mathbf{m}, \sigma}^\dagger c_{\mathbf{m}, \sigma} - V \sum_{\langle \mathbf{i}, \mathbf{m} \rangle, \sigma} \left(c_{\mathbf{i}, \sigma}^\dagger c_{\mathbf{m}, \sigma} + c_{\mathbf{m}, \sigma}^\dagger c_{\mathbf{i}, \sigma} \right), \end{aligned} \quad (5.4)$$

\mathbf{i} runs over host sites, \mathbf{m} over impurity sites, σ is the electron spin and the brackets denote nearest neighbors only. Since the transport properties do not depend explicitly on t , we express the other parameters in units of t (see below).

The electrical conductivity and the Seebeck coefficient at electron density n and temperature T are calculated from the TDF, equations (2.51) and (2.52). The chemical potential μ is set to give the correct electron density when the DOS $\rho(E)$ is integrated. From the Mott formula, equation (2.55) and equation (2.56), σ is the thermal average of Σ around the Fermi level μ , while S is basically the logarithmic derivative of Σ around μ . Therefore, high Seebeck coefficients arise from strong, sharp variations in the TDF (i.e. large values of $|\frac{d\Sigma}{dE}|$). Most theoretical studies of doped thermoelectric materials compute the TDF within the framework of the Boltzmann transport equation with the relaxation time approximation. They either consider impurity scattering to be negligible compared to electron-phonon scattering [74, 281, 282, 283, 139], or estimate the electron-impurity scattering rate by second-order perturbation theory (i.e. Fermi's Golden Rule) using a model description for the impurity scattering [284, 59, 161]. This is reasonable when the doping does not significantly alter the electronic structure and causes only weak electron-impurity scattering, as is the case of La or Nb doped SrTiO₃ for instance [166]. But the whole point of resonant states is that they distort the band structure of the host material and introduce strong scattering. Therefore, in this study, we go beyond the semi-classical Boltzmann formalism to incorporate the full effects of disorder and multiple resonant scattering. We use the Kubo formula expressed in terms of the Green's function \hat{G} of the system [285, 157, 250, 251]

$$\Sigma(E) = \frac{\hbar e^2}{\pi \Omega} \langle \text{Tr}(\text{Im} \hat{G}(E) \hat{v}_x \text{Im} \hat{G}(E) \hat{v}_x) \rangle, \quad (5.5)$$

brackets denote disorder averaging, Ω is the total volume, $\hat{v}_x = \frac{it}{\hbar} \sum_{\langle \mathbf{i}, \mathbf{j} \rangle, \sigma} (x_{\mathbf{i}} - x_{\mathbf{j}}) (c_{\mathbf{i}, \sigma}^\dagger c_{\mathbf{j}, \sigma} -$

$c_{\mathbf{j},\sigma}^\dagger c_{\mathbf{i},\sigma}$) is the velocity operator along the transport direction x , and the Green's function writes

$$\hat{G}(E) = \frac{1}{E - \hat{H} + i\frac{\gamma_{\text{in}}}{2}}. \quad (5.6)$$

A constant imaginary part has been introduced in the denominator of $\hat{G}(E)$ to account for the presence of inelastic scattering mechanisms in the system, such as electron-phonon (e-ph) or electron-electron (e-e) collisions. It will be further discussed thereafter. Σ can be expressed in terms of the adimensioned TDF $\tilde{\Sigma}$, $\Sigma = \frac{e^2}{a\hbar}\tilde{\Sigma}$, and likewise for the power factor, $\text{PF} = \frac{k_B^2}{a\hbar}\tilde{\text{PF}}$. For definiteness, we set $a = 4\text{\AA}$, which gives the same volume per atom as in Si or PbTe, leading to $\frac{e^2}{a\hbar} = 6.08 \times 10^3 \text{ S/cm}$ and $\frac{k_B^2}{a\hbar} = 45.18 \mu\text{W} \cdot \text{cm}^{-1} \cdot \text{K}^{-2}$.

The exact diagonalization of the Hamiltonian (5.4) would drastically limit the system sizes that could be studied with a reasonable amount of memory and computational time. Therefore, we use the Chebyshev-Polynomial Green's Function method (CPGF), presented in section 4.3.2 and in Ref. [262, 261], to compute $\Sigma(E)$ exactly, fully including vertex corrections. The CPGF is a real-space approach particularly suitable for addressing the physics in disordered systems. Around 1800×1800 moments are sufficient for the TDF to fully converge. Periodic boundary conditions are used to reach the thermodynamic limit more easily. Here, we compute the TDF on systems of size $N = 1200 \times 200 \times 200$ (48×10^6 sites), this slab geometry allows faster convergence. The trace in equation (5.5) is evaluated efficiently by a stochastic method involving random vectors as described in section 4.3.2. When calculating the TDF for such a large system size, only a few random vectors and disorder configurations are necessary. We have checked that the clean limit is perfectly recovered for both open and periodic boundary conditions.

Regarding γ_{in} in equation (5.6), it can be interpreted as the inelastic contribution to the electron relaxation time [141]. In thermoelectric materials, scattering rates at room temperature typically range from 1 meV to 100 meV. In certain Half-Heuslers such as ZrNiSn, for instance, particularly weak e-ph couplings lead to inelastic scattering rates varying between 1 meV and 20 meV [286] while strong e-e scattering in SrTiO₃ leads to γ_{in} ranging from 50 meV to 200 meV and even higher [166]. In between, scattering rates vary from 10 meV to 100 meV in Si [287, 288, 161] or from 20 meV to 60 meV in pristine and doped SnSe [289]. From the bandwidth in these compounds, we estimate t ranging from 0.3 eV to 1 eV, therefore we will consider $0.02t \leq \gamma_{\text{in}} \leq 0.2t$. This corresponds to γ_{in} ranging from 10 meV to 200 meV and mean free paths between 50 Å and 500 Å in the pristine case, which is well in line with calculated values in PbTe [281], for instance. As we will see shortly, a small inelastic scattering is most favorable for resonant enhancements of the PF, therefore we set $\gamma_{\text{in}} = 0.02t$ unless specified otherwise. The choice of a constant γ_{in} preserves the generality of this investigation, since incorporating energy and temperature dependences requires a material-specific study. Note also that computations for smaller γ_{in} would imply a strong increase in the number of calculated moments before convergence is reached.

5.1.2 Boosting the power factor

In what follows, we consider the set of values $\epsilon = -4t$ and $V = 0.3t$ that were found optimal in a previous study that completely ignored disorder [276]. Unless specified otherwise, the electronic properties will be calculated using these values. Fig. 5.4(a) shows the TDF and the DOS (inset) for different impurity concentrations $x = \frac{N_{\text{imp}}}{N}$, with N_{imp} the number of randomly distributed defects. Five concentrations are considered, from $x = 0\%$ (the pristine reference case) to $x = 5\%$. The defects introduce a local peak in the DOS, which is considered the main signature of resonant states in the literature, and the mechanism by which the transport properties are enhanced. The higher the impurity concentration, the bigger and sharper the peak, so we would expect the best thermoelectric performances from the highest concentrations. As we will see shortly, this is not the case. The resonant

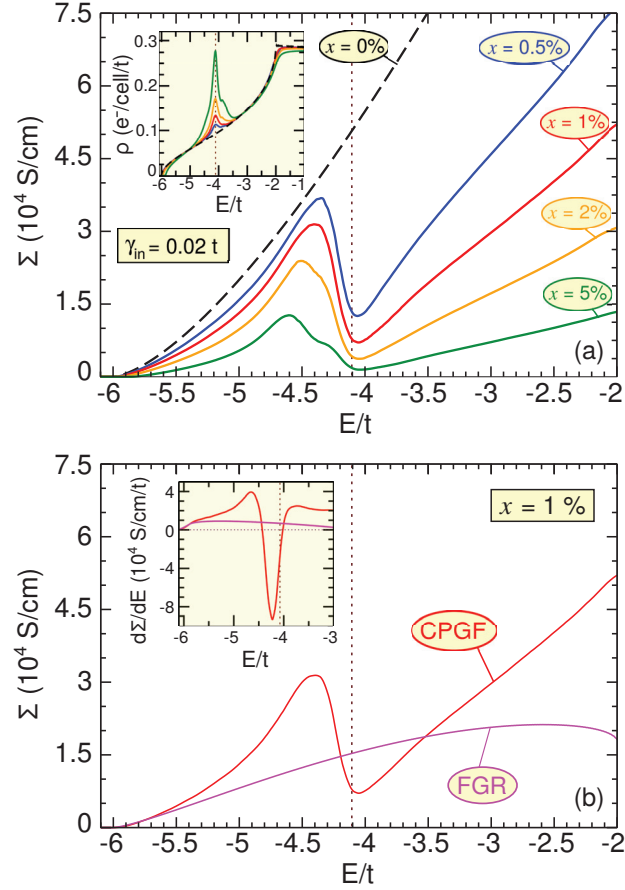


Figure 5.4: From Ref. [274]. (a) Transport distribution function $\Sigma(E)$ and density of states $\rho(E)$ (inset) for five impurity concentrations, from $x = 0\%$ (reference, black dashed line) to $x = 5\%$. A vertical dashed line marks the position of the resonant peak. (b) $\Sigma(E)$ and its derivative (inset) for $x = 1\%$ calculated exactly (CPGF) and by second-order perturbation theory (FGR).

peak gives rise in the TDF to a sharp, asymmetrical dip, as the extended states acquire a more localized character by hybridizing with impurity states. At high defect concentrations, electron transport is more suppressed across the whole energy range so the variations of the TDF are gentler ($|\frac{d\Sigma}{dE}|$ is reduced as x increases). We compare in Fig. 5.4(b) the TDF and $\frac{d\Sigma}{dE}$ calculated by CPGF and by the often used Fermi's Golden Rule (FGR). Matthiessen's rule states that the total scattering rate is $\gamma_{\text{tot}} = \gamma_{\text{imp}} + \gamma_{\text{in}}$ with γ_{imp} the impurity scattering rate. FGR leads to $\gamma_{\text{imp}}(E) = 2\pi x \epsilon^2 \rho_0(E)$, $\rho_0(E)$ being the DOS of the clean system. The FGR transport distribution function is given by $\Sigma_{\text{FGR}}(E) = \frac{\gamma_{\text{in}}}{\gamma_{\text{tot}}} \Sigma^{(0)}(E)$ where $\Sigma^{(0)}(E)$ is the pristine TDF. Notice that the exact $\Sigma(E)$ cannot be cast into such an analytical form. Clearly, the FGR approach completely fails to give the correct dependance of the TDF. In particular, the dip is entirely absent. The discrepancy is even worse for the derivatives, which are directly linked to the Seebeck coefficients. Therefore, when resonant states are involved, second-order perturbation theory breaks down.

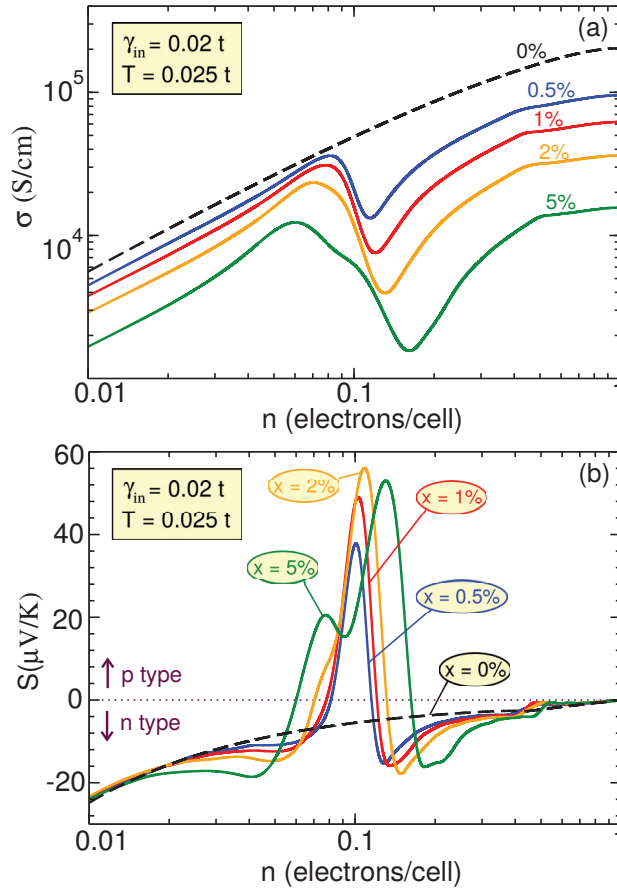


Figure 5.5: From Ref. [274]. (a) Electrical conductivity σ and (b) Seebeck coefficient S as a function of the electron density n for five impurity concentrations, from $x = 0\%$ to $x = 5\%$.

From the results of Fig. 5.4(a), we compute the room-temperature electrical conductivity

σ and Seebeck coefficient S , as plotted in Fig. 5.5 as a function of the electron density n . T is set to $0.025t$ which corresponds to room temperature if $t \approx 1$ eV. σ is reduced by the disorder and still exhibits the same features as $\Sigma(E)$ (T being relatively small). This reduction would be detrimental to the PF, but the sharp variations in the TDF lead to a boost of the Seebeck coefficient that overcompensates the suppression of σ . This is accompanied by a sign inversion of S around $n = 0.1$ electrons/cell. Thus, S can change sign in the disordered systems, while it remains n-type in the absence of resonant states. This interesting feature opens the possibility of changing the thermoelectric material from n-type to p-type just by introducing the appropriate impurity or dopant. Therefore, one could build a device with both n and p legs from the same semiconductor host. This would be advantageous for device performance and reliability, provided that the PF is sufficiently large.

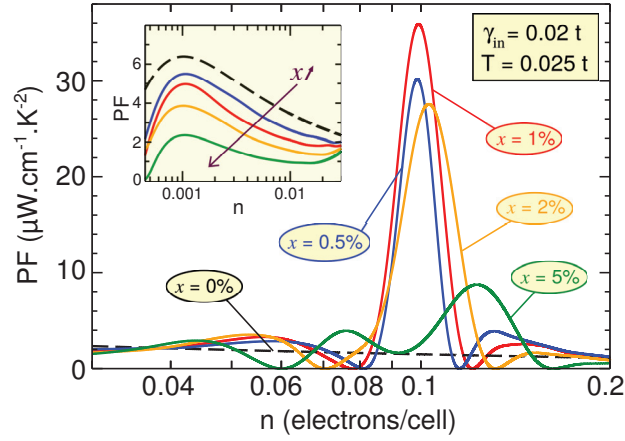


Figure 5.6: From Ref. [274]. Power factor σS^2 as a function of the electron density n for five impurity concentrations, from $x = 0\%$ to $x = 5\%$. Inset: PF for lower electron densities.

The PF is plotted in Fig. 5.6 as a function of n . The pristine system exhibits a maximum of $6.3 \mu\text{W} \cdot \text{cm}^{-1} \cdot \text{K}^{-2}$ around $n = 10^{-3}$ electrons/cell, corresponding to a conductivity of 400 S/cm and a Seebeck coefficient of $-130 \mu\text{V}/\text{K}$. Note that this relatively low value of the power factor is partly due to the absence of band degeneracy and anisotropy in our single-band model. The effects of resonant impurities relative to the pristine case would not be affected by band degeneracy, while the case of anisotropic orbitals will be examined thereafter. When resonant defects are introduced, the PF is suppressed at low densities (inset), because multiple impurity scatterings have a stronger effect on the long wavelength carriers. By contrast, around $n = 0.1$ electrons/cell, the PF now exhibits a large enhancement due to the boost of the Seebeck coefficient that overcompensates the drop in conductivity. The largest increase corresponds to $x = 1\%$, for which the PF reaches its maximum $35.9 \mu\text{W} \cdot \text{cm}^{-1} \cdot \text{K}^{-2}$, a sixfold enhancement compared to that of the clean system. For $x = 5\%$, the boost is still present but less spectacular (a ratio less than 2) due to the gentler variations in the TDF. This is an important and surprising finding: to achieve an efficient enhancement of the thermoelectric properties with resonant states, the defect

	$x = 0\%$	0.5%	1%	2%	5%
$\epsilon = -4t$ $V = 0.3t$	6.3	30.2	35.9	27.6	8.7
$\epsilon = -5.5t$ $V = 0.3t$	6.3	1.3	1.7	1.8	1.8
$\epsilon = -4t$ $V = t$	6.3	0.01	0.05	0.06	0.05

Table 5.1: Room-temperature optimum power factor in $\mu\text{W} \cdot \text{cm}^{-1} \cdot \text{K}^{-2}$ for $\gamma_{\text{in}} = 0.02t$ and several values of the on-site potential and hybridization parameter.

concentration should be kept relatively low, typically around 1%. From an experimental point of view, that is favorable, because such concentrations usually lie below the solubility limit [290]. Co-doping with a donor atom acting as an electron reservoir is necessary to shift the Fermi level inside the resonant peak, where the PF is enhanced and the Seebeck inversion occurs. This carrier density optimization still requires at most 10% co-doping, which is reasonable. We define PF_{max} as the optimum PF with respect to the carrier concentration. PF_{max} extracted from Fig. 5.6 are shown in the first row of table 5.1.

5.1.3 The influence of the model parameters

We now address the influence of both ϵ and V on the transport properties. In Fig. 5.7(a), the DOS and TDF are plotted for $x = 1\%$ resonant impurities with $\epsilon = -5.5t$ and $V = 0.3t$. The increase of the on-site potential shifts the position of the resonant peak much closer to the bottom of the conduction band. The resulting TDF also features a much smaller dip in $\Sigma(E)$ at the position of the peak in $\rho(E)$. Consequently, $|\frac{d\Sigma}{dE}|$ remains quite weak, and so does the Seebeck coefficient. There is still a sign inversion, but no boost in the PF. Indeed it is even suppressed by a factor 3-4 with respect to the reference value of $6.3 \mu\text{W} \cdot \text{cm}^{-1} \cdot \text{K}^{-2}$ (see the second row of table 5.1). Thus the resonant peak should not be too close to the band edge, but deep inside the conduction band. We now focus on the effect of a larger hybridization, which implies a stronger coupling between conduction and defect states. Results are depicted in Fig. 5.7(b). The increase in hybridization also pushes the resonant states at the very edge of the band, and severely suppresses the TDF below $-5t$ (notice the scale in the inset). There is still a small dip in $\Sigma(E)$ and a sign inversion of S , but because the carriers are now so localized in this energy range, the PF shrinks by at least two orders of magnitude compared to that of the reference. For $x = 1\%$, PF_{max} is now $0.05 \mu\text{W} \cdot \text{cm}^{-1} \cdot \text{K}^{-2}$ (see the third row of table 5.1 for the other concentrations). This suppression of the PF is entirely due to a huge reduction in the conductivity caused by multiple scattering events that become important at low energy in the presence of stronger disorder. These findings are consistent with the results obtained in Ref. [273] for Tl-doped PbTe, in which the Tl doping creates a resonant bump at the edge of the valence band associated with a much higher resistivity compared to that of Na doping which behaves as

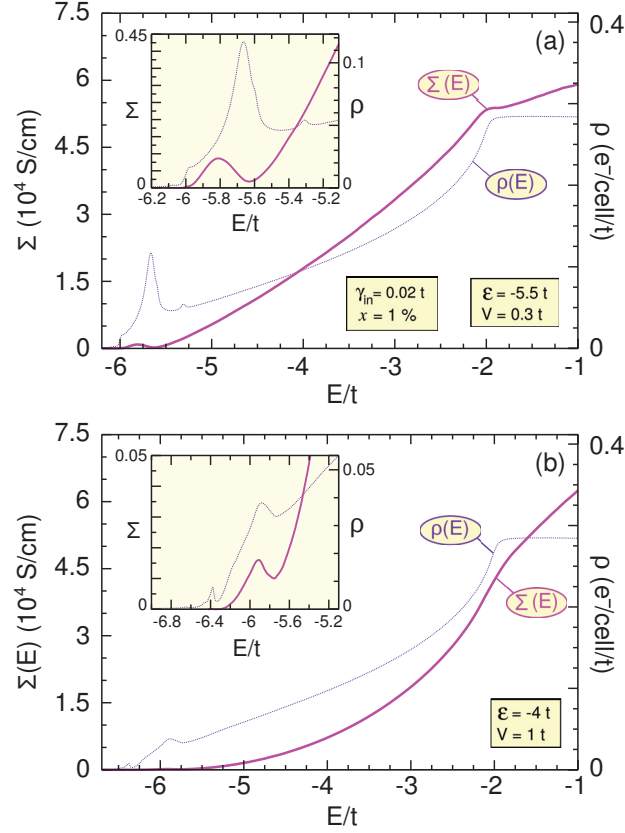


Figure 5.7: From Ref. [274]. Density of states $\rho(E)$ (dotted line, right axis) and transport distribution function $\Sigma(E)$ (left axis) for $x = 1\%$ with (a) $\epsilon = -5.5t$, $V = 0.3t$ and (b) $\epsilon = -4t$, $V = t$. Inset: zoom on the bottom of the conduction band, notice the different scales for the TDF.

a reservoir. It should also be mentioned that resonant states formed by antisites in Fe_2VAl have been found to suppress the PF by more than an order of magnitude while changing the sign of S [291]. The takeaway to obtain a boost of the PF is that the substituting element should be suitably selected in order to create a resonant peak far from the band edge. This could also explain why many claims of experimental enhancement of the PF by resonant states remain controversial, and why no sign inversion of the Seebeck coefficient has been observed so far. These effects are indeed sensitive to the hybridization, on-site potential and position of the Fermi level. Additionally, it is difficult to rule out other enhancement mechanisms, such as energy filtering effects resulting from ionized impurity scattering, for instance.

Since thermoelectric materials are meant to be used in a wide range of temperature, we now discuss the T -dependence of PF_{max} . Fig. 5.8 shows PF_{max} as a function of temperature for the same impurity concentrations as in Fig. 5.6. It increases when the temperature rises, reaching a broad maximum, and then decreases slowly in the disordered systems. This high

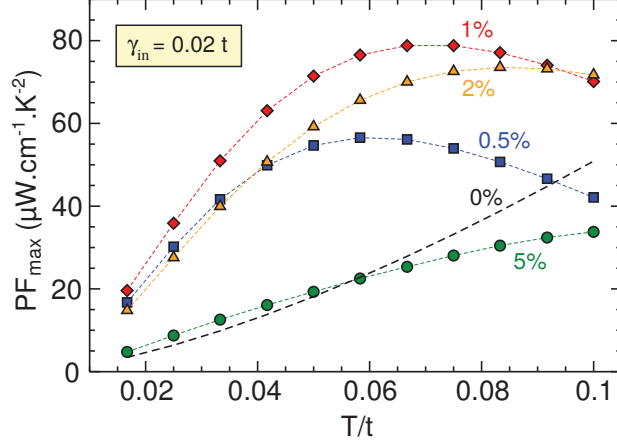


Figure 5.8: From Ref. [274]. Optimum power factor as a function of temperature for five impurity concentrations, from $x = 0\%$ to $x = 5\%$.

temperature behaviour results from the sharp variations in the TDF being smoothed out by the thermal average. Accordingly, at high values of x , the variations in the TDF are broader and are less sensitive to the thermal average, so the maximum region is shifted to higher temperatures. An important finding is that PF_{max} itself is robust, suggesting that resonant states could be efficient for both low and high temperature power generation.

We now propose to investigate the role of inelastic scattering. In Fig. 5.9(a), we plot PF_{max} as a function of γ_{in} . Clearly, the PF is completely suppressed if the inelastic scattering is too strong. This results from the competition between resonant impurity scatterings (elastic processes) and inelastic scatterings. In Fig. 5.9(b) is presented the TDF for $\gamma_{\text{in}} = 0.02t$, $0.08t$ and $0.2t$ with $x = 1\%$. The inset shows the impurity scattering rate γ_{imp} , extracted from an analysis of the single-particle spectral function, defined in section 4.1.1. γ_{imp} exhibits a non-monotonic behavior and large variations across the resonant peak, from $4 \times 10^{-3}t$ at $E = -4.5t$ to $2 \times 10^{-1}t$ at $-4t$. At the position of the dip in the TDF, where the electronic states have a stronger localized character, transport is not very sensitive to the strength of γ_{in} because $\gamma_{\text{imp}} \approx 2 \times 10^{-1}t$ dominates. In contrast, if γ_{imp} is smaller than γ_{in} , which is the case for states associated with large values of the TDF ($\gamma_{\text{imp}} \approx 4 \times 10^{-3}t$ at $E = -4.5t$), then increasing γ_{in} strongly suppresses $\Sigma(E)$. Thus, large inelastic scattering rates have the overall effect of reducing the disparities in the TDF, leading to poor values of the Seebeck coefficient. If we now consider small values of γ_{in} (below $0.03t$) for $x \leq 2\%$, we observe a huge increase of PF_{max} as γ_{in} is reduced. If we extrapolate to $\gamma_{\text{in}} \leq 0.02t$ for $x = 1\%$, an enhancement factor of more than an order of magnitude could even be reached. Hence, due to the competition between elastic and inelastic scattering, the impurity concentration should be tuned with respect to the inelastic scattering rate in the host material to reach an optimal boost of the PF. Compounds exhibiting strong e-ph or e-e scattering should not be the best candidates for resonant substitution doping.

Till now, we have been considering an isotropic electronic structure (s-type orbitals), but it is worth considering the influence of orbital anisotropy [292, 278]. Low-dimensional

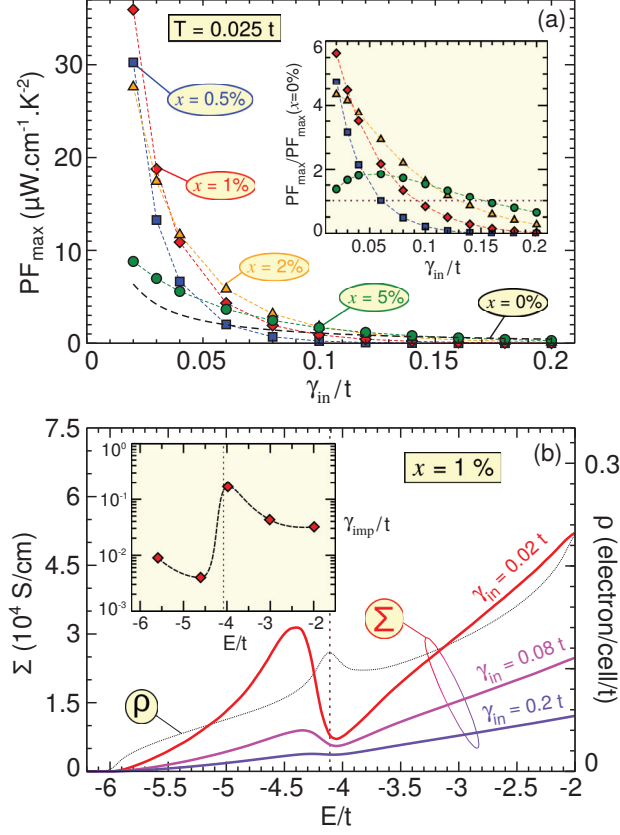


Figure 5.9: From Ref. [274]. (a) Optimum power factor as a function of the inelastic scattering rate γ_{in} for five impurity concentrations, from $x = 0\%$ to $x = 5\%$. Inset: Ratio of the optimum power factor with respect to that of the clean system. (b) $\Sigma(E)$ for $x = 1\%$ with $\gamma_{\text{in}} = 0.02t$, $0.08t$ and $0.2t$ (left axis). $\rho(E)$ is also shown (dotted line, right axis). A vertical dashed line marks the position of the resonant peak. Inset: the calculated impurity scattering rate along the Γ -X direction as a function of energy. The dashed curve is a guide to the eye.

confinement is expected to introduce sharp structures in the DOS and thus sharp variations in the TDF, thereby boosting the Seebeck coefficient. To evaluate the gain in the PF that could be obtained from resonant states in anisotropic systems, we now introduce a different hopping t_{\perp} in a direction perpendicular to transport. The optimum PF for the reference $x = 0\%$ and for $x = 1\%$ is presented in Fig. 5.10 as a function of t_{\perp}/t . First notice that the PF of the pristine system strongly increases with the anisotropy, from $6.3 \mu\text{W} \cdot \text{cm}^{-1} \cdot \text{K}^{-2}$ (3D) to $73.3 \mu\text{W} \cdot \text{cm}^{-1} \cdot \text{K}^{-2}$ (2D). This confirms that two-dimensional confinement in itself does favor good performances. The maximum PF (p-type) for $x = 1\%$ also increases with the anisotropy, from $35.9 \mu\text{W} \cdot \text{cm}^{-1} \cdot \text{K}^{-2}$ (3D) to $74.4 \mu\text{W} \cdot \text{cm}^{-1} \cdot \text{K}^{-2}$ (2D). Surprisingly, for $t_{\perp} = 0$ we find no boost in the PF, suggesting that the presence of resonant states in fully confined systems might not further enhance the thermoelectric properties. However,

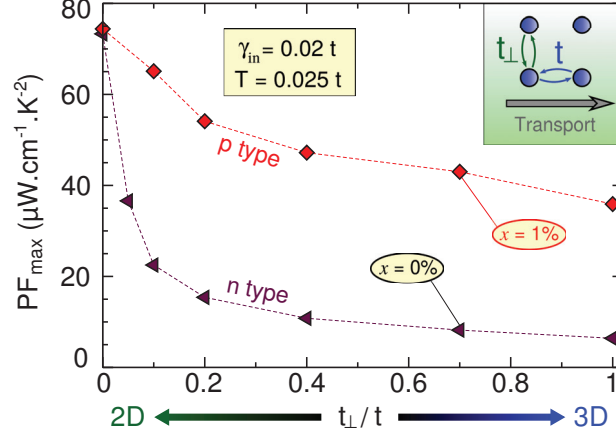


Figure 5.10: From Ref. [274]. Optimum power factor as a function of the anisotropy ratio t_{\perp}/t for $x = 0\%$ (reference) and $x = 1\%$.

one should emphasize that even for finite but low ratios t_{\perp}/t (down to 0.05), the PF can be significantly increased by resonant states. This is promising for bulk systems in which charge carriers populate highly anisotropic orbitals. This is, for instance, the case of n-doped SrTiO₃, in which the Titanium 3d orbitals exhibit a $t_{\perp}/t \approx 0.1$ [293, 166]. Moreover, using resonant states in fully confined materials could be interesting for the sign inversion of S alone.

To conclude, we have used the Chebyshev-Polynomial Green's Function method to address the effects of resonant impurities on electron transport. Although resonant states suppress the electrical conductivity, they may also lead to a boost and a sign inversion of the Seebeck coefficient. Consequently, the power factor can increase by one order of magnitude. However, the resonant peak should be located far from the band edge, otherwise the thermoelectric performances are destroyed. Additionally, the optimal boost of the power factor depends crucially on the interplay between elastic and inelastic scattering. Strong electron-phonon or electron-electron scattering are found to preclude the possibility of enhancing thermoelectric transport. Therefore, materials featuring long electron mean free paths and weak inelastic scattering, such as PbTe [281], certain Half-Heuslers compounds [286] or even graphene [294, 295] should be promising candidates. Finally, the resonant boost of the power factor is found robust in the case of anisotropic orbitals. This study will hopefully contribute to a better understanding of resonant states in the context of thermoelectric power generation.

5.2 Ab initio investigation of the role of vanadium impurity states in SrTiO₃ for thermoelectricity

As we have seen in chapter 3, oxide TE materials have the advantages of being non-toxic, earth-abundant, low-cost and chemically stable. The perovskite material SrTiO₃

(STO) is particularly interesting because it has already a relatively large power factor of the order of $39 \mu\text{W.cm}^{-1}.\text{K}^{-2}$ [196], that is comparable to that of the best known TE materials such as Bi_2Te_3 [192]. However, because of its relatively high thermal conductivity of $\kappa \approx 11 \text{ W.m}^{-1}.\text{K}^{-1}$ [169], STO exhibits a relatively modest ZT of only 0.1, unlike Bi_2Te_3 which has a κ around $1.6 \text{ W.m}^{-1}.\text{K}^{-1}$ and a $ZT \simeq 0.96$ [296, 297]. Herein, we report on the theoretical basis of *ab initio* calculations the promising use of vanadium to dope STO which advantageously exhibits resonant states leading to a large boost of the Seebeck coefficient.

5.2.1 Computing the thermoelectric properties

In what follows, the TE properties are calculated using the Landauer formalism combined with *ab initio* calculations. In the linear response regime, the electrical conductance and the Seebeck coefficient can be written as:

$$G = -\frac{2e^2}{\hbar}L_0, \quad S = -\frac{1}{k_B T}L_1/L_0, \quad (5.7)$$

with

$$L_n = \int_{-\infty}^{+\infty} (E - E_F)^n \tilde{T}(E) \left(\frac{\partial f}{\partial E} \right) dE, \quad (5.8)$$

where T is the temperature, E_F the Fermi level, f the Fermi distribution and $\tilde{T}(E)$ the energy dependent transmission. For a conductor of length l_z , the transmission can be recast as $\tilde{T}(E) = \frac{\lambda(E)}{l_z} M(E)$, where $\lambda(E)$ is the mean free path and $M(E)$ the density of modes (DOM) (see Ref. [155] and section 2.2.2). For this work, we have used a constant mean free path approximation [298] i.e. $\lambda(E) = \lambda_0$ with $\lambda_0 \simeq 20 \text{ \AA}$ which reproduces the room-temperature resistivity measured in 10 % La-doped STO samples [166, 192, 196]. The DOM can be evaluated by a direct diagonalization of the Hamiltonian of the system using the eigenvalues (see for instance Ref. [160]). This DOM corresponds to a count of the bands intersecting the energy of interest. Finally, the electrical conductivity is defined as $\sigma = \frac{l_z}{l_x \times l_y} G$, where l_x and l_y are the dimensions of the system perpendicular to the transport direction.

The *ab initio* calculations are performed with the DFT package SIESTA [112]. This code is very well suited to study oxides as it is based on atomic like orbitals. We have used the Perdew, Burke & Ernzerhof [123] exchange-correlation functional corresponding to a generalized gradient approximation. A Troullier-Martin norm-conserving pseudopotentials [191] has been used. The basis corresponds to a double- ζ -polarized basis optimized with the simplex tool of the SIESTA package. All the atomic structures were optimized up to forces less than 0.01 eV/\AA and to an hydrostatic pressure less than 0.1 kbar. Finally, a Monkhorst-pack of $6 \times 6 \times 6$ k-points has been used for the self consistent calculations ($80 \times 80 \times 80$ for the transport calculations) along with a mesh cutoff of 400 Ry.

5.2.2 vanadium doping

In Fig. 5.11 is given the band structure along with the density of states (DOS) of pristine STO and vanadium doped STO. As pointed out in section 3.1 the lowest conduction bands

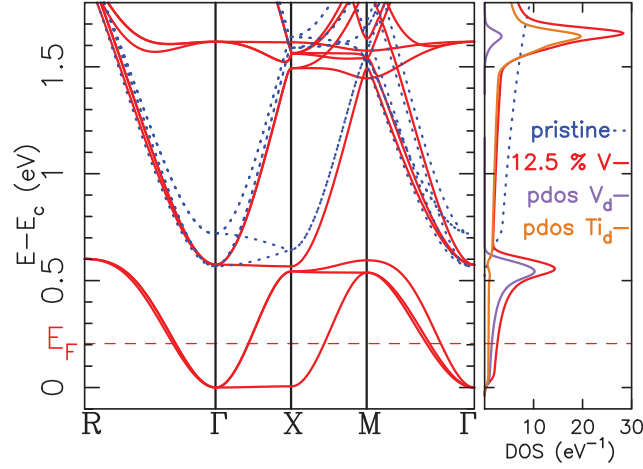


Figure 5.11: From Ref. [279]. Band structure and density of states for pristine SrTiO_3 and $\text{SrTi}_{0.875}\text{V}_{0.125}\text{O}_3$ along with its projected density of states for the d orbitals of V and Ti as function of the energy (centered relatively to the bottom of the conduction band of $\text{SrTi}_{0.875}\text{V}_{0.125}\text{O}_3$ and denoted E_c).

of pristine STO are mainly due to the d -type orbitals of Ti (namely, it corresponds to t_{2g} orbitals). When doped with vanadium (in substitution of a Ti atom), the crucial issue is the occurrence of impurity bands at the bottom of the conduction bands. As illustrated by the projected density of states, these bands are mainly due to the d orbitals of V and, as can be seen, they are acting as resonant states. Indeed, they are in close vicinity of the t_{2g} bands and this is leading to a large increase of the DOS and, as pointed hereafter, of the Seebeck coefficient. However, in order to use these resonant states for TE application, the Fermi level must be in close vicinity of them. For the vanadium concentration used in Fig. 5.11, the Fermi level is definitely located far from the resonant region. This point raises the need to fill the conduction bands up to the resonant states either by means of a device based on a field effect or by using a co-dopant that would shift the Fermi level.

In Fig 5.12 is represented the electrical conductivity σ , the Seebeck coefficient S and the power factor (PF) $\sigma \cdot S^2$ using a rigid band shift model for n-type doping. This model, which consists in moving rigidly the Fermi level, illustrates the equivalent effect of a field effect device. As a guide to the eyes, we have added at the top of the figure the corresponding equivalent doping of lanthanum in the hypothesis of a perfect electron reservoir. We have investigated the pristine case (undoped STO) and STO doped with vanadium for 2 different concentrations. It should be noted that the abscissa corresponds to the added carrier charge with respect to the neutral material. It is obtained by integrating the DOS from the Fermi level. For this reason, the conductivity for V doped STO at zero added carrier charge has a non-zero value. Conversely, for pristine STO the conductivity is exactly zero at zero added carrier charge.

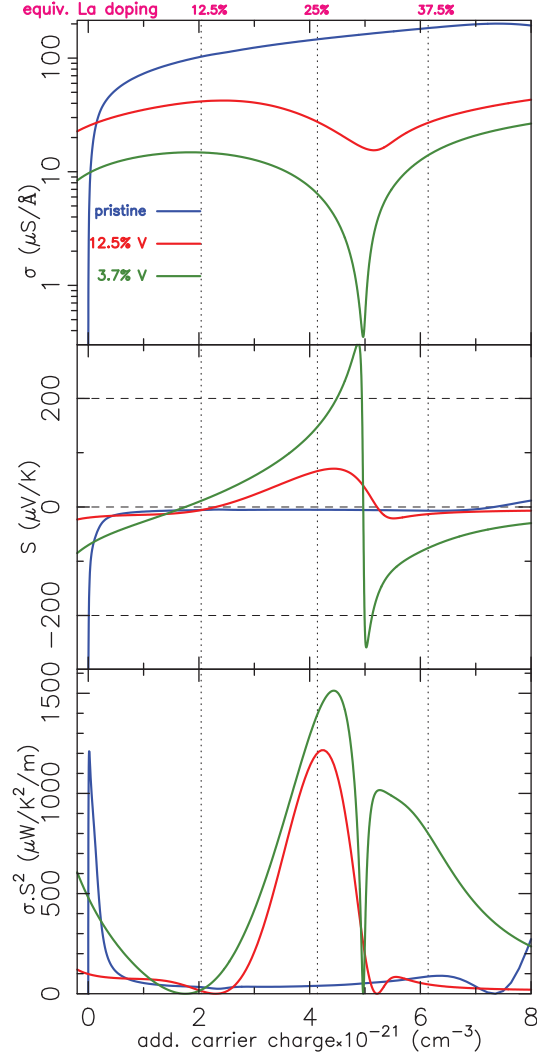


Figure 5.12: From Ref. [279]. From top to bottom, electrical conductivity, Seebeck coefficient and power factor obtained with a rigid band shift model for pristine and V doped STO as function of the added carrier charge to the neutral material. On top is given the theoretical equivalent La co-doping required to achieve the corresponding added carrier charge.

For pristine STO the behavior is quite conventional. As a matter of fact, the conductivity increases with the added carrier charge and the Seebeck coefficient is negative and decreases with the added carrier. This is leading to the familiar behavior for the PF with a sharp peak linked with the two opposite trends of S and σ .

For doped STO, the behavior is completely different. The major effect occurs for the Seebeck coefficient which exhibits a sign inversion close to the resonant states. This point, as

we have already pointed out in a previous work [276], is opening tremendous perspectives for obtaining both n and p-type TE materials using the same dopant. Moreover, for a concentration of 3.7%, the amplitude of the Seebeck coefficient (at the maximum of the PF) is of the same amplitude that pristine STO. One can argue that the increase of the Seebeck comes with a decrease of the conductivity, but as the PF depends on the square of the Seebeck coefficient, the resulting PF is as large as that of the pristine material. Finally, it should be noted that the range of the carrier charge, for which these large values of the PF are observed with V doped STO, is much greater than the pristine case.

5.2.3 Co-doping

Another way to fill the conduction band up to the resonant state could come from a second dopant which would act as an electron reservoir for STO *i.e.* which would lead to a significant charge transfer without modifying the band structure. Actually, La in substitution to Sr appears to be a very good candidate for electron doping in STO [166]. For instance, this reservoir behavior is also observed with yttrium and niobium doping [299, 198]. The whole strategy is thus to use vanadium to create resonant states and to use a co-dopant as an electron reservoir in order to fill the conduction band up to these resonant states. However, it is definitely not obvious that for STO doped with both vanadium and a co-dopant the particular behavior pointed out previously will be preserved.

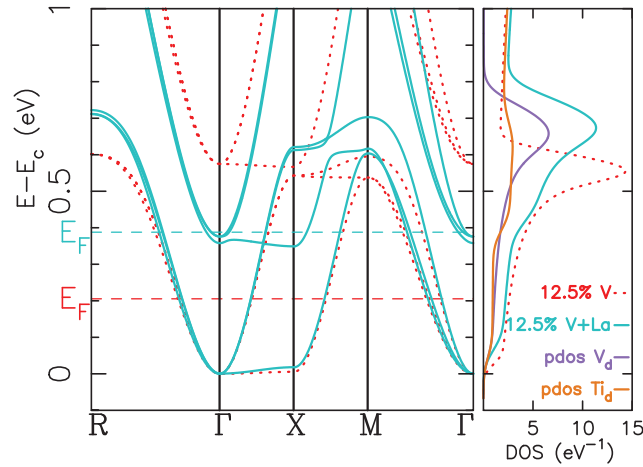


Figure 5.13: From Ref. [279]. Band structure and density of states (DOS) for $\text{SrTi}_{0.875}\text{V}_{0.125}\text{O}_3$ and $\text{Sr}_{0.875}\text{La}_{0.125}\text{Ti}_{0.875}\text{V}_{0.125}\text{O}_3$ along with its projected density of states for the d orbitals of V and Ti as function of the energy (centered relatively to the bottom of the conduction band).

In Fig. 5.13 is given the band structure along with the DOS of co-doped STO with V and La. We have also represented the band structure of STO doped only with V (same as in Fig. 5.11) for comparison purposes. It can be noticed that La has not a neutral role

when combined with V. The impurity bands induced by vanadium are still observed, but these bands are shifted at higher energy and are actually overlapping with the t_{2g} bands. Indeed, at the top of the impurity bands, we have now a clear mix with the intrinsic bands of STO. This behavior is very specific to the co-doping and for a doping with La alone, we have verified that the band structure of pristine STO is preserved *i.e.* that La is an electron reservoir. This mixing (or pinning) of the impurity bands with the t_{2g} ones has an influence on the resonant state as can be seen on the DOS. First, the resonant states are now shifted at higher energy and second, the amplitude of the DOS is reduced compared to the case where V is used alone. As presented hereafter, the amplitude of the Seebeck coefficient at the resonant states is affected too by this phenomenon.

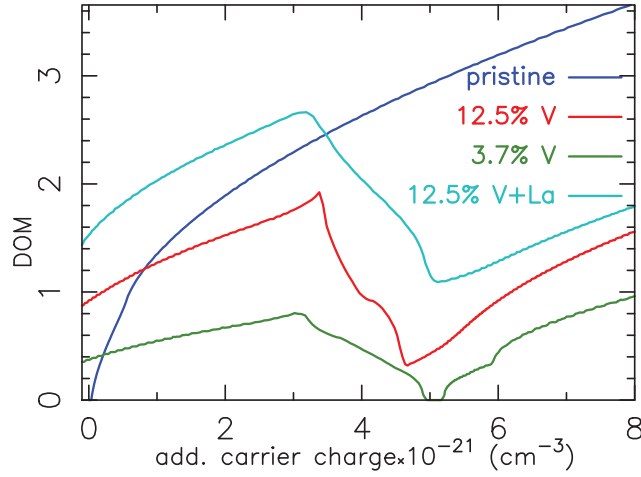


Figure 5.14: From Ref. [279]. Density of modes (DOM) for pristine SrTiO_3 , $\text{SrTi}_{1-x}\text{V}_x\text{O}_3$ ($x = 12.5\%$ and 3.7%) and $\text{Sr}_{0.875}\text{La}_{0.125}\text{Ti}_{0.875}\text{V}_{0.125}\text{O}_3$ as function of the added carrier charge to the materials.

In order to have some insights on the effects associated with the co-doping, the DOM for pristine STO, V doped STO and co-doped STO with V and La are presented in Fig. 5.14. First of all, the sign inversion of the Seebeck coefficient pointed out previously (see Fig. 5.12) for V doped STO is actually directly linked with the slope inversion of the DOM. For pristine STO, the slope is strictly positive and thus the sign of the Seebeck coefficient remains constant. Conversely, for V doped STO this slope exhibits an inversion which is fully related to the resonant states induced by the vanadium. This phenomenon is observed for all doping concentrations and also when a co-dopant is introduced. However, a close examination of the expression of the Seebeck (see equation (5.7) and (5.8)) leads us to the conclusion that, in order to obtain a large Seebeck coefficient, we both need a negative slope for the DOM and a slope transition which tends as close as possible to zero. This situation is achieved for STO solely doped with V when the dopant concentration is small enough. For co-doped STO we obtain a negative slope almost equivalent but, due to the

pinning of the impurity bands with the t_{2g} bands, the DOM does not tend to zero. For this reason, and as presented hereafter, the amplitude of the Seebeck coefficient for co-doped STO is smaller than that of STO doped with V only.

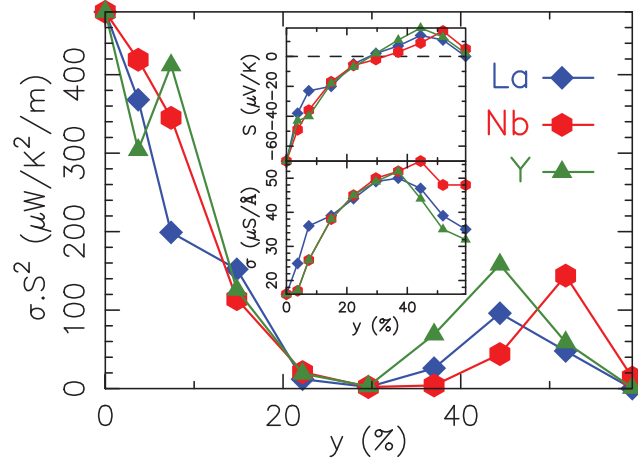


Figure 5.15: From Ref. [279]. Power factor for $\text{Sr}_{1-y}\text{La}_y\text{Ti}_{1-x}\text{V}_x\text{O}_3$, $\text{Sr}_{1-y}\text{Y}_y\text{Ti}_{1-x}\text{V}_x\text{O}_3$ and $\text{SrTi}_{1-x-y}\text{V}_x\text{Nb}_y\text{O}_3$ with $x = 3.7\%$ as function of the co-dopant concentration. The Seebeck coefficient and the conductivity are given in inset.

In Fig. 5.15 is given the PF (the Seebeck and the conductivity are in inset) for co-doped STO. It corresponds to a vanadium concentration of 3.7% which has been observed to be the best choice to take benefit of the resonant states. The concentration of the co-dopant is ranging from 0 to almost 60%. We have considered three different co-dopants (La, Nb and Y) which all have been observed experimentally to be electron dopants for STO [299, 198]. However, as can be seen in this figure, all of them are leading to a very similar behavior.

The Seebeck coefficient is behaving in a rather close way to what we have already observed in Fig. 5.12, that is to say a sign which can be either positive or negative depending on the co-dopant concentration. For small co-dopant concentration, we have a negative sign for the Seebeck (as conventionally observed for electron doping) but for large concentration the Seebeck coefficient tends to zero and becomes positive. This behavior has a direct impact on the PF.

For low co-dopant concentration, the PF decreases when the co-dopant concentration increases. It goes to zero when the Seebeck coefficient sign reverses and finally increases and reaches a second maximum but now with a positive Seebeck coefficient for large co-dopant concentration. This behavior is actually opening the perspective to obtain both n and p type TE materials doped with exactly the same dopants. In this paradigm, the n or p nature is chosen by modifying only the co-dopant concentration. However, due to the pinning effect mentioned previously, further investigations are required in order to improve the amplitude of the Seebeck coefficient and thus of the PF.

In the present work, the mechanism for SrTiO₃ doped with vanadium based on resonant states to boost the power factor has been presented. This mechanism, conversely to the accepted picture of a boost of the density of states, is linked with a reduction of the conductivity together with a boost of the Seebeck coefficient against all odds. This result opens the perspective to use only a single dopant to obtain both n and p type semiconductor for thermoelectricity thanks to the sign inversion of the Seebeck coefficient observed in the vicinity of the resonant peak. Moreover, by using co-dopant such as La, Nb or Y, an actual sign inversion of the Seebeck coefficient is observed by modifying the co-dopant concentration of the compound. However, the power factor amplitude is less significant than that observed within a rigid band shift which indicates that these co-dopants are no more simple electron reservoirs in V doped SrTiO₃.

5.3 Resonant states and vanadium doping in SrTiO₃, BaTiO₃ and CaTiO₃: effects of disorder and localization on the thermoelectric properties

The previous section investigates vanadium doping in SrTiO₃ through a DFT supercell study, and consequently it does not include any disorder effect associated with the random distribution of V atoms. Since the bottom of the SrTiO₃ conduction band is strongly affected by the V-doping, these effects are expected to be important and can even lead to Anderson localization. In this section, we combine the CPGF methodology used in section 5.1 with the realistic tight-binding Hamiltonian for the conduction band of SrTiO₃ presented in section 3.1 and with a simple modelization of V substitution doping, both obtained through Wannier projections of DFT calculations. We then investigate the influence of different impurities on the class of perovskite oxides SrTiO₃, BaTiO₃ and CaTiO₃ by exploring the range of modelization parameters.

5.3.1 Anderson localization from vanadium doping in SrTiO₃

The first step is to model the substitution of a Ti atom by a V atom in terms of tight-binding parameters. To that end, Wannier projections on the Ti and V 3d orbitals of a $2 \times 2 \times 2$ supercell of SrTiO₃ containing one V atom (12.5% doping) are performed using the Wannier90 software [128] interfaced with the SIESTA package [112]. The DFT simulation parameters are the same as in section 5.2. The matrix elements of the Kohn-Sham Hamiltonian on the Wannier basis are then compared with the hopping terms of pristine SrTiO₃. The main difference is found to be an on-site potential $\epsilon = -1.4$ eV on the orbitals of the V atom, while the hopping terms and on-site potentials of the neighboring atoms are little affected. Therefore, we retain only this potential ϵ in order to preserve the simplicity of the tight-binding Hamiltonian. To test the validity of this approximation, we show in Fig. 5.16 the DOS and TDF calculated for the $2 \times 2 \times 2$ supercell containing one V atom with either the full DFT Hamiltonian or the model Hamiltonian including only the on-site potential ϵ . The TDF is calculated from the Boltzmann transport equation

assuming a constant mean-free path of 20 \AA as in section 5.2. In both calculations, the DOS exhibits a peak near the bottom of the band due to the V impurities, although it is somewhat sharper in the full *ab initio* case. The TDF predicted by the model is very close to that predicted by DFT. It features in particular the same maximum at the energy of the peak, although the downward slope is slightly smoother than predicted by DFT. This confirms that the essential physics of V substitution is captured by the model Hamiltonian, thus validating our approach.

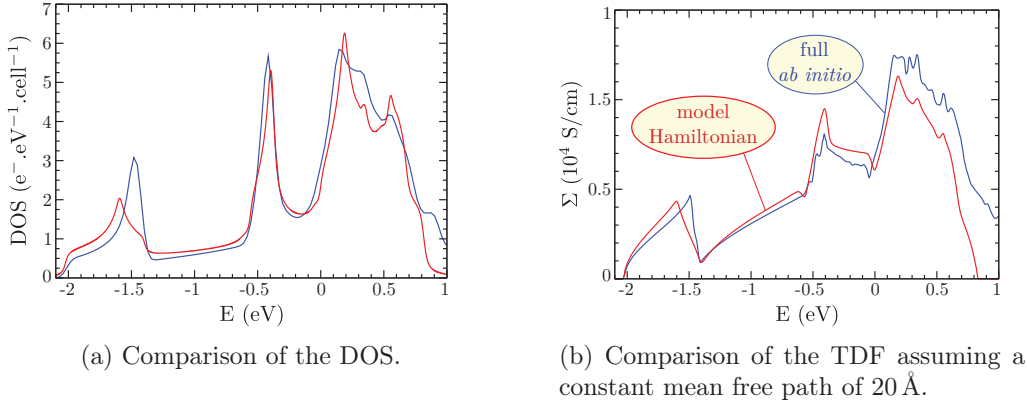


Figure 5.16: From Ref. [280]. Comparison of the DOS and TDF of a 12.5% V-doped SrTiO_3 supercell between fully *ab initio* calculations (thick blue line) and the model Hamiltonian (thin red line).

Now in possession of a realistic tight-binding Hamiltonian for both pristine SrTiO_3 and the substitution of a Ti atom by a V atom, we can study the electronic structure and transport properties of a SrTiO_3 crystal containing an arbitrary concentration x of randomly distributed V atoms. We use the Chebyshev polynomial Green's function method (CPGF) and in addition we perform exact diagonalizations (ED) of the Hamiltonian, two complementary approaches that allow for an exact treatment of disorder (see section 4.3). The CPGF method is based on an expansion on the Chebyshev polynomial basis of the electron Green's function

$$\hat{G}(E) = \frac{1}{E - \hat{H} + i\frac{\gamma_{\text{in}}}{2}}, \quad (5.9)$$

where \hat{H} is the full disordered tight-binding Hamiltonian and γ_{in} can be interpreted as an inelastic scattering rate. The TDF is calculated from the Kubo formula

$$\Sigma(E) = \frac{\hbar e^2}{\pi \Omega} \langle \text{Tr}(\text{Im} \hat{G}(E) \hat{v}_x \text{Im} \hat{G}(E) \hat{v}_x) \rangle, \quad (5.10)$$

where Ω is the volume of the system, \hat{v}_x is the velocity operator along the x direction and the brackets denote disorder averaging. The trace is evaluated by a stochastic average involving N_r random vectors as described in section 4.3.2. The transport calculations are performed on systems of size $N = 900 \times 180 \times 180$ ($\approx 30 \times 10^6$ sites) with 2000×2000

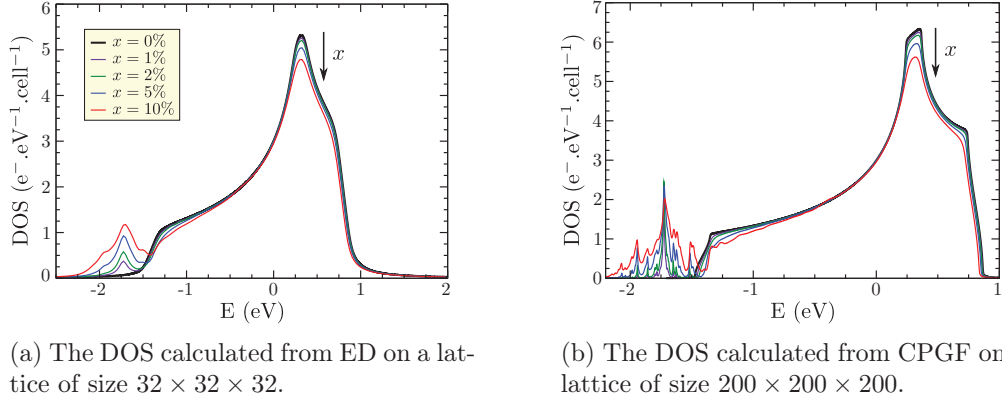


Figure 5.17: From Ref. [280]. The DOS for V-doped SrTiO_3 (x from 0% to 10%) calculated from (a) ED and (b) CPGF. The thick black line is the reference ($x = 0\%$).

moments included in the Chebyshev expansion. For such system sizes, only one disorder configuration and 20 random vectors are enough to get converged values of the TDF. Exact diagonalization of the Hamiltonian is limited to much smaller systems of size $L^3 \approx 30^3$ but gives access to the eigenstates $|\mu\rangle$ and to the eigenvalues ϵ_μ . From ED we can evaluate the diffusivity $D(E) = \Sigma(E)/e^2\rho(E)$ (with $\rho(E)$ the DOS per unit volume) in the absence of inelastic scattering. The Kubo formalism gives an expression for the diffusivity D_μ of the eigenstate $|\mu\rangle$ (see section 4.3.1)

$$D_\mu = \pi\hbar \sum_\nu |\langle\mu|\hat{v}_x|\nu\rangle|^2 \delta(\epsilon_\mu - \epsilon_\nu). \quad (5.11)$$

In order to estimate the thermodynamic limit, each delta peak $\delta(\epsilon_\mu - \epsilon_\nu)$ is broadened into a lorentzian of half-width equal to twenty-five times the average level separation in an energy range around ϵ_μ . The D_μ are then averaged over an energy interval of 25 meV. All transport calculations are performed in the x direction on the xy orbital only, and the spin degeneracy and equivalent contribution of the xz orbital are taken into account by a factor 4. The yz orbital conduction can safely be neglected due to the very low yz hopping in the x direction (see section 3.1). Periodic boundary conditions are used in all directions to reach the thermodynamic limit more easily.

Fig. 5.17 shows the DOS calculated from ED and the CPGF method. The much greater system sizes reachable through the CPGF method allow for a much better resolution of the structures in the DOS. It is clear, in particular, that impurity states are created approximately 0.2 eV below the bottom of the SrTiO_3 conduction band for 1% and 2% V-doping. As the doping concentration is increased ($x = 5\%$ and $x = 10\%$), these defect states merge with the main conduction band. Thus, V-doping in SrTiO_3 does not result in proper resonant states, rather they have the character of shallow impurity states.

In Fig. 5.18 is shown the diffusivity as a function of the Fermi level, calculated from ED and CPGF. The CPGF calculation is performed with a low inelastic scattering $\gamma_{\text{in}} = 5$ meV

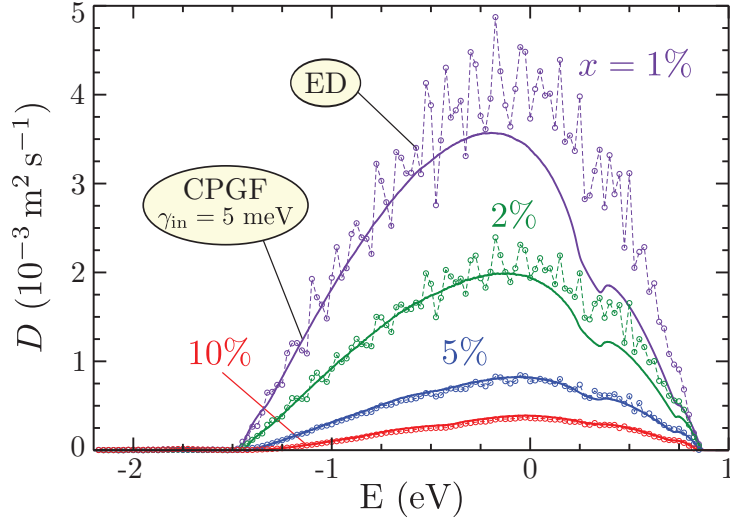


Figure 5.18: From Ref. [280]. The zero-temperature diffusivity as a function of the Fermi level for V-doped SrTiO₃ (x from 1% to 10%) calculated from ED (dots) and CPGF (solid lines). The ED diffusivity is calculated on a lattice of size $32 \times 32 \times 32$, while the CPGF diffusivity is calculated with an inelastic scattering rate $\gamma_{\text{in}} = 5 \text{ meV}$.

for comparison with ED. Note that investigating lower values of $\gamma_{\text{in}} = 5 \text{ meV}$ is possible but would have required the inclusion of more terms in the expansion of the Green's function on the Chebyshev polynomials basis, leading to a greater computation time and memory usage. The diffusivities predicted by the two methods are in very good agreement, especially for high values of the V concentration, which confirms the validity of the results obtained from the CPGF method. For smaller values of x (1% and 2%), finite size effects are prominent in the ED diffusivity due to the small size ($32 \times 32 \times 32$) of the lattice. The small discrepancies between the two methods at high energy are most likely due to the presence of the inelastic scattering γ_{in} in the CPGF results which, although small, still influences the transport properties for $x = 1\%$ and $x = 2\%$ far from the bottom of the conduction band. As can be expected, the diffusivity is found to decrease with the V-doping concentration due to a more intense electron-defect scattering. The energy region below -1.5 eV , corresponding to the impurity states, exhibits almost no conduction, suggesting that the defects states are entirely localized even for $x = 10\%$.

In order to confirm the Anderson localization of the impurity states and estimate the position of the mobility edges, we perform a finite size study of the inverse participation ratio (IPR) calculated from the eigenstates obtained through ED (see section 4.3.1, equation (4.30)). For extended states, the IPR is expected to decrease as $1/L^3$ as the system size increases, while for localized states with a localization length ξ it is expected to converge towards a finite value around $1/\xi^3$. We plot the cubic root of the IPR (averaged over 25 meV) as a function of the inverse length of the system $1/L$ for several Fermi levels: an

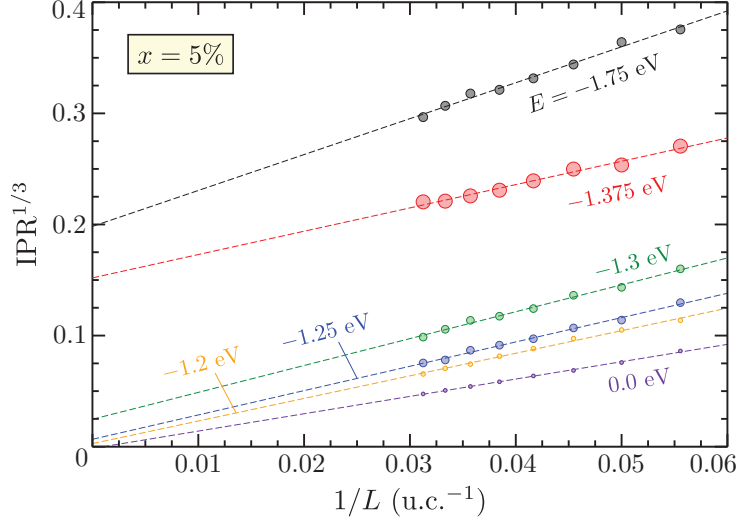


Figure 5.19: From Ref. [280]. The cubic root of the IPR as a function of the inverse length of the system for 5% V-doped SrTiO₃ at several Fermi levels. The IPR is averaged over 25 meV. The size of the symbols are a rough estimate of the error bars. Linear fits of the IPR are shown as dashed lines: the values for $1/L = 0$ correspond approximately to the inverse of the localization length.

example of such plot is shown in Fig. 5.19 for $x = 5\%$. Linear fits of the IPR, shown as dashed lines, indicate the localized or extended character of states since their values for $1/L = 0$ give an estimate of the localization length ξ . The case $E = -1.75$ eV, corresponding to the middle of the impurity states, shows a clear Anderson localization with $\xi \approx 5$ unit cells, confirming the localized character of the defect states even for $x = 5\%$. Conversely, the states at the middle of the conduction band ($E = 0$ eV) are clearly extended (infinite value for the localization length). The crossover between these two behaviors happens around $E = -1.25$ eV and $E = -1.2$ eV, which gives an estimate of the mobility edge, $E_c \approx -1.225$ eV, for $x = 5\%$. Similarly, the mobility edges are estimated to be $E_c \approx -1.425$ eV for $x = 1\%$, $E_c \approx -1.375$ eV for $x = 2\%$ and $E_c \approx -1$ eV for $x = 10\%$. The localized regions of the DOS, as predicted by the IPR, are shown as greyed areas in Fig. 5.20. Also shown are the typical DOS, defined as the geometrical average of the local DOS, which is an order parameter for the Anderson transition at zero temperature and in the absence of inelastic scattering (see section 4.3.2, equation (4.40)). It is calculated here on lattices of size $160 \times 160 \times 160$, with an average performed over 6 disorder configurations and 100 lattice sites per configuration, and a small value $\gamma_{\text{in}} = 0.5$ meV that requires 30000 terms in the expansion of the Green's function on the Chebyshev polynomials basis. The typical DOS is much smaller than the average DOS in the impurity states region, again confirming the localization of these states. Due to the inelastic scattering term and the finite size of the lattice, it does not exhibit a critical behavior at the mobility edge. For this

value of γ_{in} , the localized region corresponds roughly to the energies for which the typical DOS falls below $\approx 50\%$ of the average DOS. The IPR, by contrast, does not contain any inelastic scattering and therefore allows for a more precise determination of the mobility edges.

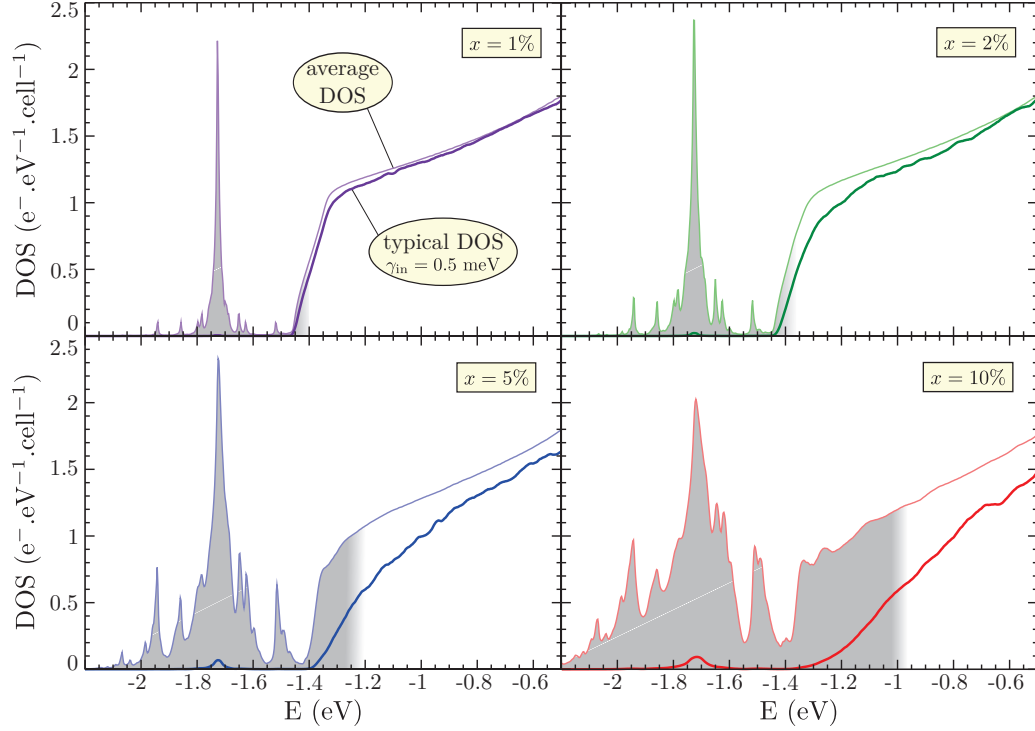


Figure 5.20: From Ref. [280]. The typical DOS (thick solid lines) and the average DOS (thin solid line) calculated from CPGF for V-doped SrTiO_3 (x from 1% to 10%) with the greyed regions indicating the localized part of the spectrum as predicted by the IPR. The typical DOS is calculated on a lattice of size $160 \times 160 \times 160$ with an inelastic scattering rate $\gamma_{\text{in}} = 0.5 \text{ meV}$.

We now calculate the room-temperature thermoelectric transport properties for V-doped SrTiO_3 from the CPGF method. At room temperature, strong electron-electron scattering dominates the transport properties in the clean compound (see section 3.1). To keep our modelization simple, we set $\gamma_{\text{in}} = 130 \text{ meV}$, a reasonable value that gives the correct electrical conductivity in Nb or La doped SrTiO_3 for an electron concentration $n = 10\%$. In Fig. 5.21a, we plot the TDF for a vanadium concentration from 0% (reference, the thick black line) to 10%. Again, we find that the TDF decreases with increasing V concentration due to stronger electron-defect scattering. A small but finite conduction can also be observed at energies corresponding to the localized impurity states. This is due to the presence of strong inelastic scattering acting as a dephasing mechanism, partly destroying the quantum interferences and thus counteracting the effects of Anderson localization.

As shown in the inset for the $x = 10\%$ case, lowering the inelastic scattering rate actually decreases the TDF in this region, in violation of Matthiessen's rule that would predict an increase of the conduction. In Fig. 5.21b is shown the power factor (PF) and the electrical conductivity (in inset) as a function of the carrier concentration. Although the localization effects are partly destroyed by the inelastic scattering, the conductivity in V-doped systems shows a clear crossover between a low-conductivity region, corresponding to the impurity states, and a high-conductivity region associated with extended states of the conduction band, while the reference case (clean SrTiO₃) exhibits no such behavior. As a consequence, the PF is strongly suppressed (by more than an order of magnitude with respect to the reference case) when the Fermi level lies in the impurity states region. Therefore, introducing vanadium impurities in SrTiO₃ actually turns out to be extremely detrimental to the thermoelectric performances because of the effects of Anderson localization.

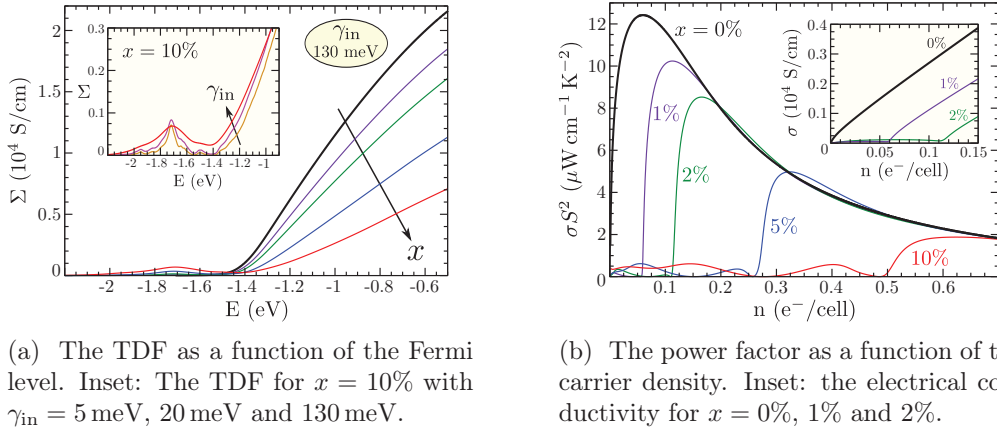


Figure 5.21: From Ref. [280]. The room-temperature thermoelectric transport properties of V-doped SrTiO₃ (x from 0% to 10%) calculated from CPGF with $\gamma_{\text{in}} = 130 \text{ meV}$.

5.3.2 Resonant states in SrTiO₃, BaTiO₃ and CaTiO₃

This poor performance of vanadium doping in SrTiO₃ can be attributed to several causes. First, the strong on-site potential $\epsilon = -1.4 \text{ eV}$ on the orbitals of the V atoms gives rise to impurity states below the conduction band. In section 5.1, it was shown that proper resonant states positioned well inside the conduction band are necessary to observe an enhancement of the thermoelectric properties. Likewise, the hopping parameter t' between the vanadium orbitals and the neighboring Ti orbitals are the same as the hopping parameters t between neighboring Ti orbitals in pristine SrTiO₃. Such a strong hybridization between the defects and regular lattice sites was also shown to push the resonant peak to the edge of the conduction band in section 5.1, resulting in very poor thermoelectric performances. Finally, the strong inelastic scattering γ_{in} present in SrTiO₃ would destroy a resonant boost of the power factor. This last point is most problematic because, unlike the parameters ϵ and t' , it is not specific to vanadium doping and therefore seems to preclude the possibility

of enhancing the power factor in SrTiO₃ using a better resonant dopant than vanadium. However, the perovskite oxides BaTiO₃ and CaTiO₃ have almost the same conduction band structure as SrTiO₃ (see Fig. 3 of Ref. [300]) but electronic transport in these compounds may be characterized by a different inelastic scattering mechanism. Thus, it is relevant to consider ϵ , t' and γ_{in} as parameters and to explore a range of values that could potentially correspond to other resonant dopants in the family of materials SrTiO₃, BaTiO₃ and CaTiO₃ sharing the same conduction band structure. The conduction band structure of the pristine material will be kept identical to SrTiO₃. A more precise approach would be to perform DFT calculations and Wannier projections on BaTiO₃ and CaTiO₃ to take into account their specific electronic structure, but as *ab initio* computations predict only around 15% variations in their dispersion relation and transport properties with respect to SrTiO₃ (Fig. 2 and Fig. 3 of Ref. [300]), we do not expect this approximation to lead to large errors. Since a low inelastic scattering rate is necessary for a resonant boost of the power factor, as shown in section 5.1, we set $\gamma_{\text{in}} = 5$ meV comparable to the scattering rate predicted in certain Half-Heuslers such as ZrNiSn exhibiting weak electron-phonon coupling [286]. For the on-site potential, we consider the values $\epsilon = -1.4$ eV, -1.2 eV, -1.0 eV and -0.8 eV

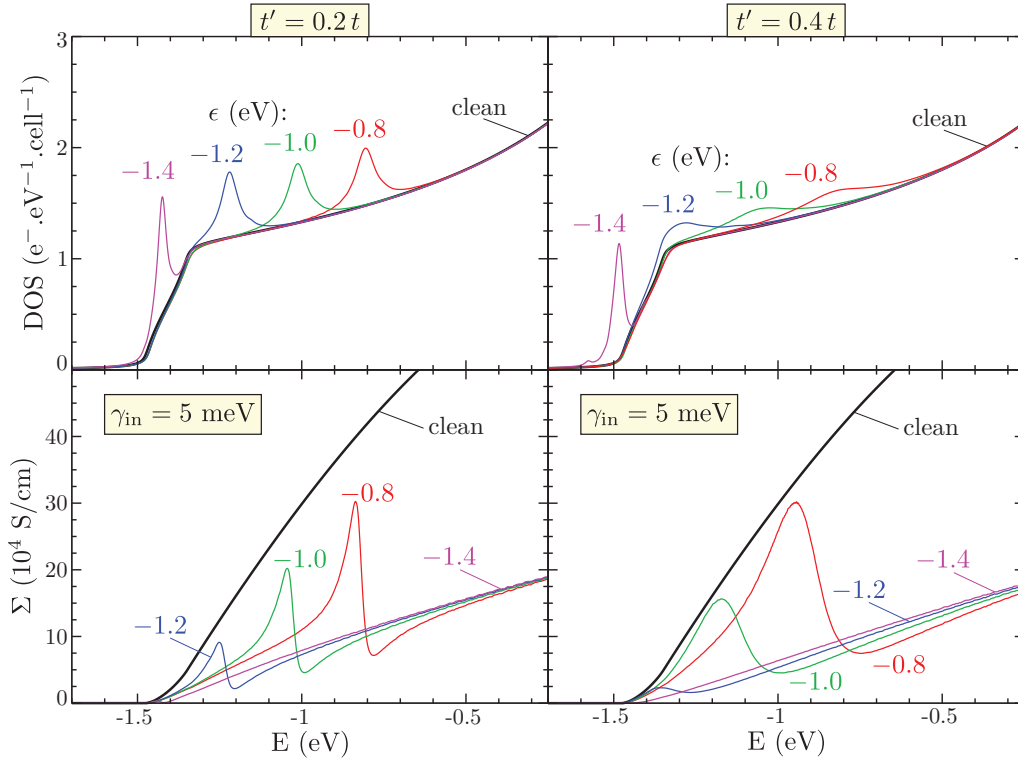


Figure 5.22: From Ref. [280]. The DOS and TDF as a function of the Fermi level for SrTiO₃/BaTiO₃/CaTiO₃, pristine (thick black line) and 1% doped with a low-hybridization resonant dopant ($t' = 0.2t, 0.4t$) for several values of ϵ .

(lower values would bring the resonant states too far from the conduction band minimum). For the hopping parameter between the resonant dopants and the neighboring Ti atoms, we start by studying thermoelectric transport for low hybridization values $t' = 0.2t$ and $0.4t$, before examining the higher values $t' = 0.7t$ and $1.0t$. We set the resonant defect concentration to $x = 1\%$, the value found optimal in section 5.1.

Fig. 5.22 shows the DOS and TDF for low-hybridization dopants ($t' = 0.2t, 0.4t$). The doping gives rise to resonant peaks whose position is controlled by the value of ϵ , with $\epsilon = -1.4\text{ eV}$ creating a peak at the very edge of the conduction band. The resonant peaks are sharper for $t' = 0.2t$ than for $t' = 0.4t$. For $\epsilon = -1.2\text{ eV}$, -1.0 eV and -0.8 eV , they translate in the TDF to a sharp asymmetrical drop at the energies of the peaks, with the conduction suppressed much more broadly at higher energies than below the resonant peaks. No such effect can be observed for $\epsilon = -1.4\text{ eV}$ due to the resonant states being too close to the band edge. It should be noted that while the resonant defects seem to have a minimal influence on the DOS for $t' = 0.4t$ (only slight bumps can be observed), the effect on the TDF is quite important. Thus, the transport properties of the system cannot be predicted simply from the shape of the DOS.

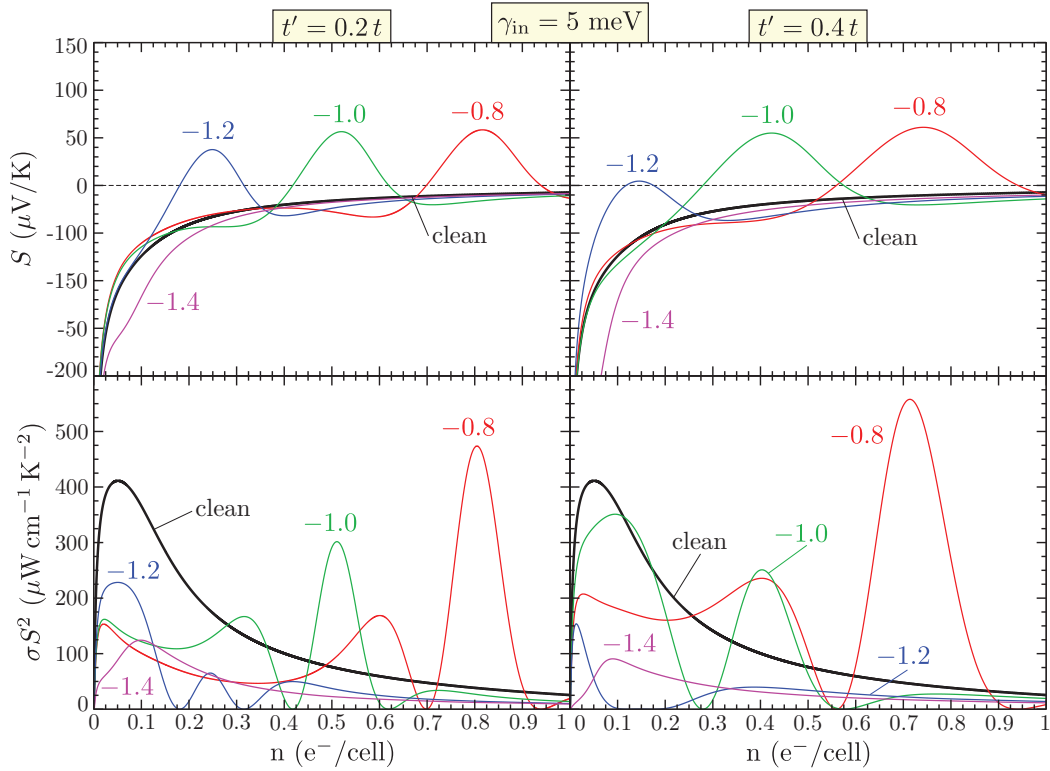


Figure 5.23: From Ref. [280]. The room-temperature Seebeck coefficient and PF as a function of the electron concentration for $\text{SrTiO}_3/\text{BaTiO}_3/\text{CaTiO}_3$, pristine (thick black line) and 1% doped with a low-hybridization resonant dopant ($t' = 0.2t, 0.4t$) for several values of ϵ .

We show in Fig. 5.23 the room-temperature Seebeck coefficient and PF as a function of the electron concentration, calculated from the results of Fig. 5.22. In this model, the clean system exhibits a very high maximum power factor around $420 \mu\text{W cm}^{-1} \text{K}^{-2}$ due in part to the low inelastic scattering rate. For $\epsilon = -1.2 \text{ eV}$, -1.0 eV and -0.8 eV , the sharp drop in the TDF leads to a sign inversion of the Seebeck coefficient (which is related to the slope of the TDF), while S always remains negative for the clean system and $\epsilon = -1.4 \text{ eV}$. For $\epsilon = -1.0 \text{ eV}$ and -0.8 eV , this is accompanied by a boost of the Seebeck coefficient. For $\epsilon = -0.8 \text{ eV}$, this boost actually overcompensates the drop in conductivity and results in an enhancement of the PF by around 15% for $t' = 0.2t$ and 35% for $t' = 0.4t$, from $420 \mu\text{W cm}^{-1} \text{K}^{-2}$ to $475 \mu\text{W cm}^{-1} \text{K}^{-2}$ and $560 \mu\text{W cm}^{-1} \text{K}^{-2}$ respectively. However, these enhanced PF values require a very high carrier concentration around $0.7\text{-}0.8 \text{ e}^-/\text{cell}$, which is probably unreachable experimentally. This weak enhancement of the PF could appear surprising given the sixfold resonant increase observed in section 5.1. This is partly due to the conduction band structure of SrTiO_3 , BaTiO_3 and CaTiO_3 , which is very anisotropic with a band mass ratio of 10 between the x and z direction for the xy orbital (see section 3.1). Resonant states were found to be much less efficient for such two-dimensional electronic structures. Additionally, the largest hopping term t between nearest-neighbors is equal to 0.27 eV , while it was assumed to be 1 eV in the minimal Hamiltonian of section 5.1. Thus the room temperature corresponds to a ratio $k_B T/t \approx 0.1$, for which only a modest increase of the PF was found.

For these sets of parameters ($\epsilon = -0.8 \text{ eV}$, $t' = 0.2t$ and $0.4t$) that lead to an enhancement of the PF, we study the influence of the inelastic scattering rate γ_{in} . We plot

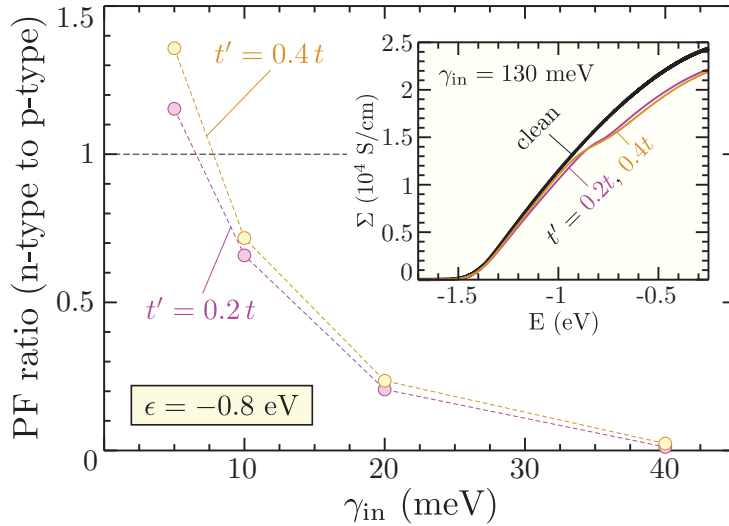


Figure 5.24: From Ref. [280]. Ratio of the maximum power factor associated with a positive Seebeck coefficient to the maximum power factor of the clean system, as a function of γ_{in} for $\epsilon = -0.8 \text{ eV}$, $t' = 0.2t$ and $0.4t$. Inset: the TDF for $\gamma_{\text{in}} = 130 \text{ meV}$.

in Fig. 5.24 as of function of γ_{in} the ratio of the maximum p-type PF in the resonant case with respect to the maximum PF of the clean system. As the inelastic scattering rate is increased, the PF ratio quickly goes from a slight increase of the PF for $\gamma_{\text{in}} = 5$ eV to a modest decrease for $\gamma_{\text{in}} = 10$ eV, then a 75% drop for $\gamma_{\text{in}} = 20$ eV and a near-complete suppression for $\gamma_{\text{in}} = 40$ eV. No sign inversion of the Seebeck coefficient occurs for $\gamma_{\text{in}} > 40$ eV. Higher inelastic scattering destroys the resonant enhancement of the PF because the transport properties become dominated by the inelastic processes that completely level the sharp variations in the TDF introduced by the resonant impurities. This is illustrated by the inset of Fig. 5.24, showing the TDF for $\gamma_{\text{in}} = 130$ eV that corresponds to the case of SrTiO₃: the resonant states have almost no influence on the transport properties for such high inelastic scattering rates.

For higher values of the hybridization ($t' = 0.7t$ and $1.0t$), the defects either do not create a resonant peak, leading to a broad decrease of the TDF due to electron-defect scattering, or they give rise to impurity bands at or below the conduction band bottom. The latter case is similar to V-doped SrTiO₃, and we show in Fig 5.25 the DOS and room-temperature power factor for several values of the on-site potential. We can define the donor level δ as the energy separation between the impurity states and the conduction band bottom. The transport properties appears to be governed by the donor level: larger values of δ lead to lower power factors if the Fermi level lies in the Anderson localized defect states. The crossover from localized to extended states is particularly clear for the largest donor level corresponding to V-doped SrTiO₃ ($t' = 1.0t$, $\epsilon = -1.4$ eV). In all cases, the maximum PF is much lower than the reference value of $420 \mu\text{W cm}^{-1} \text{K}^{-2}$.

To conclude, we have studied the effects of randomly distributed vanadium doping in SrTiO₃ by constructing a realistic tight-binding model from DFT calculations. The disorder was treated exactly through the CPGF method, validated by exact diagonalizations of

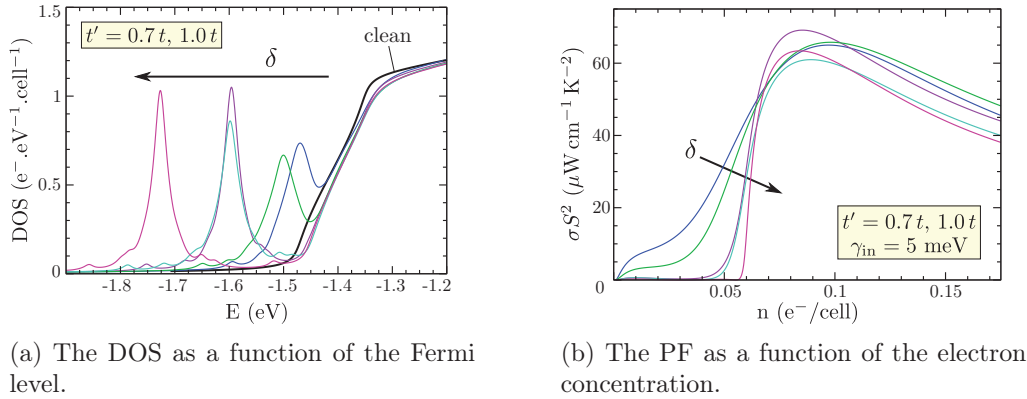


Figure 5.25: From Ref. [280]. The DOS and PF for SrTiO₃/BaTiO₃/CaTiO₃, pristine (thick black line) and 1% doped with a high-hybridization resonant dopant ($t' = 0.7t$, $1.0t$) for several values of ϵ . The donor level δ is defined as the energy separation between the impurity states and the conduction band bottom.

the Hamiltonian. We have calculated the thermoelectric transport properties (diffusivity, conductivity, Seebeck coefficient, power factor) as well as the inverse participation ratio and typical density of states to investigate the presence of Anderson localization. We have found that vanadium doping creates localized impurity states below the conduction band of SrTiO_3 , leading to poor thermoelectric performances due to Anderson localization effects. We have then varied the defect parameters and inelastic scattering to investigate a broader range of potential resonant impurities in the family of materials SrTiO_3 , BaTiO_3 and CaTiO_3 sharing a very similar conduction band structure. We have found only modest increases of the power factor associated with an unreasonably large carrier concentration and a low inelastic scattering rate, for which the maximum power factor of the clean system would already be very large. Therefore, resonant states appear to be ineffective as a strategy to boost the power factor in this class of materials. This is partly due to their strong conduction orbital anisotropy. Our results underscore the importance of treating disorder effects in a thorough and rigorous manner when studying resonant states. Our real-space methodology based on realistic tight-binding Hamiltonians extracted from DFT calculations appears well suited to adress this challenge.

Chapter 6

Defects in two-dimensional materials

I don't understand, there's no known physics model for this. Unless... Oh my god, I'm two-dimensional!

Gordon Freeman, *Freeman Across The Universe*.

Two-dimensional materials have been the focus of intense research efforts since the isolation of a single graphene layer in 2004 [301]. They offer unique opportunities to control and functionalize the geometry and chemical composition of the crystal layer through a variety of techniques, from nanolithography to physisorption of molecules, and they represent great promise for valleytronics and spintronics technological applications, among others [302, 303, 304]. Graphene is particularly interesting due to its outstanding performances in several aspects, including an extremely high mechanical strength, electron mobility and thermal conductivity [305, 306, 294]. Electronic transport in this material displays exotic properties due to the massless Dirac-like relation dispersion and chirality of the electrons [295]. In addition, it has been found that the electronic properties of a bilayer graphene system could be spectacularly affected by the rotation angle between the two sheets [307, 308].

From the point of view of thermoelectric transport, two-dimensional materials may exhibit superior electronic properties due to the quantum confinement of electrons in a single plane, which is expected to result in improved values of the power factor, as mentioned in section 1.2.2. The low-dimensionality of these compounds also influences their phonon properties. For instance, they can vibrate in the direction perpendicular to the material plane: these so-called flexural modes can display a quadratic dispersion relation in certain materials such as graphene and MoS₂ [309, 310]. A record-high thermal conductivity has been measured in graphene, making it a promising material for thermal management applications [311, 312]. Of course, efficient thermal conduction is undesirable for thermoelectric power generation, but the long phonon mean free paths in graphene suggest that the thermal properties can be suitably tuned by the introduction of impurities, vacancies, nanostructures and edge defects [313, 314].

In this chapter, we investigate both electron and phonon transport in two-dimensional materials. In section 6.1, published in Ref. [315], we study the electrical conductivity and

Seebeck coefficient of several transition-metal dichalcogenides through *ab initio* calculations, focusing on the issue of doping with substitutions and adatoms. In section 6.2, we investigate the phonon scattering rates and thermal conductivity of graphene in the presence of vacancies [316, 317] by combining DFT calculations with our Green’s function methodology.

6.1 First principle investigation on thermoelectric properties of transition metal dichalcogenides: beyond rigid band model

Two-dimensional (2D) direct band-gap [318, 319] transition-metal dichalcogenides (TMDC) with chemical composition MX_2 ($\text{M}=\text{Mo}$ or W and $\text{X}=\text{S}$ or Se) have led to a growing interest in the last decade. For instance, in the field of nanoelectronic, significant accomplishments have been done in the development of MoS_2 based transistors [320, 321, 322]. More recently people have paid attention to this material in the prospect of thermoelectricity on both theoretical [323, 324, 325, 326, 327, 328] and experimental side [329, 330, 331].

Low dimension materials like 2D compounds are expected to have higher thermoelectric figure of merit compared to bulk materials due to poor thermal conductivity [56, 57]. However, this is not so obvious for TMDC considering that the observed thermal conductivity of MoS_2 is of the order of $30 - 50 \text{ W.m}^{-1}.\text{K}^{-1}$ [332, 333, 334]. More recently a lower value of $13.3 \text{ W.m}^{-1}.\text{K}^{-1}$ has been obtained for suspended monolayer [335]. Nevertheless, even if the thermal conductivity of TMDC is not as low as some other promising thermoelectric materials [336], this issue is actually not critical for 2D materials due to recent progress in phonon engineering [313].

In order to use semiconducting materials as thermoelectric devices, it is mandatory to perform doping. However, doping issues in TMDC are actually very intriguing. When dealing with 2D material or layered material, there are 3 ways to dope the material, substitution doping is the most conventional one and it has been successfully used experimentally. For example, p-type doping has been achieved on MoS_2 by substituting Mo atoms by Nb [337] or S by P [338]. In the case of metal MoS_2 contact a significant reduction of the Schottky barrier has been reached by chloride substitution of a sulfur corresponding to an electron doping [339]. Another doping mechanism is vacancy induced doping which is suspected to have a major role in contact resistance lowering between metal and MoS_2 [340]. Finally, a very efficient way to obtain a significant doping with 2D material is based on chemical adsorption. For instance, Kong *et al* [341] have recently shown that oxygen adsorption strategy leads to an enhancement of the thermoelectric properties of MoS_2 . Furthermore, adsorbed potassium has been successfully used as electron donor in the topic of field effect transistor [342]. A comprehensive review of doping techniques of MoS_2 can be found in Ref [343].

In this section we investigate theoretically the influence of substitution and adsorption doping on the properties of the Seebeck coefficient, the electric conductance and the power factor within the Landauer Büttiker formalism (it is portrayed in Fig. 6.1 for a TMDC single layer) at room temperature ($T = 300 \text{ K}$). Within this framework, we are going beyond the

usual semiclassical Boltzmann formalism in order to analyze accurately the influence of the disorder. The guiding line of the section is to detail which doping procedure can lead to the largest power factor.

6.1.1 Theoretical framework

All the calculations are performed using the SIESTA *ab initio* package [112] under the generalized gradient approximation of Perdew, Burke & Ernzerhof [123] and using Troullier-Martin norm-conserving pseudopotentials [191]. The basis used corresponds to a double-zeta-polarized (d ζ p) basis optimized using the simplex tool of the SIESTA package. All the atomic structures were optimized up to forces less than 0.01 eV/Å. A Monkhorst-pack of 10×10 k-points have been used for the calculations using a mesh cutoff of 400 Ry.

The spin-orbit coupling is not taken into account in these calculations. One of the effect of this coupling is a band splitting [344, 319] leading to a degeneracy removal at some high symmetry points of the band structure. The expected influence of this band splitting on the transport properties is to lower a bit the Seebeck coefficient and thus the PF. However this effect is not supposed to affect significantly our results.

Based on *ab initio* calculations, the thermoelectric properties *i.e.* the Seebeck coefficient and the electrical conductance are calculated using the Landauer formalism [155, 345] for which the key ingredient is the transmission through the system. Within this formalism, the electrical conductance and the Seebeck coefficient can be expressed respectively as:

$$G(E_F) = -\frac{2e^2}{\hbar} L_0(E_F), \quad (6.1a)$$

$$S(E_F) = -\frac{1}{k_B T} L_1(E_F)/L_0(E_F), \quad (6.1b)$$

with,

$$L_n(E_F) = \int_{-\infty}^{+\infty} (E - E_F)^n T(E) \left(\frac{\partial f}{\partial E} \right) dE, \quad (6.2)$$

where $T(E)$ is the transmission, $f(E)$ the Fermi distribution and E_F the Fermi energy. The temperature dependence comes from the Fermi distribution and in the following, we have focused on room temperature ($T = 300$ K) calculations.

The conductivity σ is defined for these 2D systems as $\sigma = \frac{G}{L_\perp}$, where L_\perp is the dimension of the layer perpendicular to the transport direction. Under this definition of σ for 2D systems, the physical dimension of the conductivity is equivalent to the conventional one. This definition is underpinned by the fact that under ballistic regime, the conductance does not depend on the length L_z of the device. The transmission is computed on the basis of Green's function formalism using the Hamiltonian computed by SIESTA. The present *ab initio* quantum transport theory, fully described in Ref. [346], is similar to TRANSIESTA. [347] For all the transport calculations, we have used 80 k-points in the transverse direction.

On the basis of the Landauer-Büttiker formalism, the transmission reads:

$$T(E) = \text{tr} [\Gamma_L G^r \Gamma_R G^a] , \quad (6.3)$$

where $G^{r(a)}$ is the retarded (advanced) Green's function and $\Gamma_{L(R)}$ the coupling between the left (right) lead and the device (see Fig. 6.1). The main assets of this formalism are to allow to deal with disordered systems and to fully include the quantum backscattering processes.

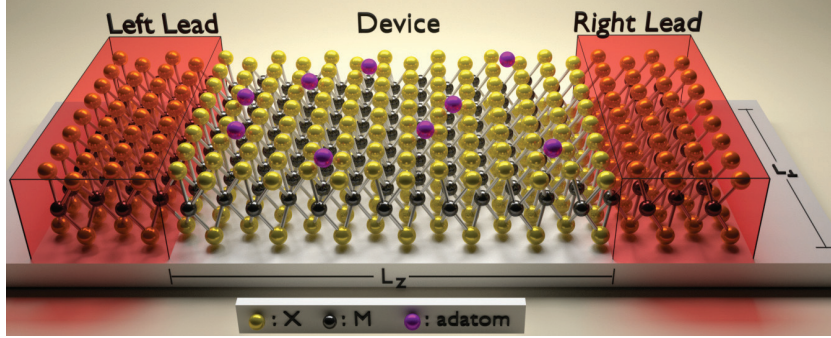


Figure 6.1: From Ref. [315]. Schematic representation of the decomposition of the system used within the Landauer formalism and corresponding to a generic MX_2 layer with adatoms.

6.1.2 Rigid band model

In order to have a starting point to evaluate the doping efficiency of the various techniques and dopants, we first present some results for the PF obtained within the rigid band model. In this model, the Seebeck coefficient and the electrical conductivity are obtained from the Landauer formalism for a pristine layer by shifting rigidly the Fermi level of the system. When the Fermi level is shifted toward the valence bands it mimics hole doping and when shifted toward the conduction bands it mimics electron doping. This approach allows to easily get a first insight on how the material is behaving under doping provided that the band structure (or at least the bands of interest) of the host material is not significantly perturbed. This kind of modeling has been used to study the thermoelectric properties of TMDC in Ref. [348] with a various number of layers but without realistic doping.

In Fig. 6.2 is depicted the PF (the Seebeck coefficient and the electrical conductivity are in inset) for the various TMDC. We have considered two major transport directions, the armchair and the zigzag ones. These directions are depicted on top of Fig. 6.2 accordingly to the TMDC structures. These plots are given as a function of the Fermi level position but they can be linked with the carrier charge density (see table 6.1 for specific values) by integration of the density of states $\rho(E)$. Negative Fermi level is equivalent to hole doping and positive Fermi level to electron doping. Basically, the maximum observed for the PF either for hole or electron doping (respectively the red and the blue curves) arises from the two opposite behavior of the Seebeck coefficient and the conductivity. When increasing

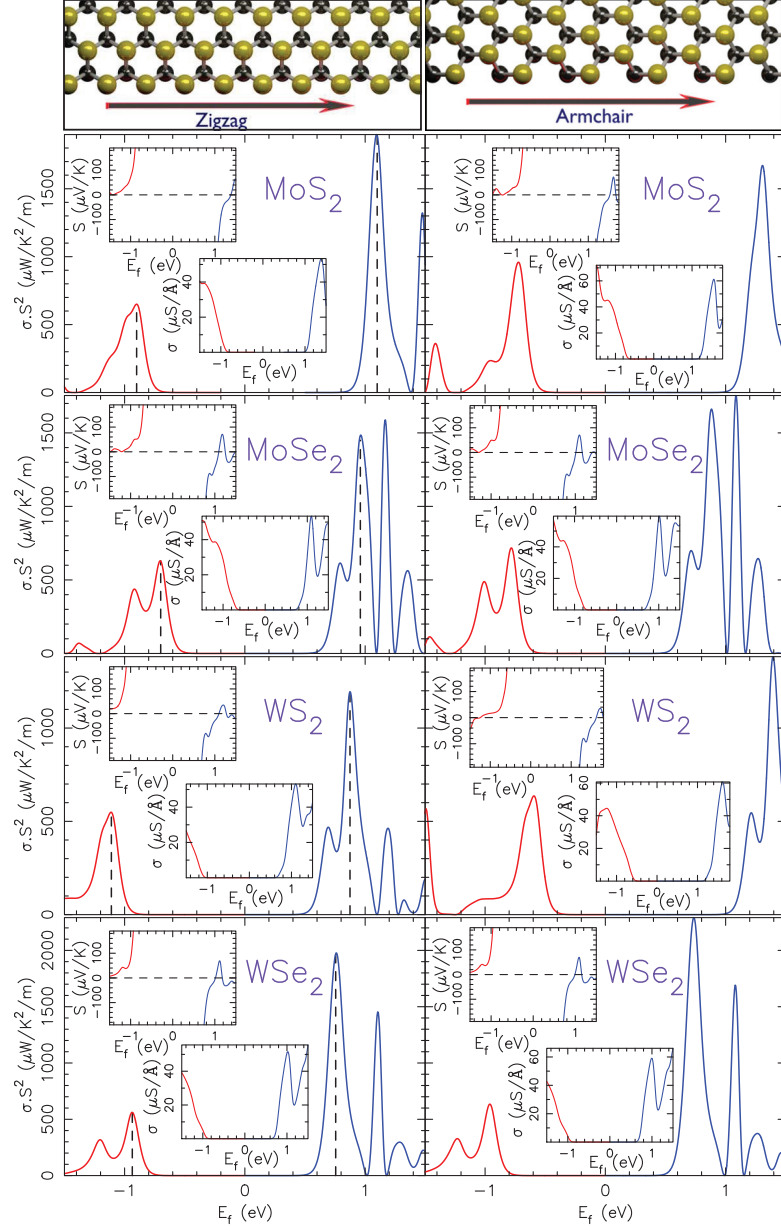


Figure 6.2: From Ref. [315]. Powerfactor for (from top to bottom) MoS_2 , MoSe_2 , WS_2 and WSe_2 . In inset is given the Seebeck coefficient and the electrical conductivity. Red and blue curves correspond resp. to hole and electron doping. On top is represented the transport direction in the TMDC layer. The black and yellow atoms are resp. the M and X atoms of MX_2 .

	$S(\mu\text{V/K})$	$\sigma(\mu\text{S}/\text{\AA})$	PF ($\mu\text{W/K}^2/\text{m}$)	carrier charge per UC
MoS ₂	-156.6	7.7	1888	+0.010
	+163.1	2.7	718	-0.012
MoSe ₂	-86.9	19.6	1480	+0.090
	+182.8	1.9	635	-0.005
WS ₂	-85.8	16.2	1193	+0.065
	+167.6	1.9	534	-0.007
WSe ₂	-172.7	6.6	1968	+0.015
	+179.0	1.8	577	-0.007

Table 6.1: Seebeck Coefficient, Conductivity and PF for the zigzag transport direction obtained at the maximum of the PF (depicted by dashed lines in Fig. 6.2) for electron and hole doping. The last column is the carrier charge per unit cell. Negative and positive charge corresponds respectively to p and n-type.

carrier charge, the Seebeck coefficient tends to zero (negatively or positively depending of the doping) and conversely, the electrical conductivity tends to increase with the carrier density. The maximum of the PF results from the combination of these two opposite trends.

At first one can notice that the PF is almost similar for both transport directions, the anisotropy of these materials is actually quite small. Second, there is a strong asymmetry between hole and electron doping. Indeed, hole doping is always leading to a lower PF than electron doping. In table 6.1 is given the Seebeck coefficient and the conductivity obtained for the maximum of the PF in the case of the zigzag transport direction (these values are pointed out in Fig. 6.2 by a dashed line). By inspecting these values, one can notice that the difference between p and n doping is mainly due to the conductivity, it is always lower for p doping compared with n doping. This can be directly linked with the density of states which is smaller at the top of the valence band compared with that of the bottom of conduction band. Therefore, the thermoelectric performance of a full p-n thermoelectric device based on these materials would necessarily suffer from the limitations due to the p side.

Anyhow, focusing at the n side, the maximum of the PF can reach a value almost as large as $2600 \mu\text{W/K}^2/\text{m}$ for WSe₂ in the armchair direction. This value is in good accordance with experimental one, for instance Yoshida *et al.* [330] have obtained a PF of the order of $3200 \mu\text{W/K}^2/\text{m}$ and a Seebeck coefficient of the order of $-150 \mu\text{V/K}$ for an ultrathin WSe₂ crystal by electrostatic doping (or field effect carrier doping) using a gate voltage. The results obtained with this technic are directly comparable to the rigid band model as the carrier concentration is solely tuned by a field effect. They have also measured the PF in Ta doped WSe₂, that was found one order of magnitude lower than that obtained by electrostatic doping. Kong *et al.* [341] have also reported values of the same order of magnitude, $300 \mu\text{W/K}^2/\text{m}$, in MoS₂ doped by MoO₂ nanoinclusions.

However, this results must be qualified by the fact that, if the maximum is occurring for large value of the Fermi level, it will correspond to a larger dopant concentration (see table 6.1 for the carrier charge per unit cell at the maximum of the PF). A material with a large PF at unrealistic dopant concentration is not useful. For instance, both MoSe₂ and WS₂ require a large carrier charge to achieve the maximum of PF (this carrier charge can be directly linked with the dopant concentration in the case a substitution doping). Thus, in the search of a material which allows to achieve a large PF, we must also take into account the energy difference between the maximum of the PF and the bottom of the conduction band. As a matter of fact, the smaller this difference the lower the needed concentration of dopant.

Within this consideration, it appears that the best candidates for electron doping would be MoS₂ and WSe₂ for which the PF maxima are obtained for Fermi levels closer to the bottom of the conduction band corresponding to a carrier charge per unit cell of 0.01 and 0.015 respectively. For comparison, Fang *et al.* [342] have measured for potassium doped MoS₂ an electron concentration of $1.0 \times 10^{13} \text{ cm}^{-2}$ which corresponds to $0.009 e^-/\text{UC}$ (using a cell parameter of 3.16 Å for MoS₂).

In order to discuss the validity of the rigid band scenario, we now consider the effects of the different kinds of doping in a more realistic manner.

6.1.3 Realistic doping

There are several ways to dope TMDC by substitution, for instance it is possible to substitute a X atom (S or Se) by an atom in the neighboring columns of the periodic table. Indeed, the substitution by a phosphorus atom is leading to a hole doping and the substitution by a chloride atom is leading to an electron doping. The same is also valid for the transition metal atom. For example, the substitution by a rhenium atom is leading experimentally to a n-type semiconductor. [349]

In Fig. 6.3 is given the density of states (DOS) obtained for two substitutional doping with either phosphorus or chloride in MoS₂, for each case we have varied the dopant concentration. For $x = 17\%$ it corresponds to a 2×3 rectangular cell and for $x = 4\%$ to a 4×6 cell. At high concentration, a significant DOS is observed at the Fermi level either at the top of the valence band (P doping) or at the bottom of the conduction band (Cl doping). However, when the concentration is decreased, it can be noticed in both cases that the DOS tends to display sharp peaks around the Fermi level. These sharp peaks are associated with almost flat bands which are an indication on the localized nature of these states. Actually, when we inspect the projected density of states (PDOS) on the significant atomic orbitals, it should be stressed that the DOS at the Fermi level is induced by the dopant states and is absent in the intrinsic DOS of pure MoS₂. The dopant hybridizes locally with Mo and S and is leading to specific bands with almost no dispersion for low dopant concentration, the only way to obtain a significant dispersion at the Fermi level is to use unrealistic doping concentration of the order of 17%. This is even more obvious when we compare the DOS obtained with the phosphorus dopant and the DOS of pristine MoS₂. We can clearly see that the DOS close to the Fermi level does not correspond to that of pristine MoS₂. Both

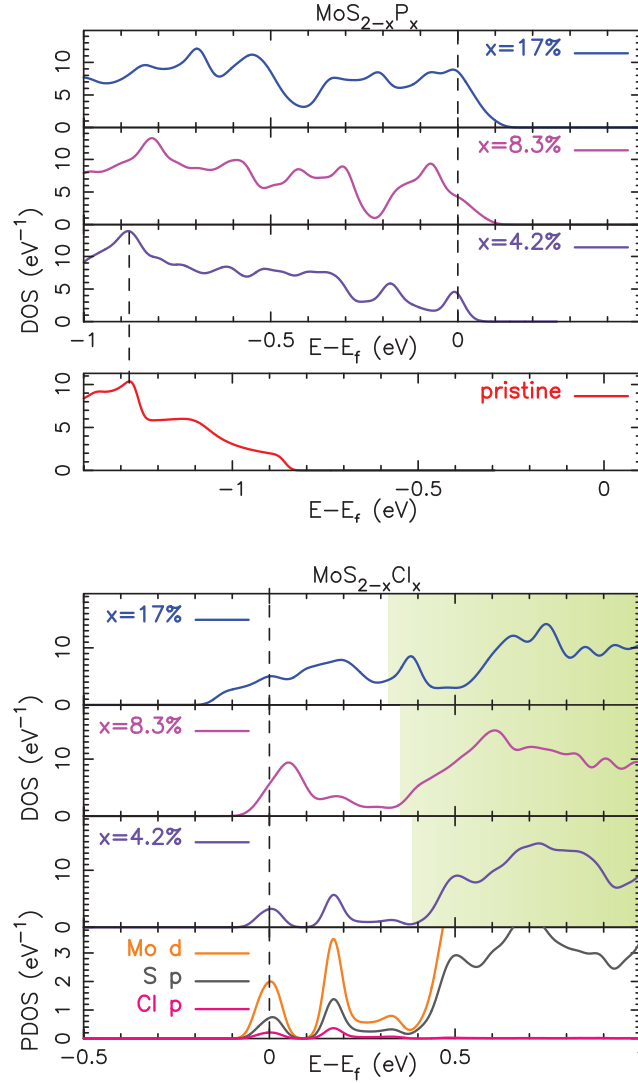


Figure 6.3: From Ref. [315]. Electronic density of states (DOS) for P (top) and Cl (bottom) doped MoS_2 . For comparison purpose, the pristine DOS is also shown (it is shifted accordingly to the 4.2% case). The projected DOS (PDOS) is given for the 4.2% Cl doped case. The green shaded backgrounds depict the location of the conduction band in the pristine case.

kind of substitutional dopant clearly modify the band structure around the Fermi level. This already suggests that the rigid band model fails for those cases. These local states are actually not specific to chloride and phosphorus and are also observed with Br, F, N and As.

One other promising strategy to dope 2D materials is chemical adsorption, this technic

has been investigated theoretically for MoS₂ [350, 351, 352] on the basis of *ab initio* calculations. However, these calculations were not focusing specifically on the link between electronic and thermoelectric properties. A variety of adatoms have been examined, and only few atoms lead to a significant doping. Alkalies seem very promising because they are leading to a significant electron doping with no local states at the Fermi level. Based on this statement, we have thus focused on alkali doping for this study on transport properties. In this work, the adsorption site used for the alkalies is at the top of a molybdenum atom, this site is actually the most energetically favorable. However, when we consider an adsorption site at the center of an hexagon (almost as favorable as at the top of Mo), it is found that it makes no difference on the thermoelectric properties.

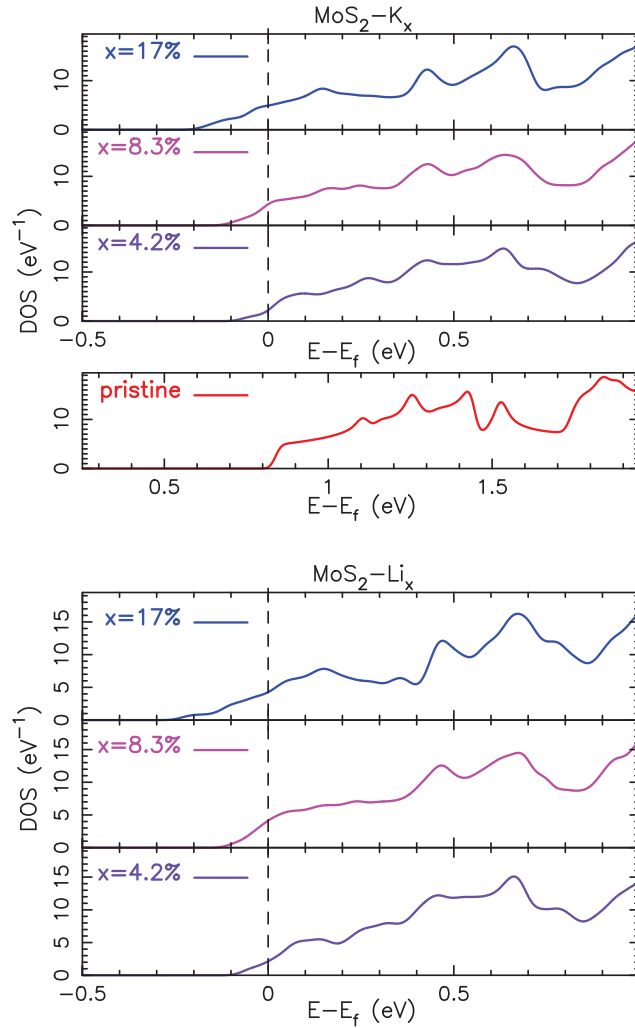


Figure 6.4: From Ref. [315]. Electronic density of states for MoS₂ doped by adsorption with K (top) and Li (bottom). The pristine case corresponds to the red curve.

In Fig. 6.4 is presented the DOS obtained in the case of MoS₂ doped with either potassium or lithium. In both cases, an electron doping results due to the donor nature of alkalis with respect to the MoS₂ layer. The influence of these adatoms concentration is mainly to shift the Fermi level with no significant modification of the pristine DOS. This can be opposed to the case of substitution doping with phosphorus and chloride for which the DOS was significantly affected by the dopant. No indication of local states is observed and the DOS at the Fermi level corresponds to bands already existing in the pristine material. Indeed, the electronic states of the alkalis are located at much higher energy and do not have any contribution at the bottom of the conduction band. This can be clearly seen by comparison with the DOS of the pristine MoS₂ layer. We have observed this behavior with all alkali atoms till rubidium. The only influence of the dopant on the DOS shape is a light spreading of the bottom of the conduction band toward lower energy. This spreading of the DOS at the bottom of the conduction band observed with alkali dopants has its origin in the degeneracy removal of some conduction bands. It is depicted in Fig. 6.5 which corresponds to the band structure for a 2×3 rectangular cell of a 17% Li doped MoS₂ layer and a pristine one. The bottom of the conduction band of the pristine MoS₂ single layer corresponds to four bands which are degenerated at the Γ and U points. This degeneracy is removed when the dopant is adsorbed on the layer. This behavior is definitely expected considering the symmetry breaking introduced by the dopant. However, it can be noticed that two bands are shifted toward lower energy at the U point leading to the spreading of DOS. The splitting at this point is 0.26 eV and it has, as it is described hereafter, a significant influence on the Seebeck coefficient.

We now provide an overview of the thermoelectric properties of MoS₂ realistically doped either with substitution or adsorbed atoms introduced in the previous paragraphs. Transport properties of these doped materials are still performed within the Landauer formalism.

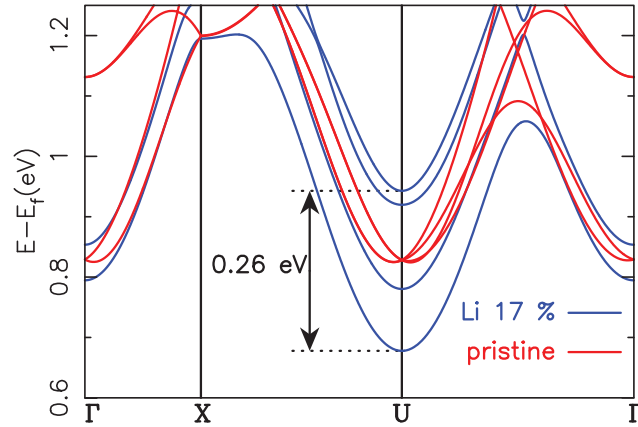


Figure 6.5: From Ref. [315]. Band structure of a 2×3 rectangular MoS₂ lattice for pristine and Li doped (17%). For Li doped, the energy is shifted for comparison with the pristine case.

On Fig. 6.6 is represented the PF for three different dopants: Chloride dopant corresponds to a substitution doping and potassium and lithium dopants to adsorption doping. For comparison purpose, we have also plotted the result within the rigid band approximation. The PF is represented as function of the carrier charge per unit cell. It actually corresponds for alkalis to the charge transferred by the adatom to the MoS₂ layer, this charge is estimated by means of Mulliken analysis. We have also checked with Voronoï and Hirshfeld analysis the consistency of the estimated charge and the resulting relative uncertainty is about 10% for the largest concentration and about 5% for the smallest one. One should notice that under substitution doping by chloride the dopant concentration (referenced as x on Fig. 6.3) is equivalent to the carrier charge per unit cell. However, this is not true for adsorption doping for which the carrier charge (or the transferred charge) is linked with the affinity between the adatom and the host layer. Note that this charge is always lower than the carrier charge obtained with an equivalent substitution doping concentration.

Concerning the substitution with chloride, one can notice that the PF is much lower than the hypothetical one obtained from the rigid band model. On one side, starting from high concentration and decreasing it, the enhancement of the Seebeck coefficient leads firstly to an increase of the PF. On the other side, due to the local states, the conductivity then decreases dramatically and leads to a very rapid drop of the PF. Conversely, doping with alkali adatoms leads to larger values of the PF and are actually closer to the rigid band model. As argued previously, in the case of alkali doping, the bands involved in the transport are almost unaffected by the dopants and so we obtain a PF which is behaving more or less as the rigid band model but with smaller values. Indeed, due to the degeneracy removal induced by the dopants, the Seebeck coefficient obtained with alkalis is smaller than that obtained with the rigid band model (the conductivity is almost not affected).

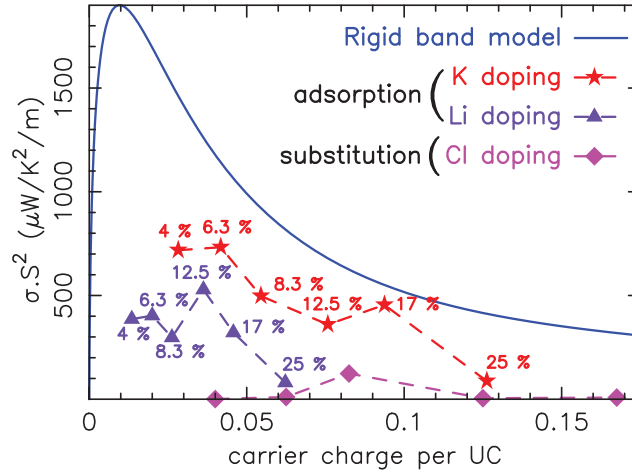


Figure 6.6: From Ref. [315]. Power factor for MoS₂ with 3 different dopants: K, Li and Cl, as well as the rigid band calculation (for comparison purpose) plotted as a function of the carrier charge per unit cell.

	4.2%	$\sigma(\mu\text{S}/\text{\AA})$	$S(\mu\text{V}/\text{K})$	$\text{PF}(\mu\text{W}/\text{K}^2/\text{m})$
MoS ₂	Li	3.6	-104.0	389.4
	Na	1.8	-105.5	200.3
	K	5.2	-116.9	710.6
	Rb	5.7	-113.0	727.8
MoSe ₂	K	4.6	-79.1	287.8
WS ₂		5.9	-85.3	429.3
WSe ₂		4.1	-150.5	928.7

Table 6.2: Conductivity, Seebeck coefficient and power factor for various alkali adatoms with a 4.2% concentration.

This is the reason why the PF is always smaller than that obtained within the rigid band model.

When we compare the different alkalis, a significant difference can be noticed. Li is leading to poorer PF compared with K. In table 6.2 is given the PF for various alkali adatoms (concentration of 4.2%) and for the four different TMDC. One can notice that small alkalis like Li or Na lead to smaller PF than large adatoms such as K or Rb. The difference is actually coming from the conductivity and linked with the charge transfer between the alkali and the MoS₂ layer which is smaller for Na and Li than K and Rb. This is leading, for the same dopant concentration, to a lower DOS at the Fermi level and thus to a lower conductance. The comparison between the four TMDC clearly points out that MoS₂ and WSe₂ are the best candidate for thermoelectric applications considering their high power factors at rather low dopant concentration.

6.1.4 Influence of the disorder

One issue which have not yet been argued is the influence of the disorder. All the results presented previously are made artificially periodic by supercell construction and do not fully take into account the natural disordered location of the dopants. In order to have an insight on the influence of disorder, we have now considered systems where the dopants are randomly distributed. Indeed, it is possible within the Green's function formalism to define an aperiodic device (see Fig. 6.1). Moreover, using the tridiagonal shape of the Hamiltonian, we have dealt with system with length up to 50 nm, corresponding to 100 unit cells or more than 2500 atoms. We have thus defined systems on which the dopants are randomly distributed among the adsorption/substitution sites and by varying the length of the system, it is then possible to evaluate the effects of the disorder on the thermoelectric properties. One should notice that we have voluntarily focused on scattering by static disorders and other scattering mechanisms as phonon scattering are not considered. We justify this approach by the fact that it has previously been shown [353] that phonon scattering is not likely to be the limiting mechanism in MoS₂ for the dopant concentration

used here.

The results are presented in Fig. 6.7 for chloride substitution and potassium adsorption. In these plots, each point corresponds to an average over 10 different systems with same length but with different random locations of the dopants. The uncertainty on these values is of the order of the marker size for K. For Li the uncertainty is increasing with length, below 10 nm it is of the order of the marker size and for 32 nm the PF value is $(9 \pm 6) \cdot 10^{-4} \mu\text{W}/\text{K}^2/\text{m}$. For these calculations, the length perpendicular to the transport direction (L_{\perp}) is kept constant and only the length L_z in the transport direction is varied. As expected, chloride doping is leading to very poor power factor when the length of the disordered system is increased. With raising the length of the system, an Anderson localization phenomenon is occurring, leading to an exponential decrease of the conductivity which is not compensated by the Seebeck increase. In these conditions, the PF is dropping very rapidly by 5 orders of magnitude with the length of the system. Conversely, for potassium the influence of the disorder is very small and the PF is only reduced by a factor of 3. One key quantity to estimate quantitatively the influence of the disorder is the localization length. [155, 354] For disordered systems, the conductivity can be expressed as a decaying law with the length for which, the localization length (L_c) comes as a reference length of the system. It can be expressed as:

$$\sigma(L) = \frac{\sigma_0}{e^{2L/L_c} - 1}. \quad (6.4)$$

We have represented the corresponding law for the two dopants in Fig. 6.7 as dotted

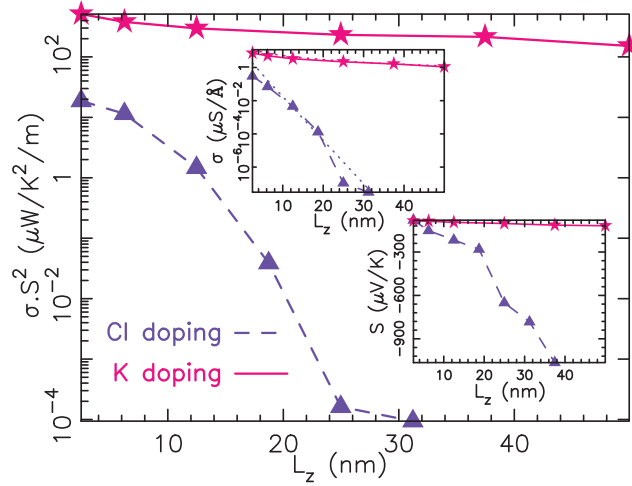


Figure 6.7: From Ref. [315]. Power factor for Cl and K doped MoS_2 as function of the device length (L_z). The dopant concentration is set to 12.5%. In inset is represented the Seebeck coefficient and the conductivity (the dotted lines corresponds to the fits). Each point corresponds to an average over 10 different configurations (random locations of the dopants)

lines (for K, it is almost not distinguishable from the data). This law is rather well verified, in the chloride case it is leading to a localization length of 3.5 nm and for potassium the derived L_c is about $1.5\ \mu\text{m}$. However, this last value is extracted from a very short length range compared with L_c and it must thus be taken as a lower bound of the possible L_c value for potassium. Anyhow, the 3 orders of magnitude between these two values is clearly illustrating the localization phenomenon occurring with chloride dopant.

In summary, we have investigated the thermoelectric properties of single layer transition metal dichalcogenide on the basis of *ab initio* quantum transport within the Landauer Büttiker formalism. We conclude, on the basis of rigid band model, that MoS_2 and WSe_2 are leading, for equivalent doping concentration, to the largest PF under electron doping compared to MoSe_2 and WS_2 . Moreover, by performing realistic doping, we observe that the substitution doping mechanism by chloride is inducing local states at the Fermi level, leading at low dopant concentration to a poor PF. In contrast, alkalis are acting as almost perfect electron donors, the band structure at the Fermi level is then very close to the band structure of the pristine TMDC layer. However, due to a degeneracy removal phenomenon, the PF obtained with alkali doping is not as large as the one obtained within the rigid band model. This point is tempering a bit the attractivity of TMDC for thermoelectric applications. Finally, we have investigated the influence of the disorder induced by the dopant. In case of adsorption doping by potassium the PF is barely affected by the disorder. Conversely, the disorder induced by substitution doping by chloride leads to an exponential drop of the PF within a typical length scale of 30 nm. This last point highlights the utmost importance of the Anderson localization phenomenon for TMDC materials when evaluating the transport properties.

6.2 Drastic effects of vacancies on thermal transport in graphene

Over the past decade, and because of its unique mechanical, electronic, optical and thermal properties, the 2D material prototype, graphene, has been at the heart of a plethora of publications [355, 295, 305]. Among all these remarkable properties, the particular topic of thermal transport has attracted much attention over the past years. Graphene exhibits an unusually high thermal conductivity [311, 356, 357, 358], that could, in the near future, make this two dimensional material one of the best candidates for efficient thermal dissipation in microelectronics. In addition, nanostructuring [359] and disorder [360] in graphene based compounds could be promising pathways for high-efficiency thermoelectric devices to transform waste heat into electrical energy. The desired effects are a drastic suppression of the thermal conductivity and significant improvement of the Seebeck coefficient, both required to reach a large thermoelectric efficiency.

Many efforts are still devoted to understanding the lattice thermal conductivity in graphene, but no clear consensus has been reached so far, the topic remains controversial. Experimentally, the measured room temperature thermal conductivity (κ) spans over a large range of values, typically between $400\ \text{W.m}^{-1}\text{K}^{-1}$ and $600\ \text{W.m}^{-1}\text{K}^{-1}$ for supported samples [357, 361] and $1500\ \text{W.m}^{-1}\text{K}^{-1}$ to $5400\ \text{W.m}^{-1}\text{K}^{-1}$ for suspended ones. [311, 357, 362] The important fluctuations in the measured values can be attributed

to (i) large measurement uncertainties, (ii) variations in the processing conditions and (iii) graphene quality. This could indicate a high sensitivity to intrinsic defects such as vacancies, lattice reconstruction, edge roughness or even ripples. From the theoretical side [363, 364, 365, 366, 367, 368], the scenario is even more open. The estimates of κ at room temperature in graphene vary by more than one order of magnitude, typically it ranges from $500 \text{ W.m.}^{-1}\text{K}^{-1}$ to about $9000 \text{ W.m.}^{-1}\text{K}^{-1}$.

In this section, using state of the art first principle based approaches, we address the issue of vacancies' effects on lattice thermal transport in single mono-layer graphene. For that purpose, we follow a two steps procedure. First, we calculate the vacancy induced multiple scattering contribution to the phonon lifetime by an exact real space treatment of the disorder. Notice that, in most of the existing theoretical studies, disorder is treated perturbatively. As will be seen, the second order perturbation theory appears to severely overestimate the phonon lifetimes. Note however, that the perturbation theory often used in the case of isotopic disorder is reasonable, because of the weak effects of the substitution of ^{12}C by ^{13}C . In the second step, we calculate the thermal conductivity as a function of the vacancy concentration by including phonon-phonon scattering (Normal and Umklapp processes) and going beyond the relaxation time approximation (RTA). It should be emphasized that all calculations are parameter free, since the disordered phonon dynamical matrix is obtained from first principle calculations.

6.2.1 Exact disorder contribution to the phonon dispersion and lifetimes

Fig. 6.8(left) shows the calculated dispersion in the pristine graphene monolayer along the Γ -M-K- Γ path in the Brillouin Zone (BZ). The inter-atomic force constants (IFC) $\phi_{\mathbf{ij}}^{\alpha\beta}$ have been calculated from first principle simulations, \mathbf{i} and \mathbf{j} are the positions of the C atoms and $\alpha, \beta = x, y$ and z .

The *ab initio* calculations are performed with the DFT package SIESTA [112]. The exchange-correlation functional used here corresponds to the generalized gradient approximation as proposed by Perdew, Burke & Ernzerhof [123]. However, the local density approximation leads to similar results. Troullier-Martin norm-conserving pseudopotentials [191] are used. The basis corresponds to a double- ζ -polarized basis optimized with the simplex tool of the SIESTA package. All the atomic structures were optimized up to forces less than 10^{-4} eV/\AA and to an hydrostatic pressure smaller than 10 bar. Finally, a Monkhorst-pack of $10 \times 10 \times 1$ k-points is used for the calculations along with a mesh cutoff of 600 Ry.

The IFC, $\phi_{\mathbf{ij}}^{\alpha\beta}$, were calculated by the finite displacement method. The displacement amplitude was 0.04 Bohr. Note that, we use the local constraint $\phi_{\mathbf{ii}}^{\alpha\beta} = -\sum_{\mathbf{j} \neq \mathbf{i}} \phi_{\mathbf{ij}}^{\alpha\beta}$ that ensures that no force results from a global translation of the whole system.

In the presence of a C vacancy, two different supercells have been used to compute the inter atomic force constants. First, we have considered a large rectangular supercell with dimensions $21.3 \text{ \AA} \times 24.6 \text{ \AA}$ (199 C atoms) and second a smaller diamond shaped supercell that contains 97 atoms. In both cases, the nearest-neighbours IFC ($\phi_{\mathbf{n}-\mathbf{n}}^{zz}$) exhibit the same axial symmetry (y-axis) as that of the chosen supercell. The average value of the $\phi_{\mathbf{n}-\mathbf{n}}^{zz}$

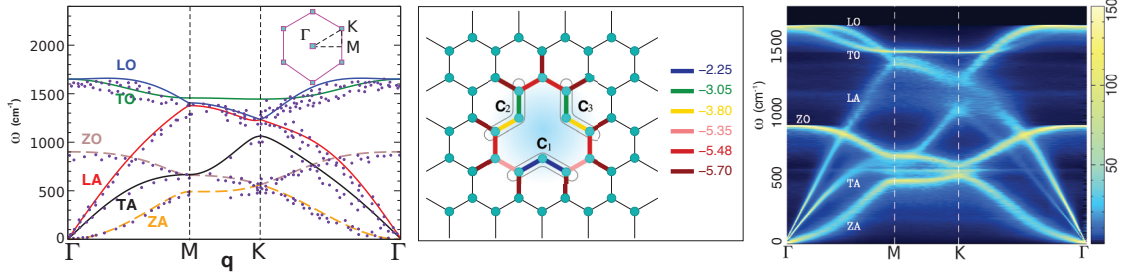


Figure 6.8: From Ref. [316]. (left) Calculated phonon dispersions in pristine graphene along the Γ -M-K- Γ path (continuous lines) for LA, TA, LO, TO, ZA and ZO branches. The dotted symbols are experimental data from Ref. [369, 370, 371]. (middle) *ab initio* calculated nearest-neighbour inter-atomic force constants for the ZA and ZO modes in the vicinity of a vacancy (in $\text{eV}/\text{\AA}^2$). (right) 2D color plot of the calculated averaged phonon dynamical spectral function $A_s(\mathbf{q}, \omega)$ in the presence of 5% of vacancies. The chosen polarisation for the in-plane modes is $\mathbf{e}_s = \frac{1}{\sqrt{2}}(\mathbf{e}_x + \mathbf{e}_y)$.

of the 2-coordinated atoms is $-3.03 \text{ eV}/\text{\AA}^2$ for the largest supercell and $-2.82 \text{ eV}/\text{\AA}^2$ for the smallest. The fluctuations around the average, were about $0.8 \text{ eV}/\text{\AA}^2$ and $0.4 \text{ eV}/\text{\AA}^2$ respectively for the rectangular and diamond shaped supercells. These fluctuations originates from the non-symmetric free relaxation of the C atoms in the supercells. The angles involving C_2 and C_3 of Fig. 1 in the manuscript are close to 121° , in contrast, that of C_1 is around 126° for the largest supercell, and the distance were slightly shorter for the bonds involving C_1 .

Note that in the case of graphene, in-plane (xy) and out of plane (z) modes are decoupled. We observe an excellent agreement between our calculations and the experimental data, over the whole BZ. We should emphasize that, we have retained the first 6 nearest neighbour shells for the calculations, including further shells has negligible effects.

In Fig. 6.8(middle) are plotted the nearest-neighbour inter-atomic force constants ϕ_{n-n}^{zz} for the out of plane modes (ZA and ZO) in the vicinity of a vacancy. The rectangular supercell used for the calculations contains 199 C atoms. In a pure graphene mono-layer ϕ_{n-n}^{zz} is $-6.1 \text{ eV}/\text{\AA}^2$. When a vacancy is introduced, ϕ_{n-n}^{zz} is strongly affected. More precisely, for the 2-coordinated C atoms the average value is only $-3.03 \text{ eV}/\text{\AA}^2$. As we move away from the vacancy we rapidly recover the value in the pristine compound. For larger distances between C atoms (beyond nearest-neighbours), the IFC are less affected by the presence of the vacancy. In what follows, and for simplicity, the inclusion of a vacancy is treated as follows: (i) a removal of a C atom and the corresponding bonds and (ii) a reduction by a factor 2 of the nearest neighbour IFC of the 2-coordinated C atoms, for both in and out of plane modes. We should mention, in contrast to what has been reported recently in a semi-empirical theoretical study [364], that the $\phi_{n-n}^{\alpha\beta}$ are not enhanced by a factor 2 but strongly suppressed as revealed by our first principle calculations.

To obtain the vacancy induced multiple scattering contribution to the phonon scattering rate, we evaluate numerically on large systems (typically 10^6 C atoms) the phonon dynamical

ical spectral function. Note that this function is directly accessible from inelastic neutron scattering experiments. For a fixed concentration of vacancies and given configuration of disorder (random positions of the vacancies), the dynamical spectral function reads (see section 4.1.2),

$$A_s(\mathbf{q}, \omega) = -\frac{2}{\pi} \omega \Im(G_s(\mathbf{q}, \omega)), \quad (6.5)$$

where

$$G_s(\mathbf{q}, \omega) = \lim_{\eta \rightarrow 0} \langle \mathbf{q}, s | \left[(\omega^2 + i\eta) \hat{\mathbf{1}} - \hat{\mathbf{D}} \right]^{-1} | \mathbf{q}, s \rangle, \quad (6.6)$$

where $\hat{\mathbf{D}}$ is the dynamical matrix and $|\mathbf{q}, s\rangle$ is a Bloch state with momentum \mathbf{q} and polarisation vector \mathbf{e}_s , and η is a small imaginary part. We define the plane wave state,

$$|\mathbf{q}, \alpha\rangle = \frac{1}{\sqrt{N}} \sum_{\mathbf{i}} e^{i\mathbf{q} \cdot \mathbf{r}_i} |\mathbf{i}, \alpha\rangle, \quad (6.7)$$

where the sum runs over the sites occupied by C atoms. For in plane modes, for a chosen polarisation vector $\mathbf{e}_s = \cos(\theta_s) \cdot \mathbf{e}_x + \sin(\theta_s) \cdot \mathbf{e}_y$, we define $|\mathbf{q}, s\rangle = \cos(\theta_s) |\mathbf{q}, x\rangle + \sin(\theta_s) |\mathbf{q}, y\rangle$. Hence, $\mathbf{e}_s = (\frac{q_x}{|\mathbf{q}|}, \frac{q_y}{|\mathbf{q}|})$, $(\frac{-q_y}{|\mathbf{q}|}, \frac{q_x}{|\mathbf{q}|})$ and $(\frac{1}{\sqrt{2}}, \frac{1}{\sqrt{2}})$ for respectively longitudinal, transverse and (1,1)-axis polarisation. For the out of plane modes (ZO, ZA) $\mathbf{e}_s = \mathbf{e}_z$. The matrix element $D_{\mathbf{ij}}^{\alpha\beta} = \frac{\phi_{\mathbf{ij}}^{\alpha\beta}}{\sqrt{m_i m_j}} x_i x_j$, where $x_i = 0$ if the site \mathbf{i} is occupied by a vacancy, otherwise $x_i = 1$. In addition, for 2-coordinated atoms $\phi_{\mathbf{ij}}^{\alpha\beta}$ is half of its value in the pristine compound for nearest-neighbour IFC only. For a given \mathbf{q} of the BZ, the peaks in $A_s(\mathbf{q}, \omega)$ provide both the energy of the phonon modes and the lifetimes that correspond to the inverse of the full width at half maximum (FWHM) of the peaks. To extract reliably and accurately the phonon peak positions and more particularly the FWHM that are strongly η dependent for low energy modes, the calculations are performed using the powerful iterative Chebyshev Polynomial Green's Function approach (CPGF) [262, 261] (see section 4.3.2). A similar methodology involving Chebyshev Polynomials to expand the time evolution operator has been developed earlier to address the dc conductivity in quasi crystals [372]. Note that performing a direct exact diagonalization of the disordered dynamical matrix, would require a large amount of both memory and CPU time. In particular the CPU time scales as N^3 , where N is the total number of C atoms. In contrast, the calculation using CPGF scales linearly with the system size and the memory required is small, because there is no need to store large matrices. We should emphasize that, within CPGF the treatment of the disorder is exact. Thus, quantum interferences and localization phenomena are fully included.

Fig. 6.8(right) represents the disorder averaged dynamical spectral function for both in plane and out of plane modes and a concentration of vacancies set to $x = 5\%$. Note that, because of the large system sizes considered here, a few configurations of disorder are enough to get reliable statistical average. In addition, in this figure, a small finite η has been kept for the sake of visibility. However, in what follows and in order to properly extract

the exact disorder contribution to the phonon lifetime the limit $\eta \rightarrow 0$ will be properly carried out. In the vicinity of the Γ point the phonon modes are well defined, but the ZA modes appear to have a much broader width than that of the in-plane acoustic modes. As we move away, along the Γ -M or Γ -K path, first the phonon width of the acoustic modes increases significantly (lifetime reduces) and then becomes almost constant. The case of the optical modes is slightly different. In particular, for TO branch, the width first increases rapidly then reaches a maximum and as we approach the zone boundary it decreases again. Along the M-K path, ZA, ZO and especially TO modes are very sharp in contrast to LA, TA and LO modes. In this region, it is difficult to separate LO and LA modes. It is worth mentioning two other interesting features: a well defined vacancy induced flat band located

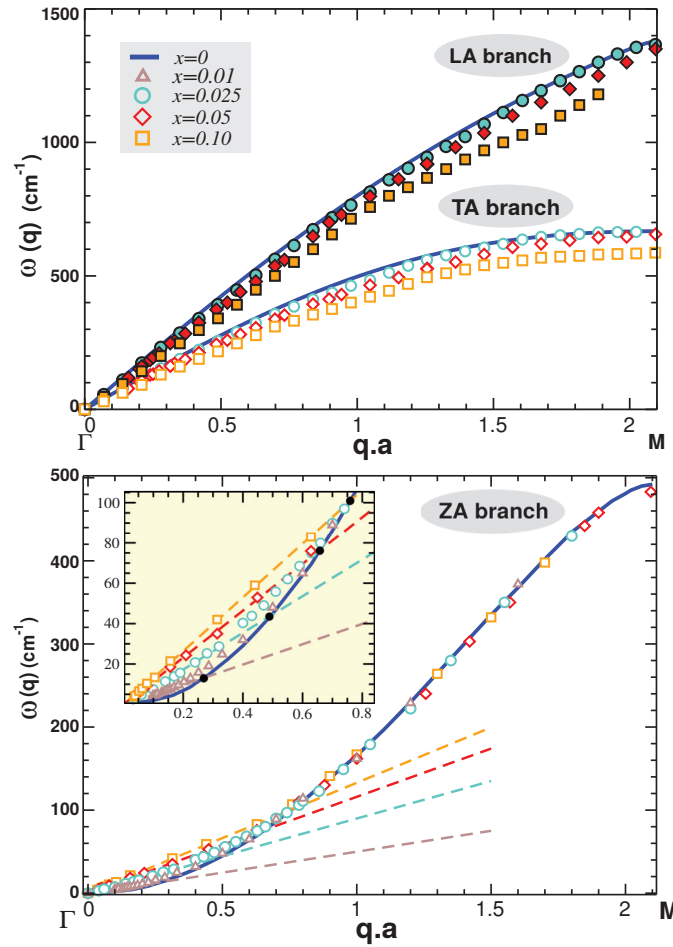


Figure 6.9: From Ref. [316]. (top) LA and TA phonon dispersions along the Γ -M direction for various concentrations of vacancies ranging from $x = 0$ to 0.1. (bottom) ZA phonon dispersion in the Γ M direction for the same concentrations. The dashed lines correspond to linear fits for the long wavelength phonons. The inset shows a zoom of this region.

at about 500 cm^{-1} and the disappearance (fuzzy region) of the phonon modes around 1200 cm^{-1} in the vicinity of the K point.

Let us now discuss the effects of the vacancy concentration (x) on phonon dispersions. We choose here to focus our attention on the Γ -M direction. The results for the acoustic modes LA, TA and ZA are depicted in Fig. 6.9. We first observe that both dispersions and velocities of LA and TA modes are weakly affected, the effects start to be visible for relatively large vacancy concentration of the order of 10%. In contrast, the situation is very different for the ZA branch. For large values of the momentum $|\mathbf{q}|$, the dispersion is insensitive to the vacancy concentration. However, in the vicinity of the Γ point the dispersion goes from quadratic to linear. The long wavelength modes develop a finite velocity v_{ZA} that depends on x . For instance, if we set $x = 5\%$, we find that v_{ZA} is as large as $0.15 v_{LA}$. As clearly shown in the inset, the region of linear dispersion rapidly increases with the concentration of defects.

We now propose to analyse the effects of vacancies on the phonon modes FWHM denoted $\Gamma(\omega)$. $A_s(\mathbf{q}, \omega)$ has been calculated in the whole BZ. Typically 200 to 300 \mathbf{q} -points uniformly distributed over the BZ have been targeted. Note that the number of Chebyshev polynomials (CP) considered were typically of the order of $2 \cdot 10^4$ for \mathbf{q} -points far from the BZ center. However, for the acoustic modes in the vicinity of the BZ center, because of the tiny values of the FWHM, it was necessary to include up to $3 \cdot 10^6$ CP to get converged results denoted "highly accurate calculations". $\Gamma(\omega)$ (rescaled by $x(1-x)$) as a function of the phonon mode energy is plotted in Fig. 6.10 for both LA and TA branches. The highly accurate calculations for the low energy modes in the Γ M direction are also shown. First, we observe for both branches a non monotonic behaviour of $\Gamma(\omega)$. We also find for $\omega \leq 400 \text{ cm}^{-1}$ that the data points obtained for various vacancy concentrations lie on the same curve. Beyond 400 cm^{-1} , we observe, for a given energy, larger fluctuations around the average value. They are relatively small for the LA branch, of the order of 10 %. In contrast, they are much larger for the TA modes. For instance, for $\omega = 600 \text{ cm}^{-1}$ the fluctuations are of the order of 30 %. However, beyond 700 cm^{-1} the fluctuations are strongly suppressed. In addition, for $\omega \leq 500 \text{ cm}^{-1}$, the FWHM is found cubic in energy: $\Gamma_\lambda(\omega) = x(1-x) \frac{\omega^3}{\omega_{0,\lambda}^2}$ where $\omega_{0,\lambda} = 288 \text{ cm}^{-1}$ and 236 cm^{-1} respectively for $\lambda = \text{LA}$ and TA . The cubic power law found here is in agreement with perturbation theory (PT) that gives $\Gamma_\lambda^{PT}(\omega) = x \frac{\pi}{2} (\frac{\Delta M}{M})^2 \omega^2 \rho_\lambda(\omega)$, ΔM is the mass variation of the substituted atom and $\rho_\lambda(\omega)$ denotes the phonon density of states in the pristine compound [150]. In the particular case of vacancies $\frac{\Delta M}{M} = -\frac{M_a}{M} - 2 \approx -3$, M_a being the mass of the missing atom and M the average mass per atom, -2 accounts for the potential energy of the missing linkage [151, 373]. For LA and TA modes the density of states is $\rho_\lambda(\omega) = \frac{\Omega}{2\pi v_\lambda^3} \omega$ where Ω is the primitive cell area. The comparison between PT and our exact results leads to $\Gamma_{LA}^{PT} \approx 0.018 \Gamma_{LA}$ and $\Gamma_{TA}^{PT} \approx 0.03 \Gamma_{TA}$. Thus, perturbation theory drastically underestimates the vacancy contribution to the scattering rate. This is not surprising considering the non-perturbative nature of such defects compared to isotopic disorder. Note that in a recent study [374] devoted to thermal transport in irradiated graphene, a value of $(\frac{\Delta M}{M})^2$ of the order of 590 instead of 9 was found necessary to reproduce the experimental data. This is entirely consistent with our finding that LA scattering rate is about 55 times larger

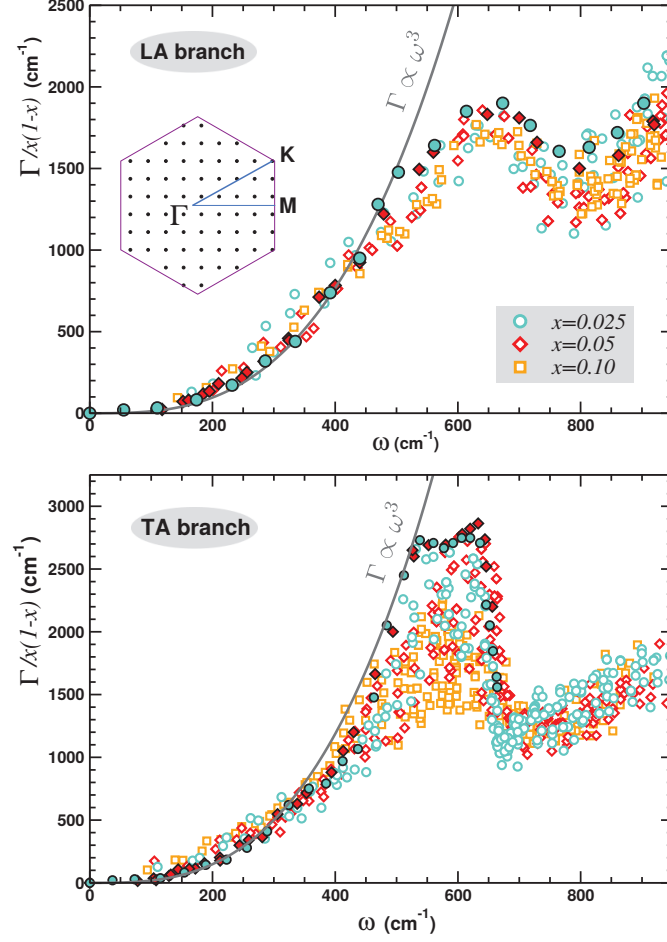


Figure 6.10: From Ref. [316]. (top) LA phonon full width at half maximum (rescaled by $x(1-x)$) at $T = 0$ K as a function of the phonon energy ω for $x = 0.025, 0.05$ and 0.1 . A grid of 200 to 300 \mathbf{q} -points uniformly distributed over the whole Brillouin zone has been used. The filled symbols correspond to highly accurate calculations in the Γ -M direction (see text). The continuous line is a cubic fit of this set of data up to 500 cm^{-1} . (bottom) Same as in the top figure but for TA branch.

than that predicted by PT.

The case of the ZA branch is even more interesting. $\Gamma(\omega)$ for the ZA branch is plotted in Fig. 6.11. First, after rescaling, the data points lie on a single curve as seen previously for in plane modes. The behaviour is non monotonic, $\Gamma(\omega)$ exhibits a maximum at about 200 cm^{-1} and a strong decrease as we approach the BZ boundary (M and K points). The fluctuations for a given ω are found relatively small, at most of the order of 10% to 15% around the average value. Unexpectedly, as we introduce vacancies, we find a linear behaviour of Γ_{ZA} as a function of the mode energy in the vicinity of the BZ center. The fluctuations are very small in this region as clearly seen in the inset. A linear fit for $\omega \leq 100$

cm^{-1} leads to $\Gamma_{ZA}(\omega) = 20x(1-x)\omega$. This linear scaling of the ZA width in the long

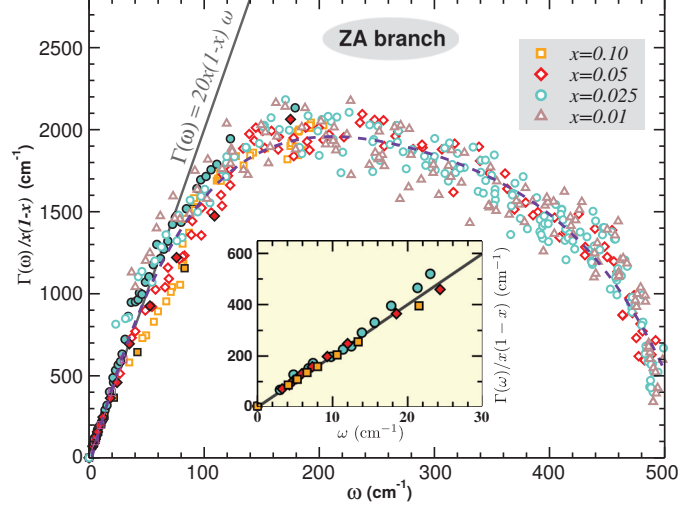


Figure 6.11: From Ref. [316]. ZA phonon full width at half maximum (rescaled by $x(1-x)$) at $T = 0$ K as a function of the phonon energy ω for $x = 0.01, 0.025, 0.05$ and 0.1 . A grid of 200 to 300 \mathbf{q} -points uniformly distributed over the whole Brillouin zone has been used. The filled symbols correspond to highly accurate calculations in the Γ -M direction (see text). The continuous line is a linear fit for the low energy modes (see inset).

wavelength regime means that these modes are marginal since $\lim_{\omega \rightarrow 0} \frac{\Gamma_{ZA}}{\omega} = 20x(1-x)$. For well defined excitations, one expects this ratio to be zero. Furthermore, $\Gamma_{ZA}(\omega) \geq \omega$ for $x \geq 0.05$, hence the phonon quasi-particles are not well defined in this range of vacancy concentrations. These findings are in strong contrast with perturbation theory. Indeed, it is expected that $\Gamma_{ZA}^{PT}(\omega) = x(\frac{\Delta M}{M})^2 \frac{\Omega}{8D} \omega^2$ where D is the stiffness of the ZA branch in the pristine compound, i.e. $\omega(\mathbf{q}) = D|\mathbf{q}|^2$ in the long wavelength limit. Therefore, the prediction of a quadratic power law from perturbation theory is inconsistent with the exact numerical results. For example, for $\omega = 50 \text{ cm}^{-1}$ and 100 cm^{-1} we find $\frac{\Gamma_{ZA}^{PT}}{\Gamma_{ZA}} = 0.045$ and 0.09 respectively. Once again, perturbation theory severely overestimates the phonon lifetime and hence the mean free path of the ZA phonon modes in the presence of vacancies. Because the thermal conductivity is dominated by the ZA modes in both pristine graphene and in the presence of C isotopes[375], we naturally expect in the calculation of κ a strong deviation from PT as vacancies are introduced.

6.2.2 Effects of vacancies on the thermal conductivity

Linearized Boltzmann Transport Equation (BTE) is a frequently used and efficient theoretical approach to address the thermal conductivity in 2D and 3D materials (see section 2.2.1). In the great majority of studies, and because solving exactly the BTE is more cumbersome [376, 377], the relaxation time approximation (RTA) is often assumed. However, comparative studies have revealed that RTA calculated thermal conductivity is often much smaller

than the full BTE solution in 3D [378, 379, 380, 381]. The discrepancy is even stronger in 2D compounds such as pristine or natural graphene monolayer [365, 375, 382]. The origin of the discrepancy is the fact that within RTA, Umklapp (U) and Normal (N) phonon-phonon scattering processes are treated on equal footings, as resistive. However, N processes are not resistive, the thermal conductivity is expected to diverge in the absence of U scattering. There is an alternative to full BTE that can be implemented more easily and corrects the shortcomings intrinsic to the RTA approach. Several decades ago, Callaway proposed a theory that allows U and N processes to be treated separately [152, 153, 154]. It has been found that the Callaway theory leads to thermal conductivities that agree very well with the full BTE approach in 3D systems such as Si [383] and even in graphene [134]. Here, we propose to address the effects of the vacancies on thermal conductivity using the Callaway approach (see section 2.2.1, the details of the calculation are given in appendix A). Within this approach the thermal conductivity in the α -direction reads,

$$\kappa^\alpha = \kappa_{RTA}^\alpha + \Delta\kappa^\alpha, \quad (6.8)$$

the first term is the RTA contribution and the second one is the correction due to the appropriate separation between resistive and non-resistive processes. κ_{RTA}^α is given by,

$$\kappa_{RTA}^\alpha = \frac{1}{k_B T^2} \frac{1}{N \Omega \delta} \sum_{\mathbf{q}, \lambda} (\hbar \omega_\lambda)^2 (v_\lambda^\alpha)^2 \tau_\lambda^{tot} f_\lambda^0 (f_\lambda^0 + 1), \quad (6.9)$$

δ is the separation of carbon planes in graphite, f_λ^0 is the Bose-Einstein distribution for the λ -branch and v_λ^α the velocity in the α -direction. According to Mathiessen's rule the total phonon lifetime is $1/\tau_\lambda^{tot} = 1/\tau_\lambda^N + 1/\tau_\lambda^U + 1/\tau_\lambda^D$. We remind that the disorder contribution is $\tau_\lambda^D = \frac{\hbar}{\Gamma_\lambda}$. The full expression of $\Delta\kappa^\alpha$ is given in section 2.2.1 and appendix A.

To compute numerically the total conductivity as a function of temperature, we need the temperature dependence of τ_λ^N and τ_λ^U . We use the *ab initio* calculated scattering rate at room temperature (T_0) for both U and N processes ($\tau_{0,\lambda}^N, \tau_{0,\lambda}^U$) extracted from Ref. [366]. We make the following ansatz to have the full T variation of the scattering rates,

$$1/\tau_\lambda^N(T) = (1/\tau_{0,\lambda}^N) \frac{T}{T_0} \quad (6.10)$$

and the Umklapp scattering rate is,

$$1/\tau_\lambda^U(T) = (1/\tau_{0,\lambda}^U) \frac{T}{T_0} e^{-\frac{\omega_{D\lambda}}{3} (\frac{1}{T} - \frac{1}{T_0})}. \quad (6.11)$$

This ansatz is motivated by the fact that the form usually assumed for the N and U process are, $1/\tau_\lambda^N = \omega^a T^b$ and $1/\tau_\lambda^U \propto (1/\tau_\lambda^N) e^{-\frac{\omega_{D\lambda}}{cT}}$ where $a = 1$ or 2 , $b = 1, 2$ or 3 and c is often set to 3 [152, 384, 385, 386]. For the vacancy concentration dependent scattering $1/\tau_\lambda^D$ we use the results found in the present study.

In Fig. 6.12, the average thermal conductivity $\kappa = (\kappa^x + \kappa^y)/2$ (see eq. (6.8)) is plotted as a function of temperature for various concentrations of vacancies. In the clean limit ($x = 0$), we find very high values of the thermal conductivity and because of the presence

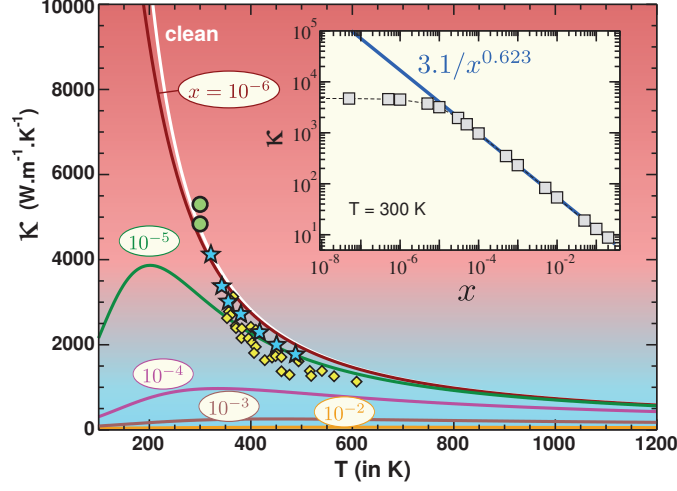


Figure 6.12: From Ref. [316]. Thermal conductivity κ in $\text{W.m}^{-1}\text{K}^{-1}$ as a function of temperature for various concentrations of vacancies ranging from 0 to 0.01 (continuous lines). The symbols (circles, stars and diamonds) are experimental measurements extracted from Refs. [311, 358, 312]. The inset represents the variation of the room temperature κ as a function of x , the blue continuous line is a fit for $x \geq 10^{-5}$.

of the U-processes, we observe a $1/T$ suppression of κ . As we introduce a very small amount of vacancies of the order of $x = 10^{-5}$ only, the effects are dramatic below 200 K. At room temperature, κ is already reduced by 40 % and the suppression is even stronger for $x = 10^{-4}$. Indeed, for this concentration, $\kappa = 1000 \text{ W.m}^{-1}\text{K}^{-1}$ at room temperature, five times smaller than that of pristine graphene. As we increase the vacancy concentration to 0.1%, the thermal conductivity falls to $\kappa = 200 \text{ W.m}^{-1}\text{K}^{-1}$, 25 times smaller than that of pristine. The variation of κ at 300 K is plotted in the inset as a function of x and reveals a crossover around $x = 10^{-5}$. Below this concentration, κ is weakly sensitive to the defects concentration, and above, κ decreases rapidly with a power law decay $\kappa \propto 1/x^{0.623}$. There is no simple way to anticipate such an exponent. Let us now compare our results to experimental measurements[311, 358, 312]. At room temperature, in the pristine limit, we obtain $\kappa = 4800 \text{ W.m}^{-1}\text{K}^{-1}$ which is in very good agreement with the highest experimental values of the thermal conductivity ever reported [311]. The agreement with the other data sets beyond room temperature is also relatively good. The measured values are consistent with an extremely low concentration of defects of the order of $x = 10^{-6}$ to 10^{-5} suggesting that the samples should be of good quality. Notice that, the agreement between theory and experiments, in the pristine case, has already been achieved in the full BTE calculations of Refs. [365, 375].

Our prediction for the thermal conductivity dependance on the vacancy concentration can be compared with the experimental measurements of Ref. [374] on suspended graphene samples subjected to electron beam irradiation. We also compare our results with those of several molecular dynamics (MD) studies of thermal transport in vacancy-ridden graphene [374, 387, 363, 388]. Due to the huge fluctuations in the theoretical and experimental values

	κ_0 (W m ⁻¹ K ⁻¹)
Our theory	4720
Exp. [a] (est.)	2000
RNEMD [a]	1249
NEMD [b]	175
NEMD [c]	475
EMD [d]	2913

Table 6.3: The room-temperature thermal conductivity κ_0 for clean graphene ($x = 0$) corresponding to the data in Fig 6.13. The MD values are taken from Ref. [374] ([a]), Ref. [387] ([b]), Ref. [363] ([c]), and Ref. [388] ([d]). The experimental value is estimated from Ref. [374].

for the room-temperature thermal conductivity of pristine graphene κ_0 (see table 6.3), it is most relevant to compare the ratio of the thermal conductivity in the presence of vacancies to the thermal conductivity of clean graphene, as shown in Fig. 6.13. Our results are in very good agreement with the experimental data, with a substantial drop in conductivity starting for very low vacancy concentrations around 10^{-5} . The MD data, on the other

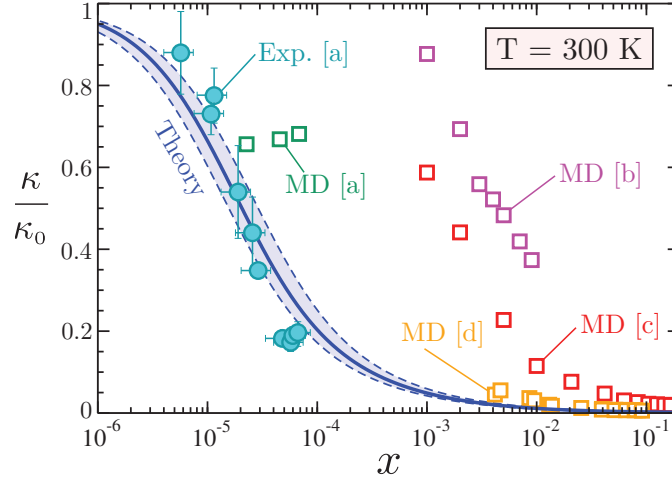


Figure 6.13: From Ref. [317]. The thermal conductivity at $T = 300$ K as a function of the vacancy concentration x and renormalized by the value κ_0 for $x = 0$. The shaded region around the solid line (our theory) corresponds to a 30% variation in the strength of the disorder scattering. The circles are experimental data from Ref. [374]. The squares are molecular dynamics data from Ref. [374] (green, [a]), Ref. [387] (magenta, [b]), Ref. [363] (red, [c]) and Ref. [388] (orange, [d]).

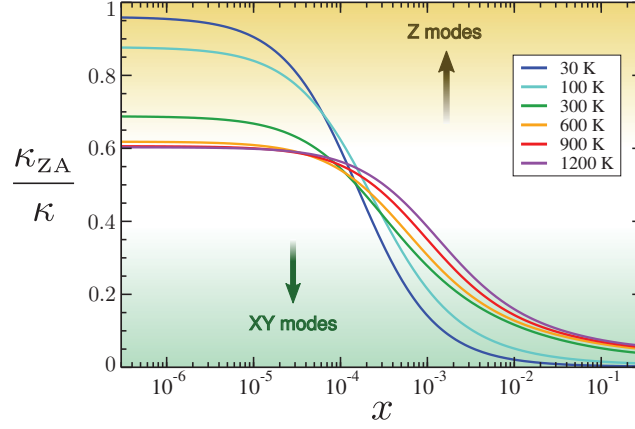


Figure 6.14: From Ref. [317]. The weight of the ZA modes in the calculated thermal conductivity as a function of the vacancy concentration x , from 30 K to 1200 K.

hand, exhibit a clear discrepancy with the measured values, at least regarding the non-equilibrium MD (NEMD) results. This is possibly due to strong finite-size effects that can be expected in NEMD simulations. Also, the interatomic potentials used in MD to describe the C-C interactions might not be well-suited for thermal conductivity calculations.

It is also instructive to investigate the relative contributions of the in-plane and out-of-plane modes in thermal transport when vacancies are present. Despite their quadratic dispersion, the ZA modes have been shown to dominate the thermal conductivity of clean graphene at room-temperature [375]. In Fig. 6.14 is shown the weight of the ZA modes in the thermal conductivity as a function of x for several temperatures. For low vacancy concentrations ($x < 10^{-4}$), the ZA contribution accounts for 60% of the total conductivity at high temperatures (600 K and beyond), 70% at room-temperature and completely dominates at low temperatures. However, because the ZA modes are very sensitive to disorder, their contribution drops when the vacancy concentration is increased to 10^{-3} , and becomes negligible in highly disordered graphene ($x = 10\%$).

6.2.3 Size effects and phonon mean free paths

A somewhat controversial aspect of thermal transport in graphene is the size dependence of the thermal conductivity. The suspended samples used in thermal conductivity measurements are only a few μm long, which is not much larger than the typical phonon mean free path in silicon, for instance [162, 67]. Consequently, ballistic phonon transport and size effects are thought to be relevant in graphene [134, 365, 375], and there are even predictions of a thermal conductivity diverging logarithmically with the system length [389]. In many experimental setups, the thermal conductivity is measured by laser heating the center of a graphene sheet suspended over a circular or rectangular hole [311, 357, 390, 356, 391]. A proper inclusion of size effects in these cases would require solving the Boltzmann transport equation in such nontrivial geometries [365]. However, a systematic experimental study of

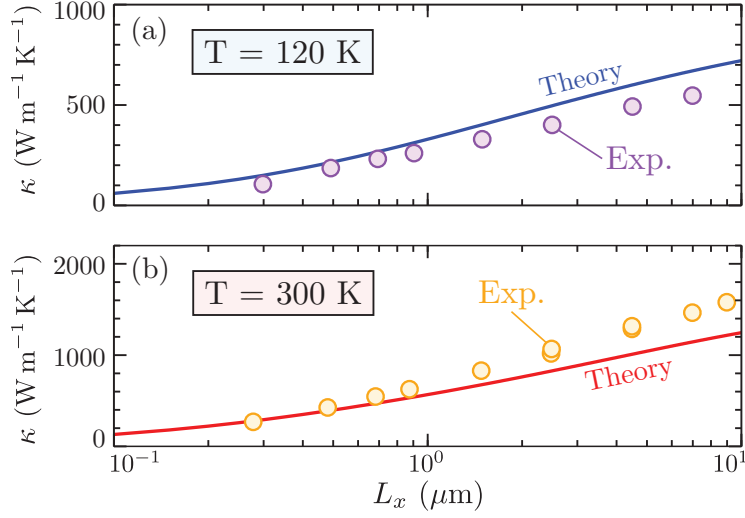


Figure 6.15: From Ref. [317]. The thermal conductivity as a function of the system length L_x , at (a) $T = 300$ K and (b) $T = 120$ K. The calculations (solid lines) are carried out with a vacancy concentration $x = 2.5 \times 10^{-5}$, a width $L_y = 1.5 \mu\text{m}$ and a specularity parameter $p = 0.85$. The circles are experimental data from Ref. [389].

the thermal conductivity dependance on the system length was performed in Ref. [389] on rectangular graphene sheets suspended between large SiN_x membranes acting as heat source and heat sink. Such a situation can be reasonably described in the framework of Boltzmann transport by introducing an energy-dependant ballistic scattering rate corresponding to a mean free path equal to the system length L_x in the transport direction (see section 2.2.2 and equation (2.83)). This procedure recovers the results of the Landauer formalism when the system length is much smaller than the mean free path associated with the usual scattering mechanisms. For the LA and TA branches, the ballistic scattering rate is a constant $\frac{1}{\tau_{\lambda}^B} = \frac{\pi}{2} \frac{v_{\lambda}}{L_x}$, while for the ZA branch it can be expressed as $\frac{1}{\tau_{\lambda}^{ZA}} = \frac{\pi}{2} \frac{\sqrt{4D\omega}}{L_x}$. As the width of the graphene sheet in Ref. [389] is $1.5 \mu\text{m}$, which is small compared to the largest length of $9 \mu\text{m}$, we also take into account the possibility of phonon scattering on the rough edges of the sample. This is done by introducing a scattering rate $\frac{1}{\tau_{\lambda}^E} = \frac{\pi}{2} \frac{v_{\lambda}}{L_y} \frac{1-p}{1+p}$ for the LA and TA branches and $\frac{1}{\tau_{\lambda}^{EA}} = \frac{\pi}{2} \frac{\sqrt{4D\omega}}{L_y} \frac{1-p}{1+p}$, where L_y is the sample width and p is the so-called specularity parameter measuring the roughness of the edges ($p = 1$ corresponds to perfect edges i.e. no resistive edge scattering). p is usually in the range $0.8 - 0.9$ and has been estimated to be approximately 0.9 from scanning electron microscopy data [392, 312, 364], therefore we choose $p = 0.85$. Fig. 6.15 shows a comparison between the experimental data from Ref. [389] and the calculated thermal conductivity at 120 K and 300 K as a function of the sample length. A very good agreement between theory and experiment is found for the vacancy concentration $x = 2.5 \times 10^{-5}$, demonstrating that the measurements are compatible with a finite value of the thermal conductivity at the thermodynamic limit $L_x = \infty$,

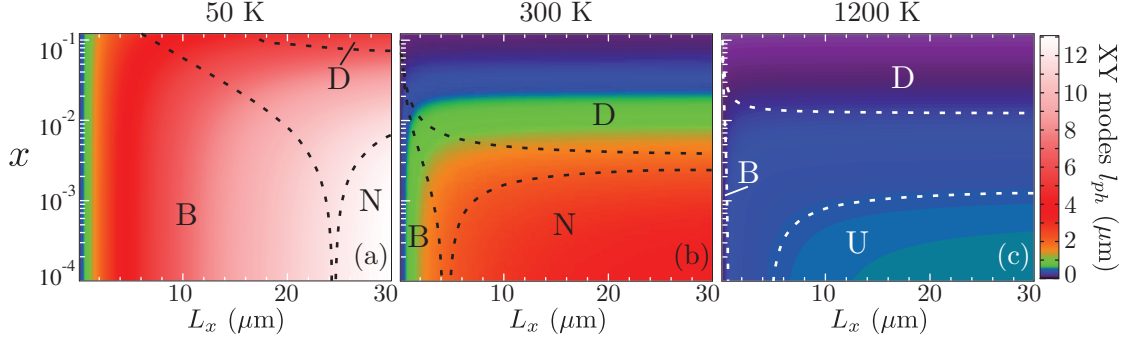


Figure 6.16: From Ref. [317]. Color graph of the energy-averaged phonon mean free path l_{ph} of the XY modes at (a) 50 K, (b) 300 K and (c) 1200 K with respect to the system length L_x and to the vacancy concentration x . The width L_y is assumed infinite. The dashed lines correspond to different regimes for l_{ph} , where it is mostly ballistic (B), dominated by disorder scattering (D), by Normal phonon-phonon scattering (N), and by Umklapp phonon-phonon scattering (U).

as opposed to a logarithmic divergence of κ .

Having validated our procedure of including a ballistic scattering rate to account for the finite size of the system, we now calculate the phonon mean free path l_{ph} , neglecting for simplicity the rough edge scattering ($L_y = \infty$). The total energy and temperature dependant scattering rate $\frac{1}{\tau_\lambda}$ is given by Matthiessen's rule:

$$\frac{1}{\tau_\lambda} = \frac{1}{\tau_\lambda^B} + \frac{1}{\tau_\lambda^D} + \frac{1}{\tau_\lambda^N} + \frac{1}{\tau_\lambda^U}. \quad (6.12)$$

The energy dependant mean free path is then calculated using equation (2.82), which yields $l_{ph}^\lambda(\omega) = \frac{\pi}{2} v_\lambda \tau_\lambda(\omega)$ for the LA and TA branches and $l_{ph}^{ZA}(\omega) = \frac{\pi}{2} \sqrt{4D\omega} \tau_{ZA}(\omega)$ for the ZA branch. We then obtain an typical value for l_{ph} by averaging the inverse mean free paths over the energy:

$$\frac{1}{l_{ph}^\lambda} = \frac{\int d\omega \rho_\lambda(\omega) f_\lambda^0(\omega) \frac{1}{l_{ph}^\lambda(\omega)}}{\int d\omega \rho_\lambda(\omega) f_\lambda^0(\omega)}. \quad (6.13)$$

In Fig. 6.16 is plotted a color map of the total phonon mean free path of the in-plane modes (LA and TA branches) as a function of the system length L_x and vacancy concentration x . Low (50 K), ambient (300 K) and high (1200 K) temperatures are considered, and the scattering regimes where different scattering mechanisms dominate are demarcated by dashed lines. We consider that disorder scattering dominates, for instance, if the mean free path is multiplied by a factor less than 2 when all the other scattering mechanisms are neglected. Overall, the mean free paths are of the order of the micrometer even at high temperatures, and can even increase to around $10 \mu\text{m}$ at low temperatures. At room temperature, there is a non-negligible ballistic regime for system sizes up to $4 \mu\text{m}$ and vacancy concentrations lower than 1%. The Normal and disorder scattering processes otherwise dominate depending on the vacancy concentration. At low temperatures, the transport

is mostly ballistic even for system sizes of $25\text{ }\mu\text{m}$, while it is overwhelmingly diffusive at high temperatures. The Umklapp processes actually dominate over Normal phonon-phonon scattering at 1200 K.

Fig. 6.17 shows the same plot for the out-of-plane modes (ZA branch). Notice that the scales for l_{ph} , L_x and x are different. The ZA mean free paths are about an order of magnitude smaller than their LA and TA counterparts and, due to the high sensitivity of the in-plane modes to the presence of vacancies, the disorder quickly dominates transport for vacancy concentrations as low as $0.01 - 0.1\%$. Thermal transport is actually mostly diffusive at room temperature for the Z modes, with scattering dominated by the Normal phonon-phonon processes at low vacancy concentration. This does not necessary means, however, that the size effects observed in fig. 6.15 are only due to the XY modes, because the N processes are not resistive and the phonon mean free path cannot be directly related to the thermal conductivity. Nevertheless, the phonon-phonon processes are quite weak at low temperature, which does suggest a high sensitivity of the thermal conductivity to the sample geometry and quality. At all temperatures, the Normal processes dominate over the Umklapps, indicating a probable failure of the RTA for the thermal conductivity, at least for $x < 0.1\%$.

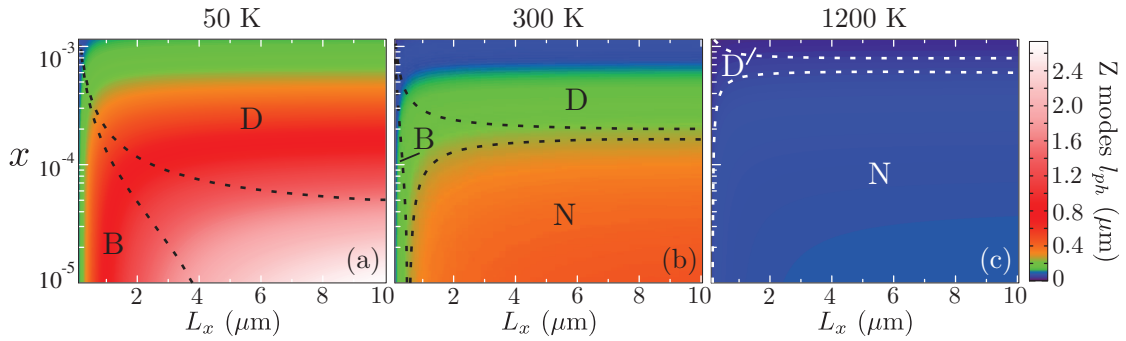


Figure 6.17: From Ref. [317]. Color graph of the energy-averaged phonon mean free path l_{ph} of the Z modes at (a) 50 K, (b) 300 K and (c) 1200 K with respect to the system length L_x and to the vacancy concentration x . The width L_y is assumed infinite. The dashed lines correspond to different regimes for l_{ph} , where it is mostly ballistic (B), dominated by disorder scattering (D), and by Normal phonon-phonon scattering (N).

Finally, it is interesting to comment on the validity of the RTA approximation. In Fig. 6.18 is shown the ratio $\frac{\Delta\kappa}{\kappa_{RTA}}$ as a function of T . Let us first consider low vacancy concentrations ($x \leq 10^{-4}$). For this range of concentration, the correction $\Delta\kappa^\alpha(T)$ is important and even dominates. For instance the ratio $\Delta\kappa/\kappa_{RTA}$ is 1, 4.5 and 7.5 for $x = 10^{-4}$, 10^{-5} and for the pristine case at room temperature. On the other hand, when the vacancy concentration is large enough beyond 0.1% of the C atoms, the correction becomes very small, it is less than 15% of the RTA value. For $x = 1\%$ the correction to RTA represents only 5% of the total conductivity. These results show that in the presence of a sufficient amount of C vacancies, beyond 0.1%, the RTA approach becomes appropriate for the evaluation of the thermal conductivity, provided that the scattering rates are calculated

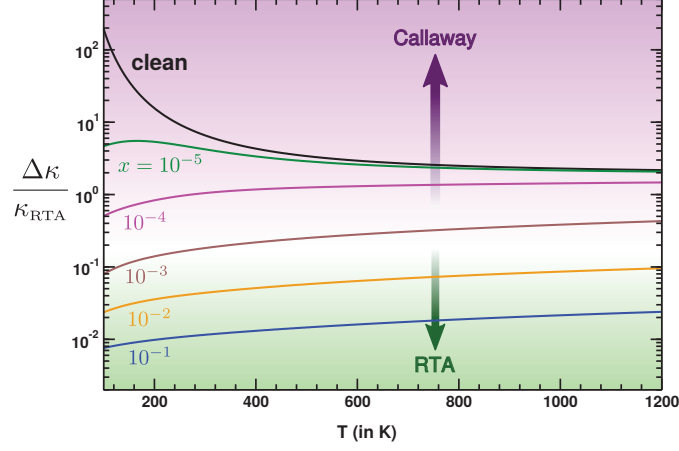


Figure 6.18: From Ref. [316]. (Color online) Callaway's correction to the total thermal conductivity over RTA contribution as a function of temperature, for various concentrations of C vacancies. The green area corresponds to negligible Callaway correction ("RTA regime") and the purple one to dominant Callaway correction.

accurately.

Combining state of the art *ab initio* approaches with a full and exact treatment of the disorder, we have addressed the impact of vacancies on phonon thermal transport in graphene. It has been found that the vacancy induced multiple scattering contribution to phonon lifetimes are much larger than predicted by second order perturbation theory. Furthermore, vacancies have drastic effects on both dispersion and lifetime of ZA modes. The ZA dispersion becomes linear in the vicinity of the Brillouin zone center and the vacancy induced scattering rate is linear in energy instead of the quadratic behaviour often assumed. We have also shown that the vacancies have dramatic effects on the thermal conductivity calculated beyond the relaxation time approximation. A mere 0.1% of vacancies leads to a spectacular 95% suppression of the thermal conductivity at room temperature. This strong dependance of thermal transport on the vacancy concentration is found in agreement with experimental data from electron beam irradiated samples. We have modeled the ballistic-to-diffusive transition in the framework of Boltzmann transport and found a good agreement with experimental measurements, suggesting that the thermal conductivity does not diverge at the thermodynamic limit. These findings contribute to a better understanding of thermal transport in 2D materials and could be promising for high-efficiency thermoelectric power generation as the high lattice conductivity in natural graphene is the major obstacle. It is also worth noticing that our methodology is very general, it could easily incorporate other features such as extended defects, porosity and nanostructuring.

Conclusions and perspectives

In this thesis, we have used a combination of density functional theory calculations and real-space methods to study the thermoelectric transport properties of several compounds through the Boltzmann transport equation or the Kubo formalism. This approach has proved well-suited to tackle the challenges posed by the optimization strategies of thermoelectric materials, which often involve strong disorder effects in large systems.

It has allowed us to investigate the electronic transport properties of two oxides, SrTiO₃ and rutile TiO₂. While we predict low thermoelectric performances for TiO₂ due to the strong electron-phonon coupling in this material, n-doped SrTiO₃ exhibits a very good maximum power factor at room temperature, on par with current state-of-the-art thermoelectric materials such as bismuth telluride. This is in part due to the strong orbital anisotropy in strontium titanate, which gives a two-dimensional character to electronic transport and mimics the effects of quantum confinement. This band-structure anisotropy has negative consequences as well: we predict that confining the conduction electrons in a single atomic layer of SrTiO₃ would be counterproductive for the thermoelectric performances, in addition to being technically difficult. Moreover, the introduction of resonant states in SrTiO₃, and indeed also in BaTiO₃ and CaTiO₃ that share a very similar band-structure, appears to be a dead end, in part because of the two-dimensional character of the Ti orbitals in these compounds. Vanadium doping in SrTiO₃, in particular, is found to destroy the thermoelectric performances due to Anderson localization effects. Still, resonant states remain a promising prospect to boost the power factor, particularly in materials exhibiting weak electron-phonon scattering, such as lead telluride [281] or certain Half-Heusler alloys like ZrNiSn [286].

We have studied the transport properties of two-dimensional materials, in which electrons and phonons are confined in an atomic plane. Fully *ab initio* calculations of electronic transport in single-layer transition-metal dichalcogenides show that doping should be done using adatoms rather than substitutional impurities which lead to a localization of the charge carriers. We have also calculated the phonon scattering rates and thermal conductivity of graphene in the presence of vacancies. The out-of-plane vibrational modes are found very sensitive to disorder, and even low vacancy concentrations lead to a huge reduction of the thermal conductivity. This encouraging result for thermoelectric applications could be supplemented by a similar study of electron transport in vacancy-ridden graphene, which would yield a complete picture of thermoelectric transport in this material and would allow a full prediction of the figure of merit.

The use of defects and disorder appears to be a particularly efficient and promising

strategy to suppress and curtail the thermal conductivity, not just in graphene but in three-dimensional materials as well. The generally long mean-free paths of phonons (they reach the micrometer scale in silicon, for instance [162, 67]) should give ample opportunity to tune and control thermal transport by introducing strong, perhaps anisotropic disorder. Filled clathrates and skutterudites, for instance, are exemplars of very successful thermal conductivity suppression using point defects [50]. Our methodology is well suited to study different types of impurities and disorder and their effect on phonon transport. Such theoretical investigations could guide experimentalists towards the most efficient systems for thermal management and energy applications.

More generally, combining *ab initio* calculations with a real-space treatment of disorder based on the single-particle Green's function should constitute an efficient approach to study electron and phonon transport in the presence of extended defects and nanostructures. Introducing grain boundaries and random nanoinclusions, for instance, has become a standard strategy to decrease the thermal conductivity of thermoelectric materials [67]. However, the theoretical modelling of their effects on both electron and phonon transport remains challenging as the validity of the Boltzmann picture is doubtful for small grain sizes (see Fig. 6.19a). Another example of extended defect that could influence the transport properties are ripples and strain fields expected to be present in two-dimensional materials, both suspended or supported by a substrate (see Fig. 6.19b). In graphene, such out-of-plane deformations are typically 10 Å high, several nanometers long, and have been proposed as the dominant electron scattering mechanism in high-quality samples [393, 394].

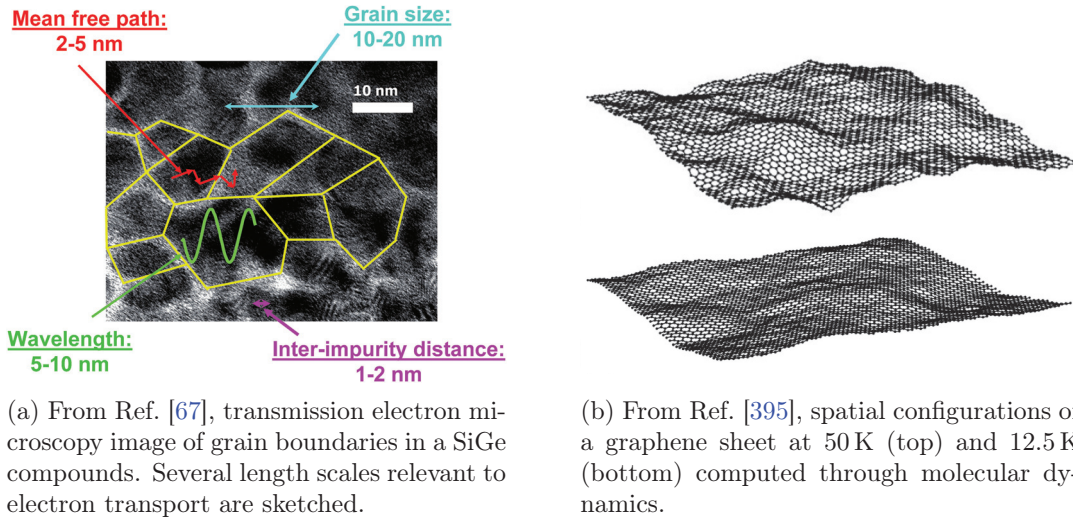
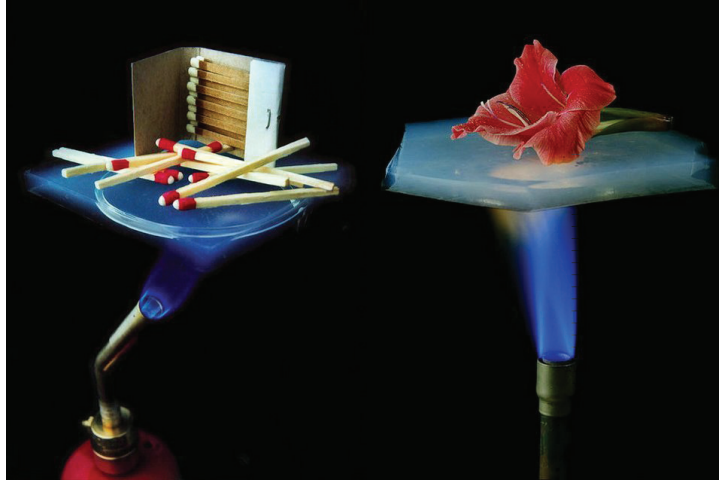
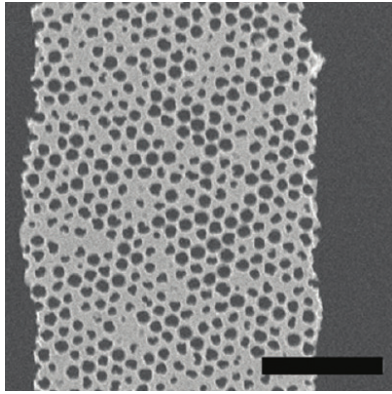


Figure 6.19

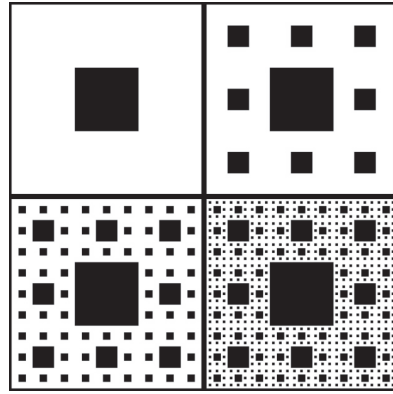
Nanoporous materials, i.e. solids with a high density of empty spaces (pores) in their structure, display remarkable properties and constitute another potential area in which our methodology could be usefully applied (see Fig. 6.20a and Fig. 6.20b). They are classified as microporous if the pore size is less than 2 nm, mesoporous if it is between 2 nm and 50 nm, and macroporous if it is more than 50 nm [397]. In the case of nanoporous silicon, these



(a) A demonstration of the thermal insulating properties of silica aerogels.



(b) From Ref. [396], scanning electron microscopy image of nanopores in a thin silicon membrane.



(c) The first steps of a Sierpinski carpet.

Figure 6.20

structures can be efficiently synthesized, are easily scalable, and represent a promising optimization strategy for thermoelectric power generation [398]. Both numerical simulations (Monte Carlo, DFT and molecular dynamics) [399, 400] and experimental measurements [396, 401] show a suppression of the thermal conductivity by orders of magnitude, while electronic transport may be weakly affected. Finally, fractal materials are crystalline or molecular compounds featuring self-similar nanostructures, such as pores in a Sierpinski carpet configuration (see Fig. 6.20c). These materials can now be synthesized from two-dimensional compounds through nanolithography and etching techniques [402] or directly from molecules through bottom-up self-assembly processes [403]. Neither periodic nor disor-

dered, they constitute an altogether different class of systems whose electronic and thermal properties likely exhibit unique properties. In recent years, several numerical studies of the thermal and electrical conductivity in fractal crystals based on either graphene [404, 405] or model lattices [406, 407, 408] have been carried out. Using a variety of approaches, such as the Landauer and NEGF formalisms, molecular dynamics simulations and expansion of the time-dependant evolution operator on the Chebyshev polynomial basis, they have found remarkable transport properties related to the geometrical pattern of the nanostructures, including self-similarity in the energy-dependant electronic transmission. In these systems, too, our methodology could prove extremely fruitful.

List of publications

Published

S. Thébaud, Ch. Adessi, and G. Bouzerar. **Large enhancement of the thermoelectric power factor in disordered materials through resonant scattering.** *Phys. Rev. B*, 99:245203, Jun 2019.

G. Bouzerar, S. Thébaud, R. Bouzerar, S. Pailhès, and Ch. Adessi. **Absence of confinement in $(\text{SrTiO}_3)/(\text{SrTi}_{0.8}\text{Nb}_{0.2}\text{O}_3)$ superlattices.** *Phys. Rev. Materials*, 2:035402, Mar 2018.

S. Thébaud, Ch. Adessi, S. Pailhès, and G. Bouzerar. **Boosting the power factor with resonant states: A model study.** *Phys. Rev. B*, 96:075201, Aug 2017.

G. Bouzerar, S. Thébaud, Ch. Adessi, R. Debord, M. Apreutesei, R. Bachelet, and S. Pailhès. **Unified modelling of the thermoelectric properties in SrTiO_3 .** *EPL*, 118(6):67004, 2017.

Ch. Adessi, S. Thebaud, R. Bouzerar, and G. Bouzerar. **First principle investigation on thermoelectric properties of transition metal dichalcogenides: Beyond the rigid band model.** *The Journal of Physical Chemistry C*, 121(23):12577–12584, 2017.

Submitted or in preparation

Ch. Adessi, S. Thébaud, and G. Bouzerar. **Ab initio investigation of the role of vanadium impurity states in SrTiO_3 for thermoelectricity.** Accepted in *the Journal of Physics and Chemistry of Solids*.

G. Bouzerar, S. Thébaud, and Ch. Adessi. **Dramatic effects of vacancies on phonon lifetime and thermal conductivity in graphene monolayer.** Submitted.

S. Thébaud, Ch. Adessi, and G. Bouzerar. **Investigating the high-temperature thermoelectric properties of n-type rutile TiO₂.** Submitted.

Ch. Adessi, S. Thébaud, and G. Bouzerar. **First principle investigation of the influence of sulfur vacancies on the thermoelectric properties of single layered 2H-MoS₂.** To be submitted.

S. Thébaud, Ch. Adessi, and G. Bouzerar. **Phonon transport in finite-size and irradiated graphene.** To be submitted.

S. Thébaud, Ch. Adessi, and G. Bouzerar. **Resonant states and vanadium doping in SrTiO₃, BaTiO₃ and CaTiO₃: effects of disorder and localization on the thermoelectric properties.** To be submitted.

S. Thébaud and G. Bouzerar. **Localization in Mn-doped InP and GaAs: breakdown of the valence band scenario.** To be submitted.

Appendix A

The Callaway theory in graphene

The full and detailed derivation of the Callaway method can be found in Refs. [152, 153, 154]. In this appendix, we just summarize the main results and detail their application in the case of graphene. The total conductivity in the α -direction can be written,

$$\kappa^\alpha(T) = \kappa_{RTA}^\alpha(T) + \Delta\kappa^\alpha(T), \quad (\text{A.1})$$

where, the RTA contribution is,

$$\kappa_{RTA}^\alpha = \frac{1}{k_B T^2} \frac{1}{N \Omega \delta} \sum_{\mathbf{q}, \lambda} (\hbar \omega_\lambda)^2 (v_\lambda^\alpha)^2 \tau_\lambda^{tot} f_\lambda^0 (f_\lambda^0 + 1), \quad (\text{A.2})$$

N is the total number of unit cells, λ the mode index (LA, TA, ZA), Ω the primitive cell area, δ the distance between graphene sheets in graphite, f_λ^0 is the Bose distribution, $\hbar \omega_\lambda$ the mode energy, v_λ^α its velocity in the α -direction and τ_λ^{tot} the inverse of the total scattering rate for the branch λ . According to Mathiessen's rule the total phonon lifetime is,

$$1/\tau_\lambda^{tot} = 1/\tau_\lambda^N + 1/\tau_\lambda^U + 1/\tau_\lambda^{dis}. \quad (\text{A.3})$$

The first step consists in replacing in the standard Boltzmann equation the collision rate by,

$$\left(\frac{\partial f_\lambda}{\partial t} \right)_c = \frac{f_\lambda^d - f_\lambda}{\tau_N} + \frac{f_\lambda^0 - f_\lambda}{\tau_R}, \quad (\text{A.4})$$

f_λ^d is the drifted distribution function, and we have defined the scattering rate for resistive processes, $1/\tau_\lambda^R = 1/\tau_\lambda^U + 1/\tau_\lambda^{dis}$. Only the resistive processes tend to bring f_λ back to its equilibrium value. The drifted distribution f_λ^d is defined by

$$f_\lambda^d = \frac{1}{e^{\beta(\omega_\lambda(\mathbf{q}) - \mathbf{v}_d \cdot \mathbf{q})} - 1}, \quad (\text{A.5})$$

where we have introduced as a Lagrange multiplier the drift velocity \mathbf{v}_d . This quantity is determined by the condition that the normal processes conserve the momentum. By following step by step Callaway's derivation we find,

$$\Delta\kappa^\alpha(T) = \frac{(A^\alpha(T))^2}{B^\alpha(T)}, \quad (\text{A.6})$$

where the numerator $A^\alpha(T) = \sum_\lambda A_\lambda^\alpha(T)$ and,

$$A_\lambda^\alpha(T) = \frac{1}{k_B T^2} \frac{1}{N \Omega \delta} \sum_{\mathbf{q}} \frac{\tau_\lambda^{tot}}{\tau_\lambda^N} \hbar \omega_\lambda v_\lambda^\alpha q_\lambda^\alpha f_\lambda^0 (f_\lambda^0 + 1), \quad (\text{A.7})$$

and the denominator $B^\alpha(T) = \sum_\lambda B_\lambda^\alpha(T)$ and,

$$B_\lambda^\alpha(T) = \frac{1}{k_B T^2} \frac{1}{N \Omega \delta} \sum_{\mathbf{q}} \frac{\tau_\lambda^{tot}}{\tau_\lambda^N \tau_\lambda^R} (q_\lambda^\alpha)^2 f_\lambda^0 (f_\lambda^0 + 1). \quad (\text{A.8})$$

To facilitate the calculations we replace the discrete sum over \mathbf{q} by an integral over energy and thus we introduce Debye frequencies for LA, TA and ZA modes. This leads to,

$$A_\lambda^\alpha(T) = c_\lambda \frac{1}{\Omega \delta} \int_0^{\omega_{D\lambda}} \frac{\tau_\lambda^{tot}}{\tau_\lambda^N} \omega \rho_\lambda(\omega) \frac{\partial f^0}{\partial T} d\omega, \quad (\text{A.9})$$

where the coefficient $c_\lambda=1/2$ for LA and TA branches and 1 for ZA. Similarly $B_\lambda^\alpha(T)$ can be rewritten,

$$B_\lambda^\alpha(T) = \frac{1}{2 \hbar \Omega \delta} \int_0^{\omega_{D\lambda}} \frac{\tau_\lambda^{tot}}{\tau_\lambda^N \tau_\lambda^R} g_\lambda(\omega) \rho_\lambda(\omega) \frac{\partial f^0}{\partial T} d\omega. \quad (\text{A.10})$$

The density of states is $\rho_\lambda(\omega) = \frac{\Omega}{2\pi v_\lambda^2} \omega$ for both LA and TA, and $\frac{\Omega}{4\pi D}$ for ZA. v_λ is the velocity at the Γ point for LA and TA, and D is the stiffness of the ZA branch. $g_\lambda(\omega) = \frac{\omega}{v_\lambda^2}$ for LA and TA, and $1/D$ for ZA. Note that, in eq.(A.9) and (A.10) we have used the linear dispersion for LA and TA and the quadratic one for ZA.

Appendix B

The current density operator in tight-binding representation

This appendix deals with the definition of the current density and velocity operators for a tight-binding Hamiltonian written in a basis of Wannier functions. We write the single-particle Hamiltonian of the full disordered system in the presence of a vector potential \vec{A} :

$$\hat{H}_{\text{tot}} = \hat{H}_{\text{hop}} + \hat{H}_{\text{loc}} \quad (\text{B.1})$$

in which \hat{H}_{loc} are on-site terms and \hat{H}_{hop} is composed of hopping term between orbitals on different atoms:

$$\hat{H}_{\text{hop}} = \sum_{\langle i,j \rangle} \hat{\kappa}_{ij} \quad (\text{B.2})$$

in which $\langle i, j \rangle$ designates couples of neighboring atoms, and where

$$\hat{\kappa}_{ij} = - \left(\underline{t}_{ij} c_j^\dagger c_i + \underline{t}_{ij}^* c_i^\dagger c_j \right) \quad (\text{B.3})$$

is the hopping operator between the neighboring orbitals i and j , in which

$$\underline{t}_{ij} = t_{ij} e^{i \frac{q}{\hbar} \vec{A}_{ij} \cdot (\vec{r}_j - \vec{r}_i)} \quad (\text{B.4})$$

is the hopping term between i and j with the Peirls substitution, \vec{A}_{ij} being an appropriate value of the vector potential for the hopping between i and j .

It is necessary to clarify the expressions of the current, velocity and current density operators in this formalism. One can start with the conservation of the charge, by differentiating the charge on the atom i in Heisenberg representation, $\hat{Q}_i(t) = q c_i^\dagger(t) c_i(t)$:

$$\frac{\partial \hat{Q}_i(t)}{\partial t} = \frac{q}{i\hbar} \left[c_i^\dagger(t) c_i(t), \hat{H}(t) \right] \quad (\text{B.5})$$

yielding the conservation equation:

$$\frac{\partial \hat{Q}_i(t)}{\partial t} + \sum_{j \text{ neigh } i} \frac{iq}{\hbar} \left(\underline{t}_{ij} c_j^\dagger c_i - \underline{t}_{ij}^* c_i^\dagger c_j \right) = 0 \quad (\text{B.6})$$

from which we deduce that the charge current between atom i and atom j is:

$$\hat{I}_{ij} = \frac{iq}{\hbar} \left(\underline{t}_{ij} c_j^\dagger c_i - \underline{t}_{ij}^* c_i^\dagger c_j \right) \quad (\text{B.7})$$

From this expression, it is intuitive that the velocity of electrons between i and j writes:

$$\hat{v}_{ij} = \frac{i}{\hbar} (\vec{r}_j - \vec{r}_i) \left(\underline{t}_{ij} c_j^\dagger c_i - \underline{t}_{ij}^* c_i^\dagger c_j \right) \quad (\text{B.8})$$

and indeed this expression is consistent with the definition of the velocity as the time derivative of the position:

$$\hat{v}(t) = \frac{1}{i\hbar} \left[\hat{r}(t), \hat{H}(t) \right] = \sum_{\langle i,j \rangle} \hat{v}_{ij}(t) \quad (\text{B.9})$$

The current density is the symmetrized product of the charge density and the velocity:

$$\hat{j}(\vec{r}) = \frac{q}{2} \left(\hat{n}(\vec{r}) \hat{v} + \hat{v} \hat{n}(\vec{r}) \right) \quad (\text{B.10})$$

The electron density must be expressed in terms of the Wannier orbitals $\chi_i(\vec{r})$:

$$\hat{n}(\vec{r}) = \sum_{i,j} \chi_i^*(\vec{r}) \chi_j(\vec{r}) |i\rangle \langle j| \quad (\text{B.11})$$

Since the Wannier orbitals are localized, the electron density varies rapidly inside the crystal unit cell. Clearly, we are not interested in such microscopic variations. Therefore, the electron density (and with it the current density) should be space-averaged over a mesoscopic volume $\tau(\vec{r})$ centered on \vec{r} and covering a large number of atoms:

$$\hat{n}_{\tau(\vec{r})} = \frac{1}{\tau(\vec{r})} \int_{\tau(\vec{r})} d^3\vec{r}' \hat{n}(\vec{r}') = \frac{1}{\tau(\vec{r})} \sum_{i,j} |i\rangle \langle j| \int_{\tau(\vec{r})} d^3\vec{r}' \chi_i^*(\vec{r}') \chi_j(\vec{r}') \quad (\text{B.12})$$

The overlap integral over the volume $\tau(\vec{r})$ vanishes if either the i or j orbital is well outside $\tau(\vec{r})$, and gives δ_{ij} if they are both inside. The orbitals near the border are neglected as $\tau(\vec{r})$ is assumed to comprise many atoms. We then find:

$$\hat{n}_{\tau(\vec{r})} = \frac{1}{\tau(\vec{r})} \sum_{i \in \tau(\vec{r})} |i\rangle \langle i| \quad (\text{B.13})$$

The current density averaged over $\tau(\vec{r})$ then gives (again, neglecting the orbitals near the border):

$$\hat{j}_{\tau(\vec{r})} = \frac{1}{\tau(\vec{r})} \int_{\tau(\vec{r})} d^3\vec{r}' \hat{j}(\vec{r}') = \frac{1}{\tau(\vec{r})} \sum_{\langle i,j \rangle \in \tau(\vec{r})} q \hat{v}_{ij} \quad (\text{B.14})$$

Noting $N_{l,\tau(\vec{r})}$ the number of neighbors $\langle i, j \rangle$ (links) in the volume $\tau(\vec{r})$, we can define a "density of link" $n_l = N_{l,\tau(\vec{r})}/\tau(\vec{r})$, that should be independant of $\tau(\vec{r})$ if it is chosen large enough. The current density averaged over $\tau(\vec{r})$ then writes:

$$\hat{j}_{\tau(\vec{r})} = \frac{1}{N_{l,\tau(\vec{r})}} \sum_{\langle i,j \rangle \in \tau(\vec{r})} q n_l \hat{v}_{ij} \quad (\text{B.15})$$

From this expression, it is clear that we can define $\hat{j}_{ij} = q n_l \hat{v}_{ij}$ as a current density operator for the link $\langle i, j \rangle$, keeping in mind that it is meaningful only when averaged over a mesoscopic volume. Now, we should check that the current density, when summed over a "mesoscopic surface" S (i.e. a surface with a mesoscopic width l), gives the electrical current through the surface:

$$\begin{aligned} \int_S \hat{j} \cdot d\vec{S} &= \frac{1}{l} \int_{S_{\text{meso}}} \hat{j} \cdot d\vec{S} dl = \frac{1}{l} \int_S \hat{j}_{l dS} \cdot l d\vec{S} = \frac{1}{l} \int_S \sum_{\langle i, j \rangle \in l dS} q \hat{v}_{ij} \cdot \frac{d\vec{S}}{dS} \\ &= \frac{1}{l} \int_S \sum_{\langle i, j \rangle \in l dS} \hat{I}_{ij} (\vec{r}_j - \vec{r}_i) \cdot \frac{d\vec{S}}{dS} \end{aligned} \quad (\text{B.16})$$

Using the conservation equation, one can then show that this expression corresponds to the current across S . In practical calculations of the conductance for finite systems, we will only use the exact expression for the current density integrated over the whole system:

$$\int_{\Omega} d^3\vec{r} \hat{j}(\vec{r}) = \sum_{\langle i, j \rangle} q \hat{v}_{ij} = q \hat{v} \quad (\text{B.17})$$

Appendix C

The Kubo formalism of quantum transport

In this appendix, expression (4.25) for the electrical conductivity is derived in the framework of the Kubo formalism. The demonstration has been carried out in Ref. [250] and Ref. [157], but it is instructive to go through it. The system under consideration is a disordered system that includes semi-infinite leads, whose single particle Hamiltonian is noted \hat{H} . It is in unperturbed equilibrium at time $t = -\infty$, therefore the density matrix at that time is the grand-canonical density matrix $\hat{\rho}_0$. The system is then subjected to the adiabatic switch-on of an electrical field \vec{E} deriving from a small vector potential \vec{A} :

$$\vec{A}(\vec{r}, t) = \int \frac{d\omega}{2\pi} \vec{A}(\vec{r}, \omega + i\eta) e^{-i(\omega + i\eta)t} = \int \frac{d\omega}{2\pi} \frac{\vec{E}(\vec{r}, \omega + i\eta)}{i(\omega + i\eta)} e^{-i(\omega + i\eta)t} \quad (\text{C.1})$$

where the small imaginary part η has been introduced to force the adiabatic turn-on. Since we are interested only in the steady-state regime, the limit $\eta \rightarrow 0$ should be taken in the final result.

The perturbed Hamiltonian writes:

$$\begin{aligned} \hat{H}(t) = \hat{H} \Big|_{\vec{A}=0} + \int d^3\vec{r} \frac{\delta \hat{H}}{\delta \vec{A}(\vec{r})} \Big|_{\vec{A}=0} \vec{A}(\vec{r}, t) \\ + \frac{1}{2} \int d^3\vec{r} d^3\vec{r}' \frac{\delta^2 \hat{H}}{\delta \vec{A}(\vec{r}) \delta \vec{A}(\vec{r}')} \Big|_{\vec{A}=0} \vec{A}(\vec{r}, t) \vec{A}(\vec{r}', t) + O(\vec{A}^3) \end{aligned} \quad (\text{C.2})$$

and we can define the first-order perturbation operator:

$$\hat{V}(t) = \int d^3\vec{r} \frac{\delta \hat{H}}{\delta \vec{A}(\vec{r})} \Big|_{\vec{A}=0} \vec{A}(\vec{r}, t) \quad (\text{C.3})$$

The electron current density is:

$$\hat{J}(\vec{r}, t) = -\frac{\delta \hat{H}(t)}{\delta \vec{A}(\vec{r}, t)} = -\frac{\delta \hat{H}}{\delta \vec{A}(\vec{r})} \Big|_{\vec{A}=0} - \int d^3\vec{r}' \frac{\delta^2 \hat{H}}{\delta \vec{A}(\vec{r}) \delta \vec{A}(\vec{r}')} \Big|_{\vec{A}=0} \vec{A}(\vec{r}', t) + O(\vec{A}^2) \quad (\text{C.4})$$

The last term is called the diamagnetic contribution to the current, while the first term is called the paramagnetic component $\hat{j}(\vec{r})$:

$$\hat{j}(\vec{r}) = - \frac{\delta \hat{H}}{\delta \vec{A}(\vec{r})} \Big|_{\vec{A}=0} \quad (\text{C.5})$$

The time evolution of the density matrix under the perturbation can be written in the interaction representation:

$$\hat{\rho}_I(t) = \hat{\rho}_0 - \frac{i}{\hbar} \int_{-\infty}^t dt_1 [\hat{V}_I(t_1), \hat{\rho}_I(t_1)] = \hat{\rho}_0 - \frac{i}{\hbar} \int_{-\infty}^t dt_1 [\hat{V}_I(t_1), \hat{\rho}_0] + O(\hat{V}^2) \quad (\text{C.6})$$

The average current density at time t is (here the brackets denote the quantum expectation value and not disorder averaging):

$$\begin{aligned} \langle \hat{J}(\vec{r}, t) \rangle &= \text{Tr} \left(\hat{\rho}_I(t) \hat{J}_I(\vec{r}, t) \right) \\ &= \text{Tr} \left(\hat{\rho}_0 \hat{J}_I(\vec{r}, t) \right) - \frac{i}{\hbar} \int_{-\infty}^t dt_1 \text{Tr} \left([\hat{V}_I(t_1), \hat{\rho}_0] \hat{J}_I(\vec{r}, t) \right) + O(\hat{V}^2) \\ &= \text{Tr} \left(\hat{\rho}_0 \hat{J}(\vec{r}, t) \right) - \frac{i}{\hbar} \int_{-\infty}^t dt_1 \text{Tr} \left(\hat{\rho}_0 [\hat{J}_I(\vec{r}, t), \hat{V}_I(t_1)] \right) + O(\hat{V}^2) \\ &= \langle \hat{j}(\vec{r}) \rangle_0 - \int d^3 \vec{r}' \left\langle \frac{\delta^2 \hat{H}}{\delta \vec{A}(\vec{r}) \delta \vec{A}(\vec{r}')} \Big|_{\vec{A}=0} \right\rangle_0 \vec{A}(\vec{r}', t) \\ &\quad + \frac{i}{\hbar} \int d^3 \vec{r}' \int_{-\infty}^t dt_1 \vec{A}(\vec{r}', t_1) \langle [\hat{j}_I(\vec{r}, t), \hat{j}_I(\vec{r}', t_1)] \rangle_0 + O(\vec{A}^2) \end{aligned}$$

where the paramagnetic current $\hat{j}_I(\vec{r}, t)$ appears in the last term instead of $\hat{J}_I(\vec{r}, t)$ because the diamagnetic contribution gives a term quadratic in the vector potential. The 0 index denotes an expectation value using the unperturbed density matrix $\hat{\rho}_0$. Since no current flows through the sample in equilibrium, we can forget about $\langle \hat{j}(\vec{r}) \rangle_0$. We can also define the current-current correlation tensor and its Fourier transform:

$$\chi(\vec{r}, t; \vec{r}', t') = -i\Theta(t - t') \langle [\hat{j}_I(\vec{r}, t), \hat{j}_I(\vec{r}', t')] \rangle_0 \quad (\text{C.7})$$

$$\chi(\omega + i\eta, \vec{r}, \vec{r}') = \int dt \chi(\vec{r}, t; \vec{r}', 0) e^{i(\omega + i\eta)t} \quad (\text{C.8})$$

so that:

$$\begin{aligned}
\langle \hat{J}(\vec{r}, t) \rangle &= - \int d^3 \vec{r}' \left\langle \frac{\delta^2 \hat{H}}{\delta \vec{A}(\vec{r}) \delta \vec{A}(\vec{r}')} \right|_{\vec{A}=0} \rangle_0 \vec{A}(\vec{r}', t) \\
&\quad - \frac{1}{\hbar} \int d^3 \vec{r}' \int_{-\infty}^{\infty} dt_1 \vec{A}(\vec{r}', t_1) \chi(\vec{r}, t; \vec{r}', t_1) + O(\vec{A}^2) \\
&= \int \frac{d\omega}{2\pi} e^{-i(\omega+i\eta)t} \int d^3 \vec{r}' \frac{\vec{E}(\vec{r}', \omega + i\eta)}{i(\omega + i\eta)} \left[- \left\langle \frac{\delta^2 \hat{H}}{\delta \vec{A}(\vec{r}) \delta \vec{A}(\vec{r}')} \right|_{\vec{A}=0} \right]_0 \\
&\quad - \frac{1}{\hbar} \int_{-\infty}^{\infty} dt_1 e^{i(\omega+i\eta)(t-t_1)} \chi(\vec{r}, t; \vec{r}', t_1) \right]
\end{aligned}$$

and the Fourier component of the average current density is:

$$\begin{aligned}
\langle \hat{J}(\vec{r}, \omega + i\eta) \rangle &= \int d^3 \vec{r}' \frac{i}{\omega + i\eta} \left[\left\langle \frac{\delta^2 \hat{H}}{\delta \vec{A}(\vec{r}) \delta \vec{A}(\vec{r}')} \right|_{\vec{A}=0} \right]_0 \\
&\quad + \frac{1}{\hbar} \chi(\omega + i\eta, \vec{r}, \vec{r}') \vec{E}(\vec{r}', \omega + i\eta)
\end{aligned} \tag{C.9}$$

Comparing this last equation to the definition of the conductivity tensor, equation (4.23), we find:

$$\sigma(\omega + i\eta, \vec{r}, \vec{r}') = \frac{i}{\omega + i\eta} \left[\left\langle \frac{\delta^2 \hat{H}}{\delta \vec{A}(\vec{r}) \delta \vec{A}(\vec{r}')} \right|_{\vec{A}=0} \right]_0 + \frac{1}{\hbar} \chi(\omega + i\eta, \vec{r}, \vec{r}') \tag{C.10}$$

where η is an infinitely small imaginary part. This is a very general version of the Kubo formula that is valid even when many-body interactions are present. It emphasizes the connexion between the linear response coefficient σ and the equilibrium correlation function χ (fluctuation-dissipation theorem).

To obtain a more convenient expression for the conductivity, we use the single-particle nature of the Hamiltonian. Since the system is infinite, the Hamiltonian has a continuum of eigenstates $|\alpha\rangle$ associated to eigenenergies ϵ_α . The expectation value of an operator \hat{F} is simply

$$\langle \hat{F} \rangle_0 = \int d\alpha \langle \alpha | \hat{F} | \alpha \rangle f(\epsilon_\alpha) \tag{C.11}$$

where $f(E)$ is the Fermi-Dirac distribution. Thus, the Kubo formula (C.10) can be rewritten

$$\begin{aligned}
\sigma(\omega + i\eta, \vec{r}, \vec{r}') &= \frac{i}{\omega + i\eta} \left[\int d\alpha \langle \alpha | \frac{\delta^2 \hat{H}}{\delta \vec{A}(\vec{r}) \delta \vec{A}(\vec{r}')} \right|_{\vec{A}=0} | \alpha \rangle f(\epsilon_\alpha) \\
&\quad - \frac{i}{\hbar} \int dt \Theta(t) e^{i(\omega+i\eta)t} \int d\alpha \langle \alpha | [\hat{J}_I(\vec{r}, t), \hat{J}_I(\vec{r}', 0)] | \alpha \rangle f(\epsilon_\alpha) \right]
\end{aligned} \tag{C.12}$$

The first derivative in the diamagnetic term can be redistributed (keeping in mind that the derivatives should be evaluated for $\vec{A} = 0$):

$$\begin{aligned} \langle \alpha | \frac{\delta^2 \hat{H}}{\delta \vec{A}(\vec{r}) \delta \vec{A}(\vec{r}')} | \alpha \rangle f(\epsilon_\alpha) &= \frac{\delta}{\delta \vec{A}(\vec{r})} \left(\langle \alpha | \frac{\delta \hat{H}}{\delta \vec{A}(\vec{r}')} | \alpha \rangle f(\epsilon_\alpha) \right) \\ &- \langle \alpha | \frac{\delta \hat{H}}{\delta \vec{A}(\vec{r}')} | \alpha \rangle \frac{\delta f(\epsilon_\alpha)}{\delta \vec{A}(\vec{r})} - \frac{\delta \langle \alpha | \frac{\delta \hat{H}}{\delta \vec{A}(\vec{r}')} | \alpha \rangle}{\delta \vec{A}(\vec{r})} f(\epsilon_\alpha) - \langle \alpha | \frac{\delta \hat{H}}{\delta \vec{A}(\vec{r}')} \frac{\delta | \alpha \rangle}{\delta \vec{A}(\vec{r})} f(\epsilon_\alpha) \end{aligned} \quad (\text{C.13})$$

Time-independant quantum perturbation theory gives (the degenerate eigenvectors should be chosen to diagonalize the perturbation):

$$\frac{\delta | \alpha \rangle}{\delta \vec{A}(\vec{r})} = \int_{\epsilon_\alpha \neq \epsilon_\beta} d\beta \frac{\langle \beta | \frac{\delta \hat{H}}{\delta \vec{A}(\vec{r})} | \alpha \rangle}{\epsilon_\alpha - \epsilon_\beta} | \beta \rangle \quad (\text{C.14})$$

and so, taking into account that $\hat{j}(\vec{r}) = -\frac{\delta \hat{H}}{\delta \vec{A}(\vec{r})}$ and $\langle \alpha | \hat{j}(\vec{r}) | \alpha \rangle = -\frac{\delta \epsilon_\alpha}{\delta \vec{A}(\vec{r})}$, we find

$$\begin{aligned} \int d\alpha \langle \alpha | \frac{\delta^2 \hat{H}}{\delta \vec{A}(\vec{r}) \delta \vec{A}(\vec{r}')} | \alpha \rangle f(\epsilon_\alpha) &= -\frac{\delta}{\delta \vec{A}(\vec{r})} \langle \hat{j}(\vec{r}') \rangle_0 \\ &+ \int d\alpha \left(-\frac{\partial f}{\partial E}(\epsilon_\alpha) \right) \langle \alpha | \hat{j}(\vec{r}) | \alpha \rangle \langle \alpha | \hat{j}(\vec{r}') | \alpha \rangle \\ &- \int \int_{\epsilon_\alpha \neq \epsilon_\beta} d\alpha d\beta \frac{f(\epsilon_\alpha) - f(\epsilon_\beta)}{\epsilon_\alpha - \epsilon_\beta} \langle \alpha | \hat{j}(\vec{r}) | \beta \rangle \langle \beta | \hat{j}(\vec{r}') | \alpha \rangle \end{aligned} \quad (\text{C.15})$$

where the eigenstate indices have been switched to find the last term.

The current-current correlation term can also be expressed in the eigenstate basis:

$$\begin{aligned} \int d\alpha \langle \alpha | \left[\hat{j}_I(\vec{r}, t), \hat{j}_I(\vec{r}', 0) \right] | \alpha \rangle f(\epsilon_\alpha) &= \\ \int \int d\alpha d\beta \left(e^{\frac{i}{\hbar}(\epsilon_\alpha - \epsilon_\beta)t} \langle \alpha | \hat{j}(\vec{r}) | \beta \rangle \langle \beta | \hat{j}(\vec{r}') | \alpha \rangle \right. \\ &\quad \left. - e^{\frac{i}{\hbar}(\epsilon_\beta - \epsilon_\alpha)t} \langle \beta | \hat{j}(\vec{r}) | \alpha \rangle \langle \alpha | \hat{j}(\vec{r}') | \beta \rangle \right) f(\epsilon_\alpha) \\ &= \int \int_{\epsilon_\alpha \neq \epsilon_\beta} d\alpha d\beta (f(\epsilon_\alpha) - f(\epsilon_\beta)) e^{\frac{i}{\hbar}(\epsilon_\alpha - \epsilon_\beta)t} \langle \alpha | \hat{j}(\vec{r}) | \beta \rangle \langle \beta | \hat{j}(\vec{r}') | \alpha \rangle \end{aligned} \quad (\text{C.16})$$

where the eigenstate indices have been switched for the last equality. Thus, performing the time integration in equation (C.12), we find

$$\begin{aligned} &-\frac{i}{\hbar} \int dt \Theta(t) e^{i(\omega + i\eta)t} \int d\alpha \langle \alpha | \left[\hat{j}_I(\vec{r}, t), \hat{j}_I(\vec{r}', 0) \right] | \alpha \rangle f(\epsilon_\alpha) = \\ &\frac{1}{\hbar} \int \int_{\epsilon_\alpha \neq \epsilon_\beta} d\alpha d\beta (f(\epsilon_\alpha) - f(\epsilon_\beta)) \langle \alpha | \hat{j}(\vec{r}) | \beta \rangle \langle \beta | \hat{j}(\vec{r}') | \alpha \rangle \frac{1}{\omega + i\eta + \frac{\epsilon_\alpha - \epsilon_\beta}{\hbar}} \end{aligned} \quad (\text{C.17})$$

For the next step, it should be noticed that

$$\frac{1}{\omega + i\eta + \frac{\epsilon_\alpha - \epsilon_\beta}{\hbar}} = \frac{\hbar}{\epsilon_\alpha - \epsilon_\beta} - \frac{\hbar(\omega + i\eta)}{(\epsilon_\alpha - \epsilon_\beta)(\omega + i\eta + \frac{\epsilon_\alpha - \epsilon_\beta}{\hbar})} \quad (\text{C.18})$$

When putting everything together, the first term of equation (C.18) actually cancels the last term of equation (C.15). We end up with:

$$\begin{aligned} \sigma(\omega + i\eta, \vec{r}, \vec{r}') = & \frac{i}{\omega + i\eta} \left[-\frac{\delta}{\delta \vec{A}(\vec{r})} \langle \hat{\vec{j}}(\vec{r}') \rangle_0 \right. \\ & \left. + \int d\alpha \left(-\frac{\partial f}{\partial E}(\epsilon_\alpha) \right) \langle \alpha | \hat{\vec{j}}(\vec{r}) | \alpha \rangle \langle \alpha | \hat{\vec{j}}(\vec{r}') | \alpha \rangle \right] \\ & + i \int \int_{\epsilon_\alpha \neq \epsilon_\beta} d\alpha d\beta \frac{f(\epsilon_\alpha) - f(\epsilon_\beta)}{\epsilon_\beta - \epsilon_\alpha} \frac{\langle \alpha | \hat{\vec{j}}(\vec{r}) | \beta \rangle \langle \beta | \hat{\vec{j}}(\vec{r}') | \alpha \rangle}{\omega + i\eta + \frac{\epsilon_\alpha - \epsilon_\beta}{\hbar}} \end{aligned} \quad (\text{C.19})$$

The term $\frac{\delta}{\delta \vec{A}(\vec{r})} \langle \hat{\vec{j}}(\vec{r}') \rangle_0$ involves permanent currents in the presence of a magnetic fields. As discussed in Ref. [250] and Ref. [157], such currents cannot create a net current in the leads, and moreover they are destroyed on a length scale such that the inelastic scattering rate is much greater than the Thouless energy [252], which is precisely the regime that is relevant for our work (see section 4.2). Therefore, we can neglect this term in large disordered systems, although it can be useful to keep it in other circumstances (see appendix D). Putting the remaining two terms together, we find

$$\begin{aligned} \sigma(\omega + i\eta, \vec{r}, \vec{r}') = & i \int d\alpha \left(-\frac{\partial f}{\partial E}(\epsilon_\alpha) \right) \frac{\langle \alpha | \hat{\vec{j}}(\vec{r}) | \alpha \rangle \langle \alpha | \hat{\vec{j}}(\vec{r}') | \alpha \rangle}{\omega + i\eta} \\ & + i \int \int_{\epsilon_\alpha \neq \epsilon_\beta} d\alpha d\beta \frac{f(\epsilon_\alpha) - f(\epsilon_\beta)}{\epsilon_\beta - \epsilon_\alpha} \frac{\langle \alpha | \hat{\vec{j}}(\vec{r}) | \beta \rangle \langle \beta | \hat{\vec{j}}(\vec{r}') | \alpha \rangle}{\omega + i\eta + \frac{\epsilon_\alpha - \epsilon_\beta}{\hbar}} \end{aligned} \quad (\text{C.20})$$

which is identical to equation (4.25).

Appendix D

The Drude formalism and the sum rule

Even though the term corresponding to permanent currents in equation (C.19) can be discarded for large systems, it can also be kept in order to express the conductivity in a different way. The terms inside the brackets can be simplified:

$$-\frac{\delta}{\delta \vec{A}(\vec{r})} \langle \hat{j}(\vec{r}') \rangle_0 - \int d\alpha \frac{\partial f}{\partial E}(\epsilon_\alpha) \langle \alpha | \hat{j}(\vec{r}) | \alpha \rangle \langle \alpha | \hat{j}(\vec{r}') | \alpha \rangle = \int d\alpha \frac{\delta^2 \epsilon_\alpha}{\delta \vec{A}(\vec{r}) \delta \vec{A}(\vec{r}')} f(\epsilon_\alpha) \quad (\text{D.1})$$

This quantity, called the Drude weight $D(\vec{r}, \vec{r}')$, is a second derivative of the ground-state energy of the system with respect to vector potentials. Taking the limit $\eta \rightarrow 0$, the real part σ_r of the conductivity can then be expressed as

$$\sigma_r(\omega, \vec{r}, \vec{r}') = \pi D(\vec{r}, \vec{r}') \delta(\omega) + \sigma_{\text{reg}}(\omega, \vec{r}, \vec{r}') \quad (\text{D.2})$$

where

$$\sigma_{\text{reg}}(\omega, \vec{r}, \vec{r}') = \pi \int \int_{\epsilon_\alpha \neq \epsilon_\beta} d\alpha d\beta \frac{f(\epsilon_\alpha) - f(\epsilon_\beta)}{\epsilon_\beta - \epsilon_\alpha} \langle \alpha | \hat{j}(\vec{r}) | \beta \rangle \langle \beta | \hat{j}(\vec{r}') | \alpha \rangle \delta \left(\omega + \frac{\epsilon_\alpha - \epsilon_\beta}{\hbar} \right) \quad (\text{D.3})$$

is called the regular part of the conductivity and vanishes at $\omega = 0$. Thus, expression D.2 separates the DC part of the conductivity (Drude peak at $\omega = 0$) from the transitions between different levels taking place at finite frequencies.

The real part of the conductivity satisfies a well-known sum rule when integrated over the frequency axis. This can be easily shown from equation (C.10). Because the current-current correlation function obeys the Kramers-Kronig relations and is real in the time domain, it is straightforward to show that, when $\eta \rightarrow 0$:

$$\int_0^\infty d\omega \operatorname{Re} \left(\frac{i}{\omega + i\eta} \chi(\omega + i\eta, \vec{r}, \vec{r}') \right) = 0 \quad (\text{D.4})$$

Thus, the sum rule is

$$\int_0^\infty d\omega \sigma_r(\omega, \vec{r}, \vec{r}') = \frac{\pi}{2} \left\langle \frac{\delta^2 \hat{H}}{\delta \vec{A}(\vec{r}) \delta \vec{A}(\vec{r}')} \right|_{\vec{A}=0} \rangle_0 \quad (\text{D.5})$$

It is simply the diamagnetic term, which is generally not very sensitive to perturbations of the Hamiltonian, especially on-site perturbations. For an electron gas in a parabolic band subjected to an on-site disorder, for instance, the integral of the conductivity associated with an uniform electrical field is just $\frac{\pi}{2} \frac{n_e e^2}{m_b}$, where n_e is the electron density and m_b is the band mass. The Drude weight, by contrast, is very sensitive to disorder and interactions, and is actually a critical quantity in the event of a metal-insulator transition: it vanishes in insulating phases. Thus the effects of disorder can be seen as transferring spectral weight from the Drude peak to the regular part of the conductivity.

Equation (D.2) gives an infinite DC conductivity if the Drude weight is finite, which makes sense because no energy dissipation mechanism has been introduced. An somewhat phenomenological procedure to obtain physically meaningful values for the conductivity is to replace delta peak $\delta(\omega)$ by a lorentzian with a width corresponding to a finite scattering rate \hbar/τ . Then, the DC conductivity for a uniform electric field associated with a vector potential \vec{A} is simply:

$$\sigma_{DC} = \frac{1}{\Omega} \int d\vec{r} d\vec{r}' \sigma_r(\omega = 0, \vec{r}, \vec{r}') = D\tau \quad (\text{D.6})$$

where Ω is the system size and

$$D = \frac{1}{\Omega} \int d\vec{r} d\vec{r}' D(\vec{r}, \vec{r}') = \frac{1}{\Omega} \int d\alpha \frac{\partial^2 \epsilon_\alpha}{\partial \vec{A}^2} f(\epsilon_\alpha) \quad (\text{D.7})$$

For a clean, periodic system, the Peierls substitution amounts to replacing the crystal momentum \vec{k} with $\vec{k} + \frac{e}{\hbar} \vec{A}$. Thus, the Drude weight can be expressed in this case as

$$D = \frac{e^2}{\hbar^2} \sum_n \int \frac{d\vec{k}}{(2\pi)^d} \frac{\partial^2 \epsilon_n(\vec{k})}{\partial \vec{k}^2} f(\epsilon_n(\vec{k})) \quad (\text{D.8})$$

where n is the band index. This expression is identical to equation (2.58) because of the periodicity of the band structure in the Brillouin zone (there can be discrepancies for a finite number of \vec{k} points, denoting the possible presence of permanent currents in finite systems). Thus, equation (D.6) recovers the solution of the Boltzmann transport equation under the relaxation time approximation, equation (2.48). It is often more convenient to calculate the conductivity from equation (D.7), because there is no need to introduce a broadening of delta peaks.

Finally, it is informative to consider the effects of boundary conditions on the conductivity of a clean system, for instance a simple cubic lattice with only nearest-neighbor hopping t for which analytical expressions are available. For periodic boundary conditions, the regular part of the conductivity (like the current-current correlation function) vanishes because the total current operator is diagonal in the eigenstate basis. So we are just left with a peak

at $\omega = 0$, the Drude peak. For open boundary conditions, on the other hand, the Drude weight vanishes because the eigenvalues are insensitive to a uniform vector potential that can be interpreted as a twist of the boundary conditions for a different gauge choice. In this case, the spectral weight has been displaced at finite frequencies. The zero-temperature conductivity writes:

$$\sigma(\omega) = \frac{\pi \hbar e^2}{\Omega} \sum_{\epsilon_\alpha < E < \epsilon_\beta} \frac{|v_x^{\alpha\beta}|^2}{\epsilon_\beta - \epsilon_\alpha} \delta(\hbar\omega + \epsilon_\alpha - \epsilon_\beta) \quad (\text{D.9})$$

where the eigenstates can be labeled by integer quantum numbers l_x , l_y and l_z between 1 and L_x , L_y and L_z respectively. The eigenenergy of the eigenstate (l_x, l_y, l_z) is simply $\epsilon_{l_x, l_y, l_z} = -2t \cos(\frac{\pi l_x}{L_x+1}) - 2t \cos(\frac{\pi l_y}{L_y+1}) - 2t \cos(\frac{\pi l_z}{L_z+1})$. The velocity matrix element between states (l_x, l_y, l_z) and (l'_x, l'_y, l'_z) is non-zero only if $l_y = l'_y$, $l_z = l'_z$ and $l_x + l'_x$ is odd, in which case it is given by

$$v_x^{l_x, l'_x} = \frac{2iat}{\hbar(L_x + 1)} \left(\frac{\sin\left(\frac{\pi}{L_x+1} \frac{l_x + l'_x}{2}\right)}{\sin\left(\frac{\pi}{L_x+1} \frac{l_x - l'_x}{2}\right)} - \frac{\sin\left(\frac{\pi}{L_x+1} \frac{l_x - l'_x}{2}\right)}{\sin\left(\frac{\pi}{L_x+1} \frac{l_x + l'_x}{2}\right)} \right), \quad (\text{D.10})$$

where a is the lattice constant.

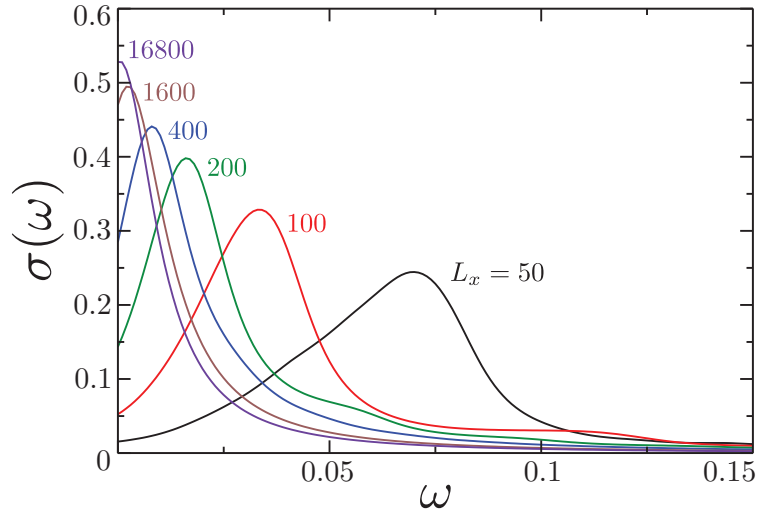


Figure D.1: The zero-temperature conductivity for a simple cubic lattice with a nearest-neighbor hopping term t and open boundary conditions. The parameters are chosen to be $\eta = 0.01t$, $E = -5.5t$, $L_y = L_z = 50$.

For large systems at the thermodynamic limit, the two situations (periodic and open boundary conditions) should give the same conductivity. What happens is that, for open boundary conditions, the peak at finite frequency shifts closer and closer to $\omega = 0$ as the

system size increases (see Fig. D.1). Thus, for an infinite system we end up with a peak at $\omega = 0^+$. Note that due to the broadening of the delta peaks in Fig. D.1, around half the spectral weight is in the negative frequency domain for the largest systems, violating the sum rule. This is an artefact of the broadening procedure, which is purely numerical. Thus, when studying the low-frequency conductivity, the full expression (4.26) should be used, with a small inelastic scattering introduced in the Green's functions. This procedure has a clear physical meaning and ensures that the closed and open boundary conditions yield the same conductivities at the thermodynamic limit.

Appendix E

The convergence of the CPGF method

In this appendix, we give some details on the convergence properties of the CPGF method, presented in section 4.3.2. We take as an example the calculation of the TDF in SrTiO_3 doped with 1% Vanadium impurities, which was carried out in section 5.3.1 on lattices of size $900 \times 180 \times 180$ using 1 disorder configuration, 20 random vectors and $N_m = 2000$ terms in the Chebyshev expansion of the Green's function (for a total of 2000×2000 calculated moments). To illustrate the convergence issues, we take a small value $\gamma_{\text{in}} = 5 \text{ meV}$ for the inelastic scattering.

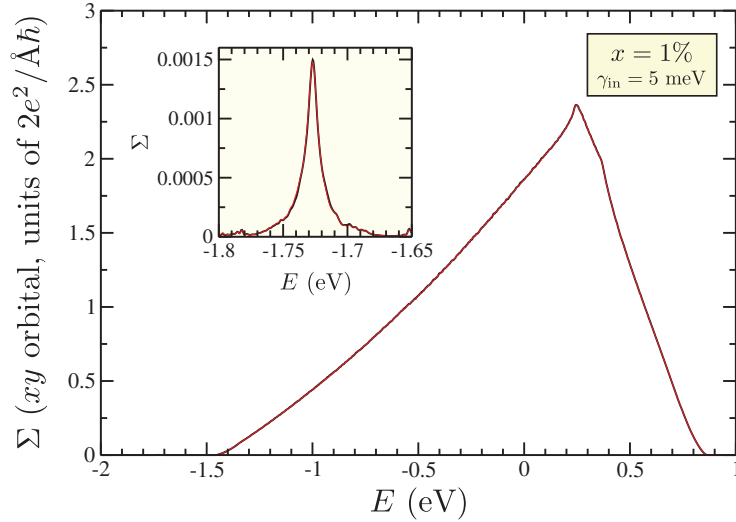


Figure E.1: The TDF of the xy orbital in 1% V-doped SrTiO_3 for $\gamma_{\text{in}} = 5 \text{ meV}$ and two different disorder configurations (red and black lines). Inset: a zoom on the energies corresponding to the V impurity band.

In Fig. E.1 we show the TDF calculated with two different disorder configurations. The results are almost identical on the entire energy range, demonstrating that the TDF is self-averaged for such large system sizes. Thus, only one disorder configuration is necessary to obtain meaningful results.

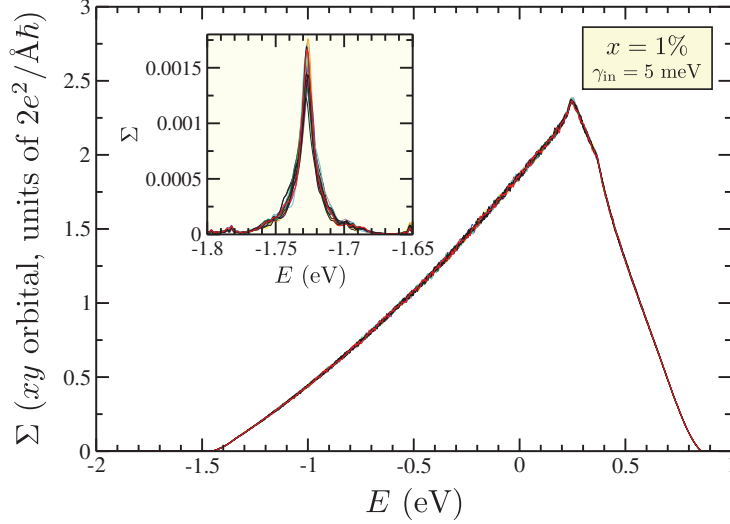
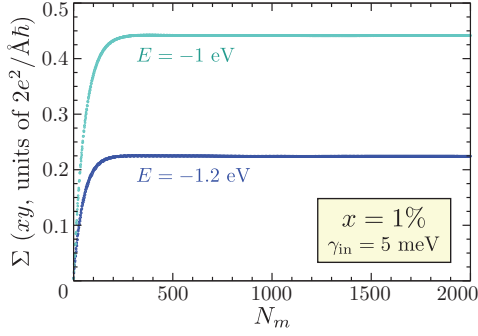


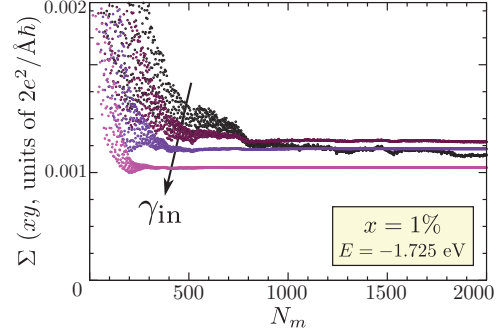
Figure E.2: The TDF of the xy orbital and two different disorder configurations (red and black lines). Inset: a zoom on the energies corresponding to the V impurity band.

We now turn to the convergence of the TDF with respect to the random vectors used in the stochastic calculation of the trace in equation (4.36). Fig E.2 shows the TDF calculated when the trace is evaluated using only one of the 20 different random vectors. The results are very close for each random vector, indicating that an average over just a few of them is sufficient to obtain converged quantities. Again, the large size of the system makes the convergence faster due to self-averaging.

Finally, it is interesting to examine the convergence properties with respect to the number of terms in the Chebyshev expansion of the Green's function, N_m . We plot in Fig. E.3a the value of the TDF as a function of N_m for $E = -1$ eV and $E = -1.2$ eV, corresponding to extended states in the main conduction band. The convergence is very fast, indeed only about 300 terms are necessary at these energies. From this example, it is clear that the rule of thumb $N_m \approx 5/\tilde{\eta}$, which would lead to $N_m \approx 2000$ (the rescaling factor is 2.2 eV here), is but an upper limit on the required number of terms in the Chebyshev expansion. For localized states, characterized by a much lower TDF, the picture is rather different. The TDF at the center of the impurity band is plotted in Fig. E.3b as a function of N_m for several values of γ_{in} between 2.5 meV and 20 meV. For the lowest value of γ_{in} , the TDF has not quite converged yet. For $\gamma_{\text{in}} = 5$ meV, between 1500 and 2000 terms are necessary, while the TDF is converged at $N_m \approx 1000$ for $\gamma_{\text{in}} = 10$ meV and at $N_m \approx 500$ for $\gamma_{\text{in}} = 20$ meV. Thus, the rule of thumb appears to be adequate in this more delicate case.



(a) The convergence with respect to N_m of the xy TDF in 1% V-doped SrTiO_3 with $\gamma_{\text{in}} = 5$ meV for the energies $E = -1$ eV and $E = -1.2$ eV corresponding to extended states.



(b) The convergence with respect to N_m of the xy TDF in 1% V-doped SrTiO_3 with $\gamma_{\text{in}} = 2.5$ meV, 5 meV, 10 meV and 20 meV for $E = -1.725$ eV corresponding to the center of the localized V impurity band.

Figure E.3

It should be noted that if γ_{in} is set at 130 meV, a value chosen on the physical grounds that it reproduces the resistivity of 10% La or Nb doped SrTiO_3 , then only about a hundred terms in the Chebyshev expansion are necessary.

Bibliography

- [1] Steven Pinker. *Enlightenment Now: The Case for Reason, Science, Humanism, and Progress*. Viking, 2018.
- [2] François Bourguignon and Christian Morrisson. Inequality Among World Citizens: 1820-1992 . *American Economic Review*, 92(4):727–744, 2002.
- [3] Max Roser. Our World in Data.
- [4] The Sustainable Development Goals Report 2018. Technical report, United Nations, 2018.
- [5] Jean-Marc Jancovici. How much of a slave master am I?, 2005.
- [6] V Smil. *Energy Transitions: History, Requirements, Prospects*. Praeger, 2010.
- [7] Pennsylvania State University. EARTH 104 - Energy and the Environment.
- [8] BP Statistical Review of World Energy 2018. Technical report, BP, 2018.
- [9] Core Writing Team, R.K. Pachauri, and L.A. Meyer. Climate Change 2014: Synthesis Report. Contribution of Working Groups I, II and III to the Fifth Assessment Report of the Intergovernmental Panel on Climate Change. Technical report, IPCC, Geneva, Switzerland, 2014.
- [10] François Gemenne. Why the numbers don’t add up: A review of estimates and predictions of people displaced by environmental changes. *Global Environmental Change*, 21:S41–S49, 2011.
- [11] EPA. Global Greenhouse Gas Emissions Data, 2017.
- [12] Clemens Forman, Ibrahim Kolawole Muritala, Robert Pardemann, and Bernd Meyer. Estimating the global waste heat potential. *Renewable and Sustainable Energy Reviews*, 57:1568–1579, 2016.
- [13] Albert Polman, Mark Knight, Erik C Garnett, Bruno Ehrler, and Wim C Sinke. Photovoltaic materials: Present efficiencies and future challenges. *Science*, 352(6283):aad4424, apr 2016.

- [14] K R Anjana and R S Shaji. A review on the features and technologies for energy efficiency of smart grid. *International Journal of Energy Research*, 42(3):936–952, mar 2018.
- [15] Axel Groß. Fundamental Challenges for Modeling Electrochemical Energy Storage Systems at the Atomic Scale. *Topics in Current Chemistry*, 376(3):17, 2018.
- [16] Pushker A Kharecha and James E Hansen. Prevented Mortality and Greenhouse Gas Emissions from Historical and Projected Nuclear Power. *Environmental Science & Technology*, 47(9):4889–4895, may 2013.
- [17] John Asafu-Adjaye, Linus Blomqvist, Stewart Brand, Barry Brook, Ruth DeFries, Erle Ellis, Christopher Foreman, David Keith, Martin Lewis, Mark Lynas, Ted Nordhaus, Roger Pielke, Rachel Pritzker, Joyashree Roy, Mark Sagoff, Michael Shellenberger, Robert Stone, and Peter Teague. *An Ecomodernist Manifesto*. jun 2015.
- [18] Pathways to Deep Decarbonization, 2014 report. Technical report, Deep Decarbonization Pathways Project, Sustainable Development Solutions Network, Institute for Sustainable Development and International Relations, 2014.
- [19] Arshad Raza, Raoof Gholami, Reza Rezaee, Vamegh Rasouli, and Minou Rabiei. Significant aspects of carbon capture and storage – A review. *Petroleum*, 2018.
- [20] Mohammed D Aminu, Seyed Ali Nabavi, Christopher A Rochelle, and Vasilije Manovic. A review of developments in carbon dioxide storage. *Applied Energy*, 208:1389–1419, 2017.
- [21] Ruth Shortall, Brynhildur Davidsdottir, and Guðni Axelsson. Geothermal energy for sustainable development: A review of sustainability impacts and assessment frameworks. *Renewable and Sustainable Energy Reviews*, 44:391–406, 2015.
- [22] Arvind Thekdi and Sachin U. Nimbalkar. Industrial Waste Heat Recovery - Potential Applications, Available Technologies and Crosscutting R&D Opportunities. Technical report, E3M. Inc North Potomac, Oak Ridge National Lab., United States, 2015.
- [23] Daniel Champier. Thermoelectric generators: A review of applications. *Energy Conversion and Management*, 140:167–181, 2017.
- [24] Lon E Bell. Cooling, Heating, Generating Power, and Recovering Waste Heat with Thermoelectric Systems. *Science*, 321(5895):1457 LP – 1461, sep 2008.
- [25] Yuan Deng, Wei Zhu, Yao Wang, and Yongming Shi. Enhanced performance of solar-driven photovoltaic–thermoelectric hybrid system in an integrated design. *Solar Energy*, 88:182–191, 2013.
- [26] Jinsheng Xiao, Tianqi Yang, Peng Li, Pengcheng Zhai, and Qingjie Zhang. Thermal design and management for performance optimization of solar thermoelectric generator. *Applied Energy*, 93:33–38, 2012.

- [27] R Amatya and R J Ram. Solar Thermoelectric Generator for Micropower Applications. *Journal of Electronic Materials*, 39(9):1735–1740, 2010.
- [28] Jyoti Parikh, Kalpana Balakrishnan, Vijay Laxmi, and Haimanti Biswas. Exposure from cooking with biofuels: pollution monitoring and analysis for rural Tamil Nadu, India. *Energy*, 26(10):949–962, 2001.
- [29] Lars Onsager. Reciprocal Relations in Irreversible Processes. I. *Physical Review*, 37(4):405–426, feb 1931.
- [30] Veljko Zlatić and René Monnier. *Modern theory of thermoelectricity*. Oxford University Press, 2014.
- [31] H Julian Goldsmid. *Introduction to Thermoelectricity*. Springer, 2009.
- [32] D M Rowe. *CRC Handbook of Thermoelectrics*. CRC Press, 1995.
- [33] G Jeffrey Snyder and Eric S Toberer. Complex thermoelectric materials. *Nature Mater.*, 7:105–114, 2008.
- [34] Kryotherm. Thermoelectric modules for power generation, 2019.
- [35] G Jeffrey Snyder and Tristan S Ursell. Thermoelectric Efficiency and Compatibility. *Physical Review Letters*, 91(14):148301, oct 2003.
- [36] Ran He, Gabi Schierning, and Kornelius Nielsch. Thermoelectric Devices: A Review of Devices, Architectures, and Contact Optimization. *Advanced Materials Technologies*, 3(4):1700256, 2018.
- [37] Ali Shakouri. Recent Developments in Semiconductor Thermoelectric Physics and Materials. *Annual Review of Materials Research*, 41(1):399–431, 2011.
- [38] II-VI Marlow. Thermoelectric Generator (TEG) Modules, 2019.
- [39] Cronin B Vining. An inconvenient truth about thermoelectrics. *Nature Materials*, 8:83, feb 2009.
- [40] Ali Shakouri and Mona Zebbarjadi. Nanoengineered Materials for Thermoelectric Energy Conversion. In Sebastian Volz, editor, *Thermal Nanosystems and Nanomaterials*, pages 225–299. Springer Berlin Heidelberg, Berlin, Heidelberg, 2009.
- [41] Saniya LeBlanc, Shannon K Yee, Matthew L Scullin, Chris Dames, and Kenneth E Goodson. Material and manufacturing cost considerations for thermoelectrics. *Renewable and Sustainable Energy Reviews*, 32:313–327, 2014.
- [42] Shannon K Yee, Saniya LeBlanc, Kenneth E Goodson, and Chris Dames. \$ per W metrics for thermoelectric power generation: beyond ZT. *Energy & Environmental Science*, 6(9):2561–2571, 2013.

- [43] Kazuaki Yazawa and Ali Shakouri. Energy Payback Optimization of Thermoelectric Power Generator Systems, 2010.
- [44] D R Lide. *CRC Handbook of Chemistry and Physics, 84th Edition*. CRC HANDBOOK OF CHEMISTRY AND PHYSICS. Taylor & Francis, 2003.
- [45] Clemens J. M. Lasance. The Seebeck Coefficient, 2006.
- [46] J A Dean and N A Lange. *Lange’s Handbook of Chemistry*. Number v. 15 in Lange’s Handbook of Chemistry. McGraw-Hill, 1999.
- [47] A Stranz, J Kähler, A Waag, and E Peiner. Thermoelectric Properties of High-Doped Silicon from Room Temperature to 900 K. *Journal of Electronic Materials*, 42(7):2381–2387, 2013.
- [48] G Eranna. *Crystal Growth and Evaluation of Silicon for VLSI and ULSI*. Taylor & Francis, 2014.
- [49] Xiao Zhang and Li-Dong Zhao. Thermoelectric materials: Energy conversion between heat and electricity. *J. Materiomics*, 1:92–105, 2015.
- [50] M Rull-Bravo, A Moure, J F Fernández, and M Martín-González. Skutterudites as thermoelectric materials: revisited. *RSC Advances*, 5(52):41653–41667, 2015.
- [51] Bed Poudel, Qing Hao, Yi Ma, Yucheng Lan, Austin Minnich, Bo Yu, Xiao Yan, Dezhi Wang, Andrew Muto, Daryoosh Vashaee, Xiaoyuan Chen, Junming Liu, Mildred S Dresselhaus, Gang Chen, and Zhifeng Ren. High-Thermoelectric Performance of Nanostructured Bismuth Antimony Telluride Bulk Alloys. *Science*, 320(5876):634–638, 2008.
- [52] Xiao Yan, Bed Poudel, Yi Ma, W S Liu, G Joshi, Hui Wang, Yucheng Lan, Dezhi Wang, Gang Chen, and Z F Ren. Experimental Studies on Anisotropic Thermoelectric Properties and Structures of n-Type Bi₂Te_{2.7}Se_{0.3}. *Nano Letters*, 10(9):3373–3378, sep 2010.
- [53] Z H Dughaish. Lead telluride as a thermoelectric material for thermoelectric power generation. *Physica B: Condensed Matter*, 322(1):205–223, 2002.
- [54] Giri Joshi, Hohyun Lee, Yucheng Lan, Xiaowei Wang, Gaohua Zhu, Dezhi Wang, Ryan W Gould, Diana C Cuff, Ming Y Tang, Mildred S Dresselhaus, Gang Chen, and Zhifeng Ren. Enhanced Thermoelectric Figure-of-Merit in Nanostructured p-type Silicon Germanium Bulk Alloys. *Nano Letters*, 8(12):4670–4674, dec 2008.
- [55] X W Wang, H Lee, Y C Lan, G H Zhu, G Joshi, D Z Wang, J Yang, A J Muto, M Y Tang, J Klatsky, S Song, M S Dresselhaus, G Chen, and Z F Ren. Enhanced thermoelectric figure of merit in nanostructured n-type silicon germanium bulk alloy. *Applied Physics Letters*, 93(19):193121, nov 2008.

- [56] L D Hicks and M S Dresselhaus. Effect of quantum-well structures on the thermoelectric figure of merit. *Physical Review B*, 47(19):12727–12731, may 1993.
- [57] L D Hicks and M S Dresselhaus. Thermoelectric figure of merit of a one-dimensional conductor. *Physical Review B*, 47(24):16631–16634, jun 1993.
- [58] Mohamed Hamid Elsheikh, Dhafer Abdulameer Shnawah, Mohd Faizul Mohd Sabri, Suhana Binti Mohd Said, Masjuki Haji Hassan, Mohamed Bashir Ali Bashir, and Mahazani Mohamad. A review on thermoelectric renewable energy: Principle parameters that affect their performance. *Renewable and Sustainable Energy Rev.*, 30:337–355, 2014.
- [59] M Zebarjadi, K Esfarjani, M S Dresselhaus, Z F Ren, and G Chen. Perspectives on thermoelectrics: from fundamentals to device applications. *Energy & Environmental Science*, 5(1):5147–5162, 2012.
- [60] Yanzhong Pei, Heng Wang, and Snyder G J. Band Engineering of Thermoelectric Materials. *Adv. Mater.*, 24:6125–6135, 2012.
- [61] Hao Zhu, Chong Xiao, and Yi Xie. Design of Highly Efficient Thermoelectric Materials: Tailoring Reciprocal-Space Properties by Real-Space Modification. *Advanced Materials*, 30(48):1802000, 2018.
- [62] Jun Mao, Zihang Liu, and Zhifeng Ren. Size effect in thermoelectric materials. *Npj Quantum Materials*, 1:16028, 2016.
- [63] Mercuri G Kanatzidis. Nanostructured thermoelectrics: the new paradigm? *Chem. Mater.*, 22:648–659, 2010.
- [64] Ran He, Wieland Heyn, Felix Thiel, Nicolás Pérez, Christine Damm, Darius Pohl, Bernd Rellinghaus, Christian Reimann, Maximilian Beier, Jochen Friedrich, Hangtian Zhu, Zhifeng Ren, Kornelius Nielsch, and Gabi Schierning. Thermoelectric properties of silicon and recycled silicon sawing waste. *Journal of Materiomics*, 2018.
- [65] C J Glassbrenner and Glen A Slack. Thermal Conductivity of Silicon and Germanium from 3K to the Melting Point. *Physical Review*, 134(4A):A1058–A1069, may 1964.
- [66] Sabah K Bux, Richard G Blair, Pawan K Gogna, Hohyun Lee, Gang Chen, Mildred S Dresselhaus, Richard B Kaner, and Jean-Pierre Fleurial. Nanostructured Bulk Silicon as an Effective Thermoelectric Material. *Advanced Functional Materials*, 19(15):2445–2452, aug 2009.
- [67] A J Minnich, Milfred S Dresselhaus, Z F Ren, and G Chen. Bulk nanostructured thermoelectric materials: current research and future prospects. *Energy Environ. Sci.*, 2:466–479, 2009.

- [68] Wolfgang G. Zeier, Alex Zevalkink, Zachary M. Gibbs, Geoffroy Hautier, Mercuri G. Kanatzidis, and G. Jeffrey Snyder. Thinking Like a Chemist: Intuition in Thermoelectric Materials. *Angewandte Chemie - International Edition*, 55(24):6826–6841, 2016.
- [69] Martin Wagner. *Simulation of Thermoelectric Devices*. PhD thesis, TU Wien - Institute for Microelectronics, 2007.
- [70] Christopher J Vineis, Ali Shakouri, Arun Majumdar, and Mercuri G Kanatzidis. Nanostructured Thermoelectrics: Big Efficiency Gains from Small Features. *Adv. Mater.*, 22:3970–3980, 2010.
- [71] Gangjian Tan, Shiqiang Hao, Riley C Hanus, Xiaomi Zhang, Shashwat Anand, Trevor P Bailey, Alexander J E Rettie, Xianli Su, Ctirad Uher, Vinayak P Dravid, G Jeffrey Snyder, Chris Wolverton, and Mercuri G Kanatzidis. High Thermoelectric Performance in SnTe–AgSbTe₂ Alloys from Lattice Softening, Giant Phonon–Vacancy Scattering, and Valence Band Convergence. *ACS Energy Letters*, 3(3):705–712, mar 2018.
- [72] M S Dresselhaus, G Chen, M Y Tang, R G Yang, H Lee, D Z Wang, Z F Ren, J.-P. Fleurial, and P Gogna. New Directions for Low-Dimensional Thermoelectric Materials. *Adv. Mater.*, 19:1043–1053, 2007.
- [73] Sang Il Kim, Kyu Hyoung Lee, Hyeon A Mun, Hyun Sik Kim, Sung Woo Hwang, Jong Wook Roh, Dae Jin Yang, Weon Ho Shin, Xiang Shu Li, Young Hee Lee, G Jeffrey Snyder, and Sung Wng Kim. Dense dislocation arrays embedded in grain boundaries for high-performance bulk thermoelectrics. *Science*, 348(6230):109–114, 2015.
- [74] Jifeng Sun and David J Singh. Thermoelectric properties of AMg₂X₂, AZn₂Sb₂ (A = Ca, Sr, Ba; X = Sb, Bi), and Ba₂ZnX₂ (X = Sb, Bi) Zintl compounds. *Journal of Materials Chemistry A*, 5(18):8499–8509, 2017.
- [75] Klaus Habicht. Skutterudites, 2018.
- [76] Susan M Kauzlarich, Shawna R Brown, and G Jeffrey Snyder. Zintl phases for thermoelectric devices. *Dalton Transactions*, (21):2099–2107, 2007.
- [77] Holger Kleinke. New bulk Materials for Thermoelectric Power Generation: Clathrates and Complex Antimonides. *Chemistry of Materials*, 22(3):604–611, feb 2010.
- [78] Yuhao Fu, Xin He, Lijun Zhang, and David J Singh. Collective-Goldstone-mode-induced ultralow lattice thermal conductivity in Sn-filled skutterudite SnFe₄Sb₁₂. *Physical Review B*, 97(2):24301, jan 2018.
- [79] Yanzhong Pei, Zachary M Gibbs, Andrei Gloskovskii, Benjamin Balke, Wolfgang G Zeier, and G Jeffrey Snyder. Optimum Carrier Concentration in n-Type PbTe Thermoelectrics. *Advanced Energy Materials*, 4(13), 2014.

- [80] Xun Shi, Jiong Yang, James R Salvador, Miaofang Chi, Jung Y Cho, Hsin Wang, Shengqiang Bai, Jihui Yang, Wenqing Zhang, and Lidong Chen. Multiple-Filled Skutterudites: High Thermoelectric Figure of Merit through Separately Optimizing Electrical and Thermal Transports. *Journal of the American Chemical Society*, 133(20):7837–7846, may 2011.
- [81] Chenguang Fu, Shengqiang Bai, Yintu Liu, Yunshan Tang, Lidong Chen, Xinbing Zhao, and Tiejun Zhu. Realizing high figure of merit in heavy-band p-type half-Heusler thermoelectric materials. *Nature Communications*, 6:8144, sep 2015.
- [82] Hanhui Xie, Heng Wang, Chenguang Fu, Yintu Liu, G Jeffrey Snyder, Xinbing Zhao, and Tiejun Zhu. The intrinsic disorder related alloy scattering in ZrNiSn half-Heusler thermoelectric materials. *Scientific reports*, 4:6888, nov 2014.
- [83] Tiejun Zhu, Yintu Liu, Chenguang Fu, Joseph P Heremans, Jeffrey G Snyder, and Xinbing Zhao. Compromise and Synergy in High-Efficiency Thermoelectric Materials. *Advanced Materials*, 29(14):1605884, 2017.
- [84] Yanzhong Pei, Aaron LaLonde, Shiho Iwanaga, and G Jeffrey Snyder. High thermoelectric figure of merit in heavy hole dominated PbTe. *Energy Environ. Sci.*, 4(6):2085–2089, 2011.
- [85] Andrew F May, Jean-Pierre Fleurial, and G Jeffrey Snyder. Thermoelectric performance of lanthanum telluride produced via mechanical alloying. *Physical Review B*, 78(12):125205, sep 2008.
- [86] Trinh Vo, Paul von Allmen, Chen-Kuo Huang, James Ma, Sabah Bux, and Jean-Pierre Fleurial. Electronic and thermoelectric properties of Ce_3Te_4 and La_3Te_4 computed with density functional theory with on-site Coulomb interaction correction. *Journal of Applied Physics*, 116(13):133701, oct 2014.
- [87] Arash Mehdizadeh Dehkordi, Mona Zebarjadi, Jian He, and Terry M Tritt. Thermoelectric power factor: Enhancement mechanisms and strategies for higher performance thermoelectric materials. *Materials Science and Engineering: R: Reports*, 97:1–22, 2015.
- [88] Bo Yu, Mona Zebarjadi, Hui Wang, Kevin Lukas, Hengzhi Wang, Dezhi Wang, Cyril Opeil, Mildred Dresselhaus, Gang Chen, and Zhifeng Ren. Enhancement of Thermoelectric Properties by Modulation-Doping in Silicon Germanium Alloy Nanocomposites. *Nano Letters*, 12(4):2077–2082, apr 2012.
- [89] N W Ashcroft and N D Mermin. *Solid State Physics*. Saunders College, 1976.
- [90] G D Mahan and J O Sofo. The best thermoelectric. *Proceedings of the National Academy of Sciences*, 93(15):7436–7439, 1996.
- [91] Yanzhong Pei, Xiaoya Shi, Aaron LaLonde, Heng Wang, Lidong Chen, and G Jeffrey Snyder. Convergence of electronic bands for high performance bulk thermoelectrics. *Nature*, 473:66–69, 2011.

- [92] Jiong Yang, Lili Xi, Wujie Qiu, Lihua Wu, Xun Shi, Lidong Chen, Jihui Yang, Wenqing Zhang, Ctirad Uher, and David J Singh. On the tuning of electrical and thermal transport in thermoelectrics: an integrated theory–experiment perspective. *npj Computational Materials*, 2:15015, 2015.
- [93] Wei Liu, Xiaojian Tan, Kang Yin, Huijun Liu, Xinfeng Tang, Jing Shi, Qingjie Zhang, and Ctirad Uher. Convergence of Conduction Bands as a Means of Enhancing Thermoelectric Performance of n-Type $\text{Mg}_2\text{Si}_{1-x}\text{Sn}_x$ Solid Solutions. *Physical Review Letters*, 108(16):166601, apr 2012.
- [94] J M O Zide, D Vashaee, Z X Bian, G Zeng, J E Bowers, A Shakouri, and A C Gossard. Demonstration of electron filtering to increase the Seebeck coefficient in $\text{In}_{0.53}\text{Ga}_{0.47}\text{As}/\text{In}_{0.53}\text{Ga}_{0.28}\text{Al}_{0.19}\text{As}$ superlattices. *Physical Review B*, 74(20):205335, nov 2006.
- [95] M Sabarinathan, M Omprakash, S Harish, M Navaneethan, J Archana, S Ponnusamy, H Ikeda, T Takeuchi, C Muthamizhchelvan, and Y Hayakawa. Enhancement of power factor by energy filtering effect in hierarchical BiSbTe_3 nanostructures for thermoelectric applications. *Applied Surface Science*, 418:246–251, 2017.
- [96] Xianfu Meng, Zihang Liu, Bo Cui, Dandan Qin, Huiyuan Geng, Wei Cai, Liangwei Fu, Jiaqing He, Zhifeng Ren, and Jiehe Sui. Grain Boundary Engineering for Achieving High Thermoelectric Performance in n-Type Skutterudites. *Advanced Energy Materials*, 7(13):1602582, jul 2017.
- [97] L D Hicks, T C Harman, X Sun, and M S Dresselhaus. Experimental study of the effect of quantum-well structures on the thermoelectric figure of merit. *Physical Review B*, 53(16):R10493–R10496, apr 1996.
- [98] Joseph P Heremans, Bartłomiej Wiendlocha, and Audrey M Chamoire. Resonant levels in bulk thermoelectric semiconductors. *Energy & Environmental Science*, 5(2):5510–5530, 2012.
- [99] J P Heremans. Low-Dimensional Thermoelectricity. *Proceedings of the XXXIV International School of Semiconducting Compounds*, 108:609–634, 2005.
- [100] Paothep Pichanusakorn and Bandaru Prabhakar. Nanostructured thermoelectrics. *Mater. Science and Engineering R*, 67:19–63, 2010.
- [101] Rama Venkatasubramanian, Edward Siivola, Thomas Colpitts, and Brooks O’Quinn. Thin-film thermoelectric devices with high room-temperature figures of merit. *Nature*, 413:597–602, 2001.
- [102] Yoriko Mune, Hiromichi Ohta, Kunihiro Koumoto, Teruyasu Mizoguchi, and Yuichi Ikuhara. Enhanced Seebeck coefficient of quantum-confined electrons in $\text{SrTiO}_3/\text{SrTi}_{0.8}\text{Nb}_{0.2}\text{O}_3$ superlattices. *Applied Physics Letters*, 91(19):192105, nov 2007.

- [103] Joseph P Heremans, Vladimir Jovovic, Eric S Toberer, Ali Saramat, Ken Kurosaki, Anek Charoenphakdee, Shinsuke Yamanaka, and G Jeffrey Snyder. Enhancement of Thermoelectric Efficiency in PbTe by Distortion of the Electronic Density of States. *Science*, 321:554–557, 2008.
- [104] Christopher M Jaworski, Vladimir Kulbachinskii, and Joseph P Heremans. Resonant level formed by tin in Bi₂Te₃ and the enhancement of room-temperature thermoelectric power. *Phys. Rev. B*, 80:233201, 2009.
- [105] David J Singh. Doping-dependent thermopower of PbTe from Boltzmann transport calculations. *Phys. Rev. B*, 81:195217, 2010.
- [106] E Bringuier. Kinetic theory of high-field transport in semiconductors. *Physical Review B*, 57(4):2280–2285, jan 1998.
- [107] Srinivasan Krishnamurthy, A Sher, and A.-B. Chen. High-field transport in semiconductors based on eigenvalue solution to Boltzmann equation. *Applied Physics Letters*, 55(10):1002–1004, sep 1989.
- [108] Supriyo Datta. The non-equilibrium Green’s function (NEGF) formalism: An elementary introduction. *Digest. International Electron Devices Meeting.*, pages 703–706, 2002.
- [109] Jozef T Devreese and Alexandre S Alexandrov. Fröhlich polaron and bipolaron: recent developments. *Reports on Progress in Physics*, 72(6):66501, 2009.
- [110] J T Devreese. Fröhlich Polarons. Lecture course including detailed theoretical derivations - 8th edition, 2016.
- [111] W Kohn. Nobel Lecture: Electronic structure of matter—wave functions and density functionals. *Reviews of Modern Physics*, 71(5):1253–1266, oct 1999.
- [112] José M Soler, Emilio Artacho, Julian D Gale, Alberto García, Javier Junquera, Pablo Ordejón, and Daniel Sánchez-Portal. The SIESTA method for *ab initio* order-*N* materials simulation. *Journal of Physics: Condensed Matter*, 14(11):2745–2779, 2002.
- [113] Paolo Giannozzi, Stefano Baroni, Nicola Bonini, Matteo Calandra, Roberto Car, Carlo Cavazzoni, Davide Ceresoli, Guido L Chiarotti, Matteo Cococcioni, Ismaila Dabo, Andrea Dal Corso, Stefano de Gironcoli, Stefano Fabris, Guido Fratesi, Ralph Gebauer, Uwe Gerstmann, Christos Gougoussis, Anton Kokalj, Michele Lazzeri, Layla Martin-Samos, Nicola Marzari, Francesco Mauri, Riccardo Mazzarello, Stefano Paolini, Alfredo Pasquarello, Lorenzo Paulatto, Carlo Sbraccia, Sandro Scandolo, Gabriele Sclauzero, Ari P Seitsonen, Alexander Smogunov, Paolo Umari, and Renata M Wentzcovitch. QUANTUM ESPRESSO: a modular and open-source software project for quantum simulations of materials. *Journal of Physics: Condensed Matter*, 21(39):395502, 2009.

- [114] Richard M Martin. *Electronic Structure: Basic Theory and Practical Methods*. Cambridge University Press, Cambridge, 2004.
- [115] Robert G Parr. *Density Functional Theory of Atoms and Molecules BT - Horizons of Quantum Chemistry*. Springer Netherlands, Dordrecht, 1980.
- [116] P Hohenberg and W Kohn. Inhomogeneous Electron Gas. *Physical Review*, 136(3B):B864–B871, nov 1964.
- [117] Mel Levy. Universal variational functionals of electron densities, first-order density matrices, and natural spin-orbitals and solution of the v -representability problem. *Proceedings of the National Academy of Sciences*, 76(12):6062 LP – 6065, dec 1979.
- [118] Elliott H Lieb. Density functionals for coulomb systems. *International Journal of Quantum Chemistry*, 24(3):243–277, sep 1983.
- [119] W Kohn and L J Sham. Self-Consistent Equations Including Exchange and Correlation Effects. *Physical Review*, 140(4A):A1133–A1138, nov 1965.
- [120] R P Feynman. Forces in Molecules. *Physical Review*, 56(4):340–343, aug 1939.
- [121] A D Becke. Density-functional exchange-energy approximation with correct asymptotic behavior. *Physical Review A*, 38(6):3098–3100, sep 1988.
- [122] John P Perdew and Yue Wang. Accurate and simple analytic representation of the electron-gas correlation energy. *Physical Review B*, 45(23):13244–13249, jun 1992.
- [123] John P Perdew, Kieron Burke, and Matthias Ernzerhof. Generalized Gradient Approximation Made Simple. *Physical Review Letters*, 77(18):3865–3868, oct 1996.
- [124] Benjamin Kaduk, Tim Kowalczyk, and Troy Van Voorhis. Constrained Density Functional Theory. *Chemical Reviews*, 112(1):321–370, jan 2012.
- [125] G Kresse and J Furthmüller. Efficient iterative schemes for ab initio total-energy calculations using a plane-wave basis set. *Physical Review B*, 54(16):11169–11186, oct 1996.
- [126] Gregory H Wannier. The Structure of Electronic Excitation Levels in Insulating Crystals. *Physical Review*, 52(3):191–197, aug 1937.
- [127] Nicola Marzari and David Vanderbilt. Maximally localized generalized Wannier functions for composite energy bands. *Physical Review B*, 56(20):12847–12865, nov 1997.
- [128] Arash A Mostofi, Jonathan R Yates, Young-Su Lee, Ivo Souza, David Vanderbilt, and Nicola Marzari. wannier90: A tool for obtaining maximally-localised Wannier functions. *Computer Physics Communications*, 178(9):685–699, 2008.
- [129] Nicola Marzari, Arash A Mostofi, Jonathan R Yates, Ivo Souza, and David Vanderbilt. Maximally localized Wannier functions: Theory and applications. *Reviews of Modern Physics*, 84(4):1419–1475, oct 2012.

- [130] Atsushi Togo and Isao Tanaka. First principles phonon calculations in materials science. *Scripta Materialia*, 108:1–5, 2015.
- [131] Shao-Feng Wang, Hui-Li Zhang, and Xiao-Zhi Wu. A new rotation sum rule for the atomic force constants. *Journal of Physics: Condensed Matter*, 19(38):386233, 2007.
- [132] M S Dresselhaus. SOLID STATE PHYSICS, PART I: Transport Properties of Solids, 2001.
- [133] R Knorren, G Bouzerar, and K H Bennemann. Theory for the dynamics of excited electrons in noble and transition metals. *Journal of Physics: Condensed Matter*, 14(27):R739–R765, 2002.
- [134] Andrea Cepellotti, Giorgia Fugallo, Lorenzo Paulatto, Michele Lazzeri, Francesco Mauri, and Nicola Marzari. Phonon hydrodynamics in two-dimensional materials. *Nature Communications*, 6:6400, mar 2015.
- [135] T J Scheidemanter, C Ambrosch-Draxl, T Thonhauser, J V Badding, and J O Sofo. Transport coefficients from first-principles calculations. *Phys. Rev. B*, 68(12):125210, sep 2003.
- [136] M Jonson and G D Mahan. Mott’s formula for the thermopower and the Wiedemann-Franz law. *Physical Review B*, 21(10):4223–4229, may 1980.
- [137] M Jonson and G D Mahan. Electron-phonon contribution to the thermopower of metals. *Physical Review B*, 42(15):9350–9356, nov 1990.
- [138] Melvin Cutler and N F Mott. Observation of Anderson Localization in an Electron Gas. *Physical Review*, 181(3):1336–1340, may 1969.
- [139] X H Yang, X Y Qin, D Li, J Zhang, C J Song, Y F Liu, L Wang, and H X Xin. Thermo-electric properties of homogeneously and non-homogeneously doped $\text{CdTe}_{15/16}\text{M}_{1/16}$ ($\text{M} = \text{N}, \text{P}, \text{As}, \text{Sb}$) and $\text{Cd}_{15/16}\text{TeM}_{1/16}$ ($\text{M} = \text{Na}, \text{K}, \text{Rb}, \text{Cs}$). *J. of Physics and Chem. of Solids*, 86:74–81, 2015.
- [140] Dylan Bayerl and Emmanouil Kioupakis. Theoretical limits of thermoelectric figure of merit in n -type TiO_2 polymorphs. *Physical Review B*, 91(16):165104, apr 2015.
- [141] G D Mahan. *Many Particle Physics, Third Edition*. Plenum, 2000.
- [142] Mark Lundstrom. *Fundamentals of Carrier Transport*. Cambridge University Press, Cambridge, 2 edition, 2000.
- [143] Feliciano Giustino. Electron-phonon interactions from first principles. *Reviews of Modern Physics*, 89(1):15003, feb 2017.
- [144] Feliciano Giustino, Marvin L Cohen, and Steven G Louie. Electron-phonon interaction using Wannier functions. *Physical Review B*, 76(16):165108, oct 2007.

- [145] J Sjakste, N Vast, M Calandra, and F Mauri. Wannier interpolation of the electron-phonon matrix elements in polar semiconductors: Polar-optical coupling in GaAs. *Physical Review B*, 92(5):54307, aug 2015.
- [146] D. L. Maslov. SOLID STATE II: Electron-electron interaction and the Fermi-liquid theory, 2014.
- [147] Giorgia Fugallo and Luciano Colombo. Calculating lattice thermal conductivity: a synopsis. *Physica Scripta*, 93(4):43002, 2018.
- [148] Giorgia Fugallo, Michele Lazzeri, Lorenzo Paulatto, and Francesco Mauri. Ab initio variational approach for evaluating lattice thermal conductivity. *Physical Review B*, 88(4):45430, jul 2013.
- [149] Wu Li, Jesús Carrete, Nebil A. Katcho, and Natalio Mingo. ShengBTE: A solver of the Boltzmann transport equation for phonons. *Computer Physics Communications*, 185(6):1747–1758, 2014.
- [150] Shin-ichiro Tamura. Isotope scattering of dispersive phonons in Ge. *Physical Review B*, 27(2):858–866, jan 1983.
- [151] C A Ratsifaritana and P G Klemens. Scattering of phonons by vacancies. *International Journal of Thermophysics*, 8(6):737–750, 1987.
- [152] Joseph Callaway. Model for Lattice Thermal Conductivity at Low Temperatures. *Physical Review*, 113(4):1046–1051, feb 1959.
- [153] Philip B Allen. Improved Callaway model for lattice thermal conductivity. *Physical Review B*, 88(14):144302, oct 2013.
- [154] Jinlong Ma, Wu Li, and Xiaobing Luo. Examining the Callaway model for lattice thermal conductivity. *Physical Review B*, 90(3):35203, jul 2014.
- [155] S Datta. *Electronic Transport in Mesoscopic Systems*. Cambridge University Press, 1995.
- [156] Branislav Nikolić. *Quantum Transport in Finite Disordered Electron Systems*. PhD thesis, State University of New York at Stony Brook, 2000.
- [157] A D Stone and A Szafer. What is measured when you measure a resistance?—The Landauer formula revisited. *IBM Journal of Research and Development*, 32(3):384–413, 1988.
- [158] Changwook Jeong, Supriyo Datta, and Mark Lundstrom. Full dispersion versus Debye model evaluation of lattice thermal conductivity with a Landauer approach. *Journal of Applied Physics*, 109(7):73718, apr 2011.
- [159] Changwook Jeong, Supriyo Datta, and Mark Lundstrom. Thermal conductivity of bulk and thin-film silicon: A Landauer approach. *Journal of Applied Physics*, 111(9):93708, may 2012.

- [160] Changwook Jeong, Raseong Kim, Mathieu Luisier, Supriyo Datta, and Mark Lundstrom. On Landauer versus Boltzmann and full band versus effective mass evaluation of thermoelectric transport coefficients. *Journal of Applied Physics*, 107(2):23707, jan 2010.
- [161] Bo Qiu, Zhiting Tian, Ajit Vallabhaneni, Bolin Liao, Jonathan M Mendoza, Oscar D Restrepo, Xiulin Ruan, and Gang Chen. First-principles simulation of electron mean-free-path spectra and thermoelectric properties in silicon. *EPL (Europhysics Letters)*, 109(5):57006, 2015.
- [162] Puqing Jiang, Lucas Lindsay, and Yee Kan Koh. Role of low-energy phonons with mean-free-paths $>0.8 \mu\text{m}$ in heat conduction in silicon. *Journal of Applied Physics*, 119(24):245705, jun 2016.
- [163] Yinong Yin, Bharati Tudu, and Ashutosh Tiwari. Recent advances in oxide thermoelectric materials and modules. *Vacuum*, 146:356–374, 2017.
- [164] Lian Ji. 3 - Metal oxide-based thermoelectric materials. In Yuping B T Metal Oxides in Energy Technologies Wu, editor, *Metal Oxides*, pages 49–72. Elsevier, 2018.
- [165] Hiromichi Ohta. Thermoelectrics based on strontium titanate. *Materials Today*, 10(10):44–49, 2007.
- [166] G Bouzerar, S Thébaud, Ch. Adessi, R Debord, M Apreutesei, R Bachelet, and S Pailhès. Unified modelling of the thermoelectric properties in SrTiO_3 . *EPL (Europhysics Letters)*, 118(6):67004, 2017.
- [167] G Bouzerar, S Thébaud, R Bouzerar, S Pailhès, and Ch. Adessi. Absence of confinement in $(\text{SrTiO}_3)/(\text{SrTi}_{0.8}\text{Nb}_{0.2}\text{O}_3)$ superlattices. *Physical Review Materials*, 2(3):35402, mar 2018.
- [168] S Thébaud, Ch. Adessi, and G Bouzerar. Investigating the high-temperature thermoelectric properties of n-type rutile TiO_2 . In prep., 2019.
- [169] Hiroaki Muta, Ken Kurosaki, and Shinsuke Yamanaka. Thermoelectric properties of reduced and La-doped single-crystalline SrTiO_3 . *Journal of Alloys and Compounds*, 392(1):306–309, 2005.
- [170] José M Vila-Funqueiriño, Romain Bachelet, Guillaume Saint-Girons, Michel Gendry, Marti Gich, Jaume Gazquez, Etienne Ferain, Francisco Rivadulla, Juan Rodriguez-Carvajal, Narcis Mestres, and Adrián Carretero-Genevri. Integration of functional complex oxide nanomaterials on silicon. *Frontiers in Physics*, 3:38, 2015.
- [171] L F Mattheiss. Energy Bands for KNiF_3 , SrTiO_3 , KMoO_3 , and KTaO_3 . *Physical Review B*, 6(12):4718–4740, dec 1972.
- [172] T Wolfram and S Ellialtioglu. Density-of-states and partial-density-of-states functions for the cubic d -band perovskites. *Physical Review B*, 25(4):2697–2714, feb 1982.

- [173] N Shanthi and D D Sarma. Electronic structure of electron doped SrTiO₃: SrTiO_{3- δ} and Sr_{1- x} La _{x} TiO₃. *Physical Review B*, 57(4):2153–2158, jan 1998.
- [174] Hidetomo Usui, Shinsuke Shibata, and Kazuhiko Kuroki. Origin of coexisting large Seebeck coefficient and metallic conductivity in the electron doped SrTiO₃ and KTaO₃. *Physical Review B*, 81(20):205121, may 2010.
- [175] Zhicheng Zhong, Anna Tóth, and Karsten Held. Theory of spin-orbit coupling at LaAlO₃/SrTiO₃ interfaces and SrTiO₃ surfaces. *Physical Review B*, 87(16):161102, apr 2013.
- [176] Walter Kohn. Theory of the Insulating State. *Physical Review*, 133(1A):A171–A181, jan 1964.
- [177] D Pines and P Nozières. *The Theory of Quantum Liquids*. Addison-Wesley, 1989.
- [178] A J Millis and S N Coppersmith. Interaction and doping dependence of optical spectral weight of the two-dimensional Hubbard model. *Physical Review B*, 42(16):10807–10810, dec 1990.
- [179] Douglas J Scalapino, Steven R White, and Shoucheng Zhang. Insulator, metal, or superconductor: The criteria. *Physical Review B*, 47(13):7995–8007, apr 1993.
- [180] Georges Bouzerar and Richard Bouzerar. Optical conductivity of Mn-doped GaAs. *New Journal of Physics*, 13(2):23002, 2011.
- [181] Alexis Baratoff and Gerd Binnig. Mechanism of superconductivity in SrTiO₃. *Physica B+C*, 108(1):1335–1336, 1981.
- [182] D van der Marel, J L M van Mechelen, and I I Mazin. Common Fermi-liquid origin of T^2 resistivity and superconductivity in n -type SrTiO₃. *Physical Review B*, 84(20):205111, nov 2011.
- [183] Evgeny Mikhhev, Burak Himmetoglu, Adam P Kaidos, Pouya Moetakef, Tyler A Cain, Chris G Van de Walle, and Susanne Stemmer. Limitations to the room temperature mobility of two- and three-dimensional electron liquids in SrTiO₃. *Applied Physics Letters*, 106(6):62102, feb 2015.
- [184] S N Klimin, J Tempere, D van der Marel, and J T Devreese. Microscopic mechanisms for the Fermi-liquid behavior of Nb-doped strontium titanate. *Physical Review B*, 86(4):45113, jul 2012.
- [185] J L M van Mechelen, D van der Marel, C Grimaldi, A B Kuzmenko, N P Armitage, N Reyren, H Hagemann, and I I Mazin. Electron-Phonon Interaction and Charge Carrier Mass Enhancement in SrTiO₃. *Physical Review Letters*, 100(22):226403, jun 2008.

- [186] C Z Bi, J Y Ma, J Yan, X Fang, B R Zhao, D Z Yao, and X G Qiu. Electron–phonon coupling in Nb-doped SrTiO₃ single crystal. *Journal of Physics: Condensed Matter*, 18(8):2553–2561, 2006.
- [187] Woo Seok Choi, Hyang Keun Yoo, and Hiromichi Ohta. Polaron Transport and Thermoelectric Behavior in La-Doped SrTiO₃ Thin Films with Elemental Vacancies. *Advanced Functional Materials*, 25(5):799–804, feb 2015.
- [188] A S Alexandrov and A M Bratkovsky. Giant thermopower and figure of merit of semiconducting polaronic nanolayers. *Physical Review B*, 81(15):153204, apr 2010.
- [189] Woo Seok Choi, Hiromichi Ohta, Soon Jae Moon, Yun Sang Lee, and Tae Won Noh. Dimensional crossover of polaron dynamics in Nb : SrTiO₃/SrTiO₃ superlattices: Possible mechanism of thermopower enhancement. *Physical Review B*, 82(2):24301, jul 2010.
- [190] David Vanderbilt. Soft self-consistent pseudopotentials in a generalized eigenvalue formalism. *Physical Review B*, 41(11):7892–7895, apr 1990.
- [191] N Troullier and José Luís Martins. Efficient pseudopotentials for plane-wave calculations. *Physical Review B*, 43(3):1993–2006, jan 1991.
- [192] T Okuda, K Nakanishi, S Miyasaka, and Y Tokura. Large thermoelectric response of metallic perovskites: Sr_{1-x}La_xTiO₃ ($0 \leq x \leq 0.1$). *Physical Review B*, 63(11):113104, mar 2001.
- [193] Monica Sonne, Ngo Van Nong, Zeming He, Nini Pryds, and Søren Linderøth. Improvement of Niobium Doped SrTiO₃ by Nanostructuring, 2010.
- [194] Tyler A Cain, Adam P Kajdos, and Susanne Stemmer. La-doped SrTiO₃ films with large cryogenic thermoelectric power factors. *Applied Physics Letters*, 102(18):182101, may 2013.
- [195] Jun Okamoto, Gen Shimizu, Shugo Kubo, Yasuji Yamada, Hiroyuki Kitagawa, Akiyuki Matsushita, Yuh Yamada, and Fumihiko Ishikawa. Thermoelectric properties of B-doped SrTiO₃ single crystal. *Journal of Physics: Conference Series*, 176:12042, 2009.
- [196] Bharat Jalan and Susanne Stemmer. Large Seebeck coefficients and thermoelectric power factor of La-doped SrTiO₃ thin films. *Applied Physics Letters*, 97(4):42106, jul 2010.
- [197] H P R Frederikse, W R Thurber, and W R Hosler. Electronic Transport in Strontium Titanate. *Physical Review*, 134(2A):A442–A445, apr 1964.
- [198] Shingo Ohta, Takashi Nomura, Hiromichi Ohta, and Kunihito Koumoto. High-temperature carrier transport and thermoelectric properties of heavily La- or Nb-doped SrTiO₃ single crystals. *Journal of Applied Physics*, 97(3):34106, jan 2005.

- [199] Shingo Ohta, Takashi Nomura, Hiromichi Ohta, Masahiro Hirano, Hideo Hosono, and Kunihiro Koumoto. Large thermoelectric performance of heavily Nb-doped SrTiO₃ epitaxial film at high temperature. *Applied Physics Letters*, 87(9):92108, aug 2005.
- [200] Pouya Moetakef and Tyler A Cain. Metal-insulator transitions in epitaxial Gd_{1-x}Sr_xTiO₃ thin films grown using hybrid molecular beam epitaxy. *Thin Solid Films*, 583:129–134, 2015.
- [201] Xiao Lin, Benoît Fauqué, and Kamran Behnia. Scalable T₂ resistivity in a small single-component Fermi surface. *Science*, 349(6251):945 LP – 948, aug 2015.
- [202] Evgeny Mikhhev, Santosh Raghavan, Jack Y Zhang, Patrick B Marshall, Adam P Kajdos, Leon Balents, and Susanne Stemmer. Carrier density independent scattering rate in SrTiO₃-based electron liquids. *Scientific Reports*, 6:20865, feb 2016.
- [203] N Mingo. Thermoelectric figure of merit and maximum power factor in III–V semiconductor nanowires. *Applied Physics Letters*, 84(14):2652–2654, apr 2004.
- [204] Shadyar Farhangfar. Size-dependent thermoelectricity in nanowires. *Journal of Physics D: Applied Physics*, 44(12):125403, 2011.
- [205] Jun Zhou, Ronggui Yang, Gang Chen, and Mildred S Dresselhaus. Optimal Bandwidth for High Efficiency Thermoelectrics. *Phys. Rev. Lett.*, 107(22):226601, nov 2011.
- [206] Rama Venkatasubramanian. Lattice thermal conductivity reduction and phonon localizationlike behavior in superlattice structures. *Physical Review B*, 61(4):3091–3097, jan 2000.
- [207] T C Harman, P J Taylor, M P Walsh, and B E LaForge. Quantum Dot Superlattice Thermoelectric Materials and Devices. *Science*, 297(5590):2229 LP – 2232, sep 2002.
- [208] T C Harman, P J Taylor, D L Spears, and M P Walsh. Thermoelectric quantum-dot superlattices with high ZT. *Journal of Electronic Materials*, 29(1):L1–L2, 2000.
- [209] C J Vineis, T C Harman, S D Calawa, M P Walsh, R E Reeder, R Singh, and A Shakouri. Carrier concentration and temperature dependence of the electronic transport properties of epitaxial PbTe and PbTe/PbSe nanodot superlattices. *Physical Review B*, 77(23):235202, jun 2008.
- [210] Hiromichi Ohta, SungWng Kim, Yoriko Mune, Teruyasu Mizoguchi, Kenji Nomura, Shingo Ohta, Takashi Nomura, Yuki Nakanishi, Yuichi Ikuhara, Masahiro Hirano, Hideo Hosono, and Kunihiro Koumoto. Giant thermoelectric Seebeck coefficient of a two-dimensional electron gas in SrTiO₃. *Nature Materials*, 6:129, jan 2007.
- [211] Daniel I Bilc, Calin G Floare, Liviu P Zârbo, Sorina Garabagiu, Sebastien Lemal, and Philippe Ghosez. First-Principles Modeling of SrTiO₃ Based Oxides for Thermoelectric Applications. *The Journal of Physical Chemistry C*, 120(45):25678–25688, nov 2016.

- [212] A Kinaci, C Sevik, and T Çağın. Electronic transport properties of SrTiO_3 and its alloys: $\text{Sr}_{1-x}\text{La}_x\text{TiO}_3$ and $\text{SrTi}_{1-x}\text{M}_x\text{O}_3$ ($M = \text{Nb}, \text{Ta}$). *Physical Review B*, 82(15):155114, oct 2010.
- [213] K Ozdogan, M Upadhyay Kahaly, S R Sarath Kumar, H N Alshareef, and U Schwingenschlögl. Enhanced carrier density in Nb-doped SrTiO_3 thermoelectrics. *Journal of Applied Physics*, 111(5):54313, mar 2012.
- [214] Hiromichi Ohta. Two-dimensional thermoelectric Seebeck coefficient of SrTiO_3 -based superlattices. *physica status solidi (b)*, 245(11):2363–2368, 2008.
- [215] Woo Seok Choi, Hiromichi Ohta, and Ho Nyung Lee. Thermopower Enhancement by Fractional Layer Control in 2D Oxide Superlattices. *Advanced Materials*, 26(39):6701–6705, oct 2014.
- [216] L R Sheppard, T Bak, and J Nowotny. Electrical Properties of Niobium-Doped Titanium Dioxide. 1. Defect Disorder. *The Journal of Physical Chemistry B*, 110(45):22447–22454, nov 2006.
- [217] Hiroyuki Kitagawa, Toshimitsu Kunisada, Yasuji Yamada, and Shugo Kubo. Effect of boron-doping on thermoelectric properties of rutile-type titanium dioxide sintered materials. *Journal of Alloys and Compounds*, 508(2):582–586, 2010.
- [218] J Jaćimović, E Horváth, B Náfrádi, R Gaál, N Nikseresht, H Berger, L Forró, and A Magrez. From nanotubes to single crystals: Co doped TiO_2 . *APL Materials*, 1(3):32111, sep 2013.
- [219] Yun Lu, Katsuhiko Sagara, Liang Hao, Ziwu Ji, and Hiroyuki Yoshida. Fabrication of Non-Stoichiometric Titanium Dioxide by Spark Plasma Sintering and Its Thermoelectric Properties. *MATERIALS TRANSACTIONS*, 53(7):1208–1211, 2012.
- [220] Shan Yang, A T Brant, N C Giles, and L E Halliburton. Intrinsic small polarons in rutile TiO_2 . *Physical Review B*, 87(12):125201, mar 2013.
- [221] Peter Deák, Bálint Aradi, and Thomas Frauenheim. Quantitative theory of the oxygen vacancy and carrier self-trapping in bulk TiO_2 . *Physical Review B*, 86(19):195206, nov 2012.
- [222] Liang Zhao, Blanka Magyari-Köpe, and Yoshio Nishi. Polaronic interactions between oxygen vacancies in rutile TiO_2 . *Physical Review B*, 95(5):54104, feb 2017.
- [223] A R Elmaslmane, M B Watkins, and K P McKenna. First-Principles Modeling of Polaron Formation in TiO_2 Polymorphs. *Journal of Chemical Theory and Computation*, 14(7):3740–3751, jul 2018.
- [224] A Janotti, C Franchini, J B Varley, G Kresse, and C G Van de Walle. Dual behavior of excess electrons in rutile TiO_2 . *physica status solidi (RRL) – Rapid Research Letters*, 7(3):199–203, mar 2013.

- [225] N Aaron Deskins and Michel Dupuis. Electron transport via polaron hopping in bulk TiO_2 : A density functional theory characterization. *Physical Review B*, 75(19):195212, may 2007.
- [226] Eiichi Yagi, Ryukiti R Hasiguti, and Masakazu Aono. Electronic conduction above 4 K of slightly reduced oxygen-deficient rutile TiO_{2-x} . *Physical Review B*, 54(11):7945–7956, sep 1996.
- [227] Jochen Heyd, Gustavo E Scuseria, and Matthias Ernzerhof. Hybrid functionals based on a screened Coulomb potential. *The Journal of Chemical Physics*, 118(18):8207–8215, apr 2003.
- [228] Aliaksandr V Krukau, Oleg A Vydrov, Artur F Izmaylov, and Gustavo E Scuseria. Influence of the exchange screening parameter on the performance of screened hybrid functionals. *The Journal of Chemical Physics*, 125(22):224106, dec 2006.
- [229] A Janotti, J B Varley, P Rinke, N Umezawa, G Kresse, and C G Van de Walle. Hybrid functional studies of the oxygen vacancy in TiO_2 . *Physical Review B*, 81(8):85212, feb 2010.
- [230] M Bonn, F Wang, J Shan, T F Heinz, and E Hendry. Ultrafast scattering of electrons in TiO_2 . In Monique M Martin, James T B T Femtochemistry Hynes, and Femtobiology, editors, *Femtochemistry and Femtobiology*, pages 517–520. Elsevier, Amsterdam, 2004.
- [231] Igor Lukačević, Sanjeev K Gupta, Prafulla K Jha, and Davor Kirin. Lattice dynamics and Raman spectrum of rutile TiO_2 : The role of soft phonon modes in pressure induced phase transition. *Materials Chemistry and Physics*, 137(1):282–289, 2012.
- [232] J G Traylor, H G Smith, R M Nicklow, and M K Wilkinson. Lattice Dynamics of Rutile. *Physical Review B*, 3(10):3457–3472, may 1971.
- [233] J T Devreese, S N Klimin, J L M van Mechelen, and D van der Marel. Many-body large polaron optical conductivity in $\text{SrTi}_{1-x}\text{Nb}_x\text{O}_3$. *Physical Review B*, 81(12):125119, mar 2010.
- [234] G Verbist, F M Peeters, and J T Devreese. Extended stability region for large bipolarons through interaction with multiple phonon branches. *Ferroelectrics*, 130(1):27–34, may 1992.
- [235] G A Acket and J Volger. Hall-measurements on slightly reduced rutile (TiO_2). *Physics Letters*, 8(4):244–246, 1964.
- [236] G A Acket and J Volger. On the electron mobility and the donor centres in reduced and lithium-doped rutile (TiO_2). *Physica*, 32(10):1680–1692, 1966.
- [237] G Mattioli, F Filippone, P Alippi, and A Amore Bonapasta. Ab initio study of the electronic states induced by oxygen vacancies in rutile and anatase TiO_2 . *Physical Review B*, 78(24):241201, dec 2008.

- [238] Chungwei Lin, Donghan Shin, and Alexander A Demkov. Localized states induced by an oxygen vacancy in rutile TiO₂. *Journal of Applied Physics*, 117(22):225703, jun 2015.
- [239] Rulin Liu, Liang Fang, Yue Hao, and Yaqing Chi. Influence of Oxygen Vacancy Density on the Polaronic Configuration in Rutile. *Materials (Basel, Switzerland)*, 11(11):2156, nov 2018.
- [240] Emanuele Finazzi, Cristiana Di Valentin, and Gianfranco Pacchioni. Nature of Ti Interstitials in Reduced Bulk Anatase and Rutile TiO₂. *The Journal of Physical Chemistry C*, 113(9):3382–3385, mar 2009.
- [241] Giuseppe Mattioli, Paola Alippi, Francesco Filippone, Ruggero Caminiti, and Aldo Amore Bonapasta. Deep versus Shallow Behavior of Intrinsic Defects in Rutile and Anatase TiO₂ Polymorphs. *The Journal of Physical Chemistry C*, 114(49):21694–21704, dec 2010.
- [242] E N Economou. *Green’s Functions in Quantum Physics*. Springer, 1979.
- [243] Carlos A Polanco and Lucas Lindsay. Ab initio phonon point defect scattering and thermal transport in graphene. *Physical Review B*, 97(1):14303, jan 2018.
- [244] H Bruus and K Flensberg. *Many-body quantum theory in condensed matter physics - an introduction*. Oxford University Press, 2004.
- [245] R J Elliott, J A Krumhansl, and P L Leath. The theory and properties of randomly disordered crystals and related physical systems. *Reviews of Modern Physics*, 46(3):465–543, jul 1974.
- [246] L Schwartz, F Brouers, A V Vedyayev, and H Ehrenreich. Comparison of the Average-*t*-Matrix and Coherent-Potential Approximations in Substitutional Alloys. *Physical Review B*, 4(10):3383–3392, nov 1971.
- [247] P Lloyd. Exactly solvable model of electronic states in a three-dimensional disordered Hamiltonian: non-existence of localized states. *Journal of Physics C: Solid State Physics*, 2(10):1717–1725, 1969.
- [248] Wu Li, Haldun Sevinçli, Stephan Roche, and Gianaurelio Cuniberti. Efficient linear scaling method for computing the thermal conductivity of disordered materials. *Physical Review B*, 83(15):155416, apr 2011.
- [249] J K Flicker and P L Leath. Lattice Thermal Conductivity in High-Concentration Mixed Crystals. *Physical Review B*, 7(6):2296–2305, mar 1973.
- [250] Harold U Baranger and A Douglas Stone. Electrical linear-response theory in an arbitrary magnetic field: A new Fermi-surface formation. *Physical Review B*, 40(12):8169–8193, oct 1989.

- [251] Branislav K Nikolić. Deconstructing Kubo formula usage: Exact conductance of a mesoscopic system from weak to strong disorder limit. *Physical Review B*, 64(16):165303, oct 2001.
- [252] Alexander Altland, Yuval Gefen, and Gilles Montambaux. What is the Thouless Energy for Ballistic Systems? *Physical Review Letters*, 76(7):1130–1133, feb 1996.
- [253] Cord A Müller and Dominique Delande. Disorder and interference: localization phenomena. In *Ultracold Gases and Quantum Information*. Oxford University Press, Oxford, 2011.
- [254] Patrick A Lee and T V Ramakrishnan. Disordered electronic systems. *Reviews of Modern Physics*, 57(2):287–337, apr 1985.
- [255] J T Edwards and D J Thouless. Numerical studies of localization in disordered systems. *Journal of Physics C: Solid State Physics*, 5(8):807–820, 1972.
- [256] Richard Bouzerar. *Theory for disordered localized spins system in interaction with itinerant carriers : diluted magnetic semiconductors*. Theses, Université de Picardie Jules Verne, 2008.
- [257] John C Wheeler, Michael G Prais, and Carl Blumstein. Analysis of spectral densities using modified moments. *Physical Review B*, 10(6):2429–2447, sep 1974.
- [258] D Mayou and S N Khanna. A Real-Space Approach to Electronic Transport. *J. Phys. I France*, 5(9):1199–1211, sep 1995.
- [259] D Mayou, P E A Turchi, S Roche, and J P Julien. Electronic Structure and Transport in Non Periodic Systems: New O(N) Methods. *MRS Proceedings*, 491:231, 1997.
- [260] Stephan Roche and Didier Mayou. Formalism for the computation of the RKKY interaction in aperiodic systems. *Physical Review B*, 60(1):322–328, jul 1999.
- [261] Alexander Weiße, Gerhard Wellein, Andreas Alvermann, and Holger Fehske. The kernel polynomial method. *Reviews of Modern Physics*, 78(1):275–306, mar 2006.
- [262] Aires Ferreira and Eduardo R Mucciolo. Critical Delocalization of Chiral Zero Energy Modes in Graphene. *Physical Review Letters*, 115(10):106601, aug 2015.
- [263] John P Boyd. *Chebyshev and Fourier Spectral Methods*. Dover Books on Mathematics. Dover Publications, Mineola, NY, second edition, 2001.
- [264] Qian Zhang, Bolin Liao, Yucheng Lan, Kevin Lukas, Weishu Liu, Keivan Esfarjani, Cyril Opeil, David Broido, Gang Chen, and Zhifeng Ren. High thermoelectric performance by resonant dopant indium in nanostructured SnTe. *PNAS*, 110:13261–13266, 2013.

- [265] Qinyong Zhang, Hui Wang, Weishu Liu, Hengzhi Wang, Bo Yu, Qian Zhang, Zhiting Tian, George Ni, Sangyeop Lee, Keivan Esfarjani, Gang Chen, and Zhifeng Ren. Enhancement of thermoelectric figure-of-merit by resonant states of aluminium doping in lead selenide. *Energy Environ. Sci.*, 5:5246–5251, 2012.
- [266] Bartłomiej Wiendlocha, Jean-Baptiste Vaney, Christophe Candolfi, Anne Dauscher, Bertrand Lenoir, and Janusz Tobola. An Sn-induced resonant level in β -As₂Te₃. *Physical Chemistry Chemical Physics*, 20(18):12948–12957, 2018.
- [267] J Q Li, X Y Liu, Y Li, S H Song, F S Liu, and W Q Ao. Influence of Sn substitution on the thermoelectric properties in YbAl₃. *Journal of Alloys and Compounds*, 600:8–12, 2014.
- [268] D M Rowe, V L Kuznetsov, L A Kuznetsova, and Gao Min. Electrical and thermal transport properties of intermediate-valence YbAl₃. *Journal of Physics D: Applied Physics*, 35(17):2183–2186, 2002.
- [269] Jian Zhou, Zhimei Sun, Xuan Cheng, and Ying Zhang. Phase stability and electronic structures of YbAl_{3-x}M_x (M=Mg, Cu, Zn, In and Sn) studied by first-principles calculations. *Intermetallics*, 17(12):995–999, 2009.
- [270] H Ebert, J Minár, and D Ködderitzsch. Calculating condensed matter properties using the KKR-Green’s function method—recent developments and applications. *Reports on Progress in Physics*, 74(9):96501, 2011.
- [271] B Wiendlocha, K Kutorasinski, S Kaprzyk, and J Tobola. Recent progress in calculations of electronic and transport properties of disordered thermoelectric materials. *Scripta Materialia*, 111:33–38, 2016.
- [272] Bartłomiej Wiendlocha. Fermi surface and electron dispersion of PbTe doped with resonant Tl impurity from KKR-CPA calculations. *Phys. Rev. B*, 88(20):205205, nov 2013.
- [273] Bartłomiej Wiendlocha. Thermopower of thermoelectric materials with resonant levels: PbTe:Tl versus PbTe:Na and Cu_{1-x}Ni_x. *Phys. Rev. B*, 97(20):205203, 2018.
- [274] S Thébaud, Ch. Adessi, and G Bouzerar. Large enhancement of the thermoelectric power factor in disordered materials through resonant scattering. *Physical Review B*, 99(24):245203, jun 2019.
- [275] Joo-Hyoung Lee, Junqiao Wu, and Jeffrey C Grossman. Enhancing the Thermoelectric Power Factor with Highly Mismatched Isoelectronic Doping. *Phys. Rev. Lett.*, 104(1):16602, jan 2010.
- [276] S Thébaud, Ch. Adessi, S Pailhès, and G Bouzerar. Boosting the power factor with resonant states: A model study. *Physical Review B*, 96(7):75201, aug 2017.

- [277] Changwook Jeong, Raseong Kim, and Mark S Lundstrom. On the best bandstructure for thermoelectric performance: A Landauer perspective. *Journal of Applied Physics*, 111(11):113707, 2012.
- [278] Daniel I Bilc, Geoffroy Hautier, David Waroquiers, Gian-Marco Rignanese, and Philippe Ghosez. Low-Dimensional Transport and Large Thermoelectric Power Factors in Bulk Semiconductors by Band Engineering of Highly Directional Electronic States. *Physical Review Letters*, 114(13):136601, mar 2015.
- [279] Ch. Adessi, S Thebaud, and G Bouzerar. Ab initio investigation of the role of vanadium impurity states in SrTiO₃ for thermoelectricity. Submitted., 2019.
- [280] S Thébaud, Ch. Adessi, and G Bouzerar. Resonant states and Vanadium doping in SrTiO₃, BaTiO₃ and CaTiO₃: effects of disorder and localization on the thermoelectric properties. In prep., 2019.
- [281] Qichen Song, Te-Huan Liu, Jiawei Zhou, Zhiwei Ding, and Gang Chen. Ab initio study of electron mean free paths and thermoelectric properties of lead telluride. *Materials Today Physics*, 2:69–77, 2017.
- [282] David Parker and David J Singh. High-temperature thermoelectric performance of heavily doped PbSe. *Phys. Rev. B*, 82:35204, 2010.
- [283] Haowei Peng, Jung-Hwan Song, M G Kanatzidis, and Arthur J Freeman. Electronic structure and transport properties of doped PbSe. *Phys. Rev. B*, 84(12):125207, sep 2011.
- [284] Zhao Wang, Shidong Wang, Sergey Obukhov, Nathalie Vast, Jelena Sjakste, Valery Tyuterev, and Natalio Mingo. Thermoelectric transport properties of silicon: Toward an ab initio approach. *Physical Review B*, 83(20):205208, may 2011.
- [285] D A Greenwood. The Boltzmann Equation in the Theory of Electrical Conduction in Metals. *Proceedings of the Physical Society*, 71(4):585, 1958.
- [286] Jiawei Zhou, Hangtian Zhu, Te-Huan Liu, Qichen Song, Ran He, Jun Mao, Zihang Liu, Wuyang Ren, Bolin Liao, David J Singh, Zhifeng Ren, and Gang Chen. Large thermoelectric power factor from crystal symmetry-protected non-bonding orbital in half-Heuslers. *Nature Communications*, 9(1):1721, 2018.
- [287] Evan Witkoske, Xufeng Wang, Mark Lundstrom, Vahid Askarpour, and Jesse Maassen. Thermoelectric band engineering: The role of carrier scattering. *Journal of Applied Physics*, 122(17):175102, nov 2017.
- [288] Li Juan Zhang, Peng Qin, Chao Han, Jian Li Wang, Zhen Hua Ge, Qiao Sun, Zhen Xiang Cheng, Zhen Li, and Shi Xue Dou. Enhanced thermoelectric performance through synergy of resonance levels and valence band convergence via Q/In (Q = Mg, Ag, Bi) co-doping. *J. Mater. Chem. A*, 6(6):2507–2516, 2018.

- [289] Juan J Meléndez and Robert L González-Romero. zT factors in Ag- and Na-doped SnSe: Chemical potentials, relaxation times and predictions for other dopant species. *Journal of Alloys and Compounds*, 757:70–78, 2018.
- [290] V E Boeisenko and S G Yudin. Steady-state solubility of substitutional impurities in silicon. *physica status solidi (a)*, 101(1):123–127, may 1987.
- [291] Daniel I. Bilc and Philippe Ghosez. Electronic and thermoelectric properties of Fe₂VAl: The role of defects and disorder. *Physical Review B*, 83(20):205204, 2011.
- [292] David Parker, Xin Chen, and David J Singh. High Three-Dimensional Thermoelectric Performance from Low-Dimensional Bands. *Phys. Rev. Lett.*, 110(14):146601, 2013.
- [293] Zhicheng Zhong, Philipp Wissgott, Karsten Held, and Giorgio Sangiovanni. Microscopic understanding of the orbital splitting and its tuning at oxide interfaces. *EPL (Europhysics Letters)*, 99(3):37011, 2012.
- [294] S V Morozov, K S Novoselov, M I Katsnelson, F Schedin, D C Elias, J A Jaszczak, and A K Geim. Giant Intrinsic Carrier Mobilities in Graphene and Its Bilayer. *Physical Review Letters*, 100(1):16602, jan 2008.
- [295] A H Castro Neto, F Guinea, N M R Peres, K S Novoselov, and A K Geim. The electronic properties of graphene. *Reviews of Modern Physics*, 81(1):109–162, jan 2009.
- [296] Dambi Park, Sungjin Park, Kwangsik Jeong, Hong-Sik Jeong, Jea Yong Song, and Mann-Ho Cho. Thermal and Electrical Conduction of Single-crystal Bi₂Te₃ Nanostructures grown using a one step process. *Scientific Reports*, 6:19132, jan 2016.
- [297] Mi-Kyung Han, Yingshi Jin, Da-Hee Lee, and Sung-Jin Kim. Thermoelectric Properties of Bi₂Te₃: CuI and the Effect of Its Doping with Pb Atoms. *Materials (Basel, Switzerland)*, 10(11):1235, oct 2017.
- [298] Raseong Kim, Supriyo Datta, and Mark S Lundstrom. Influence of dimensionality on thermoelectric device performance. *Journal of Applied Physics*, 105(3):34506, feb 2009.
- [299] Haruhiko Obara, Atsushi Yamamoto, Chul-Ho Lee, Keizo Kobayashi, Akihiro Matsumoto, and Ryoji Funahashi. Thermoelectric Properties of Y-Doped Polycrystalline SrTiO₃. *Japanese Journal of Applied Physics*, 43(No. 4B):L540–L542, 2004.
- [300] Rui-zhi Zhang, Xiao-yun Hu, Ping Guo, and Chun-lei Wang. Thermoelectric transport coefficients of n-doped CaTiO₃, SrTiO₃ and BaTiO₃: A theoretical study. *Physica B: Condensed Matter*, 407(7):1114–1118, 2012.
- [301] K S Novoselov, A K Geim, S V Morozov, D Jiang, Y Zhang, S V Dubonos, I V Grigorieva, and A A Firsov. Electric Field Effect in Atomically Thin Carbon Films. *Science*, 306(5696):666 LP – 669, oct 2004.

- [302] Sheneve Z Butler, Shawna M Hollen, Linyou Cao, Yi Cui, Jay A Gupta, Humberto R Gutiérrez, Tony F Heinz, Seung Sae Hong, Jiaxing Huang, Ariel F Ismach, Ezekiel Johnston-Halperin, Masaru Kuno, Vladimir V Plashnitsa, Richard D Robinson, Rodney S Ruoff, Sayeef Salahuddin, Jie Shan, Li Shi, Michael G Spencer, Mauricio Terrones, Wolfgang Windl, and Joshua E Goldberger. Progress, Challenges, and Opportunities in Two-Dimensional Materials Beyond Graphene. *ACS Nano*, 7(4):2898–2926, apr 2013.
- [303] Ganesh R Bhimanapati, Zhong Lin, Vincent Meunier, Yeonwoong Jung, Judy Cha, Saptarshi Das, Di Xiao, Youngwoo Son, Michael S Strano, Valentino R Cooper, Liangbo Liang, Steven G Louie, Emilie Ringe, Wu Zhou, Steve S Kim, Rajesh R Naik, Bobby G Sumpter, Humberto Terrones, Fengnian Xia, Yeliang Wang, Jun Zhu, Deji Akinwande, Nasim Alem, Jon A Schuller, Raymond E Schaak, Mauricio Terrones, and Joshua A Robinson. Recent Advances in Two-Dimensional Materials beyond Graphene. *ACS Nano*, 9(12):11509–11539, dec 2015.
- [304] Claire Berger, Zhimin Song, Xuebin Li, Xiaosong Wu, Nate Brown, Cécile Naud, Didier Mayou, Tianbo Li, Joanna Hass, Alexei N Marchenkov, Edward H Conrad, Phillip N First, and Walt A de Heer. Electronic Confinement and Coherence in Patterned Epitaxial Graphene. *Science*, 312(5777):1191 LP – 1196, may 2006.
- [305] K S Novoselov, V I Falko, L Colombo, P R Gellert, M G Schwab, and K Kim. A roadmap for graphene. *Nature*, 490:192, oct 2012.
- [306] A K Geim. Graphene: Status and Prospects. *Science*, 324(5934):1530 LP – 1534, jun 2009.
- [307] G Trambly de Laissardiére, D Mayou, and L Magaud. Localization of Dirac Electrons in Rotated Graphene Bilayers. *Nano Letters*, 10(3):804–808, mar 2010.
- [308] I Brihuega, P Mallet, H González-Herrero, G Trambly de Laissardiére, M M Ugeda, L Magaud, J M Gómez-Rodríguez, F Ynduráin, and J.-Y. Veuillen. Unraveling the Intrinsic and Robust Nature of van Hove Singularities in Twisted Bilayer Graphene by Scanning Tunneling Microscopy and Theoretical Analysis. *Physical Review Letters*, 109(19):196802, nov 2012.
- [309] Eric Pop, Vikas Varshney, and Ajit K Roy. Thermal properties of graphene: Fundamentals and applications. *MRS Bulletin*, 37(12):1273–1281, 2012.
- [310] A Molina-Sánchez and L Wirtz. Phonons in single-layer and few-layer MoS₂ and WS₂. *Physical Review B*, 84(15):155413, oct 2011.
- [311] Alexander A Balandin, Suchismita Ghosh, Wenzhong Bao, Irene Calizo, Desalegne Teweldebrhan, Feng Miao, and Chun Ning Lau. Superior Thermal Conductivity of Single-Layer Graphene. *Nano Letters*, 8(3):902–907, mar 2008.
- [312] Denis L Nika and Alexander A Balandin. Two-dimensional phonon transport in graphene. *Journal of Physics: Condensed Matter*, 24(23):233203, 2012.

- [313] Alexander A Balandin and Denis L Nika. Phononics in low-dimensional materials. *Materials Today*, 15(6):266–275, 2012.
- [314] Yong Xu, Zuanyi Li, and Wenhui Duan. Thermal and thermoelectric properties of graphene, 2014.
- [315] Ch. Adessi, S Thebaud, R Bouzerar, and G Bouzerar. First Principle Investigation on Thermoelectric Properties of Transition Metal Dichalcogenides: Beyond the Rigid Band Model. *The Journal of Physical Chemistry C*, 121(23):12577–12584, jun 2017.
- [316] G Bouzerar, S Thébaud, S Pecorario, and Ch. Adessi. Drastic effects of vacancies on phonon lifetime and thermal conductivity in graphene. Submitted., 2019.
- [317] S Thébaud, Ch. Adessi, and G Bouzerar. Phonon transport in finite-size and irradiated graphene. In prep.
- [318] Kin Fai Mak, Changgu Lee, James Hone, Jie Shan, and Tony F Heinz. Atomically Thin MoS₂: A New Direct-Gap Semiconductor. *Physical Review Letters*, 105(13):136805, sep 2010.
- [319] Eugene S Kadantsev and Pawel Hawrylak. Electronic structure of a single MoS₂ monolayer. *Solid State Communications*, 152(10):909–913, 2012.
- [320] B Radisavljevic, A Radenovic, J Brivio, V Giacometti, and A Kis. Single-layer MoS₂ transistors. *Nature Nanotechnology*, 6:147, jan 2011.
- [321] Dominik Lembke and Andras Kis. Breakdown of High-Performance Monolayer MoS₂ Transistors. *ACS Nano*, 6(11):10070–10075, nov 2012.
- [322] Saptarshi Das, Hong-Yan Chen, Ashish Verma Penumatcha, and Joerg Appenzeller. High Performance Multilayer MoS₂ Transistors with Scandium Contacts. *Nano Letters*, 13(1):100–105, jan 2013.
- [323] Zelin Jin, Quanwen Liao, Haisheng Fang, Zhichun Liu, Wei Liu, Zhidong Ding, Tengfei Luo, and Nuo Yang. A Revisit to High Thermoelectric Performance of Single-layer MoS₂. *Scientific Reports*, 5:18342, dec 2015.
- [324] Wen Huang, Haixia Da, and Gengchiao Liang. Thermoelectric performance of MX₂ (M = Mo,W; X = S,Se) monolayers. *Journal of Applied Physics*, 113(10):104304, mar 2013.
- [325] D D Fan, H J Liu, L Cheng, P H Jiang, J Shi, and X F Tang. MoS₂ nanoribbons as promising thermoelectric materials. *Applied Physics Letters*, 105(13):133113, sep 2014.
- [326] Wen Huang, Xin Luo, Chee Kwan Gan, Su Ying Quek, and Gengchiao Liang. Theoretical study of thermoelectric properties of few-layer MoS₂ and WSe₂. *Physical Chemistry Chemical Physics*, 16(22):10866–10874, 2014.

- [327] Hasan Babaei, J M Khodadadi, and Sanjiv Sinha. Large theoretical thermoelectric power factor of suspended single-layer MoS₂. *Applied Physics Letters*, 105(19):193901, nov 2014.
- [328] Rui-Ning Wang, Guo-Yi Dong, Shu-Fang Wang, Guang-Sheng Fu, and Jiang-Long Wang. Variations of thermoelectric performance by electric fields in bilayer MX₂ (M = W, Mo; X = S, Se). *Physical Chemistry Chemical Physics*, 19(8):5797–5805, 2017.
- [329] Jing Wu, Hennrik Schmidt, Kiran Kumar Amara, Xiangfan Xu, Goki Eda, and Barbaros Özyilmaz. Large Thermoelectricity via Variable Range Hopping in Chemical Vapor Deposition Grown Single-Layer MoS₂. *Nano Letters*, 14(5):2730–2734, may 2014.
- [330] Masaro Yoshida, Takahiko Iizuka, Yu Saito, Masaru Onga, Ryuji Suzuki, Yijin Zhang, Yoshihiro Iwasa, and Sunao Shimizu. Gate-Optimized Thermoelectric Power Factor in Ultrathin WSe₂ Single Crystals. *Nano Letters*, 16(3):2061–2065, mar 2016.
- [331] Tongzhou Wang, Congcong Liu, Jingkun Xu, Zhengyou Zhu, Endou Liu, Yongjing Hu, Changcun Li, and Fengxing Jiang. Thermoelectric performance of restacked MoS₂ nanosheets thin-film. *Nanotechnology*, 27(28):285703, 2016.
- [332] Rusen Yan, Jeffrey R Simpson, Simone Bertolazzi, Jacopo Brivio, Michael Watson, Xufei Wu, Andras Kis, Tengfei Luo, Angela R Hight Walker, and Huili Grace Xing. Thermal Conductivity of Monolayer Molybdenum Disulfide Obtained from Temperature-Dependent Raman Spectroscopy. *ACS Nano*, 8(1):986–993, jan 2014.
- [333] Insun Jo, Michael Thompson Pettes, Eric Ou, Wei Wu, and Li Shi. Basal-plane thermal conductivity of few-layer molybdenum disulfide. *Applied Physics Letters*, 104(20):201902, may 2014.
- [334] Satyaprakash Sahoo, Anand P S Gaur, Majid Ahmadi, Maxime J.-F. Guinel, and Ram S Katiyar. Temperature-Dependent Raman Studies and Thermal Conductivity of Few-Layer MoS₂. *The Journal of Physical Chemistry C*, 117(17):9042–9047, may 2013.
- [335] Jung Jun Bae, Hye Yun Jeong, Gang Hee Han, Jaesu Kim, Hyun Kim, Min Su Kim, Byoung Hee Moon, Seong Chu Lim, and Young Hee Lee. Thickness-dependent in-plane thermal conductivity of suspended MoS₂ grown by chemical vapor deposition. *Nanoscale*, 9(7):2541–2547, 2017.
- [336] Li-Dong Zhao, Shih-Han Lo, Yongsheng Zhang, Hui Sun, Gangjian Tan, Ctirad Uher, C Wolverton, Vinayak P Dravid, and Mercouri G Kanatzidis. Ultralow thermal conductivity and high thermoelectric figure of merit in SnSe crystals. *Nature*, 508:373, apr 2014.
- [337] Joonki Suh, Tae-Eon Park, Der-Yuh Lin, Deyi Fu, Joonsuk Park, Hee Joon Jung, Yabin Chen, Changhyun Ko, Chaun Jang, Yinghui Sun, Robert Sinclair, Joonyeon

- Chang, Sefaattin Tongay, and Junqiao Wu. Doping against the Native Propensity of MoS₂: Degenerate Hole Doping by Cation Substitution. *Nano Letters*, 14(12):6976–6982, dec 2014.
- [338] Ankur Nipane, Debjani Karmakar, Naveen Kaushik, Shruti Karande, and Saurabh Lodha. Few-Layer MoS₂ p-Type Devices Enabled by Selective Doping Using Low Energy Phosphorus Implantation. *ACS Nano*, 10(2):2128–2137, feb 2016.
- [339] Lingming Yang, Kausik Majumdar, Han Liu, Yuchen Du, Heng Wu, Michael Hatzistergos, P Y Hung, Robert Tieckelmann, Wilman Tsai, Chris Hobbs, and Peide D Ye. Chloride Molecular Doping Technique on 2D Materials: WS₂ and MoS₂. *Nano Letters*, 14(11):6275–6280, nov 2014.
- [340] Stephen McDonnell, Rafik Addou, Creighton Buie, Robert M Wallace, and Christopher L Hinkle. Defect-Dominated Doping and Contact Resistance in MoS₂. *ACS Nano*, 8(3):2880–2888, mar 2014.
- [341] Shuang Kong, Tianmin Wu, Min Yuan, Zhiwei Huang, Qing-Long Meng, Qike Jiang, Wei Zhuang, Peng Jiang, and Xinhe Bao. Dramatically enhanced thermoelectric performance of MoS₂ by introducing MoO₂ nanoinclusions. *Journal of Materials Chemistry A*, 5(5):2004–2011, 2017.
- [342] Hui Fang, Mahmut Tosun, Gyungseon Seol, Ting Chia Chang, Kuniharu Takei, Jing Guo, and Ali Javey. Degenerate n-Doping of Few-Layer Transition Metal Dichalcogenides by Potassium. *Nano Letters*, 13(5):1991–1995, may 2013.
- [343] Viet Phuong Pham and Geun Young Yeom. Recent Advances in Doping of Molybdenum Disulfide: Industrial Applications and Future Prospects. *Advanced Materials*, 28(41):9024–9059, nov 2016.
- [344] Z Y Zhu, Y C Cheng, and U Schwingenschlögl. Giant spin-orbit-induced spin splitting in two-dimensional transition-metal dichalcogenide semiconductors. *Physical Review B*, 84(15):153402, oct 2011.
- [345] Supriyo Datta. *Quantum Transport: Atom to Transistor*. Cambridge University Press, Cambridge, 2005.
- [346] Ch. Adessi, Stephan Roche, and X Blase. Reduced backscattering in potassium-doped nanotubes: Ab initio and semiempirical simulations. *Physical Review B*, 73(12):125414, mar 2006.
- [347] Mads Brandbyge, José-Luis Mozos, Pablo Ordejón, Jeremy Taylor, and Kurt Stokbro. Density-functional method for nonequilibrium electron transport. *Physical Review B*, 65(16):165401, mar 2002.
- [348] Darshana Wickramaratne, Ferdows Zahid, and Roger K Lake. Electronic and thermoelectric properties of few-layer transition metal dichalcogenides. *The Journal of Chemical Physics*, 140(12):124710, mar 2014.

- [349] K K Tiong, P C Liao, C H Ho, and Y S Huang. Growth and characterization of rhenium-doped MoS₂ single crystals. *Journal of Crystal Growth*, 205(4):543–547, 1999.
- [350] X D Li, Y M Fang, S Q Wu, and Z Z Zhu. Adsorption of alkali, alkaline-earth, simple and 3d transition metal, and nonmetal atoms on monolayer MoS₂. *AIP Advances*, 5(5):57143, may 2015.
- [351] Priyank Rastogi, Sanjay Kumar, Somnath Bhowmick, Amit Agarwal, and Yogesh Singh Chauhan. Doping Strategies for Monolayer MoS₂ via Surface Adsorption: A Systematic Study. *The Journal of Physical Chemistry C*, 118(51):30309–30314, dec 2014.
- [352] Jiwon Chang, Stefano Larentis, Emanuel Tutuc, Leonard F Register, and Sanjay K Banerjee. Atomistic simulation of the electronic states of adatoms in monolayer MoS₂. *Applied Physics Letters*, 104(14):141603, apr 2014.
- [353] Kristen Kaasbjerg, Kristian S Thygesen, and Karsten W Jacobsen. Phonon-limited mobility in *n*-type single-layer MoS₂ from first principles. *Physical Review B*, 85(11):115317, mar 2012.
- [354] Rolf Landauer. Electrical resistance of disordered one-dimensional lattices. *The Philosophical Magazine: A Journal of Theoretical Experimental and Applied Physics*, 21(172):863–867, apr 1970.
- [355] A K Geim and K S Novoselov. The rise of graphene. *Nature Materials*, 6:183, mar 2007.
- [356] S Ghosh, I Calizo, D Teweldebrhan, E P Pokatilov, D L Nika, A A Balandin, W Bao, F Miao, and C N Lau. Extremely high thermal conductivity of graphene: Prospects for thermal management applications in nanoelectronic circuits. *Applied Physics Letters*, 92(15):151911, apr 2008.
- [357] Weiwei Cai, Arden L Moore, Yanwu Zhu, Xuesong Li, Shanshan Chen, Li Shi, and Rodney S Ruoff. Thermal Transport in Suspended and Supported Monolayer Graphene Grown by Chemical Vapor Deposition. *Nano Letters*, 10(5):1645–1651, may 2010.
- [358] Shanshan Chen, Arden L Moore, Weiwei Cai, Ji Won Suk, Jinho An, Columbia Mishra, Charles Amos, Carl W Magnuson, Junyong Kang, Li Shi, and Rodney S Ruoff. Raman Measurements of Thermal Transport in Suspended Monolayer Graphene of Variable Sizes in Vacuum and Gaseous Environments. *ACS Nano*, 5(1):321–328, jan 2011.
- [359] Ravi S Prasher, X J Hu, Y Chalopin, Natalio Mingo, K Lofgreen, S Volz, F Cleri, and Pawel Keblinski. Turning Carbon Nanotubes from Exceptional Heat Conductors into Insulators. *Physical Review Letters*, 102(10):105901, mar 2009.

- [360] H Sevinçli and G Cuniberti. Enhanced thermoelectric figure of merit in edge-disordered zigzag graphene nanoribbons. *Physical Review B*, 81(11):113401, mar 2010.
- [361] Jae Hun Seol, Insun Jo, Arden L Moore, Lucas Lindsay, Zachary H Aitken, Michael T Pettes, Xuesong Li, Zhen Yao, Rui Huang, David Broido, Natalio Mingo, Rodney S Ruoff, and Li Shi. Two-Dimensional Phonon Transport in Supported Graphene. *Science*, 328(5975):213 LP – 216, apr 2010.
- [362] Suchismita Ghosh, Wenzhong Bao, Denis L Nika, Samia Subrina, Evghenii P Pokatilov, Chun Ning Lau, and Alexander A Balandin. Dimensional crossover of thermal transport in few-layer graphene. *Nature Materials*, 9:555, may 2010.
- [363] Asanka Weerasinghe, Ashwin Ramasubramaniam, and Dimitrios Maroudas. Thermal conductivity of electron-irradiated graphene. *Applied Physics Letters*, 111(16):163101, oct 2017.
- [364] Guofeng Xie, Yulu Shen, Xiaolin Wei, Liwen Yang, Huaping Xiao, Jianxin Zhong, and Gang Zhang. A bond-order theory on the phonon scattering by vacancies in two-dimensional materials. *Scientific reports*, 4:5085, may 2014.
- [365] Giorgia Fugallo, Andrea Cepellotti, Lorenzo Paulatto, Michele Lazzeri, Nicola Marzari, and Francesco Mauri. Thermal Conductivity of Graphene and Graphite: Collective Excitations and Mean Free Paths. *Nano Letters*, 14(11):6109–6114, nov 2014.
- [366] Lorenzo Paulatto, Francesco Mauri, and Michele Lazzeri. Anharmonic properties from a generalized third-order ab initio approach: Theory and applications to graphite and graphene. *Physical Review B*, 87(21):214303, jun 2013.
- [367] L Lindsay, D A Broido, and Natalio Mingo. Flexural phonons and thermal transport in multilayer graphene and graphite. *Physical Review B*, 83(23):235428, jun 2011.
- [368] William J Evans, Lin Hu, and Pawel Keblinski. Thermal conductivity of graphene ribbons from equilibrium molecular dynamics: Effect of ribbon width, edge roughness, and hydrogen termination. *Applied Physics Letters*, 96(20):203112, may 2010.
- [369] Ludger Wirtz and Angel Rubio. The phonon dispersion of graphite revisited. *Solid State Communications*, 131(3):141–152, 2004.
- [370] M Mohr, J Maultzsch, E Dobardžić, S Reich, I Milošević, M Damnjanović, A Bosak, M Krisch, and C Thomsen. Phonon dispersion of graphite by inelastic x-ray scattering. *Physical Review B*, 76(3):35439, jul 2007.
- [371] J Maultzsch, S Reich, C Thomsen, H Requardt, and P Ordejón. Phonon Dispersion in Graphite. *Physical Review Letters*, 92(7):75501, feb 2004.
- [372] S Roche and D Mayou. Conductivity of Quasiperiodic Systems: A Numerical Study. *Physical Review Letters*, 79(13):2518–2521, sep 1997.

- [373] Paul G Klemens. Phonon scattering by oxygen vacancies in ceramics. *Physica B: Condensed Matter*, 263-264:102–104, 1999.
- [374] Hoda Malekpour, Pankaj Ramnani, Srilok Srinivasan, Ganesh Balasubramanian, Denis L Nika, Ashok Mulchandani, Roger K Lake, and Alexander A Balandin. Thermal conductivity of graphene with defects induced by electron beam irradiation. *Nanoscale*, 8(30):14608–14616, 2016.
- [375] L Lindsay, Wu Li, Jesús Carrete, Natalio Mingo, D A Broido, and T L Reinecke. Phonon thermal transport in strained and unstrained graphene from first principles. *Physical Review B*, 89(15):155426, apr 2014.
- [376] M Omini and A Sparavigna. An iterative approach to the phonon Boltzmann equation in the theory of thermal conductivity. *Physica B: Condensed Matter*, 212(2):101–112, 1995.
- [377] M Omini and A Sparavigna. Beyond the isotropic-model approximation in the theory of thermal conductivity. *Physical Review B*, 53(14):9064–9073, apr 1996.
- [378] D A Broido, M Malorny, G Birner, Natalio Mingo, and D A Stewart. Intrinsic lattice thermal conductivity of semiconductors from first principles. *Applied Physics Letters*, 91(23):231922, dec 2007.
- [379] Keivan Esfarjani, Gang Chen, and Harold T Stokes. Heat transport in silicon from first-principles calculations. *Physical Review B*, 84(8):85204, aug 2011.
- [380] A Ward, D A Broido, Derek A Stewart, and G Deinzer. Ab initio theory of the lattice thermal conductivity in diamond. *Physical Review B*, 80(12):125203, sep 2009.
- [381] Jesús Carrete, Wu Li, Natalio Mingo, Shidong Wang, and Stefano Curtarolo. Finding Unprecedentedly Low-Thermal-Conductivity Half-Heusler Semiconductors via High-Throughput Materials Modeling. *Physical Review X*, 4(1):11019, feb 2014.
- [382] L Lindsay, D A Broido, and Natalio Mingo. Flexural phonons and thermal transport in graphene. *Physical Review B*, 82(11):115427, sep 2010.
- [383] A Ward and D A Broido. Intrinsic phonon relaxation times from first-principles studies of the thermal conductivities of Si and Ge. *Physical Review B*, 81(8):85205, feb 2010.
- [384] M G Holland. Analysis of Lattice Thermal Conductivity. *Physical Review*, 132(6):2461–2471, dec 1963.
- [385] D T Morelli, J P Heremans, and G A Slack. Estimation of the isotope effect on the lattice thermal conductivity of group IV and group III-V semiconductors. *Physical Review B*, 66(19):195304, nov 2002.
- [386] G P Srivastava. *The Physics of Phonons*. Taylor & Francis, 1990.

- [387] Y Y Zhang, Y Cheng, Q X Pei, C M Wang, and Y Xiang. Thermal conductivity of defective graphene. *Physics Letters A*, 376(47):3668–3672, 2012.
- [388] Hengji Zhang, Geunsik Lee, and Kyeongjae Cho. Thermal transport in graphene and effects of vacancy defects. *Physical Review B*, 84(11):115460, sep 2011.
- [389] Xiangfan Xu, Luiz F C Pereira, Yu Wang, Jing Wu, Kaiwen Zhang, Xiangming Zhao, Sukang Bae, Cong Tinh Bui, Rongguo Xie, John T L Thong, Byung Hee Hong, Kian Ping Loh, Davide Donadio, Baowen Li, and Barbaros Özyilmaz. Length-dependent thermal conductivity in suspended single-layer graphene. *Nature Communications*, 5:3689, apr 2014.
- [390] Qin-Yi Li, Kailun Xia, Ji Zhang, Yingying Zhang, Qunyang Li, Koji Takahashi, and Xing Zhang. Measurement of specific heat and thermal conductivity of supported and suspended graphene by a comprehensive Raman optothermal method. *Nanoscale*, 9(30):10784–10793, 2017.
- [391] Clement Faugeras, Blaise Faugeras, Milan Orlita, M Potemski, Rahul R Nair, and A K Geim. Thermal Conductivity of Graphene in Corbino Membrane Geometry. *ACS Nano*, 4(4):1889–1892, apr 2010.
- [392] D L Nika, E P Pokatilov, A S Askerov, and A A Balandin. Phonon thermal conduction in graphene: Role of Umklapp and edge roughness scattering. *Physical Review B*, 79(15):155413, apr 2009.
- [393] Gerardo G Naumis, Salvador Barraza-Lopez, Maurice Oliva-Leyva, and Humberto Terrones. Electronic and optical properties of strained graphene and other strained 2D materials: a review. *Reports on Progress in Physics*, 80(9):96501, 2017.
- [394] Nuno J. G. Couto, Davide Costanzo, Stephan Engels, Dong-Keun Ki, Kenji Watanabe, Takashi Taniguchi, Christoph Stampfer, Francisco Guinea, and Alberto F Morpurgo. Random Strain Fluctuations as Dominant Disorder Source for High-Quality On-Substrate Graphene Devices. *Physical Review X*, 4(4):41019, oct 2014.
- [395] Juraj Hašík, Erio Tosatti, and Roman Martoňák. Quantum and classical ripples in graphene. *Physical Review B*, 97(14):140301, apr 2018.
- [396] Jinyao Tang, Hung-Ta Wang, Dong Hyun Lee, Melissa Fardy, Ziyang Huo, Thomas P Russell, and Peidong Yang. Holey Silicon as an Efficient Thermoelectric Material. *Nano Letters*, 10(10):4279–4283, oct 2010.
- [397] Jin Fang. *Thermal Transport in Nanoporous Materials for Energy Applications*. PhD thesis, University of California Los Angeles, 2012.
- [398] Gabi Schierning. Silicon nanostructures for thermoelectric devices: A review of the current state of the art. *physica status solidi (a)*, 211(6):1235–1249, jun 2014.
- [399] Joo-Hyoung Lee, Giulia A Galli, and Jeffrey C Grossman. Nanoporous Si as an Efficient Thermoelectric Material. *Nano Letters*, 8(11):3750–3754, nov 2008.

- [400] Stefanie Wolf, Neophytos Neophytou, and Hans Kosina. Thermal conductivity of silicon nanomeshes: Effects of porosity and roughness. *Journal of Applied Physics*, 115(20):204306, may 2014.
- [401] J de Boor, D S Kim, X Ao, D Hagen, A Cojocaru, H Föll, and V Schmidt. Temperature and structure size dependence of the thermal conductivity of porous silicon. *EPL (Europhysics Letters)*, 96(1):16001, 2011.
- [402] Dechao Geng, Bin Wu, Yunlong Guo, Birong Luo, Yunzhou Xue, Jianyi Chen, Gui Yu, and Yunqi Liu. Fractal Etching of Graphene. *Journal of the American Chemical Society*, 135(17):6431–6434, may 2013.
- [403] Jian Shang, Yongfeng Wang, Min Chen, Jingxin Dai, Xiong Zhou, Julian Kuttner, Gerhard Hilt, Xiang Shao, J Michael Gottfried, and Kai Wu. Assembling molecular Sierpiński triangle fractals. *Nature Chemistry*, 7:389, mar 2015.
- [404] H García-Cervantes, L M Gaggero-Sager, D S Díaz-Guerrero, O Sotolongo-Costa, and I Rodríguez-Vargas. Self-similar conductance patterns in graphene Cantor-like structures. *Scientific Reports*, 7(1):617, 2017.
- [405] Yang Kang, Fuyan Duan, Shaoxin Shangguan, Yixin Zhang, Tianpei Zhou, and Bingcheng Si. Thermal Transport of Graphene Sheets with Fractal Defects. *Molecules (Basel, Switzerland)*, 23(12):3294, dec 2018.
- [406] Edo van Veen, Shengjun Yuan, Mikhail I Katsnelson, Marco Polini, and Andrea Tomadin. Quantum transport in Sierpinski carpets. *Physical Review B*, 93(11):115428, mar 2016.
- [407] Edo van Veen, Andrea Tomadin, Marco Polini, Mikhail I Katsnelson, and Shengjun Yuan. Optical conductivity of a quantum electron gas in a Sierpinski carpet. *Physical Review B*, 96(23):235438, dec 2017.
- [408] E L da Rocha and C R da Cunha. The transition from fracton to phonon states in a Sierpinski triangle lattice. *Chaos, Solitons & Fractals*, 44(4):241–247, 2011.